On the Cutting Edge of Semiconductor Sensors

Towards Intelligent X-ray Detectors

Marten Jan Bosma

On the Cutting Edge of Semiconductor Sensors

Towards Intelligent X-ray Detectors

ACADEMISCH PROEFSCHRIFT

ter verkrijging van de graad van doctor
aan de Universiteit van Amsterdam
op gezag van de Rector Magnificus
prof. dr. D.C. van den Boom
ten overstaan van een door het college voor promoties ingestelde
commissie, in het openbaar te verdedigen in de Agnietenkapel
op vrijdag 21 december 2012, te 12:00 uur

door

Marten Jan Bosma

geboren te Heemstede

Promotor:	prof. dr. ir. E.N. Koffeman
Co-promotores:	dr. M.G. van Beuzekom
	dr. J. Visser
Overige leden:	prof. dr. J.F.J. van den Brand
	prof. dr. ir. P.J. de Jong
	prof. dr. P.M. Kooijman
	prof. dr. F.L. Linde
	prof. dr. H.B. van Linden van den Heuvell
	dr. A.P. Colijn
	dr. E.H.M. Heijne

Faculteit der Natuurwetenschappen, Wiskunde en Informatica

ISBN: 978-94-6191-535-1

This work is part of the research programme of the Foundation for Fundamental Research on Matter (FOM), which is part of the Netherlands Organisation for Scientific Research (NWO). It has been supported by NL Agency, which is a division of the Dutch Ministry of Economic Affairs, Agriculture and Innovation. The research was carried out at the National Institute for Subatomic Physics (Nikhef) in Amsterdam, the Netherlands, and at the European Organisation for Nuclear Research (CERN) in Geneva, Switzerland.

Contents

Introduction

X-rays are often used to image objects or structures that are invisible to the human eye, for example to examine the interior of the human body. Medical radiography allows for diagnosing problems or monitoring minimally invasive surgery, such as Dotter procedures[1], without physically entering the body. That does not mean, though, that X-ray imaging can be considered non-invasive. X-rays are ionising and consequently damage tissue cells. The amount of radiation absorbed by the patient should therefore be kept to a minimum. Image quality, however, strongly benefits from a high dose of X-rays. Hence, a compromise must be found between the maximum allowable dose and the image quality needed. This trade-off poses stringent demands on the performance of a detector.

Today, many medical radiography systems use flat-panel detectors, because flat-panel technology enables fabrication of electronic circuits over large areas and therefore gives access to human digital radiography. In combination with large-area sensors that convert X-rays directly into a measurable signal, such as photoconductive amorphous selenium, these detectors can provide good-quality images of large size.

Yet, current flat-panel detectors have a couple of shortcomings. First, they measure intensity by integrating the amount of charge generated by X-ray conversion in the sensor. As a result, high-energy photons count more than low-energy ones, at the expense of the signal-to-noise ratio. Secondly, the efficiency with which amorphous semiconductor material converts X-ray photons into a measurable signal is moderate. As a consequence, a substantial fraction of X-ray photons is not detected and the dose needed is higher than ideally required.

A promising candidate that could provide better image quality while using a lower dose of X-rays, is a detector that combines a high-quality crystalline semiconductor sensor with an intelligent photon counting chip (the Medipix-3 chip). This chip measures photon intensity by counting the number of converted X-rays, while determining the energy of the photon at the same time. This enables to correct for the energy dependence of the intensity attenuation through the object under study. Output images of such photon counters are therefore in better agreement with the actual X-ray intensity distribution than those of charge integrating detectors. This sophisticated way of signal processing is achieved by advanced electronic circuits that are realised in pixels of only (55 µm)^2

[1]Named after Charles Theodore Dotter, who invented angioplasty and the catheter-delivered stent.

by commercial chip processing technologies that enable fabrication of ultra-small scaled[2] electronic components. An important limitation of this technology, however, is that the probability of a circuit imperfection scales with the chip's area. Hence, such pixel chips can only be fabricated cost effectively if the maximum area is restricted. Concretely, the area of Medipix chips is limited to approximately 2 cm^2. In addition, the area of currently available semiconductor crystals that are suitable for absorbing X-rays of diagnostic energies, is limited to approximately 10 cm^2. Hence, to compete with current radiography detectors, the area of Medipix-based detectors must be increased. One solution is to realise a tessellation of multiple Medipix detectors. However, current Medipix-based detectors are insensitive at their edges and would therefore introduce seams in a tessellated image. Edgeless detectors, i.e. detectors with minimal inactive area at the edge, are therefore needed.

The development of such an edgeless detector is not trivial. First, the detector module must be designed such that the sensors can be tiled without physical seams. Secondly, the sensors itself should respond uniformly over their entire area. However, conventional crystalline semiconductor sensors have so called guard electrodes at their edges that protect the active area from unwanted effects induced by the often imperfect edge. Hence, to be able to minimise or even eliminate these guard electrodes, a good understanding of such edge effects is required.

Thesis outline

This thesis studies the influence of edge effects on the detection properties of pixels at the edge of two types of edgeless sensors: active-edge and slim-edge sensors. Both types are characterised by the fact that the distance between the active area and the physical edge of the sensor is of the order of the pixel size.

The results are preceded by three introductory chapters. Chapter 1 deals with the principles of X-ray imaging. It particularly focusses on the parameters that determine image quality and it evaluates the status of current radiography detectors. Chapter 2 covers semiconductor sensors. The first part discusses how they work and how they are fabricated, whereas the last part is concerned with edge effects as well as the design and manufacture of edgeless sensors. Chapter 3 introduces the Medipix-chip family and addresses the main bottlenecks of current Medipix detectors for the realisation of a seamless detector tessellation.

To determine the viability of active-edge sensors, the electrical characteristics of prototype active-edge sensors are studied in Chapter 4. Chapter 5 presents results on the performance of pixels at the edge of active-edge sensors and evaluates the potential of such sensors for a tessellation of detector modules. Finally, the imaging performance of edge pixels of slim-edge sensors is examined in Chapter 6. Whereas Chapters 4 and 5 focus on silicon as sensor material, materials of higher atomic number, namely gallium arsenide and cadmium telluride, are studied in Chapter 6.

[2]Nowadays, transistors with gate lengths of less than 50 nm can be realised.

1

X-ray imaging

X-ray imaging is based on the principle of material-dependent attenuation of X-rays. The extent to which various constituents of an object, such as bone or tissue in a human body, attenuate X-rays determines the flux of photons that exit from the object. This results in an intensity distribution, which is commonly mapped by a position sensitive detector. Advanced detectors consist of a pixellated sensor and an equally dimensioned read-out chip, which digitises the image. Depending on the material used, the sensor converts X-ray quanta either directly or indirectly into an electrical signal, which is subsequently processed by read-out electronics.

This chapter gives an introduction to X-ray imaging. First, the X-ray conversion processes are discussed in terms of the most dominant interaction mechanisms and the resulting photon attenuation in the diagnostic energy domain. The efficiency of the conversion process as well as the subsequent acquisition and processing of the generated signal determines to a considerable extent how much information of the original intensity distribution is conserved in the output image. This translates into image quality discussed in Section 1.2. In this context, the detective quantum efficiency is introduced, a common figure of merit to parameterise imaging performance. Subsequently, a short history of X-ray imaging systems is given, with a particular focus on the evolution from analogue to digital detectors. The last section evaluates the flat-panel detector, today's most widely used radiography system. Its main limitations may be eliminated by a novel detector that combines high-quality sensors with intelligent read-out electronics.

1.1 X-ray interaction

1.1.1 Interaction mechanisms

X-rays interact with matter through different mechanisms, three of which are dominant in the diagnostic energy domain (∼20 - 120 keV): photoelectric absorption, Compton scattering and Rayleigh scattering. Each of them is schematically depicted in Figure 1.1.

Photoelectric absorption

Photoelectric absorption involves the absorption of an incident X-ray photon by an atomic electron[1]. This electron is ejected from its parent atom, causing ionisation. The kinetic energy transferred (E_{kin}) to the liberated electron, the photoelectron, is equal to the difference between the energy of the incident X-ray photon (E_0) and the binding energy of the electron (E_{bind}):

$$E_{\mathrm{kin}} = E_0 - E_{\mathrm{bind}} \,. \tag{1.1}$$

The energy of the X-ray photon must at least equal the binding energy of an atomic electron for the photoelectric ionisation to occur. Tightly bound electrons, such as K-shell electrons, have a higher binding energy than outer-shell electrons. If absorption is not possible with inner-shell electrons, interaction may occur with outer-shell electrons. The interaction probability is highest when the X-ray photon energy equals the binding energy and decreases again with higher incident energies. This sharp increase of the interaction cross-section at the binding energy is known as an edge. Logically, they are called K-edge for K-shell electrons and L-edge for L-shell electrons. Each element has its own characteristic edges. For silicon, the K-edge energy is $\sim$ 1839 eV and the L_1-shell energy is $\sim$ 149.8 eV [1]. Bone, which consists primarily of calcium, has a K-edge energy of $\sim$ 4038 eV and an L-edge energy of 438.5 eV.

Compton scattering

Compton scattering involves the incoherent scattering of an X-ray photon by an atomic electron. This interaction mainly occurs when the X-ray photon has an energy that is much higher than the binding energy of the electron. The relation between the fractional energy loss and the scattering angle θ of the photon is given by the Klein-Nishina formula [2]:

$$\frac{E_1}{E_0} = \frac{1}{1 + \alpha(1 - \cos\theta)} \,, \tag{1.2}$$

where

$$\alpha = \frac{E_0}{m_{\mathrm{e}} c^2} \,. \tag{1.3}$$

[1] in contrast to the photoelectric effect that was discovered in 1905, which explained the ejection of electrons from the surface of crystalline structures by the absorption of visible photons.

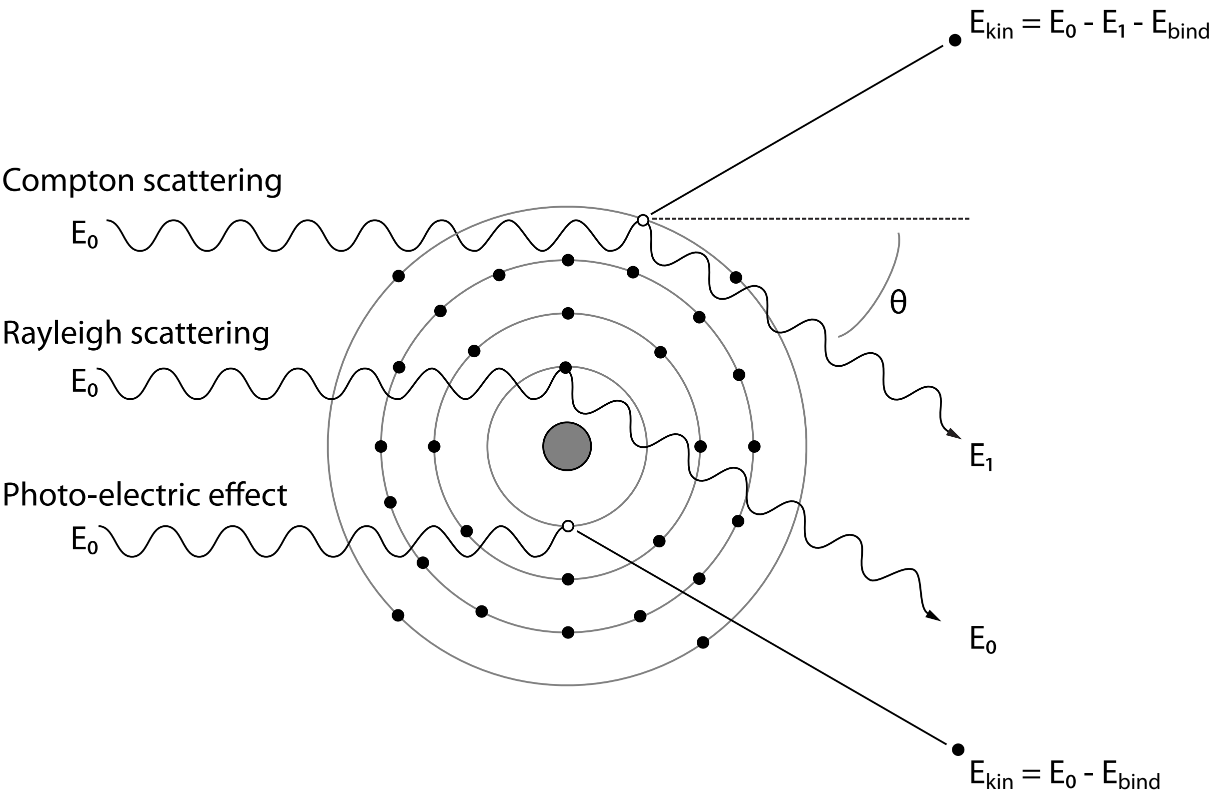

Figure 1.1: Interaction mechanisms
Schematic representation of the three interaction mechanisms in the diagnostic energy range. Whereas for both the photoelectric absorption and Compton scattering electrons are knocked out, Rayleigh scattering does not involve ionisation.

The kinetic energy of the scattered electron is equal to the difference between the initial and final photon energy minus the electron's binding energy:

$$E_{\text{kin}} = E_0 - E_1 - E_{\text{bind}} \, . \tag{1.4}$$

High-energy photons undergo small angle Compton scattering, whereas low-energy photons are more uniformly scattered.

Post-electron-ejection The vacancies left in the inner atomic shells, as a result of both photoelectric absorption and Compton scattering, are filled by outer-shell electrons. An electron of a higher atomic shell falls into the vacancy and the binding-energy difference between those shells is either emitted in the form of characteristic X-rays, also known as fluorescent X-rays, or causes ejection of Auger electrons. These are electrons from the same atom with a binding energy less than the energy released by the filling of the inner-shell vacancy. The number of fluorescent X-rays emitted per de-excitation is known as the fluorescence yield ω. Typical values for ω involving the filling of K-shell vacancies are ~ 0.05 for silicon, ~ 0.55 for gallium arsenide and ~ 0.85 for cadmium telluride [3].

Rayleigh scattering

Rayleigh scattering does not cause ionisation. Incident X-rays are coherently scattered by atomic electrons through interaction with their electric field, whereby the energy of the photons is conserved. The direction of the photons, however, is altered in this process and is quantified by the scattering angle. Similar to Compton scattering, the deflection of incident X-rays is energy dependent. Although Rayleigh scattering does not involve ionisation, it does affect image quality. Rayleigh scattering is most likely to occur at low X-ray energies in high-Z materials.

Pair creation

At higher energies, above twice the rest mass of electrons (i.e. 1022 keV), X-ray quanta can produce electron-positron pairs. Pair creation involves interaction with the electric field of the nucleus, though the atom involved is not ionised. Diagnostic energies, however, range typically from 20 to 120 keV, which is well below the pair-production threshold. Hence, pair production will not occur in medical imaging and will be ignored in this thesis.

1.1.2 Attenuation

The interaction mechanisms combine to remove X-ray photons from the incoming beam as they pass through matter. This reduction is called attenuation and involves both absorption and scattering. Attenuation is parameterised by the linear attenuation coefficient μ (cm^{-1}), which is the probability of an X-ray photon interaction per unit path length travelled through the material. This parameter can be expressed as the sum of interaction probabilities of the individual mechanisms. For the diagnostic energy regime, this is:

$$\mu = \tau + \sigma_\mathrm{R} + \sigma_\mathrm{C}\,, \tag{1.5}$$

where τ is the photoelectric interaction probability per unit length and σ_R and σ_C are the probabilities for Rayleigh and Compton scattering, respectively. Figure 1.2 shows in which energy region each mechanism is dominant for four different sensor materials. One can see that for low-Z materials, such as silicon, Compton scattering dominates when the X-ray photon energy is higher than 50 keV.

To calculate the attenuation coefficient of materials that are composed of different elements, the linear attenuation coefficient of the individual elements are commonly normalised to their density. This normalised parameter is called the mass attenuation coefficient μ/ρ (cm^2/g). Hence, following Lambert-Beer's law [4, 5], the fractional reduction of intensity (I_1/I_0) of a photon beam that passes through a slab of material is described by:

$$\frac{I_1}{I_0} = e^{-\frac{\mu}{\rho}\,\rho x}\,, \tag{1.6}$$

where x (cm) is the thickness of the material.

The individual interaction probabilities depend on the density ρ and atomic number Z of the sensor as well as the energy E of the incoming photons. For diagnostic X-rays,

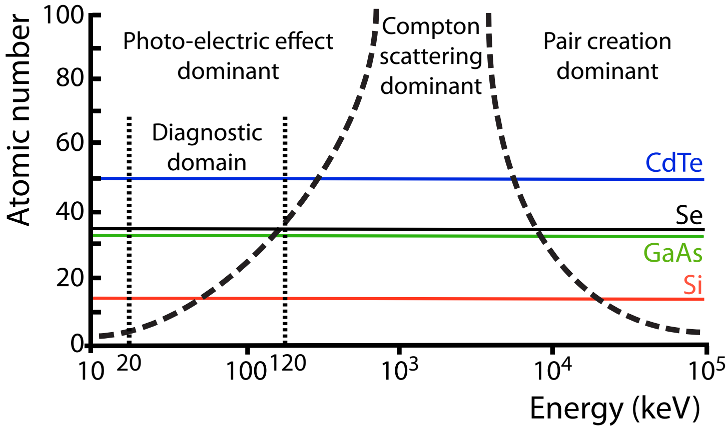

Figure 1.2: Atomic-number dependence
The energy domains in which the various X-ray interaction processes are dominant as a function of the atomic number of the absorber material. For reference, lines are drawn for the atomic numbers of silicon, gallium arsenide, selenium and cadmium telluride.

the dependencies of the photoelectric and Compton mass attenuation coefficients are approximately as follows:

$$\tau/\rho \propto (Z^{4-5}, E^{-3}) \tag{1.7}$$
$$\sigma_C/\rho \propto (Z, E\text{—independent})\,.$$

The energy dependence can be seen in Figure 1.3(a), which shows the total mass attenuation coefficient as a function of the energy of the incoming photon. The fraction by which the intensity is attenuated as a function of initial photon energy is shown in Figure 1.3(b). Curves are drawn for the sensor materials studied in this thesis and compared to that of selenium, a commonly used material in current X-ray imaging detectors.

The mass attenuation coefficient only describes the intensity reduction and does not express the amount of energy deposited in the sensor. The energy deposition is, however, important for the calculation of the signal generated. It is described by the mass energy transfer coefficient μ_{tr}/ρ (cm^2/g). It is the fraction of the mass attenuation coefficient that reflects how much of the energy of the incoming photon is transferred to kinetic energy of the photoelectron or Auger electron:

$$\frac{\mu_{tr}}{\rho} = \left(\frac{E_{kin}}{E_0}\right)\frac{\mu}{\rho}\,. \tag{1.8}$$

The mass energy absorption coefficient even takes radiative losses into account, but those are negligible in the diagnostic energy domain.

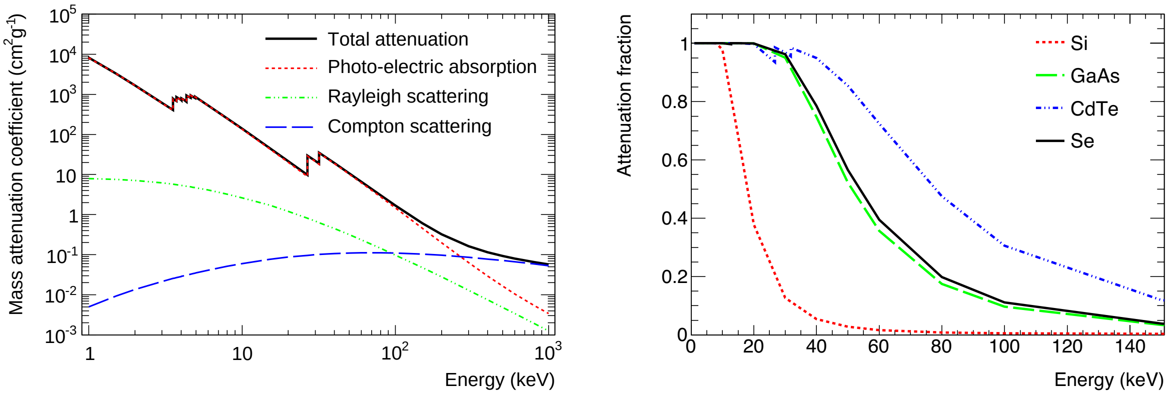

(a)

(b)

Figure 1.3: Attenuation
(a) The total mass attenuation coefficient of cadmium telluride and the contributions of the different interaction mechanisms as a function of the energy of the X-ray photon. (b) The absorption efficiency as a function of photon energy for slabs of 500 µm thick silicon (Si), gallium arsenide (GaAs), cadmium telluride (CdTe) and selenium (a-Se). Based on the mass attenuation coefficients from [6].

1.2 Image quality

The main requirement for an X-ray detection system is to deliver high-quality images using the lowest possible dose. Image quality can be parameterised by the signal-to-noise ratio, which describes the extent to which a signal exceeds the background noise. However, this is only a poor descriptor, since it contains no information about how much detail can be distinguished in the image. A better figure of merit is the detective quantum efficiency [7, 8], which defines the efficiency with which X-ray quanta are used for image formation as a function of spatial frequency. It compares a detector's signal-to-noise ratio with that of the same, but ideal detector, i.e. one that does not introduce noise. Given a certain object and radiation dose, this parameter allows to compare different imaging systems.
To be able to give an exact definition of the detective quantum efficiency, the most important parameters that determine image quality are introduced. This requires a description of both signal and noise transfer in the spatial-frequency domain. These are parameterised by the modulation transfer function and the noise power spectrum, respectively.

1.2.1 Qualitative description

Image quality is determined by a detector's ability to transfer an input intensity distribution to a digital output image with minimal loss of information.
As shown in Figure 1.4, there are several detector-induced phenomena that degrade an image. The severity of these effects on the image are commonly described in terms of

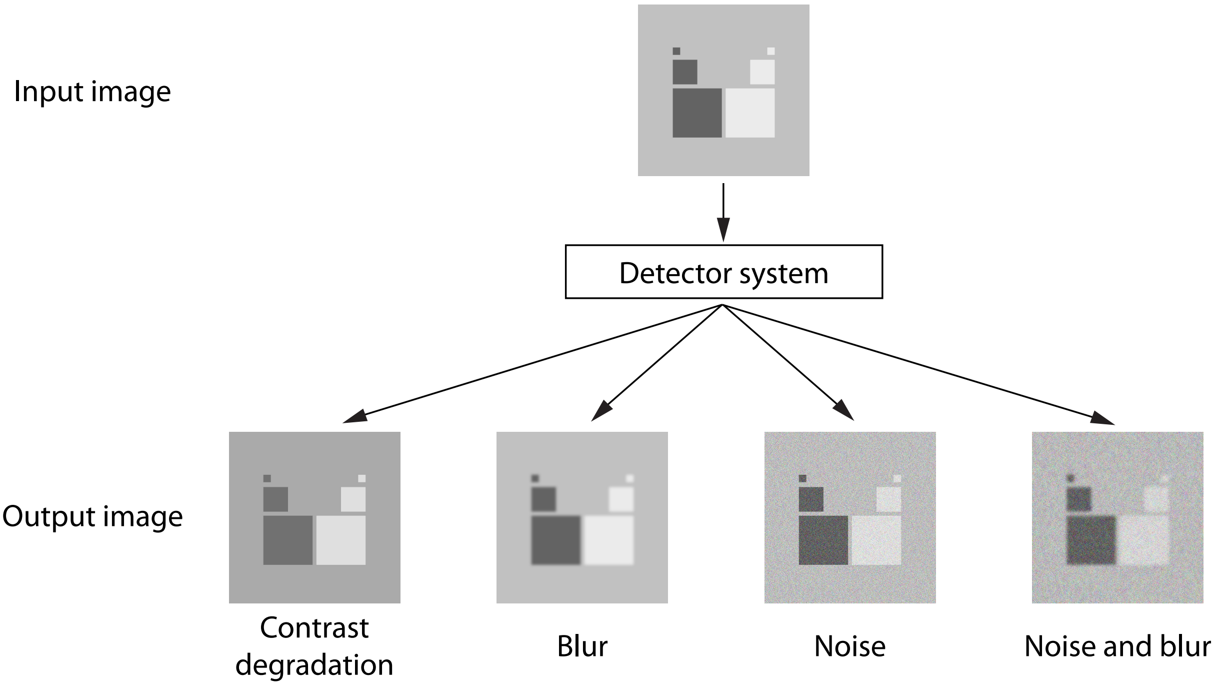

Figure 1.4: Image degradation
Image quality is determined by a detector's ability to preserve clarity of detail. The output image, however, is almost always affected by the detector. Often, a convolution of detector effects cause a degradation of the output image. Figure inspired by [9].

contrast transfer properties, spatial resolution and noise performance of the detector. The former two define image sharpness, i.e. the clarity of detail. A detector's ability to transfer contrast is parameterised by its dynamic range, determined by the bit depth of the read-out pixel (see Chapter 3). If a detector's dynamic range is insufficient, the output image will show contrast degradation with respect to the input image. Despite the fact that contrast transfer describes a detector's ability to differentiate between areas of different photon intensity, it does not express the transfer of spatial detail. This is determined by the spatial resolution of the detector, which mainly depends on the pixel size. However, several effects might compromise the position information of the incoming X-ray photon and may cause image blur. The most important effects will be evaluated in Chapter 6.

On top of contrast degradation and blur, both of which cause a reduction of image sharpness, the detector system can suffer from noise. Apart from irreducible Poisson noise due to the quantised input, the sensor and read-out electronics can introduce both stochastic and non-stochastic noise. In the rightmost image of Figure 1.4, it can be seen that noise and subsequent blur cause the smallest objects to be poorly distinguishable from their neighbouring objects. This shows that imaging performance is determined by the distance over which noise is correlated and thus demonstrates that the mean signal-to-noise ratio is only a global and hence poor descriptor of image quality.

1.2.2 The Rose model

A traditional description of signal and noise transfer is given by the Rose model [10, 11], which demonstrates that image quality is fundamentally limited by quantum statistics. The model assumes a uniform object in a uniform background and Poisson-distributed quantum noise. Consequently, the object contrast can be described by:

$$\mathrm{C_{Rose}} = \frac{(\bar{q}_b - \bar{q}_0)}{\bar{q}_b}\,, \tag{1.9}$$

with $\bar{q}_0$ representing the mean number of quanta per unit area that exits the object and $\bar{q}_b$ the mean number of background quanta per unit area ($\bar{q}_b \geq \bar{q}_0$ in the case of imaging). The signal is then defined as the difference between the number of background and object quanta integrated over the object's area A:

$$\mathrm{S_{Rose}} = A(\bar{q}_b - \bar{q}_0)\,. \tag{1.10}$$

The quantum noise is the standard deviation σ_b of the mean number of background quanta $A\bar{q}_b$, which equals to $\sqrt{A\bar{q}_b}$. In this approach, the signal-to-noise ratio as defined by Rose becomes:

$$\mathrm{SNR_{Rose}} = \frac{\mathrm{S_{Rose}}}{\sigma_b} = \frac{A(\bar{q}_b - \bar{q}_0)}{\sqrt{A\bar{q}_b}} = \mathrm{C_{Rose}}\sqrt{A\bar{q}_b}\,. \tag{1.11}$$

It shows that it is proportional to object contrast and to the square root of both the object's area and radiation dose. This demonstrates the importance of sufficient quantum statistics in image formation. The Rose model is only valid, however, for normally distributed quanta, since it does not take into account effects of spatial correlation. The image can be correlated due to scattering in the object or blur caused by the detector. To characterise these correlation effects, a Fourier-based wave approach that allows for decomposition of both signal and noise into their spatial-frequency dependent components is preferred over the uncorrelated particle approach.

1.2.3 Signal transfer

The intensity distribution at a detector's input can be seen as an ensemble of point impulses in 2D-space $\delta(x, y)$ acting on an input signal function $q(x, y)$ through integration. This function at a point (a, b) in 2D-space is then given by:

$$q(a, b) = \int_{-\infty}^{\infty}\int_{-\infty}^{\infty} q(x, y)\delta(x - a, y - b)dxdy\,. \tag{1.12}$$

Ideally, the detector's response to a point impulse is a delta function in image space. In reality, however, detector imperfections cause smearing of the input point impulse, which is parameterised by a detector's point spread function (psf). The output $d(x, y)$ is therefore expressed as a function of the input function and the point spread function:

$$d(x, y) = \int_{-\infty}^{\infty}\int_{-\infty}^{\infty} q(a, b)\mathrm{psf}(x - a, y - b)dadb\,, \tag{1.13}$$

or as the convolution of the input function with the point spread function:

$$d(x,y) = (q \otimes \mathrm{psf})(x,y)\,. \tag{1.14}$$

The output function is only representative for the entire detector if its response to a given input is both linear and shift invariant (i.e. position independent) [12]. Both linearity and shift-invariance make that the system's response to an ensemble of scaled and shifted point impulses is identical to the sum of separate responses to each of the individual point impulses and therefore allows for signal decomposition. A natural way to do this is to treat the individual signal components as single-frequency sinusoids rather than point impulses, as the output components are then eigenfunctions of their input counterparts. Since the convolution theorem states that the Fourier transform of a convolution equals the product of the individual Fourier transforms, the output as a function of spatial frequency $D(u,v)$ can be described by the product of the Fourier-transformed input function $Q(u,v)$ and the Fourier-transformed point spread function, the optical transfer function $\mathrm{OTF}(u,v)$:

$$D(u,v) = Q(u,v) \cdot \mathrm{OTF}(u,v)\,. \tag{1.15}$$

From this, it can be seen that the input function remains unchanged apart from scaling by the optical transfer function. The optical transfer function consists of a real and imaginary part: the modulation transfer function and the phase transfer function. For a shift-invariant detector, the phase transfer function equals zero and only the modulation transfer function matters.

Modulation transfer function

Clarity of detail is parameterised by the sharpness of an image. This is determined by the level of contrast as well as the spatial resolution. Both parameters are combined into one figure of merit, known as the modulation transfer function. It describes the magnitude of contrast transfer as a function of spatial frequency. Theoretically, it can be derived by considering the transfer of a sinusoidal signal using Fourier decomposition [9].
For an input signal of the following form:

$$q(x,y) = A + Be^{i2\pi(ux+vy)}\,, \tag{1.16}$$

the input modulation M_q is given by:

$$M_q = \frac{B}{A}\,. \tag{1.17}$$

Subsequently, the output $d(x, y)$ of a linear and shift-invariant system can be derived as follows:

$$\begin{aligned} d(x,y) &= \int_{-\infty}^{\infty}\int_{-\infty}^{\infty}\left(A + Be^{i2\pi(ua+vb)}\right)\mathrm{psf}(x-a, y-b)da db \\ &= \int_{-\infty}^{\infty}\int_{-\infty}^{\infty}\left(A + Be^{i2\pi(u(x-a)+v(y-b))}\right)\mathrm{psf}(a,b)da db \\ &= \left(A + Be^{i2\pi(ux+vy)}\right)\left[\int_{-\infty}^{\infty}\int_{-\infty}^{\infty} e^{-i2\pi(ua+vb)}\mathrm{psf}(a,b)da db\right] \\ &= \left(A + Be^{i2\pi(ux+vy)}\right)\cdot \mathrm{OTF}(u,v) \\ &= A\cdot \mathrm{OTF}(u,v)|_{u,v=0} + B\cdot \mathrm{OTF}(u,v)e^{i2\pi(ux+vy)}\,. \end{aligned} \tag{1.18}$$

This results in an input-modulation dependent output modulation M_d:

$$M_d = \frac{B}{A}\frac{|\mathrm{OTF}(u,v)|}{\mathrm{OTF}(0,0)} = M_q\frac{|\mathrm{OTF}(u,v)|}{\mathrm{OTF}(0,0)}\,. \tag{1.19}$$

The modulation transfer function (MTF) is then defined as the ratio between output and input modulation:

$$\mathrm{MTF} = \frac{M_d}{M_q} = \frac{|\mathrm{OTF}(u,v)|}{\mathrm{OTF}(0,0)}\,. \tag{1.20}$$

It can be seen as the magnitude of the optical transfer function at a certain frequency with respect to the optical transfer function at zero frequency. The latter is known as the detector's quantum efficiency, which expresses the ratio between the mean number of recorded photons and the actual mean number of input photons.
In other words, the modulation transfer function is a factor that scales the input modulation and equals to unity at zero frequency.

1.2.4 Noise transfer

In addition to the variance in the number of Poisson-distributed input quanta, imaging systems introduce noise to the image. Typical sources are read-out noise, intensity fluctuations of the photon beam, dark currents in the sensor and detector-response variations, known as structured or fixed-pattern noise (see Chapter 6).
All cause unwanted fluctuations of the signal, which can mask the variation of the actual signal. The power of the total of these fluctuations determines the extent to which it over-shadows the signal, which is described by the power signal-to-noise ratio for normally distributed quanta. This parameter, however, does not describe the spatial-frequency content of the noise. This is represented by the noise power spectrum (NPS), which is defined as the Fourier transform of the auto-correlation function of the noise and can be experimentally obtained by determining the ensemble average of the squared magnitude of the discrete Fourier transform of the signal fluctuations. In the two-dimensional case, it can be expressed as:

$$\mathrm{NPS}_d(u,v) = \lim_{N_x,N_y,M\to\infty}\frac{\Delta x\Delta y}{MN_xN_y}\sum_{m=1}^{M}\left|\sum_{i=1}^{N_x}\sum_{j=1}^{N_y}\Delta d(x_i,y_j)e^{-i2\pi(ux_i+vy_j)}\right|^2\,, \tag{1.21}$$

where $\Delta x \Delta y$ is the pixel area, M the number of images in the ensemble, $N_x N_y$ the number of pixels that form the region of interest and $\Delta d(x, y)$ denotes the deviation from the mean signal. More detailed information on the experimental determination of the noise power spectrum is given in Chapter 6.

1.2.5 Detective quantum efficiency

Given a modulation transfer function and noise power spectrum, the detector's signal-to-noise performance can be parameterised on an absolute scale by the noise-equivalent number of quanta (NEQ) as a function of spatial frequency:

$$\mathrm{NEQ}(\bar{q}; u, v) = \frac{\bar{q}^2 \bar{G}^2 \mathrm{MTF}^2(u, v)}{\mathrm{NPS}_d(u, v)} = \frac{\bar{d}^2 \mathrm{MTF}^2(u, v)}{\mathrm{NPS}_d(u, v)}\,, \tag{1.22}$$

where $\bar{q}$ is the mean number of input quanta per unit area, $\bar{G}$ is the quantum efficiency, which describes the ratio between $\bar{q}$ and the mean number of output quanta $\bar{d}$. The noise-equivalent number of quanta expresses image noise as the apparent number of input quanta needed for image formation if the detector would only be limited by Poisson noise. In other words, it tells how many input quanta an image is worth.
It is only dependent on $\bar{d}$, the modulation transfer function and the output noise power spectrum, all of which can be obtained from image data.

An overall figure of merit for the imaging performance of the detector system is given by the ratio between the noise-equivalent number of quanta and the mean number of photons used to form the image. This parameter is called the detective quantum efficiency (DQE) and expresses the efficiency with which the input quanta are used to produce the output image:

$$\mathrm{DQE}(u, v) = \frac{\mathrm{NEQ}(u, v)}{\bar{q}} = \frac{\bar{d}^2 \mathrm{MTF}^2(u, v)}{\bar{q}\,\mathrm{NPS}_d(u, v)}\,. \tag{1.23}$$

For the special case, in which the input and output quanta are Poisson-noise limited, i.e. there is no spatial correlation and thus no frequency dependence, the NEQ equals $\mathrm{SNR}^2_{\mathrm{out}}$ and $\mathrm{SNR}^2_{\mathrm{in}}$ equals $\bar{q}$. This simplifies the expression for the detective quantum efficiency to:

$$\mathrm{DQE} = \frac{\mathrm{SNR}^2_{\mathrm{out}}}{\mathrm{SNR}^2_{\mathrm{in}}}\,. \tag{1.24}$$

1.2.6 Sampling

One of the difficulties in measuring the DQE of digital detectors arises from the sampling of the input image due to the pixel segmentation [13]. Sampling itself is not harmful, as it only causes the Fourier transform of the input to replicate at fixed multitudes of the sampling interval. Under-sampling, though, which is the case for almost all digital imaging systems, causes overlap of the Fourier spectra near the Nyquist frequency, which is defined as $1/2b$ with b being the sampling interval, i.e. the pixel pitch.

That is the reason why the optical transfer function is generally divided into a pre-sampling stage and a digital stage. The pre-sampling optical transfer function $\mathrm{OTF}_{\mathrm{pre}}$ describes the system's response up to the stage of sampling and contains contributions from blur inferred by the sensor and includes a pixel aperture function, which describes the shape and size of the pixel's effective active area. The digital optical transfer function $\mathrm{OTF}_{\mathrm{d}}$ is defined as the Fourier convolution of the $\mathrm{OTF}_{\mathrm{pre}}$ with a comb function $\mathrm{OTF}_{\mathrm{comb}}$, which represents the pixel sampling:

$$\mathrm{OTF}_{\mathrm{d}} = \mathrm{OTF}_{\mathrm{pre}} \otimes \mathrm{OTF}_{\mathrm{comb}} \,. \tag{1.25}$$

As a consequence of under-sampling, frequency components above the Nyquist frequency show up as low-frequency aliases in the digital MTF. As a result, the digital MTF has additional contributions from the aliased components and therefore does not describe the frequency response of a single sinusoidal input. This complicates the interpretation of the digital MTF and therefore compromises its meaning as a measure of signal-transfer performance.

Under-sampling poses a further difficulty to the experimental determination of the MTF, as it makes the detector's response phase-dependent with respect to the sampling comb and thus not shift invariant at the sub-pixel level. A way to avoid the effects of aliasing and phase dependence is to over-sample the system, which enables measurement of the response to the impulse function for all phases relative to the sampling comb. This gives the pre-sampling MTF, which can be seen as the frequency response to single sinusoidal inputs. A method to obtain the digital MTF is to mathematically derive its expectation value from the measured pre-sampling MTF. It is equivalent to averaging the digital MTF over one sampling period, i.e. pixel pitch. This parameter is known as the expectation MTF (EMTF).

1.3 Radiography detectors

Since the early fifties of the last century, X-ray imaging detectors have undergone a large and rapid development. Efforts have been made to increase image quality, to reduce the dose and to make systems more convenient to use. In the 1970s, the first computerised systems were developed. In particular, these systems were faster and cheaper to use, yet analogue systems are still widely used nowadays.
A comparison of different systems, which all have been part of the evolution of the analogue film-screen detector to the currently state-of-the-art flat-panel detector, is given below. Specifically, common features and limitations of each of the detectors will be discussed.

1.3.1 Analogue systems

Analogue radiography systems take X-ray images with a cassette which contains a film that is mounted in contact with one or two intensifying phosphor screens to increase the quantum efficiency. The screen absorbs X-rays and converts them into visible photons, which subsequently expose the film.
An important benefit of film-screen technology is the intrinsic high spatial resolution of the film. Typical grain sizes vary between 10 and 30 µm. The film's response, however, is non-linear and its dynamic range is limited, thereby reducing contrast. Moreover, analogue imaging is both space and time consuming. Film needs to be developed and the pictures require physical storage space. If the radiograph is of unsatisfactory quality, for example when it is under- or over-exposed, the entire process has to be repeated. An increase in number of retakes means an unwanted increase in dose.

1.3.2 Digital systems

Some of the shortcomings of analogue systems are eliminated by digital systems [14]. In general, digital systems have a larger and sometimes adaptive dynamic range and show a linear response, while having similar spatial resolution. This results in a better signal-to-noise ratio, as a result of which the ability to detect low-contrast structures is improved. In addition, they provide a digital output image, which allows for enhancement using digital image-processing techniques and provides the possibility of a computer-aided diagnosis. This translates to a reduction of the number of possible retakes. The increased sensitivity as well as the digitisation of images therefore reduce the average dose for the patient. Moreover, they provide the possibility of immediate image preview, which gives the opportunity to do real-time imaging.
Digital detectors can be categorised into computed-radiography systems and digital-radiography systems. In analogy to film-screen detectors, computed radiography is based on the formation of a latent image which is subsequently read out and processed to obtain the final output image. The difference is that it generates a digital image instead of an analogue print. In digital radiography detectors, on the other hand, the read-out stage is integrated in the system.
In addition, digital systems can be divided into indirect and direct conversion detectors. Direct detectors convert the X-ray photons directly to charge, providing the electrical signal. Indirect conversion means there is an intermediate stage at which X-rays are first converted to visible photons before the final conversion to charge.

Indirect conversion detectors

Two commonly used indirect conversion detectors are storage-phosphor plates and image-intensifier screens.

Storage-phosphor plates Storage-phosphor plates fall under the category of computed-radiography systems. They consist of a photostimulable plate, which stores a latent image of the object as a distribution of charges. This latent image is formed by electrons and holes that are liberated by the X-ray photon and subsequently trapped in the plate. The resulting charge distribution is read out by exciting these charges locally by using laser light. The subsequent de-excitation causes emission of phosphorescent light, which is detected and converted to an electrical signal by a photomultiplier. The output of the photomultiplier is then digitised and displayed by a computer. The typical read-out time is of the order of one minute.

Image-intensifier screens Image-intensifier screens convert X-ray distributions to intensified visible images, which are the result of a multi-conversion and focussing process. The detector typically consists of an input and an output phosphor screen. The input screen first converts the X-ray quanta to light. The visible photons then liberate photoelectrons from a photocathode at the back of the input screen. These are accelerated and focussed onto an output phosphor screen, which converts the condensed photoelectron image to an intensified visible-photon image. Subsequently, this image is recorded by an optically coupled video camera or CCD, the electrical output of which is digitised and sent to a computer. As the read-out is integrated in the detector system, image intensifiers are classified as digital radiography detectors.

Although both detectors have the advantages of image digitisation as listed in the section 1.3.1, they possess some intrinsic limitations:

- Indirect conversion involves processes, such as light scatter in a phosphor screen, that cause lateral spread of information carriers and hence lead to a loss of resolution.
- Poor optical coupling to the photomultiplier, video camera or CCD reduces the number of information carriers and hence lowers the sensitivity. Also, it can introduce secondary quantum noise.
- Some excited states in the phosphor can be meta-stable. This causes a delayed relaxation and hence delayed phosphorescence, also known as after-glow. This makes these detectors slow and therefore unattractive for real-time imaging applications.
- Due to the separate read-out of photostimulable phosphors and the bulky parts of intensifier screen, they are space consuming.

Direct conversion detectors

The most widely used radiography system today is the flat-panel detector [15, 16].

Flat-panel detectors Flat-panel detectors consist of a so called active-matrix array of thin-film transistors (TFTs) that reads out a directly or indirectly converting layer of sensor material. Flat-panel technology allows for fabricating electronic circuits over glass substrates of large area and hence gives access to human digital radiography. Besides, these detectors are more compact than image intensifiers, as the read-out electronics form an integral part of the detector.

The read-out is realised by a patterned film of hydrogenated amorphous silicon deposited on a glass substrate, segmented into pixels. Each pixel contains a sensing electrode, a storage capacitor and a switching TFT. The charge created in the sensor is collected at the electrodes and stored on the capacitors. Subsequently, each capacitor is read out by addressing the switching TFTs in a row-wise manner [17, 18]. This way of signal processing makes that flat-panel detectors are denoted as charge integrators. That is to say, each capacitor integrates charge proportional to the amount of energy deposition in each pixel, which is determined by the number and energy of the incoming photons during a given acquisition time. Due to both the fact that the intensity of low-energy photons is attenuated more than that of high-energy photons and low-energy photons generate less charge in the sensor, the quantum noise contribution of low-energy photons is relatively high. The opposite is true for high-energy photons. Consequently, high-energy photons are given a higher weight than low-energy ones, at the expense of the signal-to-noise ratio. The output image will therefore not perfectly correspond to the attenuation profile of the object.

Typically, the sensor is a directly converting photoconductive layer of amorphous selenium (of typically 1 mm thickness) or an indirectly converting caesium iodide scintillator (of $\sim$ 0.5 mm) on top of an active matrix of amorphous silicon photosensors [19]. As this thesis focusses on directly converting crystalline semiconductor sensors, photoconductive amorphous selenium will be used as a reference sensor material.
An intrinsic property of photoconductors is direct conversion of X-rays into charge. As a result, lateral spread of information carriers due to multiple conversion is avoided. Nonetheless, there are some shortcomings of amorphous selenium as a sensor material. First, the atomic number of selenium as well as its charge-carrier mobility is moderate. The intensity of 70 keV photons (typically used for chest radiography) is only reduced by 28 % in 0.5 mm thick selenium (see Figure 1.3(b) on page 8). To stop a substantial amount of these photons, the sensor has to be at least twice as thick. The mean drift length of both holes and electrons, however, is only of the order of 1 mm for an electric field of 10^{5}V/cm. As a result of the moderate carrier transport properties, the number of electron-hole pairs contributing to the signal is low. Depending on the operation voltage, the effective energy to create one electron-hole pair is between 20 and 50 eV. The resulting low quantum efficiency requires long acquisition times. Consequently, even though flat-panel detectors can provide immediate image preview, the maximum frame-rate is limited to approximately 15 frames per second for $(200\ \mu m)^2$ pixels.
Moreover, selenium sensors can only operate reliably in a narrow temperature domain. Ideally, they are operated within a temperature regime between 5°C and 30°C to avoid degradation of the selenium layer. This means that the temperature has to be controlled, which makes the system more complex.

Future detectors

Flat-panel technology enables fabrication of detectors that meet many of the requirements for human X-ray imaging systems. However, as discussed above, there is room for improvement. The ideal radiography detector should provide the same or even better image quality using a lower dose. This translates into stringent detector requirements.
This thesis presents an alternative detector that combines a photon-counting chip with energy-resolving capabilities (the Medipix-3 chip) with a crystalline semiconductor sensor of high atomic number. The chip allows for correction of the energy dependence of the intensity attenuation through the object and hence provides images that are intrinsically in better agreement with the intensity distribution at the input than ones made with charge integrating detectors. Moreover, crystalline high-Z semiconductor sensors provide a high quantum efficiency due to their high absorption efficiency for diagnostic X-rays, convert X-ray directly into charge and possess good charge-transport properties.
However, the active area of the Medipix chip (~ 2 cm^2) as well as the limited area of the currently available crystals (~ 10 cm^2) form a real challenge to make competitive large area diagnostic systems. Hence, enlargement of the active area is imperative. A solution is to realise a tessellation of Medipix detectors.
The potential of such a tessellation will be explored in this thesis. In particular, the study focusses on the tile-ability of different types of edgeless sensors by examining their performance at the edge.
Before the results are presented in Chapters 4 to 6, Chapters 2 and 3 will introduce the principles, operation and fabrication of crystalline semiconductor sensors as well as the Medipix detector, respectively.

2

Semiconductor sensors

Semiconductors are eminently suitable as conversion material for particle and radiation detectors because of their conductivity, which is between that of conductors and insulators. To understand what determines conductivity, the quantum mechanical behaviour of electrons in atomic lattices must be considered.
The first section of this chapter discusses the principles of semiconductor physics [20–24] and signal formation. Section 2.2 describes the basic building blocks of semiconductor sensors: the p-n junction and metal-semiconductor contacts. Section 2.3 goes into detail on sensor fabrication, with a specific focus on wafer dicing techniques, since the sensor's performance at the edge is largely determined by the method used. The last section covers sensor design in terms of different electrode topologies, particularly focussing on edgeless sensors.

2.1 Physics concepts

2.1.1 Band theory

According to quantum mechanics [25, 26] each particle occupies a quantum state, which is described by a wave function. The square modulus of this wave function represents the probability density of measuring this particle at a given position and time. If a particle is bound to a potential, for example an electron that is bound to a nucleus, it can only occupy states of discrete energy. As a consequence, electrons are located at discrete distances from the nucleus.
Now, what happens when the spacing between atoms decreases to the order of the atomic radius? Electrons occupying the same quantum state will approach each other and their probability density functions will start to overlap. According to Pauli's exclusion principle [27], however, no two electrons can occupy the same quantum state simultaneously. As a result, the energy levels split up. It can be thought of as if one of the levels is pushed slightly upwards, the other slightly downwards. The new wave functions are a linear combination of the two individual wave functions. When many atoms are brought together, as is the case in an atomic lattice, the energy states will be divided into numerous levels.

These levels are so close to each other that they almost form a continuum. They can be seen as a band of energy states.
In this way, crystals have bands of allowed and forbidden states. The distribution of electrons over the allowed states is described by the Fermi-Dirac function [28]:

$$f_{\mathrm{F}}(E) = \frac{1}{1 + e^{\left(\frac{E - E_{\mathrm{F}}}{kT}\right)}} \,. \tag{2.1}$$

This function gives the probability that a state is occupied by an electron. E is the energy of the quantum state, E_{F} is the energy of the Fermi level[1], k is Boltzmann's constant and T the absolute temperature. The Fermi level is defined as the highest energy level occupied at absolute zero. In other words, all states of the energy band directly below the Fermi level are filled by electrons at 0 K. These electrons close the outer valence shells and are responsible for the bonding between atoms. This energy band is known as the valence band. The band immediately above the Fermi level is completely empty at 0 K, but can be filled with electrons from the valence band when the temperature increases or when excited by a photon or charged particle. These liberated electrons can freely migrate through the crystal and do not contribute to the bonding anymore. They are responsible for conduction. Hence, this band is called the conduction band. For both semiconductors and insulators there exists a forbidden area between the valence and conduction band: the band gap. No states exist in this area. The width of the band gap is determined by the energy difference E_g between the highest level in the valence band and the lowest in the conduction band and depends on the interatomic spacing. It fundamentally determines the ease with which valence electrons can surmount the band gap and serve as conduction electrons. Figure 2.1 is a schematic representation of the upper edge of the valence band relative to the lower edge of the conduction band for conductors, semiconductors and insulators. Conductors have no band gap; their valence and conduction bands overlap. Insulators have a band gap of 5 eV or greater. In the case of semiconductors, the width of the forbidden zone is of the order of 1 eV. Therefore, only little energy is needed to bring electrons into the conduction band. When this transition occurs, the electrons leave behind empty states in the valence band, called holes [29]. A valence electron can fill such an empty state, leaving behind another hole. Holes can therefore migrate and also contribute to conduction. However, they cannot be considered free carriers, since they are part of the crystal.

2.1.2 Carrier concentration

The conductivity of a semiconductor is proportional to the concentration of free carriers. This concentration is dependent on the position of the Fermi level relative to the band edges. In the Boltzmann approximation [30], the electron concentration n and hole

[1] E_{F} is also referred to as the Fermi energy.

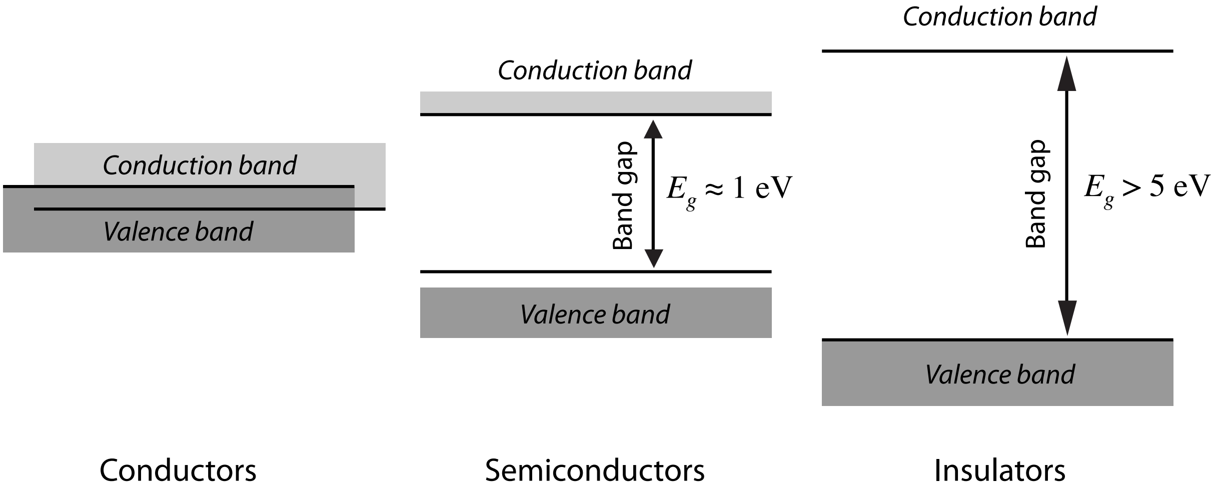

Figure 2.1: Energy bands
A schematic representation of the relative position of the edge of the valence and conduction band, in order of decreasing conductivity. Conductors have no area of disallowed states, whereas the valence and conduction band of insulators and semiconductors are separated by a forbidden zone: the band gap. At room temperature, valence electrons can be excited to the conduction band, leaving behind holes in the valence band.

concentration p are given by:

$$n = N_c e^{-\left(\frac{E_c - E_\mathrm{F}}{kT}\right)} \tag{2.2}$$

$$p = N_v e^{-\left(\frac{E_\mathrm{F} - E_v}{kT}\right)}\,, \tag{2.3}$$

where N_c is the effective density of states of the conduction band and N_v that of the valence band[2]. E_c is the energy of the lower edge of the conduction band and E_v that of the upper edge of the valence band.

Intrinsic semiconductors

A semiconductor with equal electron and hole concentration in thermal equilibrium,

$$n = p = n_i\,, \tag{2.4}$$

is called intrinsic, where n_i is the intrinsic carrier concentration. From Equations 2.2 and 2.3, it can be derived that the Fermi level of an intrinsic semiconductor is located in the middle of the band gap:

$$E_\mathrm{F} = E_i = \frac{E_c + E_v}{2} + \frac{kT}{2}\ln\left(\frac{N_v}{N_c}\right)\,, \tag{2.5}$$

[2]For silicon at 300 K, N_c and N_v are $\sim 2.8{\cdot}10^{19}$ cm^{-3} and $\sim 1.8{\cdot}10^{19}$ cm^{-3}, respectively.

where E_i is called the intrinsic Fermi level.
An important relation that applies to any semiconductor in thermal equilibrium is that the product of the electron and hole concentration is constant and only depends on the width of the band gap and temperature:

$$np = n_i^2 = N_c N_v e^{-\left(\frac{E_c - E_v}{kT}\right)} = N_c N_v e^{-\left(\frac{E_g}{kT}\right)}. \quad (2.6)$$

If the concentration of one carrier type is larger than the equilibrium concentration, equilibrium will be restored through processes (see Section 2.1.3) that reduce the concentrations of either electrons or holes to maintain $np = n_i^2$. Note that this relationship does not depend on the Fermi level and therefore also applies to semiconductors in which one carrier type concentration exceeds the other: extrinsic semiconductors.

Extrinsic semiconductors

Intrinsic semiconductors only represent the ideal case of a pure and perfect crystal. The electron and hole concentrations are balanced and no excess of electrons or holes exist. In reality, there are almost always imperfections present in the semiconductor lattice which are introduced during the fabrication process.
Typical imperfections are atomic impurities and crystalline defects. Both introduce intermediate states in the band gap. Depending on their position relative to the intrinsic Fermi level, they fall in two categories: shallow-level and deep-level states. Shallow-level states are located no further than 0.1 eV from the band edges. If the difference is larger, i.e. the states are located deeper in the band gap, one speaks of deep-level states.

Shallow-level states Shallow states can be introduced by impurity atoms. Figure 2.2 shows shallow states at two different energy levels in the band gap and their influence on the conductivity of the semiconductor material.
Atoms that have more valence electrons than the atoms of the semiconductor crystal introduce electron-filled states of energy E_d close to the conduction band. Because of their close proximity to the conduction band, their ionisation probability is high and they can easily donate electrons to the conduction band. Logically, these impurity atoms are called donors. Atoms with fewer valence electrons introduce empty states just above the valence band, which can be filled easily by valence electrons. These states of energy E_a have a large probability of accepting electrons. This can be seen as if holes are added to the valence band. These impurity atoms are called acceptors. Extrinsic semiconductors having a majority of electrons are called n-type, and similarly, those having a majority of holes are called p-type. Logically, electrons in n-type material are called majority carriers and the holes are referred to as minority carriers. The opposite applies to p-type semiconductors.
Due to donor and acceptor states, the position of the Fermi level is shifted to one of the band edges. This shift is dependent on the donor and acceptor concentrations. The Fermi

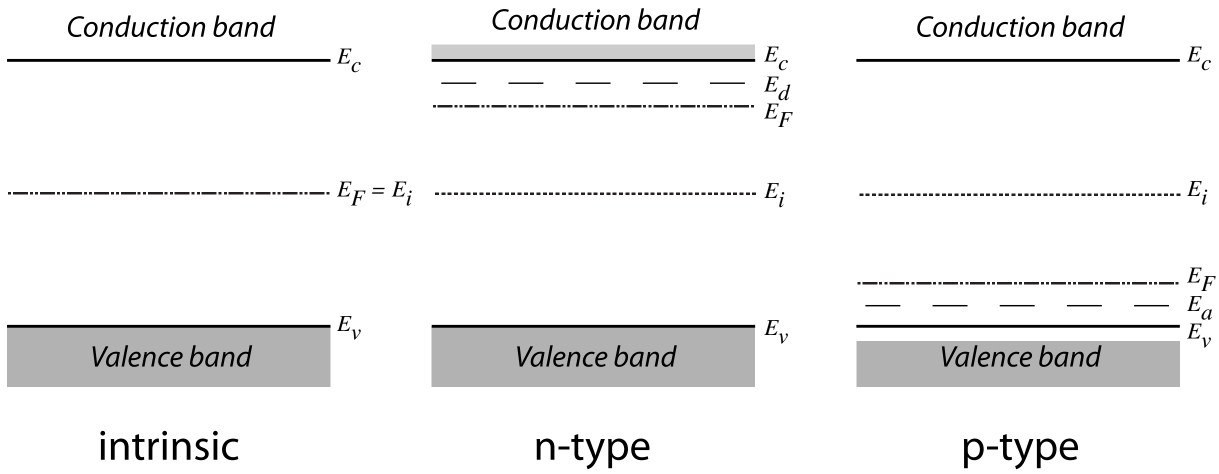

Figure 2.2: Intrinsic and extrinsic semiconductors
The band diagrams of both intrinsic and extrinsic semiconductors. The Fermi level of intrinsic semiconductors is located in the middle of the band gap. Donor and acceptor impurities introduce states that cause the Fermi level to shift to one of the band edges. Obviously, this alters the carrier concentration and thus the conductivity of the semiconductor. Donors make the semiconductor n-type, whereas acceptor-dominated semiconductors are called p-type.

level relative to the band edge becomes:

$$E_c - E_\mathrm{F} = kT \ln \left(\frac{N_c}{N_d} \right) \tag{2.7}$$

$$E_\mathrm{F} - E_v = kT \ln \left(\frac{N_v}{N_a} \right) . \tag{2.8}$$

From this, it can be seen that the Fermi level shifts towards the conduction band in the case of n-type semiconductors and towards the valence band in the case of p-type semiconductors.
Depending on the concentration of donors and acceptors, semiconductors are categorised into different types. These are listed in Table 2.1.

Deep-level states Deep-level states in the band gap have energies that differ more than 0.1 eV from the band edges. Typical deep states are introduced by metallic impurities or defects in the crystal lattice which can be caused by one of the fabrication steps. Lattice defects may consist of atomic dislocations, vacancies (i.e. lattice sites missing an atom) or interstitials (i.e. extra atoms between lattice sites). Two defects that are generally introduced during the growth of cadmium telluride are the cadmium vacancy and the tellurium interstitial.

Doping In contrast to what one would expect, it is very common in semiconductor device fabrication to introduce small and controlled amounts of impurity atoms. This

Table 2.1: Semiconductor classification in terms of donor and acceptor concentration levels.

Donor/acceptor concentration (cm^{-3})	**Type**
$\sim 10^{12}$	ν / π
$10^{13} - 10^{15}$	n^- / p^-
$10^{15} - 10^{17}$	n / p
$10^{17} - 10^{19}$	n^+ / p^+
$> 10^{19}$	n^{++}/p^{++}

process is called doping and the atoms added are named dopants. Dopants are used to manipulate the electrical properties of the material. One important reason is to negate the effects of unwanted impurities. If the donor and acceptor concentrations are equal, the extra electrons provided by the donor will fill the empty states of the acceptor, thereby cancelling out each other's influence. In this way, carrier concentrations can be restored to the intrinsic level. This resistivity tuning by free-carrier elimination is called compensation [31, 32].
Besides compensation of semiconductor bulk material, very local doping is done to manufacture electronic circuits as well sensor structures. This will be discussed in more detail in Sections 2.2 and 2.3.

2.1.3 Carrier generation and recombination

The process that involves creation of electron-hole pairs by exciting electrons from the valence band to the conduction band is called generation. This occurs, for example, when an X-ray photon interacts with the sensor. In this case, the number of generated electron-hole pairs N depends on the kinetic energy E_{kin} of the photoelectron and the average energy W needed to create an electron-hole pair:

$$N = \frac{E_{\text{kin}}}{W} \,. \tag{2.9}$$

Values for W for the sensor materials studied are listed in Table 2.2 on page 29.
The reverse process is referred to as recombination. It involves the transition of an electron from the conduction band to the valence band and the subsequent annihilation with a hole. Either one of these processes occurs whenever the product of the electron and hole concentration deviates from the thermal-equilibrium situation: $np = n_i^2$. When $np < n_i^2$ thermal generation will restore the system to equilibrium, whereas if $np > n_i^2$ recombination occurs. Both generation and recombination can involve both direct and indirect transitions between the bands. Direct means that a valence electron is elevated to the conduction without involvement of any intermediate process. Indirect transitions, on the other hand, occur through intermediate states in the band gap. The direct transition

is known as the band-to-band generation-recombination process, whereas the indirect one is referred to as the intermediate-state assisted or Shockley-Read-Hall process [33]. Figure 2.3 shows a schematic representation of both direct and indirect generation and recombination processes.

Direct and indirect semiconductors

Depending on the relative position of the valence and conduction band in momentum space, semiconductors have either a direct or indirect band gap. To understand what determines this, the concept of crystal momentum of electrons in a crystal lattice has to be introduced. The underlying theory, however, is beyond the scope of this thesis. For direct band-gap semiconductors the crystal momentum of the maximum-energy state of the valence band matches that of the minimum-energy state of the conduction band, which makes that band-gap transitions only require energy transfer. In indirect semiconductors, however, the valence-band maximum does not match the conduction-band minimum, which requires momentum transfer in addition to energy transfer. This momentum transfer is mediated by lattice vibrations, also known as phonons.

Band-to-band transitions

Band-to-band generation requires the valence-band electron to gain enough energy to surmount the band gap. Next to thermal generation, valence-band electrons can be excited to the conduction band through interactions with photons or charged particles. Conversely, conduction electrons can recombine with holes and annihilate. In direct semiconductors, the recombination energy can be converted to a photon or transferred to an Auger electron. In the case of indirect semiconductors, the band-to-band transitions require the transfer of momentum in addition to energy transfer. These transitions can be promoted by intermediate states within the band gap through two or multiple-step transitions, commonly known as Shockley-Read-Hall transitions.

Shockley-Read-Hall transitions

In a perfect single-crystal semiconductor no levels exist within the band gap and only band-to-band transitions occur. In reality, as has been discussed, semiconductors are extrinsic. As a consequence, the intermediate states can act as stepping stones for generation and recombination, or trap charges. Four intermediate-state assisted processes can be distinguished:

1. Hole emission: This process involves the capture of a valence-band electron by the intermediate state. As this electron leaves behind a hole, it can be seen as if the gap state emits a hole.

2. Electron emission: The transition of a captured electron to the conduction band.

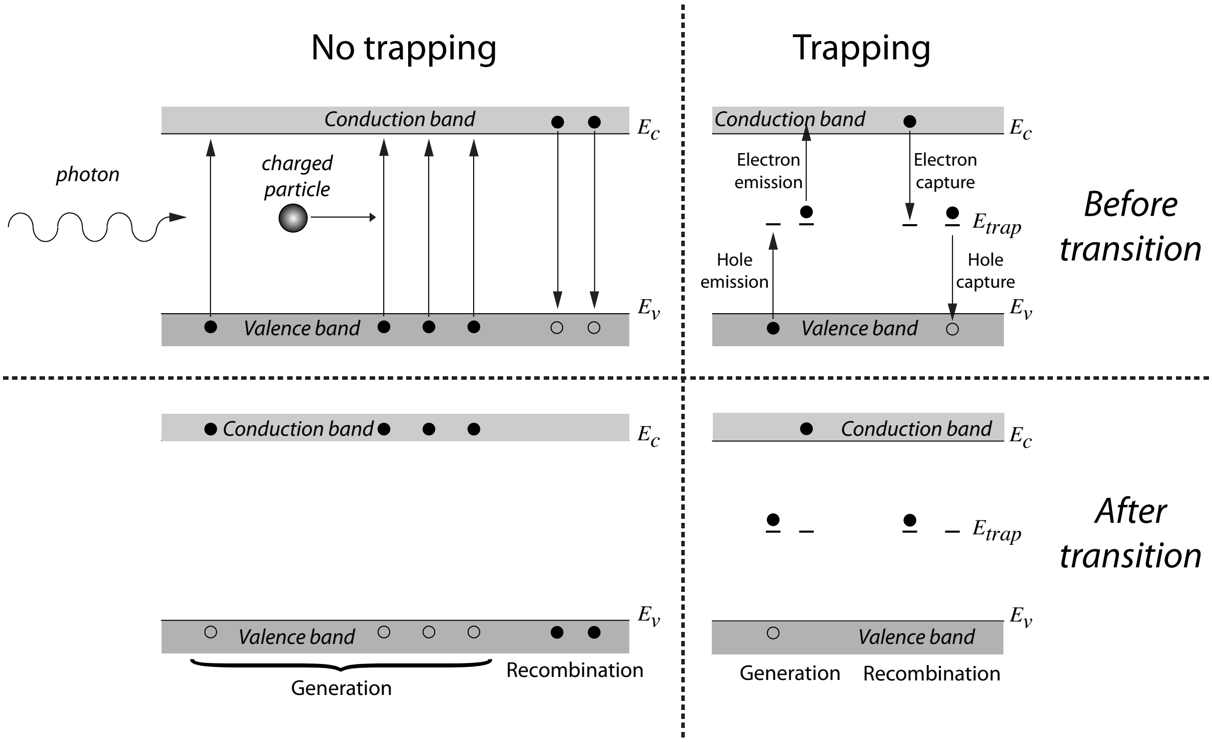

Figure 2.3: Generation and recombination
Generation and recombination processes involve both direct and indirect transitions. In addition to thermal generation, electrons can surmount the band gap when excited by photons or charged particles. Recombination is the process that involves the transition of an conduction electron to the valence band. Both generation and recombination involve direct and indirect transitions between the valence and conduction band. Indirect transitions occur via intermediate states that act as generation-recombination or trapping centres.

3. Electron capture: The process in which an electron from the conduction band is caught by a gap state.

4. Hole capture: The transition of a captured electron from a trap to the valence band, which can be seen as if a hole is captured by the intermediate state.

Emission processes 1 and 2 combine to generate electron-hole pairs, whereas the capture mechanisms 3 and 4 contribute to electron-hole recombination. In addition, a sequence of transitions 2 and 3 or transitions 1 and 4 can occur. In either case, a carrier is captured and subsequently emitted to the band where it came from and neither generation nor recombination occurs. This process is known as trapping and is predominantly mediated by shallow states. Due to their position close to the band edges, the capture probability of shallow states is high. Nonetheless, their emission probability is equally high, which means charge carriers only occupy these states for a relatively short time (of the order of ns). Deep states, however, have a considerably lower capture and emission probability.

Consequently, these states can trap carriers for a relatively long time ($0.1 - 1\ \mu$s).

2.1.4 Carrier transport

As discussed in the previous section, pairs of electrons and holes are created by excitation of valence electrons to the conduction band. These charge carriers are free to move through the crystal and are therefore responsible for conduction. The two dominant mechanisms for charge-carrier movement are diffusion and drift. Consequently, the total current is composed of a drift current and a diffusion current.

To be able to consider electrons and holes as free charge carriers in a semiconductor crystal, the concept of effective mass has to be introduced. It reflects the influence of the periodic potential of the nuclei on the movement of the charge carrier with respect to its direction of propagation. It is commonly expressed as:

$$\frac{1}{m^*} = \frac{1}{\hbar^2}\,\frac{d^2E(k)}{dk^2}\,, \tag{2.10}$$

where m^* is the effective mass, $\hbar$ the reduced Planck's constant, $E(k)$ the energy-momentum dispersion relation and k the wave vector. The mean kinetic energy of the carrier in thermal equilibrium can be defined using the equipartition theorem:

$$\frac{1}{2}m^*\bar{v}_{\mathrm{th}}^2 = \frac{3}{2}kT\,, \tag{2.11}$$

where $\bar{v}_{\mathrm{th}}$ is the carrier's mean thermal velocity, k Boltzmann's constant and T the absolute temperature. In thermal equilibrium free carriers collide with the vibrating lattice atoms and with possible dopant atoms. This random thermal motion is characterised by the carrier's mean free path λ, which describes the mean distance travelled between two collisions:

$$\lambda = \bar{v}_{\mathrm{th}} \cdot \tau_{\mathrm{c}}\,, \tag{2.12}$$

where τ_{c} is the characteristic time between collisions. In thermal equilibrium the carriers are not immobile, but the average net movement is zero.

Diffusion

In a non-uniform charge-carrier distribution, i.e. when a particle locally creates a cloud of electron-hole pairs, concentration differences cause a net carrier flow with a flux that is proportional to negative of the concentration gradient. In other words, carriers will flow from high-concentration regions to low-concentration regions. The resulting flux is described by Fick's first law [34]:

$$\vec{\Phi}_n = -D_n\vec{\nabla}n \qquad\qquad \vec{\Phi}_p = -D_p\vec{\nabla}p\,, \tag{2.13}$$

where n and p are the electron and hole concentration and $\vec{\Phi}_n$ and $\vec{\Phi}_p$ are the electron flux and hole flux, respectively. D_n and D_p are the electron and hole diffusion coefficient. They are a measure of the ease with which the respective carrier diffuses due to a concentration gradient. The resulting current-density components $\vec{J}_{n,p}^{\text{diff}}$ are given by the product of the electron or hole charge $\pm q$ and their respective flux $\vec{\Phi}_{n,p}$:

$$\vec{J}_n^{\text{diff}} = qD_n\vec{\nabla}n \qquad\qquad \vec{J}_p^{\text{diff}} = -qD_p\vec{\nabla}p\,. \tag{2.14}$$

The total current density due to diffusion is the sum of both the electron and hole current contribution:

$$\vec{J}^{\text{diff}} = \vec{J}_n^{\text{diff}} + \vec{J}_p^{\text{diff}} = qD_n\vec{\nabla}n - qD_p\vec{\nabla}p\,. \tag{2.15}$$

Drift

When a voltage is applied across a semiconductor, the resulting electric field $\vec{E}$ will exert a net force $\vec{F}$ on the free electrons and holes:

$$\vec{F} = \pm q\vec{E}\,. \tag{2.16}$$

Due to scattering processes, the charge carriers will accelerate to a mean speed, known as the drift velocity $\vec{v}_{n,p}^{\text{drift}}$. Assuming a constant electric field, it can be approximated as follows:

$$|\vec{v}_{n,p}^{\text{drift}}| \approx \frac{1}{2}|\vec{v}_{n,p}^{\text{final}}| = \frac{1}{2}\frac{|\vec{F}|}{m_{n,p}^*}\tau_c = \frac{q\tau_c}{2m_{n,p}^*}|\vec{E}| = \mu_{n,p}|\vec{E}|\,, \tag{2.17}$$

where $m_{n,p}^*$ denotes the electron's or hole's effective mass and $\mu_{n,p}$ is the electron or hole mobility, which is the proportionality factor (expressed in units of cm^2/Vs) between the electric field and its drift velocity. The carrier's mean drift length $L_{n,p}$, not to be confused with the mean free path λ, is determined by its mean lifetime $\tau_{n,p}$.

$$L_{n,p} = |\vec{v}_{n,p}^{\text{drift}}|\tau_{n,p} = (\mu\tau)_{n,p}|\vec{E}|\,. \tag{2.18}$$

Given an electric field, it means that the product of μ and τ determines the survival of the carrier during its drift towards the electrode. The $\mu\tau$-product is an important measure of the purity of the sensor, as it reflects the efficiency with which charge can be collected. Table 2.2 lists values of the $\mu\tau$-product and other fundamental parameters for high-quality crystals of the sensor materials studied in this thesis. For comparison, the values for amorphous selenium are given as well.

The current density due to drift can be expressed as the product of the charge concentration and the drift velocity:

$$\vec{J}_n^{\text{drift}} = -qn\vec{v}_n^{\text{drift}} = qn\mu_n\vec{E} \qquad\qquad \vec{J}_p^{\text{drift}} = qp\vec{v}_p^{\text{drift}} = qp\mu_p\vec{E}\,, \tag{2.19}$$

with the total current density being the sum of the electron and hole components.

$$\vec{J}^{\text{drift}} = \vec{J}_n^{\text{drift}} + \vec{J}_p^{\text{drift}} = q(n\mu_n + p\mu_p)\vec{E}\,. \tag{2.20}$$

The relation between the mobility and the diffusion coefficient is given by the Einstein relation [35]:

$$\frac{D_{n,p}}{\mu_{n,p}} = \frac{kT}{q}\,. \tag{2.21}$$

Table 2.2: Fundamental semiconductor-sensor parameters at 300 K. For comparison, also the values for amorphous selenium are given.

	Silicon	**Gallium arsenide**	**Cadmium telluride**	**a-Selenium**
Z	14	31; 33	48; 52	34
ρ (g/cm^3)	2.33	5.32	6.2	4.3
E_g (eV)	1.12	1.42	1.56	2.3
W (eV)	3.61	4.26	4.43	$20 - 50$
R (Ωcm)	$< 10^4$	10^8	10^8 - 10^9	$\sim10^{14}$
μ_n (cm^2/Vs)	1500	8500	1100	$3{\cdot}10^{-3}$
μ_p (cm^2/Vs)	450	400	100	0.12
τ_n (s)	$>10^{-3}$	$3{\cdot}10^{-6}$	$3{\cdot}10^{-6}$	$4{\cdot}10^{-4}$
τ_p (s)	$2{\cdot}10^{-3}$	$2{\cdot}10^{-8}$	$2{\cdot}10^{-6}$	$4{\cdot}10^{-5}$
$(\mu\tau)_n$ (cm^2/V)	>1	$3{\cdot}10^{-2}$	$3{\cdot}10^{-3}$	$1{\cdot}10^{-6}$
$(\mu\tau)_p$ (cm^2/V)	~1	$8{\cdot}10^{-6}$	$2{\cdot}10^{-4}$	$4{\cdot}10^{-6}$
D_n (cm^2/s)	39	220	28	$8{\cdot}10^{-5}$
D_p (cm^2/s)	12	10	2.6	$3{\cdot}10^{-3}$

Continuity equation

In the previous two sections, the diffusion and drift current were derived for both electrons and holes. The total electron and hole current can thus be expressed as follows:

$$\vec{J}_n^{tot} = \vec{J}_n^{\text{diff}} + \vec{J}_n^{\text{drift}} = \quad qD_n\vec{\nabla}n + qn\mu_n\vec{E} \tag{2.22}$$
$$\vec{J}_p^{tot} = \vec{J}_p^{\text{diff}} + \vec{J}_p^{\text{drift}} = \; -qD_p\vec{\nabla}p + qp\mu_p\vec{E}\,. \tag{2.23}$$

Because charge is a conserved quantity, the time rate of change of the charge-carrier concentration ρ must be equal to the net current density $\vec{J}$ plus the net generation-recombination rate $(G - R)$. This relationship is described by the continuity equation:

$$-\frac{\partial\rho}{\partial t} = \pm q\frac{\partial(n,p)}{\partial t} = \vec{\nabla}\cdot\vec{J}_{n,p} + G_{n,p} - R_{n,p}\,. \tag{2.24}$$

Using equations 2.22 and 2.23 for the total current densities, the time rate of change of the electron and hole concentrations is described by the following relations:

$$\frac{\partial n}{\partial t} = \; D_n\Delta n + \mu_n(\vec{E}\cdot\vec{\nabla}n + n\vec{\nabla}\cdot\vec{E}) + G_n - R_n \tag{2.25}$$
$$\frac{\partial p}{\partial t} = \; D_p\Delta n - \mu_p(\vec{E}\cdot\vec{\nabla}p - p\vec{\nabla}\cdot\vec{E}) + G_p - R_p\,. \tag{2.26}$$

2.1.5 Signal formation

The former section discussed carrier transport. Both diffusion and drift cause charge-carrier movement. As soon as the generated charge carriers start to move and separate, a signal is formed on the collecting electrodes. This can be explained by using the method of mirror charges. The introduction of charge into a sensor volume changes the electric field inside. The electric field from the charge induces mirror charges on the electrodes, the magnitude of which changes as the carriers travel towards the electrodes. The induced charge itself cannot be measured, though its time-dependent change can. This change manifests itself as a current, the time integral of which equals the total induced charge.
Signal formation through current induction is treated by the Shockley-Ramo theorem [36], which states that the instantaneous current on a given electrode a can be expressed in terms of a weighting field $\vec{E}_w$:

$$i_a = -q\vec{v}_{n,p} \cdot \vec{E}_w \,, \tag{2.27}$$

where i_a is the instantaneous current, $\vec{v}_{n,p}$ the velocity of the charge carrier, which is determined by its mobility and the electric field. The net induced charge Q_a by a carrier moving from position x_1 to position x_2 on this electrode is determined by the difference between the (dimensionless) weighting potentials $(\phi_a(x_2) - \phi_a(x_1))$ at those positions:

$$Q_a = q(\phi_a(x_2) - \phi_a(x_1)) \,. \tag{2.28}$$

The unit of the weighting field is cm^{-1} and should not be confused with the electric (drift) field. Whereas the electric field determines the trajectory and velocity of the charge carrier, the weighting field only describes how charge motion couples to a specific electrode. For a homogeneous medium, it is only determined by the configuration and geometry of the electrodes disregarding the medium through which the carrier travels. It can be seen as the component of the electric field in the direction of the charge carrier's velocity, under the following circumstances: (i) both the medium and the charge are removed, (ii) the given electrode is raised to unit potential and all the other electrodes are grounded.
This definition implies that the only situation in which the electric field and the weighting field are equal, is the parallel-plate configuration. Figure 2.4 shows an example of two weighting-potential distributions together with the induced current and charge as a function of time for both a parallel-plate and a pixellated configuration. In the parallel-plate geometry the weighting potential is uniformly distributed, which causes both the electron and hole drift current to be constant in time until all the carriers are collected. Due to the lower hole mobility, the hole current signal is smaller and lasts longer. In the pixellated configuration the weighting potential increases as the distance to the electrode decreases. The charge carrier is therefore subject to an increasing weighting field as it moves towards its collecting electrode. When electrons are created close to the cathode and the signal is acquired at the anode, the induced charge and current signal increase only slowly when the electrons begin to move. As they approach their collecting electrodes, the coupling to the electrodes strongly increases, which makes that the largest part of the signal is formed close to the electrode. This effect is commonly referred to as the small pixel effect [37] and becomes stronger as the ratio between the drift length and the pixel dimensions increases.

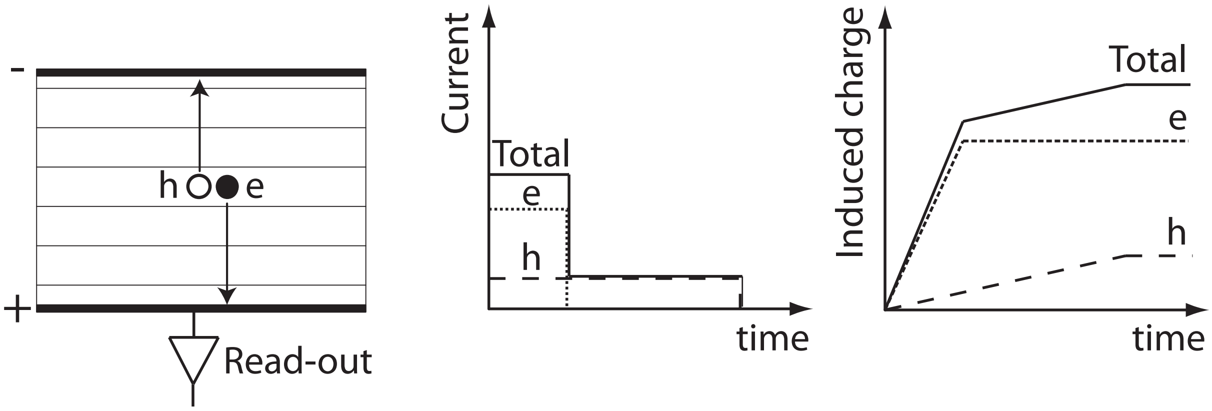

(a)

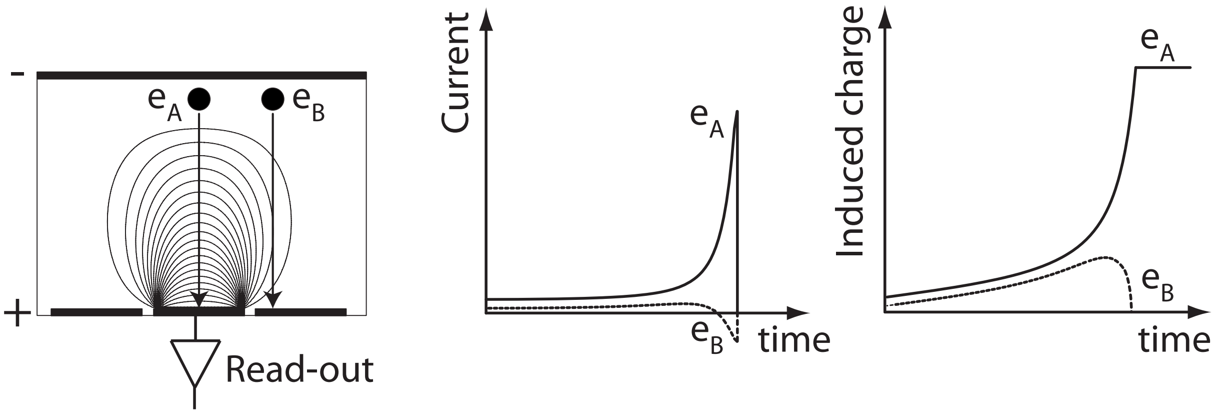

(b)

Figure 2.4: Weighting potential
The weighting-potential distributions for (a) a parallel-plate electrode configuration (simplified, I.e. assuming constant electric field) and (b) a pixellated one. The current signal and induced charge are dependent on the coupling of the carrier movement to a given collecting electrode. Figure based on [38].

Charge collection

In an ideal sensor, the total amount of induced charge is equal to the amount of charge deposited by the photon or charged particle. In reality, charge carriers have a finite lifetime and may recombine or get trapped during their travel towards the electrodes. The time a charge carrier can survive during its drift is therefore dependent on the concentration of trapping centres in the crystal. These centres reduce the amount of charge carriers available for signal formation. The remaining charge Q_{rem} relative to the total amount of generated charge Q_0 after a time t required to drift a distance x is given by:

$$\frac{Q_{\mathrm{rem}}}{Q_0} = e^{-\dfrac{t}{\tau}} = e^{-\dfrac{x}{\mu \tau E}} \,. \tag{2.29}$$

For a parallel-plate configuration with a uniform electric-field distribution, it can be derived that the net amount of induced charge Q_{ind} can be expressed by:

$$\frac{Q_{\text{ind}}}{Q_0} = \frac{E}{d}\left[(\mu\tau)_n\left(1 - e^{-\frac{x_0}{(\mu\tau)_n E}}\right) + (\mu\tau)_p\left(1 - e^{-\frac{(d-x_0)}{(\mu\tau)_p E}}\right)\right]. \tag{2.30}$$

This relation is known as the Hecht equation [39] and describes the efficiency with which the charge carriers are collected. It is strongly dependent on the electric-field strength E, the product of the carrier mobility and lifetime ($\mu\tau$), and the mean drift length x_0 (or $(d - x_0)$ for opposite-sign carriers, where d represents the thickness of the sensor).
By measuring the total amount of induced charge at different bias voltages, this relation can be used to determine an approximate value for the $\mu\tau$-product of either holes or electrons for a given sensor material. This provides a measure of the purity and homogeneity of that specific material. In order to minimise the contribution of one of the two charge-carrier types, it is commonly ensured that the electron-hole pair creation is close to the electrode opposite to the electrode used to measure the signal. Then the Hecht relation reduces to:

$$\frac{Q_{\text{ind}}}{Q_0} = \frac{E}{d}(\mu\tau)_{n,p}\left(1 - e^{-\frac{d}{(\mu\tau)_{n,p} E}}\right). \tag{2.31}$$

Polarisation An effect that reduces the charge collection efficiency and typically occurs in compound semiconductors is polarisation. It is regarded as the build-up of space charge in a crystal, which reduces the electric field and therefore results in a degradation of the detector's count-rate capability and energy response. It is believed that there are two mechanisms that cause polarisation:

1. Bias-induced polarisation [40–42]: at rectifying junctions, the band bending due to the applied potential can cause deep acceptor states (e.g. the cadmium vacancy in cadmium telluride) to cross the Fermi level, as a result of which they can get ionised. Consequently, space charge builds up, which leads to an overall reduction of the electric field across the sensor. This makes polarisation dependent on the type of electrodes used.

2. Radiation-induced polarisation [43–45]: this is schematically shown in Figure 2.5. Due to the relatively low mobility and short lifetime of holes in most compound semiconductors ($(\mu\tau)_{\text{p}}$ is in the order of 10^{-4} cm^2/V for cadmium telluride), their trapping probability is relatively high. This leads to an accumulation of holes close to the cathode, which locally shields the electric field. This shielding in turn reduces the drift velocity of the holes, which results in a further increase of the trapping probability. At a certain critical photon flux (typically of the order of $10^8 - 10^9$ photons s^{-1} mm^{-2} for good-quality cadmium telluride) the electric field is reduced to such an extent that the trapping probability is so high that more holes are trapped

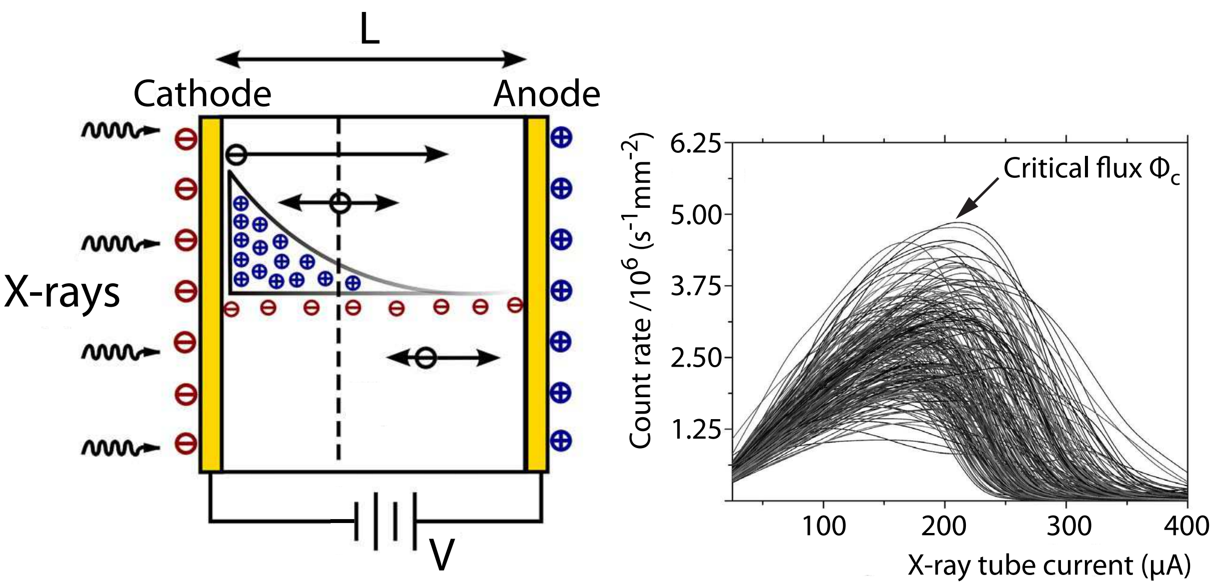

(a) (b)

Figure 2.5: Polarisation
(a) A schematic representation of the build-up of positive space charge near the cathode. Accumulation of holes shields the electric field, which in turn reduces the drift velocity of the holes. (b) The measured photon flux as a function of the incoming photon flux for a polarising detector. At a certain critical photon flux the electric field collapses and charge collection becomes impossible. Figures from [44].

than de-trapped. At this point, the electric field collapses and charge collection becomes impossible.

2.2 Pixel structures

As discussed in Section 2.1.5, a carrier's drift time must be significantly shorter than its lifetime in order to be collected. A sufficiently high electric field must therefore ensure that charges are collected quickly. Due to the unavoidable presence of imperfections, a high electric field causes an non-negligible (generation) current flow in the sensor. Since this current has nothing to do with signal current, it is also referred to as dark current or leakage current. Leakage current is a source of unwanted shot noise that is superimposed on the signal and should therefore be minimised. To achieve this, semiconductors with a relatively low band gap, such as silicon, are processed to diode structures with rectifying contacts.

2.2.1 Diode structures

There are two common ways to realise diode structures: through the formation of a p-n junction or a surface barrier using Schottky-type contacts.

p-n junctions

A typical p-n junction [46–48] is formed by locally doping an n-type semiconductor with a high concentration of acceptor atoms. The energy-band diagrams of Figure 2.6 schematically show the rectifying properties of an abrupt p-n junction.
Due to a difference in carrier concentration, the holes of the p-type region diffuse into the n-type region and the electrons of the n region move towards the p region. As a consequence, excess electrons of the n region annihilate with excess holes of the p region (and vice versa), which leaves the donor and acceptor atoms ionised. In this way, a negatively charged region is formed at the p side of the junction, and similarly a positively charged area on the n side. As a result, a region free of charge carriers forms around the junction: the depletion region. The width of the depletion region depends on both the acceptor and donor concentration. The space charge forms a potential barrier for the excess electrons and holes, as a result of which diffusion and thus barrier growth stops. This barrier is known as the built-in potential V_{bi}.

Reverse and forward bias By externally applying a potential difference V_{bias} across the p-n junction, the depletion region can either be increased or reduced. Applying a reverse bias voltage, i.e. creating an electric field in the direction of the built-in field, causes the electrons and holes to be pulled away from the junction. This widens the depletion region and that is exactly what semiconductor sensor operation is based on. The depletion region is devoid of free carriers and forms a capacitor together with the p and n regions as electrodes. At the same time, the reverse potential provides a drift field for the generated electron-hole pairs. In this way, the p-n junction diode forms an ionisation chamber.
In the case of a highly p-doped abrupt p-n junction, i.e. only a negligibly thin slice of the p region is depleted due to the many holes available, the depletion region predominantly grows in the least doped region, the width of which can be approximated by:

$$W_{\text{dep}} = \sqrt{\frac{2\epsilon_r\epsilon_0(V_{\text{bi}} - V_{\text{bias}})}{qN}}\,, \tag{2.32}$$

where V_{bias} is assumed negative, W_{dep} is the width of the depletion region, $\epsilon_r\epsilon_0$ is the permittivity of the semiconductor and N is the doping concentration of the bulk. The capacitance of the depleted volume with electrode area A can therefore be expressed as:

$$C = \frac{\epsilon_r\epsilon_0 A}{W_{\text{dep}}} = A\sqrt{\frac{\epsilon_r\epsilon_0 qN}{2(V_{\text{bi}} - V_{\text{bias}})}}\,. \tag{2.33}$$

Under forward bias, the created electric field counteracts the built-in potential barrier. As a result, conduction-band electrons of the n region can easily reach the conduction band of the p region, e.g. current can easily flow, provided that the forward bias voltage exceeds the built-in potential. For silicon diodes the built-in voltage is typically about 0.7 V.

Schottky contacts

Another way to realise rectifying structures, is to form a metal-semiconductor barrier contact, also referred to as Schottky contact [49]. For n-type semiconductors, this is achieved by depositing a metal with a work function that exceeds that of the semiconductor. Figure 2.7 shows this in terms of the energy-band diagrams before and after the materials are brought in contact.
Again, the difference in Fermi level causes band bending and thus a potential barrier for the majority carriers when both are brought in close contact. This barrier is known as the Schottky barrier ϕ_{barr} and is defined as the difference between the metal work function ϕ_m and the electron affinity χ of the semiconductor:

$$\phi_{\mathrm{barr}} = \phi_m - \chi \,. \tag{2.34}$$

The built-in potential V_{bi} equals the difference between the Schottky barrier and the electron potential at the Fermi level in the semiconductor ϕ_s:

$$V_{\mathrm{bi}} = \phi_{\mathrm{barr}} - \phi_s \,. \tag{2.35}$$

Ohmic contacts

To bias the sensor, the structure must be connected to the outside world via low-resistance contacts, so called Ohmic contacts. From Equation 2.34, it can be seen that the barrier height is not dependent on the doping concentration and can therefore easily be varied by using metals with an appropriate work function. Ohmic contacts can be realised by depositing a metal with a work function that is smaller than that of the semiconductor, as a result of which the majority carriers of the semiconductor don't experience a barrier when trying to enter the metal. However, this is not entirely true, because it turns out that intermediate states at the surface of the semiconductor have a stronger influence on the barrier height than the work function of the metal. This makes it therefore hard to manufacture Ohmic contacts with the desired electrical behaviour. The barrier width, however, can be controlled by altering the doping concentration of the semiconductor. In this way, majority carriers can tunnel through the barrier, a phenomenon that is often referred to as field emission.

2.2.2 Ohmic structures

Diode structures can only operate under reverse bias, which makes that only one carrier type can be collected at the pixel electrode. Compound semiconductors, like gallium arsenide and cadmium telluride, have a wider band gap and therefore a higher intrinsic

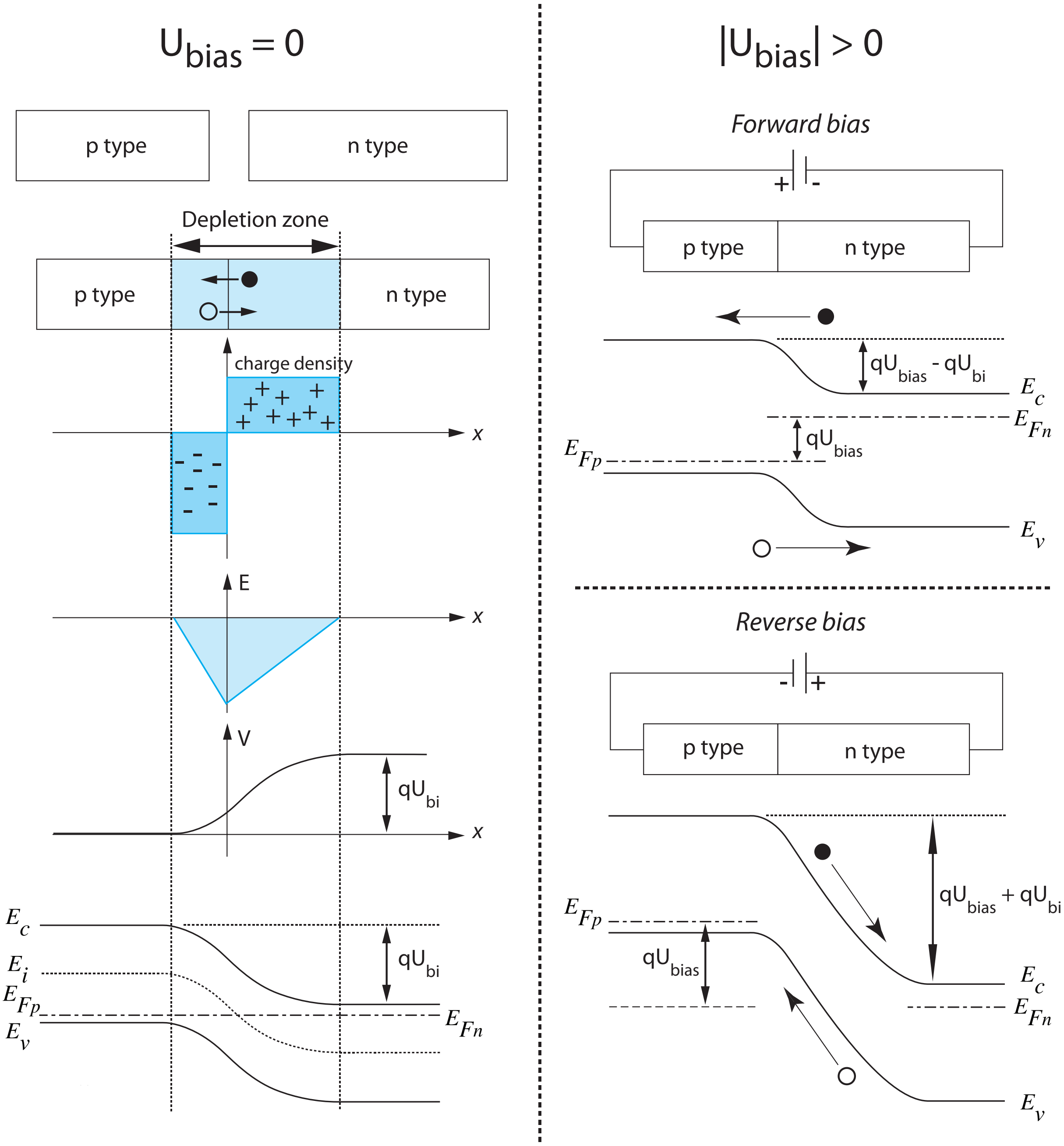

Figure 2.6: p-n junction
A p-n junction is formed by heavily doping a n-type semiconductor with acceptor atoms. Due to the difference in electron and hole concentrations of the two individual regions a potential barrier is formed by a region depleted of free carriers around the junction. This depletion region can either be expanded or reduced by applying a reverse or forward potential across the junction. A p-n junction is therefore a rectifying junction: current can only flow in one direction.

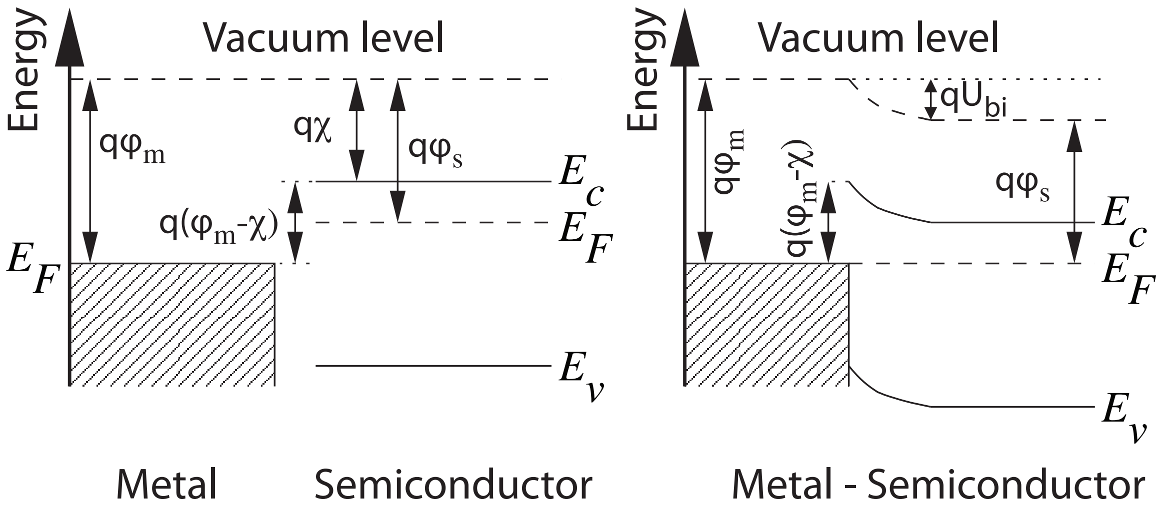

Figure 2.7: Schottky contact
A metal-semiconductor Schottky contact is formed when the work function of the metal exceeds that of the semiconductor. When they are brought in contact the original difference in Fermi level between them, causes a potential barrier for electrons, the Schottky barrier. Figure based on [50].

resistivity. These semiconductors are suitable for the use of Ohmic contacts without any rectifying junction. Use of Ohmic contacts allows for choosing which charge carrier to collect at the anode or cathode.

2.3 Sensor fabrication

The manufacturing of semiconductor sensors is a process that involves many steps [51]. First, single-crystal semiconductor material is grown in the form of a cylinder, called ingot. Subsequently, the ingot is sliced into circular wafers, which serve as the substrate material for the sensor. The substrate is then processed in order to realise patterned structures with the desired electrical properties. Patterning involves many steps, each of which will be briefly discussed hereafter. After pattering, the wafer is diced into smaller pieces to match the dimensions of the read-out chip. Dicing is an important step in the fabrication process of edgeless sensors, as it may introduce damage and contamination to the edge. Both can severely affect the sensor's performance.

2.3.1 Crystal growth

A common method for growing crystalline semiconductor material is the Czochralski technique [52]. A small piece of single-crystal material is brought into contact with its liquid-phase counterpart, which are respectively referred to as the seed and the melt. The seed is cooled and slowly pulled from the heated melt, as a result of which solidification occurs at the solid-liquid interface. Commonly, the seed is slowly rotating as well. It thereby stirs the melt and ensures a uniform temperature at the interface. The crystal grown by this process has a cylindrical shape and is called ingot. Although the Czochralski method provides silicon of acceptable purity levels for electronic circuits, for sensors the ingot is often purified to obtain even better quality. These techniques are collectively called zone refining [53]. Nowadays, detector-grade silicon ingots with a diameter of up to 300 mm can be produced. This is not the case, however, for crystalline compound semiconductor materials. Their growth is more complicated and less under control. Consequently, only ingots of smaller dimensions can be grown. Typical maximum diameters are 150 mm for gallium arsenide and 75 mm for cadmium telluride. Due to mechanical and thermal differences between the individual elements that make up the crystal, dislocations and defects are easily introduced during growth. Two common growth methods are the Bridgman technique and the Travelling Heater Method [54, 55].

After growth, the ingot is sliced into circular wafers, which are subsequently prepared for processing. Wafer preparation includes lapping to make it of uniform thickness, chemical etching to clean it and polishing to smoothen it. The resulting product is called the substrate material, which forms the basis for further processing of desired electronic structures.

2.3.2 Processing

Figure 2.8 shows the main process steps for manufacturing pixel structures on silicon substrate material. Each step will be discussed in the upcoming sections.

Oxidation

The processing of substrate materials starts with the formation of a layer of thermally grown SiO_2 in the case of silicon. That is because its di-electric properties offer an excellent base for further processing as well as a number of other benefits to the performance of the final device:

- It is a good insulator: its resistivity is of the order of $10^{14} - 10^{16}$ Ωcm.
- Its growth provides a clean interface with silicon.
- It can be etched with solvents that leave silicon unaffected.
- It is a diffusion barrier for many dopant atoms.

In the case of compound semiconductors, oxides do not play a significant role. The oxides are of worse quality and commonly they cannot be produced using a simple oxidation process.

Patterning

Often, numerous sensors are manufactured on one wafer. Their dimensions, layout and position on the wafer are determined and realised by a process called patterning, which includes several processing steps. Commonly, there is space left in between the individual structures in order to provide some margin for separating the dies from each other. This margin is often referred to as the dicing street.

Photolithography First, a thin layer of photosensitive material, the photoresist, is applied to the oxidised surface. The pattern is transferred to the substrate using a mask with the desired layout, which is aligned to and held closely above the wafer. By exposing the uncovered parts to e.g. ultraviolet light, the photoresist becomes more or less soluble, depending on whether a positive or negative photoresist is used, respectively. A developer solution removes the more soluble parts, resulting in a pattern that corresponds to either the exposed or non-exposed parts of the photoresist. This process is called photolithography.

Etching Once the photoresist is patterned, the wafer is placed in an ambient that etches the exposed silicon-oxide or other type of insulation layer without affecting the photoresist. Afterwards, the resist is stripped off using solvents for example. What remains is a positive or negative oxide image of the mask.

Doping In the case of p-n junction diodes, the pattern allows for doping the parts that are not covered by the oxide layer. Introduction of p-type (e.g. boron) or n-type (e.g. phosphorus) dopants is commonly achieved using either diffusion or ion implantation.
Doping by diffusion is accomplished by exposing the wafer to e.g evaporated source of dopant atoms. Subsequently the wafer is heated up in order to enhance the diffusion of the impurity atoms into the substrate material.
A more common doping technique used today is ion implantation. This method uses an ion beam to introduce the dopant atoms. A distinct advantage of ion implantation is that the depth and profile of the implant can be controlled accurately. In addition, the ion dose is of excellent uniformity over large areas, which provides minimal variation in the doping concentration. On the downside, the method introduces point defects such as vacancies and interstitials. Possible damage can be recovered by thermal annealing, which is a heat treatment that allows the interstitial atoms to fill the vacancies. It can be seen as a re-crystallisation process.

Metallisation After doping, contact with the outside world is established by depositing metal contacts. Two techniques are most often used: physical vapour deposition and chemical vapour deposition. Both techniques involve the deposition of thin films.
Physical vapour deposition is based on the condensation of a vaporised form of the material to be deposited. A common physical-vapour-deposition technique is sputtering.
In chemical vapour deposition the wafer is exposed to one or more gases that react with, or decompose on the surface to form a film of the deposit.

A common contact metal used for silicon sensors is aluminium. Depending on the desired current-voltage behaviour, contacts for cadmium telluride sensors can be made of platinum, gold or indium.

Passivation Once the metal contacts are realised, a passivation material (e.g. silicon nitride) is deposited to protect the structure against damage and contamination. For hybrid pixel detectors, it is important that this layer protects the sensor from the chemicals used in the bump-bonding process.

The number of process steps to fabricate a silicon sensor is typically about 20 to 30.

2.3.3 Dicing

After the build-up of several patterned layers, the individual sensors are separated from each other by splitting the wafer up into smaller autonomous units. This process is known as dicing and can be done in several ways. Dicing is a crucial step in the manufacture of edgeless sensors, as it can strongly degrade the sensor's performance at the edge. Nowadays, there are several dicing options, three of which will be discussed in the upcoming sections.

Blade dicing

The most common method used today is diamond-blade dicing [56]. The method uses a rotating circular metal blade with diamond particles on its surface. The cutting edges of the particles allow for cutting through almost any type of material. Due to the wide variety of blades, it provides the possibility to control the kerf width, depth and straightness. Hence, it can be used for many types of structures of different thickness. The main drawback of blade dicing is the mechanical load on the wafer. Though the load can be controlled to some extent, its deleterious effects cannot be eliminated entirely. Figure 2.9 shows the main adverse effects:

- Micro-cracks at the edge side-wall, which can extend tens of microns into the structure.
- Chip-outs at the front and back side of the wafer.
- Edge contamination due to material stacking in the dicing street (i.e. passivation material and metal), blade dirt and water used for cooling the blade.

One solution is to use serrated blades. This significantly reduces the load on the water and provides better cooling. The kerf width is not as accurate as with regular blades though.
Blade dicing requires a relative wide dicing street (of the order of 100 µm), which reduces the wafer area available for structure fabrication. The area loss is only significant, however, for the fabrication very small devices like integrated circuits.
Blade dicing can only be used for straight dicing streets.

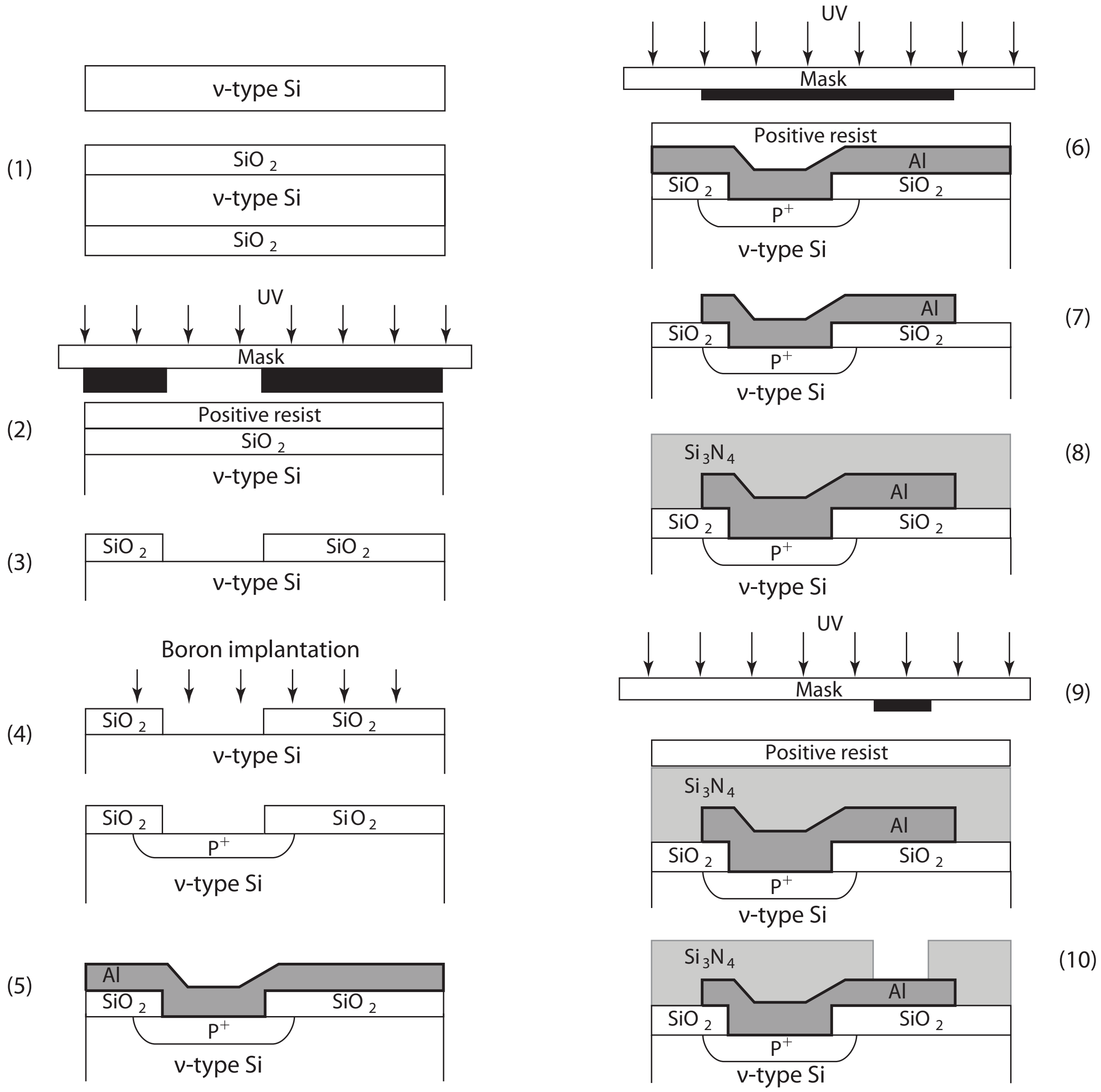

Figure 2.8: Fabrication steps

The fabrication of pixellated semiconductor sensors involves many steps. The main steps are shown for a typical silicon-sensor pixel: (1) oxidation, (2) photolithography, (3) oxide etching and photoresist removal, (4) pixel implantation / doping, (5) aluminium deposition, (6) photolithography, (7) aluminium etching and photoresist removal, (8) deposition of silicon nitride for passivation, (9) photolithography and (10) passivation etching for contact openings.

Laser dicing

Laser ablation Laser ablation is a process that involves the removal of wafer material by irradiation with laser pulses. These pulses locally generate a combination of melt and vapour. The vapour pressure drives the molten material out, as a result of which a kerf is created. The method is comparable to blade dicing in terms of edge smoothness. Although the kerf parameters can be optimised by tuning the wavelength, power and pulse duration of the laser, the resulting cut contains imperfections and contamination due to recast and debris. Also, the street width needed is non-negligible. The main advantage of laser ablation is the high removal rate and thus the short time it takes to dice a complete wafer.

Stealth dicing A method that enables to reduce the cutting waste and does not require post-cleaning is stealth dicing. Figure 2.9 shows the principle of this sub-surface dicing method. It involves the very local modification of the crystalline structure by focussing infrared laser light inside the wafer. The altered mechanical properties of this layer allow for accurate die separation by breaking using a tape-expansion technique. This minimises the transversal crack propagation, which results in a much smoother and cleaner edge. Moreover, the process speed of stealth dicing does not influence the edge quality as much as blade dicing does. Summarising, stealth dicing has the following main advantages over conventional dicing techniques:

- High-quality edge side-walls, as it is a dry and chipping-free process it provides smooth and clean edges.
- High-speed dicing possible.
- Low kerf loss, which allows for narrow streets (of the order of 10 µm) and thus higher wafer production yield.

The main limitations of stealth dicing are:

- It cannot penetrate metals or passivation material, which makes that the dicing street should be devoid of materials other than the semiconductor.
- The crystal orientation must allow for breaking along the modified layer.
- The maximum wafer thickness is limited. This due to the transmittance of the laser.

Plasma dicing

Another alternative is plasma dicing [58]. It involves etching by bombardment of ions accelerated by an electric field. This technique stems from MEMS[3] technology. It is an anisotropic process and therefore enables to create high aspect-ratio structures. It provides clean edges and moreover it can be easily implemented in the fabrication process. One

[3]Micro-Electro-Mechanical Systems

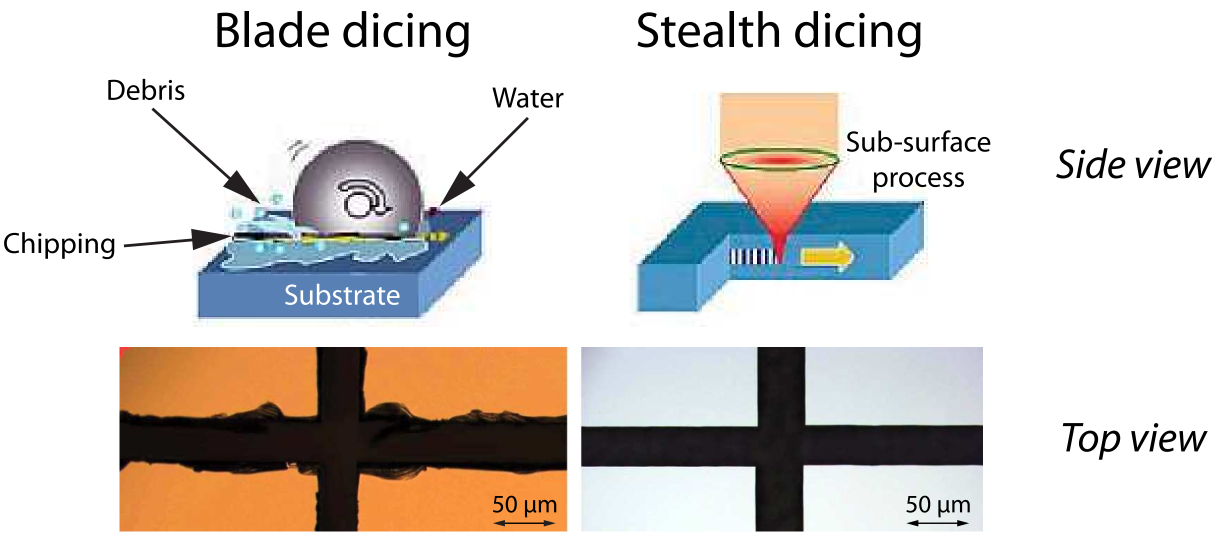

Figure 2.9: Dicing methods
Although blade dicing allows for cutting through almost any type of material, it causes chipping, contamination and micro-cracks at the edge's side-wall. A good alternative for thin wafers is stealth dicing: it provides high-quality edge side-walls with almost no kerf loss (a dicing-street width of 10 µm is already sufficient). The edge roughness resulting from either method is compared in the two bottom pictures. The gap between the stealth-diced dies is not because of kerf loss, but due to the tape expansion. Figures from [57].

example plasma-dicing technique is deep reactive ion etching, which is a derivative from reactive ion etching [59–61].

In reactive ion etching, a mixture of gases is used, only a part of which is ionised. In other words, the mixture is both chemically and physically active. Chemical action is isotropic, whereas the physical action is strongly directional, determined by the electric field in the plasma sheath above the wafer.

The physical action is typically preferred. However, the chemical action is also always present. Therefore, most of the time also a passivating component is included in the gas mixture. This passivating component does not remove material, yet deposits uniformily on the side-walls of the structure being etched. It then acts as a barrier for the chemically active components in the plasma. At the bottom of the structure, the ion bombardment removes this barrier, thereby continuously exposing the silicon to the etching plasma. With the right equilibrium of processing conditions, perpendicular sidewalls can be obtained with minimal undercut under the masking layer.

An improvement to reactive ion etching is deep reactive ion etching. The process is schematically shown in Figure 2.10. With deep reactive ion etching, the process continuously switches between etching and passivation, using two different gas mixtures and bias conditions. It provides more parameters to tune and therefore allows optimization of each individual step. This process is called the Bosch process [62] and typically results in scallops along the side-walls. The etching component typically comes from radicals of the

SF_6 molecules. A common passivating component is C_4F_8.
A distinct difference with other dicing techniques is that all dies can be separated at once.

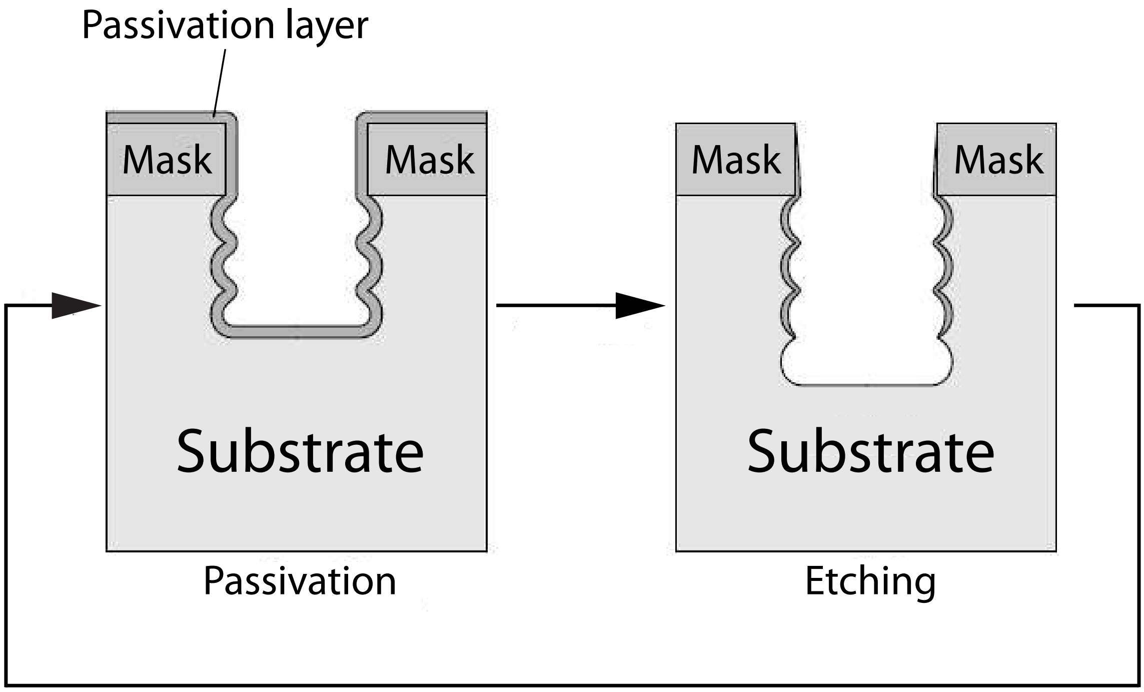

Figure 2.10: Deep reactive ion etching
Deep reactive ion etching provides clean edges and can be easily implemented in the sensor fabrication process. A typical deep-reactive-ion-etching technique is the Bosch process. The switching between etching and passivation results in scallops along the depth of the side-walls.

2.4 Sensor designs

Conventional sensors have guard electrodes around their active area to protect the pixel matrix from unwanted edge effects, which can have a width of up to a millimetre. Today, more and more applications demand near-edge sensitivity. A design change is therefore needed. Before evaluating the various options to fabricate edgeless sensors, two common types of conventional structures are described. Specifically, the effects that imperfect edges can have on the sensor's performance are discussed.

2.4.1 Conventional sensors

As discussed in Section 2.2.1, semiconductors with a moderate resistivity are commonly processed to diode-like sensor structures. In that case, either the back plane or each pixel of the matrix forms a p-n junction or Schottky contact with the semiconductor substrate. Figure 2.11(a) depicts schematic cross-sections of two different p-n junction silicon structures. The most common silicon sensor is the p-in-n structure. A matrix of p^+-type pixel electrodes is realised by patterned implantation of boron atoms in an ν-type substrate. Hence, each pixel forms a p-n junction with the substrate. The back plane is unstructured and forms an n^{++}-type Ohmic contact with the substrate by heavily doping it with phosphorus.

A different approach is the n-in-n structure. In this case, the pixels are n^{++}-type

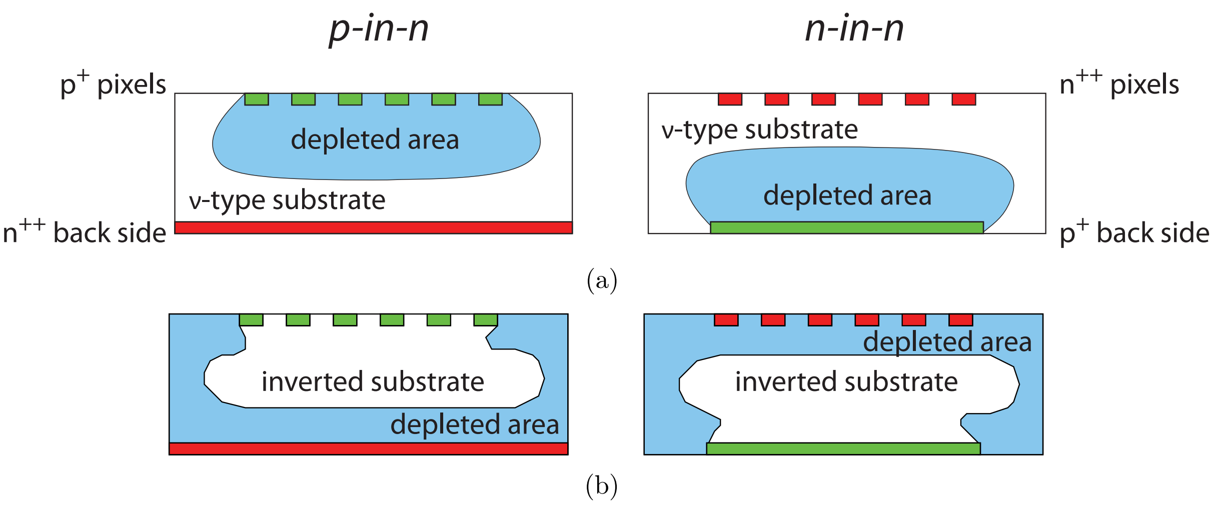

Figure 2.11: Implanted-junction structures
(a) Two common implanted-junction silicon sensors are the p-in-n and n-in-n structure. p-in-n structures are the most common approach of fabricating silicon sensors. If radiation damage is an issue, however, n-in-n sensor are more favourable. (b) Radiation-induced type inversion of the substrate causes the depleted area to grow from the side opposite to the original junction. Figure based on [50].

and the back plane is p^+. For p-in-n structures, the depleted area grows from the pixel matrix as the reverse bias voltage increases. For n-in-n structures, however, the depletion zone originates from the back plane. This requires a reverse bias voltage that depletes the entire sensor volume up to the pixel matrix. Otherwise, charge would be spread over many pixels, which implies a loss in resolution. However, the advantage of n-in-n sensors is their better radiation hardness. Radiation typically introduces defects that alter the substrate's effective doping concentration to more p-type, i.e. the bulk shows type inversion. As shown in Figure 2.11(b), the junction of n-in-n sensors will start to grow from n^+-type pixel matrix when the sensor is damaged by radiation. This allows for under-depleted operation, whereas for type-inverted p-in-n sensors the depletion region grows for the back side and hence the bias voltage has to be high enough to deplete the sensor over its full thickness. Consequently, for n-in-n sensors the applied bias voltage can still be of acceptable levels, whereas for p-in-n sensors the voltage must be increased more and more. Otherwise, like non-damaged n-in-n sensors, charge will be induced on

neighbouring pixels, which negatively affects the resolution and noise.
The main drawback of n-in-n sensors is that the process is much more complex and therefore more expensive. Since the junction grows from the back side, the back electrode must not be in contact with the edge of the sensor, which requires back side patterning. Moreover, due to electron accumulation underneath the inter-pixel oxide layers, n^{++}-type pixels must be actively isolated from each other by highly doped p-type regions.
An interesting radiation-hard alternative is the n-in-p sensor, whose potential is under study by the RD50 collaboration at CERN [63].

2.4.2 Edge effects

An important issue for almost every single-crystal semiconductor sensor is the edge. Several factors make it imperfect, each of which causes a reduction of the sensor's performance:

- At the surface and edge of the sensor the periodicity of the crystal lattice is abruptly terminated. This causes dangling bonds, which introduce a wide distribution of intermediate states in the band gap known as surface states. As the carrier lifetimes depend on the concentration of generation-recombination centres, generation currents can be considerably increased at the edge under reverse bias.

- Dicing, especially blade dicing, introduces damage and contamination at the edges (see Section 2.3.3). This damage manifests itself as micro-cracks propagating into the crystal, and chip-outs at the front and back sides. Micro-cracks reduce the crystalline integrity and increase the concentration of intermediate states in the forbidden gap. Both chip-outs and surface roughness of the edge side-wall are fertile ground for contamination and moisture, which function as excellent media for leakage paths. As a result, there can be a considerable current flow on the surface of the sensor's edges and corners.

- Due to the abrupt ending of the electric field along the outside of the pixel matrix, the field strength can be increased significantly close to the outer pixel electrodes [64, 65]. This can cause early break-down of the device.

As shown in Figure 2.12, these issues are dealt with by implanting one or multiple guard-ring electrodes around the pixel matrix [50, 66]. They gradually reduce the electric field towards the edge and prevent charge carriers generated at the edge from reaching the depletion region. As the potential difference between the front and back side is terminated, i.e. the outermost guard ring is at the same potential as the back side, surface currents that may flow along the edge towards the pixel matrix are reduced. The number of guard rings, and thus the width of the buffer zone between edge and pixel matrix, depends strongly on the required bias voltage. This periphery can be twice as wide as the thickness of the sensor. Sensors that operate in radiation-harsh environments need guard ring structures that are even wider (up to 1 mm for 300 µm thick sensors). The radiation requirement does not hold for imaging detectors, yet guard rings do take up a substantial fraction of the sensor's total area. In a tessellation of detector modules this will show up as unwanted seams in the image. To reduce the sensor's inactive periphery, both slim-edge and active-edge sensors are under study nowadays.

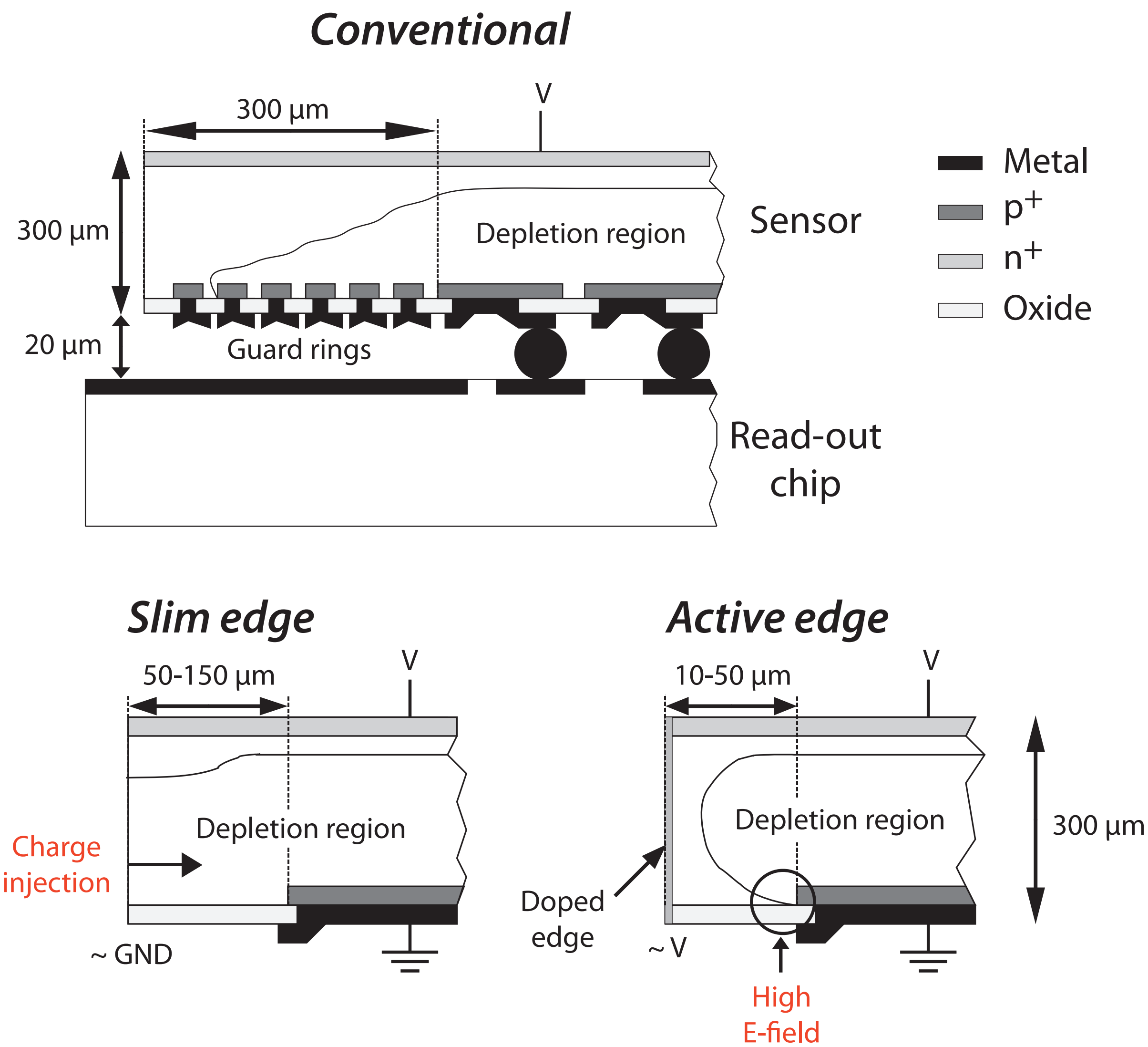

Figure 2.12: Edge processing and topology
A conventional sensor has guard rings that protect the active pixel region from unwanted edge effects. In a tessellation of detectors, this excess of material at the periphery shows up as seams. To reduce the distance between the active area and physical edge significantly, both active-edge and slim-edge sensors are being developed. Figure based on [50].

2.4.3 Edgeless sensors

To allow for a reduction of the insensitive periphery, edge effects have to be minimised. The use of minimally deleterious dicing techniques and proper surface-state passivation is therefore imperative. Today, several designs of edgeless sensors are fabricated and examined. Depending on the way the edge is terminated, they can be categorised into two types: slim-edge and active-edge sensors.

Slim edges

Slim-edge structures are manufactured by dicing the sensor closer to the pixel matrix. As a consequence, the depletion zone extends to the edge (see Figure 2.12) and any charge generated at the edge will enter the space charge region, which is being referred to as charge injection. It is therefore crucial that the defect density at the edge is minimised. This is accomplished by avoiding and mitigating the negative effects of dicing. The literature reports on:

- Laser cutting and subsequent treatment of the edge's side-wall [67, 68]: both surface-state passivation by aging in air and defect removal by chemical treatment, e.g. etching the edge with an acid solution, show improvements of the performance of the sensor's active area.
- Deep reactive ion etching [69, 70]: this die-separation technique results in less surface damage than blade dicing and it can be easily implemented in a standard micro-electronics fabrication process.
- Current terminating structures [71–80]: narrow ring electrodes along the edge at the pixel side of the sensor. An important difference with regular guard rings is that they are grounded and hence do not gradually lower the potential towards the edge. They serve as a drain for the surface current that flows along the edges.

Recently, slim-edge p-type silicon sensor were realised by partial laser dicing and cleaving, followed by Al_2O_3 side-wall surface-state passivation [81]. The Al_2O_3 forms a negatively charged layer at the edge side-wall that pushes away free electrons and hence effectively passivates the edge. In fact, the Al_2O_3 not only passivates the edge's surface, but also shapes the electric field at the edge. This is similar to what active-edge sensors are based on.

Active edges

Active-edge sensors [82–85] are basically similar to slim-edge sensors, except that the electric field is actively terminated at the edge. Impurity atoms of the same doping type and concentration as the back side are implanted in the edges' side-walls, as a result of which they form an extension of the back electrode (see Figure 2.12). This configuration allows the pixel matrix to be as close as tens of micrometers from the edge. In spite of this major achievement, active-edge technology has its drawbacks:

- The fabrication process is complex. To be able to access the side-walls of the edge in order to do wafer-level doping a support wafer is required (this will be discussed in more detail in Chapters 4 and 5).

- The doped edge causes a distortion of the electric field in the edge region, which results in an anomalous response of the outer pixels. At the same time, the edge implant can cause a strong curvature of the junction at the edge, which could dramatically lower the break-down voltage of diode structures.

2.5 Summary

Crystalline semiconductor material is very suitable as a conversion layer for imaging detectors. They provide large signals and at the same time their conductivity is high enough to avoid high leakage currents. Nevertheless, the electrical integrity of the sensor material strongly depends on the homogeneity and purity of the crystal. Nowadays, detector-grade silicon wafers with a diameter of up to 300 mm can be produced, while the growth of compound semiconductor materials is much more complicated and much less under control. Typical maximum wafer diameters are 150 mm for gallium arsenide and 75 mm for cadmium telluride, which translates into even smaller pieces of homogeneous sensor material. As a consequence, the active area of current detectors using single-crystal cadmium telluride as sensor material is limited to approximately 10 cm^2. One way to realise a larger detection area is to tile multiple smaller detectors. This requires sensors that are homogeneously responding up to the edge, which means that edge effects have to be minimised. Minimally deleterious dicing as well as proper surface-state passivation is imperative. Two types of edgeless sensors are under study nowadays: slim-edge and active-edge sensors. Slim-edge sensors are fabricated by dicing the sensor closer to the pixel matrix, whereas active-edge sensor are characterised by the fact that the edge is doped. This implant actively terminates the electric field at the edge, which allows the pixel matrix to be as close as tens of micrometers from the edge.

3

The Medipix detector

Pixel detectors with separate sensor and read-out chip are denoted as hybrid pixel detectors. All different sensors and samples that are considered in this thesis are studied in conjunction with the Medipix chip and are therefore loosely named Medipix detectors.

Hybrid technology allows for separate optimisation of both sensor and read-out chip and inherently offers the freedom to use sensor materials other than silicon. Figure 3.1 shows a schematic side view of a single Medipix-detector pixel. By design, both the Medipix chip and sensor are segmented into an equally dimensioned matrix of pixels. Subsequently, each sensor pixel is connected to its corresponding read-out pixel by means of so called bump bonds, which are tiny solder balls (typically made of an alloy of lead and tin or indium) of approximately 20 µm diameter.

The Medipix chip measures particle flux by registering the rate of signals from energy deposits in the sensor. Each photon is given the same weight, which makes the detector's response independent of the photon energy. So called charge integrators, which are common in particle physics experiments' large pixel detectors, integrate the amount of energy deposited over time and therefore weigh the photon by its energy. Inherently, the detective quantum efficiency of photon counters is higher than that of systems based on charge integration. The more so because photon counters use energy thresholds in the photon-selection process and hence enable rejection of non-photonic noise. Ideally, the photon response should be scaled to its energy-dependent attenuation [86, 87], which is proportional to E^{-3} (see Equation 1.7 on page 7). This requires a read-out device that can accurately measure the energy deposition in addition to the incoming photon flux. One promising candidate is the latest descendant of the Medipix family of chips: Medipix-3.

3.1 The Medipix chip family

The Medipix project dates back to 1995 [89]. In this year, the WA97 experiment [90] demonstrated the unique benefit of photon counting detectors in high-energy physics: their ability to exclude electronic noise and hence to preclude ambiguities in hit patterns.

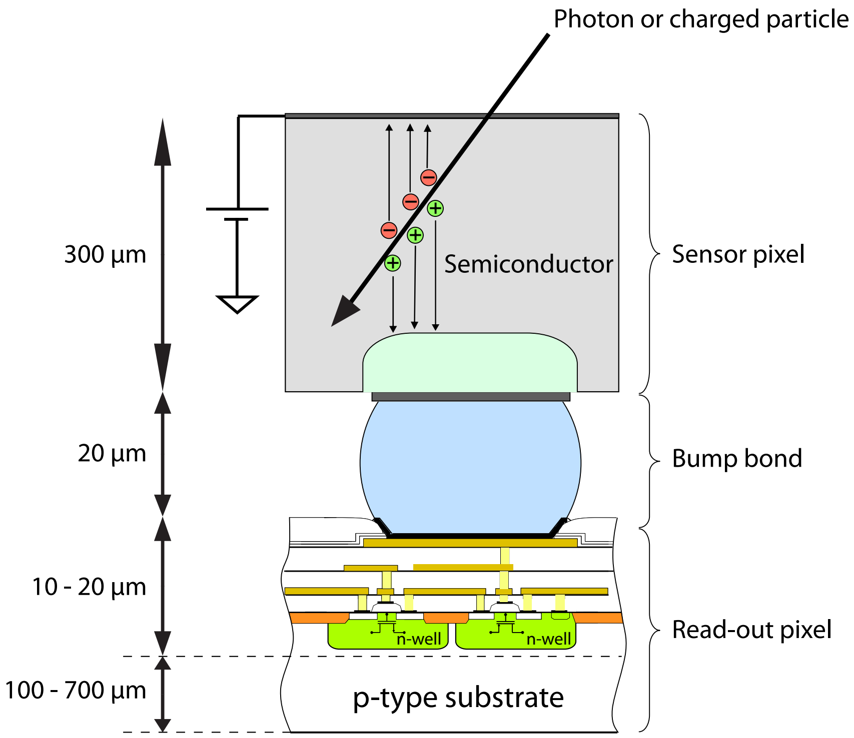

Figure 3.1: Medipix detector pixel
A schematic cross-section of a single Medipix-detector pixel. The sensor and read-out chip are equally segmented and connected by means of bump bonds. The dimensions indicated on the left are typical for Medipix detectors using silicon sensors. Figure based on [88].

This key property led the LHC experiments to adopt hybrid pixel technology for vertex detection. At the same time – due to the promising properties of photon counters – this triggered the development of a dedicated pixellated photon counting read-out chip aimed at application in fields other than particle physics, initially targeting medical imaging: the Medipix chip.

3.1.1 Medipix-2

In 1997, the first generation of Medipix chips, Medipix-1 [91], was developed. Its active matrix of 64 by 64 square pixels, each of side length 170 µm, demonstrated the outstanding performance of miniature photon counters. Images with excellent signal-to-noise ratio could be taken, mainly because of its large dynamic range and the ability to reject electronic noise. The excellent performance as well as the availability of new commercial sub-micron CMOS-processing technologies led only a few years later (1999) to the development of the Medipix-2 chip [92].
Its matrix measures 256 by 256 pixels of 55×55 µm^2 each, resulting in an active area

of approximately 2 cm^2 containing 65536 pixels. Its smaller pixel size makes the chip's resolution competitive with existing X-ray imaging detectors, though it is the pixel functionality that really stands out compared to current systems. The Medipix-2 is processed using a six-metal layer 0.25 µm CMOS technology and contains approximately 500 transistors per custom pixel cell.

Figure 3.2(a) shows the layout of one pixel. The cell is formed by an analogue and a digital part. The analogue part contains a charge sensitive amplifier and a window comparator with two identical pulse height discriminators. The digital part is formed by arbitration logic and a 14-bit counter with overflow control.

The basic building blocks of the pixel circuitry are schematically represented by the block diagram of Figure 3.2(b). The charge sensitive amplifier (CSA) is formed by dedicated circuitry[1] that amplifies and integrates the signal from the sensor and provides leakage-current compensation. It can be set for both electron and hole collection, thereby allowing for the use of different sensor materials. Subsequently, the amplifier output is compared to the lower and upper threshold values of the window comparator, which can be globally adjusted. The outputs of the discriminators are buffered and fed into an AND logic gate at the entrance of the arbitration logic. This logic decides whether a photon-induced pulse should be registered or not and can operate in two modes: window mode and single threshold mode. In window mode, the global low and high threshold values form an energy discrimination window. If the voltage pulse at the output of the amplifier falls within this window, the logic generates a fixed width pulse. In single mode, the high threshold value is set below the low threshold value. The logic then generates a pulse whenever the amplified pulse is above threshold. The pulses from the arbitration logic increment a 14-bit counter if the shutter is open and if the number of counts is below the overflow value of 11810. Both pulse height discriminators can be calibrated in order to minimise the pixel-to-pixel threshold dispersion due to transistor mismatch[2]. The calibration procedure is commonly referred to as threshold equalisation.

When the shutter is closed, the counter serves as a shift register. Subsequently, the pixel shift registers of each column are chained, which allows for column-wise read-out. This is schematically depicted in Figure 3.2(a). Each column is read out by a 256-bit fast shift register, which is located in the periphery at the bottom of the chip. Using a clock running at 100 MHz, the entire chip can be read out in approximately 9 ms through a serial port, whereas this takes only $\sim 300\ \mu$s for parallel readout. The periphery also contains thirteen 8-bit digital-to-analog converters and input/output logic to control the chip.

3.1.2 Timepix

In 2006, the pixel circuitry of the Medipix-2 chip was modified to meet the desire to measure the drift time of electrons in gaseous detectors [95].

This customised chip is equipped with an external clock that is transmitted to all pixels

[1] The circuit follows the scheme proposed by F. Krummenacher [93]

[2] This feature is especially attractive for soft X-ray imaging, as it requires a very homogeneous detector response

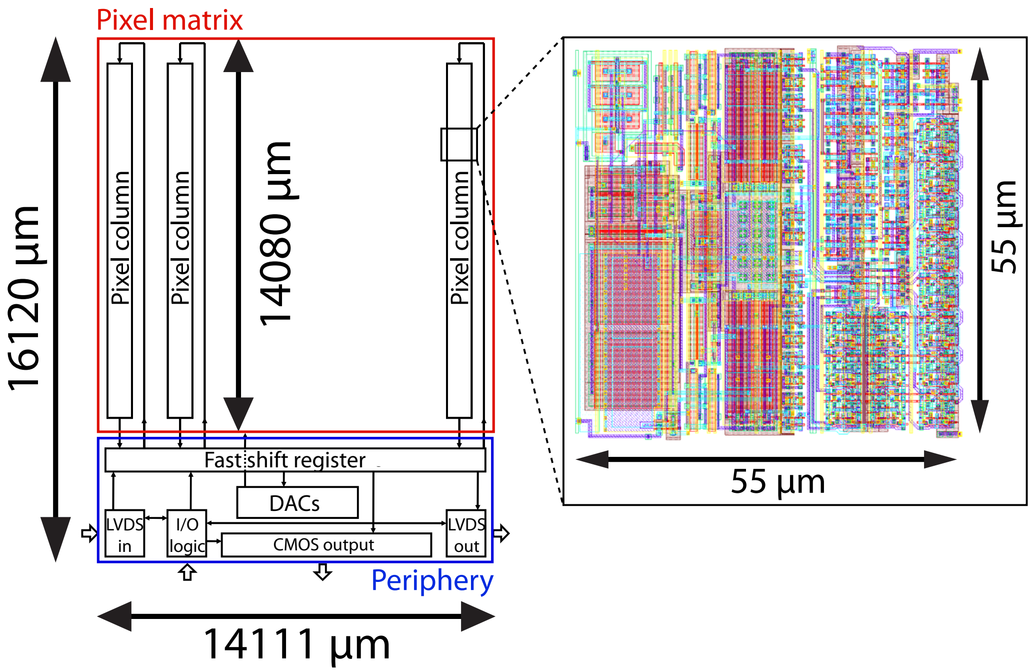

(a)

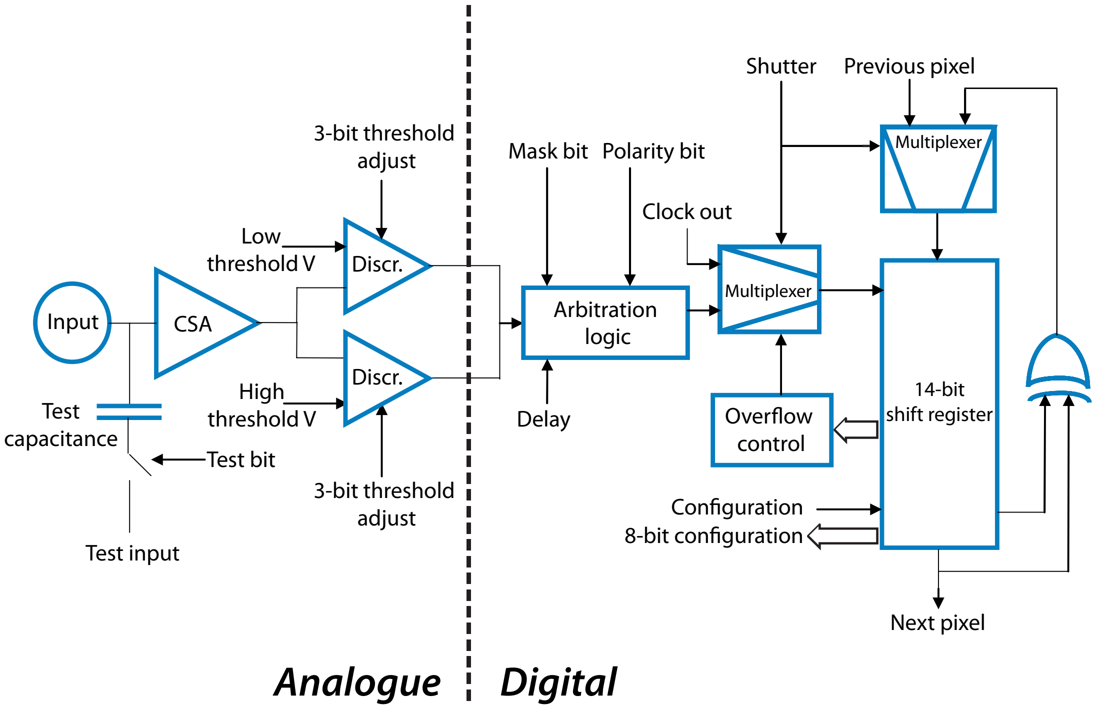

(b)

Figure 3.2: The Medipix-2 pixel cell
(a) The floor plan of the Medipix-2 chip together with a close-up view of the layout of one Medipix-2 pixel cell. (b) A block diagram of the pixel cell. The analogue part amplifies, shapes and discriminates the sensor's signal. The digital part contains logic that determines whether the photon is eligible for counting and increments a 14-bit counter if so. Figures are based on [92, 94].

and is called Timepix [96]. The clock serves two modes of operation next to the counting mode: Time-of-Arrival (ToA) and Time-over-Threshold (ToT). Although simultaneous operation in different modes would be very desirable, Timepix can only operate in one mode at a time.
In Time-of-Arrival mode, each pixel registers the arrival time of the charge carriers with respect to an external shutter signal. In this mode, each clock cycle increments the counter from the first moment the amplified pulse is above threshold until the shutter closes. This provides information on the time of arrival of the charge carrier relative to the shutter signal, which is a measure for the interaction depth in the sensor. Because of the maximum Timepix clock frequency of 100 MHz, thereby providing a 10 ns time resolution, this mode is currently only interesting for gaseous detectors (drift times in semiconductor sensors are of the order of tens of ns.)
The Time-over-Threshold mode, on the other hand, is mainly interesting for semiconductor detectors. Each clock cycle increments the counter as long as the amplified pulse is above threshold, while the shutter is open. Because the circuit of the charge sensitive amplifier provides a constant-current discharge, this duration is a measure for the pulse height, which is proportional to the amount of induced charge (if the hit rate is low with respect to the shutter length). Every pixel therefore records the amount of energy deposition in the sensor.
The acquisition mode is selected through and operated by the Timepix synchronisation logic, which is realised in the digital part of the pixel at the cost of one of the discriminators of the analogue part. Consequently, Timepix has only one discriminator per pixel, though with four bits for threshold adjustment instead of three.

Timepix-3

At the time of writing this thesis, the successor of Timepix, called Timepix-3, is being developed. This chip is supposed to be highly configurable suiting both gaseous and semiconductor detectors for a wide range of applications. Compared to Timepix, it will have more functionality, a higher time resolution and a more advanced architecture that can provide continuous read-out of sparse zero-suppressed data. Its most outstanding feature will be a fast clock that runs at 640 MHz and therefore provides a fine time resolution of only 1.6 ns. Moreover, three combined modes of operation will be possible. For example, in ToA&ToT-mode each pixel can record both arrival time and time-over-threshold simultaneously. Details are beyond the scope of this thesis and can be found in [97].

3.1.3 Medipix-3

In spite of their high functionality, there are some important limitations of both the Medipix-2 and the Timepix chip:

- Although the small pixels of only $(55\ \mu m)^2$ provide fine granularity, the probability that charge carriers created by the same photon are shared among several pixels is large. In particular, when the ratio between sensor thickness and pixel pitch is large. In Time-over-Threshold mode, charge-sharing can benefit the spatial resolution, since the fraction of the total charge deposition in each pixel correlates to the primary photon interaction point. In tracking applications, this information is used to obtain resolutions smaller than 10 µm with Timepix. For absorption and spectroscopic imaging, however, charge sharing can severely degrade the spatial and energy resolution, respectively.

- The detector is blind during read-out. As discussed in Section 3.1.1, the serial read-out time is approximately 9 ms. For 1 ms of exposure, this translates into 90% dead time and a maximum frame rate of 100 frames per second.
- Being 2 cm^2 the active area is limited, which makes it no viable substitute for today's large-area detectors yet. One solution is to realise a large area by tiling multiple Medipix detectors. This will be discussed in more detail in Section 3.2.

Mainly driven by the aim to mitigate the negative effects of charge sharing to imaging applications, this led in 2009 to the start of the design of a new chip: Medipix-3.
The Medipix-3 chip [88, 98, 99] is processed using an eight-metal 0.13 µm CMOS technology, which translates to a high functional density per pixel (approximately 1000 transistors per pixel). Each pixel contains two threshold discriminators and two counters that can also function as serial shift registers when the shutter is closed. By operation of both counters in their opposite states, the chip can read and record simultaneously, thereby eliminating dead time. That makes Medipix-3 attractive for real-time imaging applications.
In addition, a so called charge summing circuit is implemented. This circuit allows for event-by-event communication between pixels. More specifically, the collection area can be quadrupled. Within such a cluster of four pixels, the amount of charge collected by individual pixels can be combined to reconstruct the total amount of charge deposited in the sensor. This amount is subsequently assigned to the pixel that records the largest fraction of charge. In this way, the degrading effects of lateral charge spreading on the energy resolution can be minimised, without compromising the position determination.
The inter-pixel communication circuit used for charge summing can also be employed to differentiate between multiple energy windows. Four pixels of (55 µm)^2 can be grouped together to form large clustered pixels of 110 µm on the side. These can be read out as single pixels with eight identical discriminators (and corresponding counters) that can be set to form seven different energy discrimination windows. It offers the ability to do energy-resolved X-ray imaging. The diagnostic value of X-ray images can be increased significantly, as a colour can be assigned to each energy window. Figure 3.3 compares a grey-scale X-ray image of a copper and cadmium foil spiralled around a cilindrical perspex core. It shows that the use of colours substantially increases the capability to distinguish different parts in one and the same image[3]. Whereas the two metal foils are hardly dis-

[3]A related technique commonly used nowadays is dual X-ray imaging. It allows to resolve two energy bands by taking two images. This requires either two exposures, which results in a doubling of the dose, or a complicated system using two different detectors.

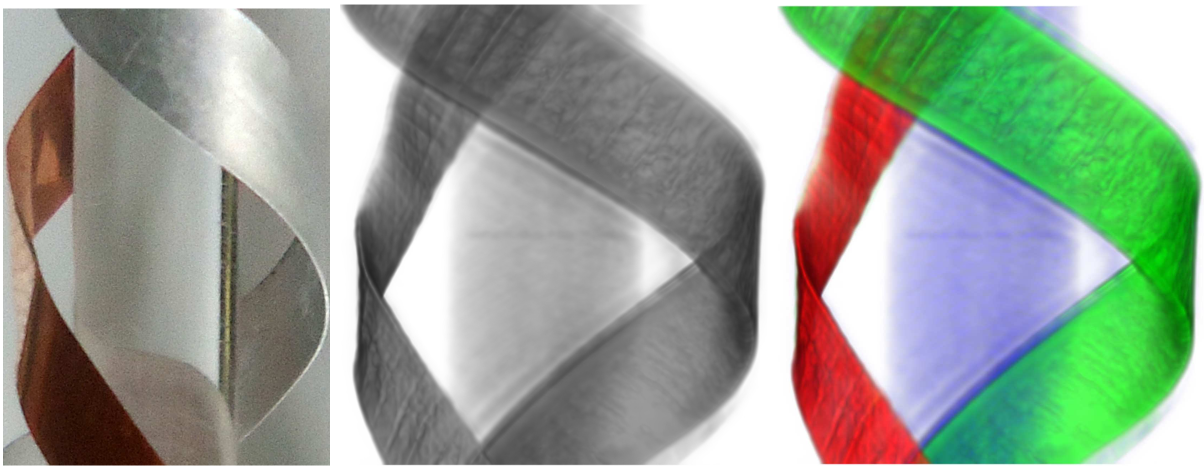

(a) (b) (c)

Figure 3.3: Grey-scale versus colour imaging
(a) A copper and cadmium foil spiralled around a cilindrical perspex core. Parts (b) and (c) show a conventional grey-tone image and its energy-resolved counterpart, respectively. It shows the great potential of energy-resolved imaging. Whereas copper and cadmium show the same grey tone in the left image, they can easily be distinguished (red and green) in the right image. The images, made with Nikhef's CT[a] setup, are from [100].

[a]Computed tomography: a medical imaging technique used to generate a three-dimensional radiograph from a large series of two-dimensional images taken around a single rotation axis

tinguishable in the grey-tone image, they can easily be told apart in the colour image.

Being able to discriminate between different photon energies, also allows for applying weighting factors that account for the energy dependence of the intensity attenuation through the object under study.
On top of the multi-functionality of the pixels, the floorplan of Medipix-3 anticipates tiling, as will be discussed in Section 3.2.2. This means an important step forward in realising a competitive large-area radio-diagnostic detector.

Table 3.1 summarises the main specifications of the Medipix family of chips. Especially the functionality of the Medipix-3 pixels is interesting for both radiography and spectroscopic X-ray imaging.

3.2 Tiling to larger areas

As discussed in the last section, the Medipix-3 chip provides unique imaging capabilities. Therefore, it is a very interesting read-out alternative for today's CCD[4]-based

[4]Charged Coupled Device

Table 3.1: Main specifications of three generations of Medipix chips. Note that in both acquisition modes of Medipix-3 the collection area can be quadrupled to do charge summing.

	Matrix (rows × columns)	**Pixel pitch** (µm)	**Collection area** (μm^2)	**Acquisition modes**
Medipix-1	64 × 64	170	170 × 170	Photon counting
Medipix-2	256 × 256	55	55 × 55	Photon counting
Timepix	256 × 256	55	55 × 55	Photon counting Time-over-Threshold Time-of-Arrival
Medipix-3	256 × 256	55	55 × 55 110 × 110	Photon counting
	128 × 128	110	110 × 110 220 × 220	Energy resolving

and TFT[5]-based digital radiography detectors. Its advanced pixel circuitry can provide electronic-noise free and fine-grained colour X-ray images of high contrast, especially when bump-bonded to a good-quality crystalline high-Z semiconductor sensor. Nevertheless, the limited active area of both the Medipix-3 chip and these kind of sensors keeps it from being a viable substitute for today's large-area X-ray imaging systems. The pixel matrix of Medipix-3 only covers approximately 1.4 × 1.4 cm^2, whereas current digital radiography detectors have sensitive areas of 35 × 40 cm^2 or larger. Moreover, only pieces of a few square centimetres of detector-grade high-Z material are currently available. A possible way to realise a large-area detector using Medipix-3 is to construct a seamless tessellation of multiple detector modules. To avoid seams in the image, this requires use of edgeless detectors.

3.2.1 The quad detector

First steps towards a larger detection area have been made with the development of a so called quad detector module [101]. It consists of four tiled Medipix chips in a 2-by-2 configuration, which read out one large sensor of approximately 3 × 3 cm^2. This assembly is mounted on a chip-carrier board, which provides mechanical support as well as electric connection to a read-out board. The read-out board reads out the chips in parallel, controls the signals to and from the chips through an FPGA[6], and supplies the necessary

[5] Thin Film Transistor

[6] Field Programmable Gate Array

voltages to the chips. A standard 1 Gigabit per second ethernet connection provides fast communication with a PC [102]. The read-out board can operate at approximately 120[7] frames per second, which makes it interesting for real-time imaging. To fit the quad assemblies side by side, the module is designed in a T-shaped configuration, i.e. the read-out board is mounted perpendicular to the carrier board. This enables tiling multiple quad detectors, which allows for realising large detection areas.
Current quad modules can only be tiled seamlessly on two of its four sides. This is due to inactive material at the periphery of both the Medipix chip and the sensor. Figure 3.4 shows the main bottlenecks.

(a) The input/output periphery at one side of the Medipix chip. This part not only contains the digital-to-analog converters and the input/output logic but also the bond pads. These are used for connecting the Medipix chip to the carrier board by means of wire bonds.

(b) The distance between the outermost pixels of two adjacent chips in a tiled configuration. Due to a safety margin for dicing on the outside of the pixel matrix, this distance exceeds the regular pixel pitch of 55 µm. For current Medipix-2 and Timepix quad detectors, this inter-chip pixel pitch is 275 µm.

(c) The presence of guard electrodes along the periphery of the sensor, which protect the active area from unwanted effects from the edge. These protecting structures can be as wide as $2 - 3$ times the thickness of the sensor used.

To realise a four-side tile-able and uniformly responding detector module, the active area has to be maximised by minimising: (i) the periphery of the Medipix chip, (ii) the distance from the outer pixels to the Medipix chip's edge and (iii) the inactive periphery surrounding the sensor's pixel matrix.
Figure 3.5 shows pictures of a single Medipix assembly, the current T-shaped quad module, and a tessellation of four quad modules mounted in a cooling block. The quad module consists of four Medipix chips that read out one large sensor of approximately 3×3 cm^2. The chips itself are read out in parallel by the perpendicularly mounted read-out board. The T-shape structure allows for tiling multiple quad modules, as depicted in Figure 3.5(c). It shows four Medipix quad modules mounted in a housing that can be cooled be either water or CO_2. Due to the wire bonds and Medipix's bottom periphery, an inactive seam of approximately 0.5 cm currently exists between the modules and therefore the modules only provide two-side tile-ability.

[7] theoretically, the maximum frame rate is 136 per second for a read-out clock frequency of 125 MHz

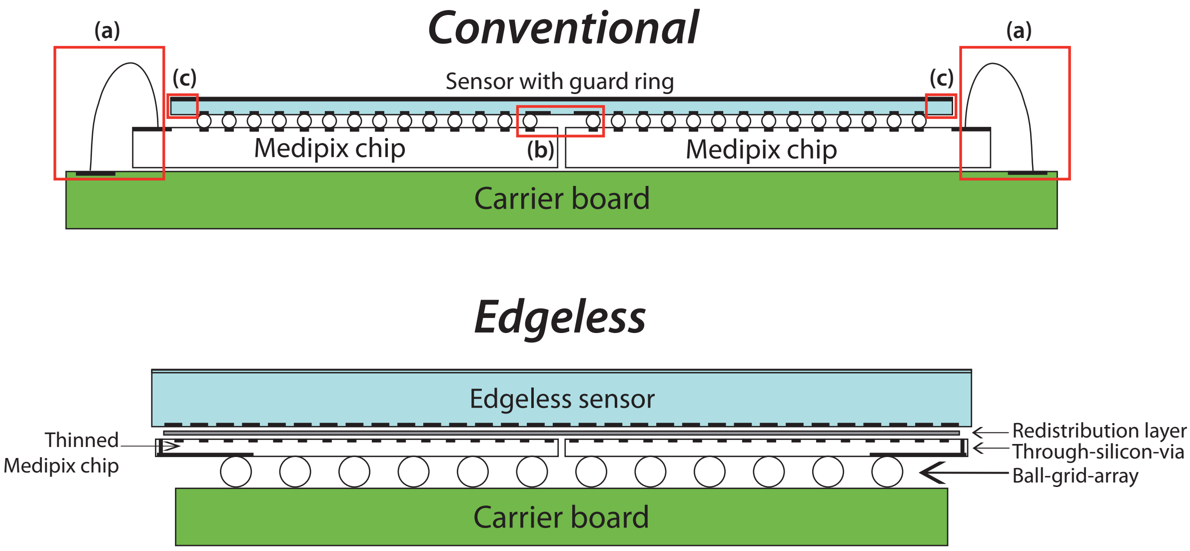

Figure 3.4: Edgeless detector modules
A schematic view of a conventional quad detector (top) and an edgeless one (bottom). To realise a uniformly responding large-area detector from multiple smaller modules, the sensors must be at least as large as the underlying electronics. The red boxes indicate the main bottlenecks that cause the limited tile-ability of current Medipix detectors.

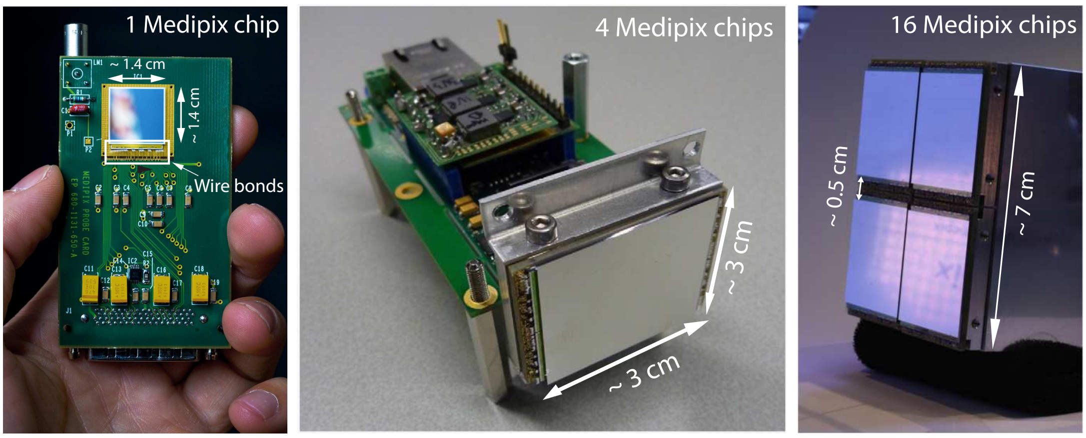

(a) (b) (c)

Figure 3.5: From single assembly to fourfold quad
(a) A single Medipix assembly mounted on an read-out board developed at CERN. (b) The quad detector module. (c) Four Medipix quad modules tiled together in a cooling rig.

3.2.2 From wire bond to through-silicon via

Medipix's active pixel area is 1.98 cm^2, which is approximately 87% of the total area of the chip. The remaining 13% is taken up by the periphery at one side of the chip, which contains the digital-to-analog converters and the input/output logic. This side also contains the input/output pads, which are used to connect the Medipix chip to the carrier board in order to power and read out the Medipix chip as well as to test and calibrate it. Traditionally, wire bonds connect the chip to the underlying carrier board, as can be seen in Figure 3.4. This makes that each single Medipix detector has an inactive region of approximately 3 mm wide at one side. As a result, the current Medipix chip only offers tile-ability on three sides of the chip. To get rid of this dead space, efforts are being made to replace the wires by vertical interconnects, so called through-silicon vias [103, 104]. Figure 3.6 shows a schematic cross-section of such a via. It can be considered as a copper pillar that connects the chip's active front side to its back side. First, small high aspect-ratio holes are realised using deep reactive ion etching [59]. Subsequently, these holes are coated with a polymer before they are filled with copper using an electro-plating process. A dedicated routing network on the back side routes the signals from the Medipix chip to the carrier board through a uniformly distributed ball-grid-array. The design of Medipix-3 anticipates the use of these state-of-the-art vias, thereby providing tile-ability on four sides. Figure 3.7 shows the different dicing options and the resulting ratios between the active and total area are listed in Table 3.2. The chip's periphery allows connection through either standard wire bonding or through-silicon vias. By using through-silicon vias only on side of the chip, the active area can be increased to 94.3% of the chip's total area. Further increase of the active area can only be obtained by reducing the size of the peripheral circuitry, for example by using vertical integration. This technique, however, is not mature enough yet.

Table 3.2: The active area as a fraction of the total area of the Medipix-3 chip as a result of the different dicing options [99]. The active area is 14080 × 14080 µm^2.

	Bonding option	**Total area** (µm^2)	$\frac{\textbf{Active area}}{\textbf{Total area}}$ (%)
Medipix-2 & Timepix	Wire bonds, 1 side	14111 × 16120	87.1
Medipix-3	Wire bonds, 2 sides	14100 × 17300	81.2
	Wire bonds, 1 side	14100 × 15900	88.4
	TSVs, 2 sides	14100 × 15300	91.9
	TSVs, 1 side	14100 × 14900	94.3

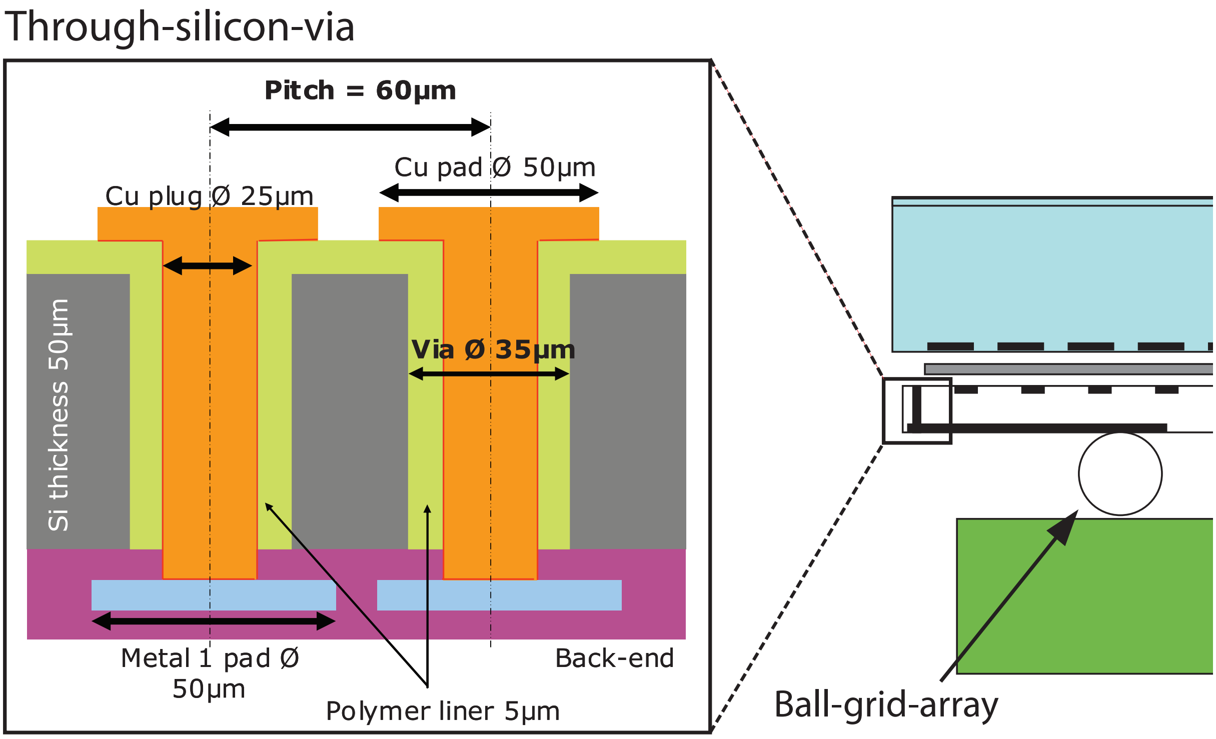

Figure 3.6: Through-silicon via
Replacement of wire bonds by through-silicon vias provides the possibility to seamlessly tile the sensors of the individual modules. The vias are realised by etching holes through the chip using high aspect-ratio deep reactive ion etching. A copper fill is used for good conductivity, where a polymer liner isolates the via from the chip. The schematic cross-section of the via is from [103].

3.2.3 Inter-chip pixel pitch reduction

Due to the wire bonds, Medipix chips are considered tile-able on three sides. However, at these sides there is a non-negligible inactive area as well. This is due to the fact that a certain tolerance has to be taken in order to avoid pixel damage in the process of separating the chips from the wafer (e.g. by using a blade dicer). As a consequence, when two chips are placed side-by-side, which is schematically shown in Figure 3.8, the distance between the outermost pixels of two adjacent chips is larger than the pixel pitch of 55 μm. In a tiled configuration, this forms a cross of inactive chip material. To ensure full coverage, this is bridged by large sensor pixels. Currently, these are three times as large as centre pixels.
The pixel-to-edge distance could be reduced by using more accurate dicing techniques, like stealth dicing [105]. This technique can reduce the width of the cross by a factor two. It is even shown that stealth dicing up to 12 μm inside the border of the Medipix chip does not harm the pixel performance [106]. More detailed information on stealth dicing is given in Chapter 2.

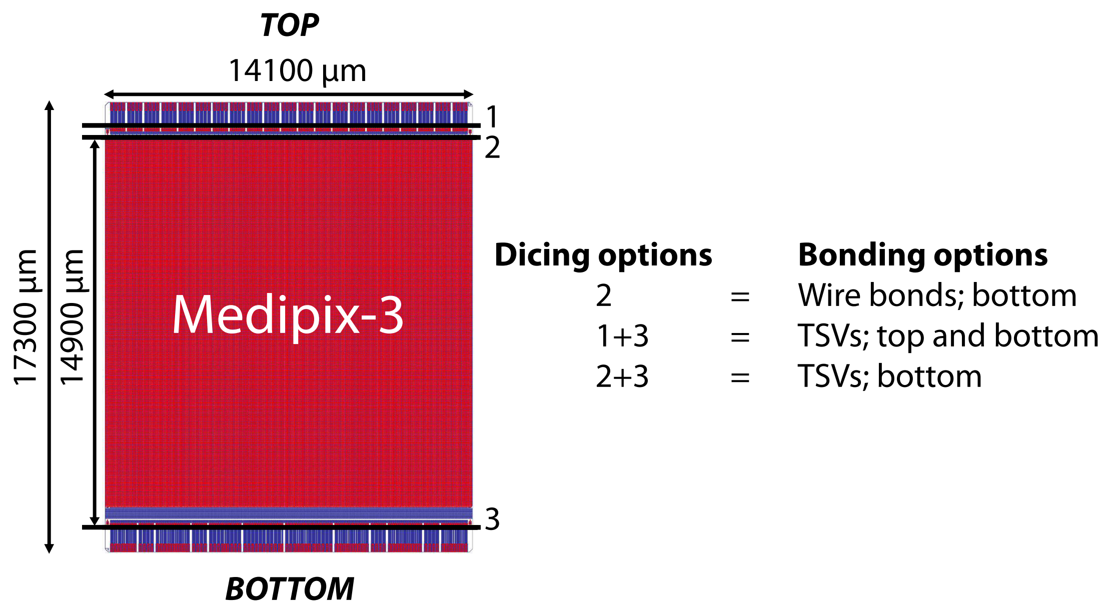

Figure 3.7: Medipix-3 dicing and bonding options
The Medipix-3 chip anticipates use of through-silicon vias and allows for multiple dicing options. Both the top and bottom periphery contain bonding pads that allow for standard wire-bond connections, but these may also be cut off in case of use of through-silicon vias. Depending on the desired powering and read-out configuration the chip can be diced and bonded accordingly. Figure based on [99].

3.2.4 From conventional to edgeless sensors

As mentioned in Section 3.2, the area of good-quality high-Z semiconductor material is limited. In addition, as discussed in Chapter 2, conventional sensors have guard ring structures that protect the sensor's active area from unwanted effects from the edge. These can take up a substantial fraction of the sensor's total area, typically they can be two times as wide as the sensor's thickness. In a tessellation of detector modules this will inevitably show up as seams in the image. To reduce the sensor's inactive periphery, both slim-edge and active-edge sensors [82] are being developed nowadays.

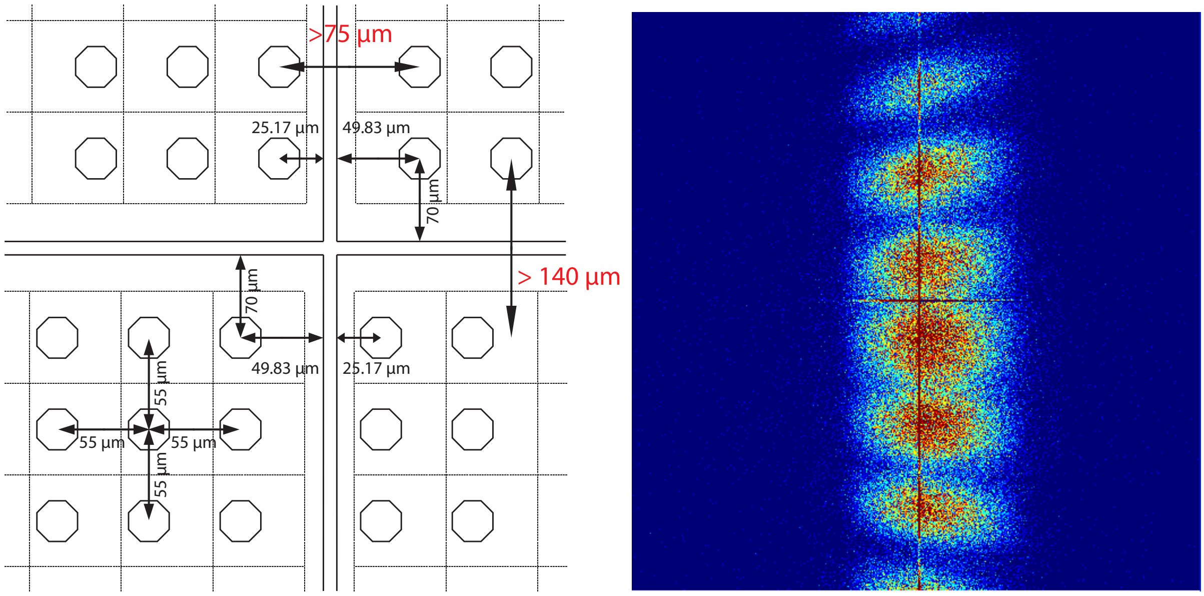

(a) (b)

Figure 3.8: Inter-chip pixel pitch
(a) Due to a safety margin, the so called chip's guard ring, the distance between the outermost pixels of two adjacent chips is larger than the pixel pitch of 55 µm. In one dimension this distance must be more than 75 µm, in the other it is at least 140 µm.(b) This requires larger sensor pixels at the adjacent edges, which causes a higher response from those pixels. As a result, a cross is observed in the image[b].

[b]The image shows a diffraction pattern, which is obtained by a line source of X-rays being split into smaller parallel beams using a soller slit. Courtesy of PANalytical, Almelo.

3.3 Summary

Medipix detectors have the potential to replace today's radiography detectors. In the first place, because Medipix is a photon counting chip and thus weights each photon equally, irrespective of its energy. Secondly, photon counting chips use energy thresholds for the photon selection and therefore enables rejection of non-photonic noise. Both properties benefit the signal-to-noise ratio and hence the detective quantum efficiency. In particular, Medipix-3 is a promising candidate for tomorrow's X-ray imaging detectors. Its intelligent circuitry per pixel offers high functionality. In continuous read-write mode, detector dead time is eliminated, which is interesting for real-time imaging. In charge-summing mode, the blurring effects of lateral charge spread are minimised, while the fine granularity of 55 µm is maintained. This greatly benefits both spatial and energy resolution. In energy-resolving mode, the chip differentiates between different energy windows, which allows for colour X-ray imaging and energy-dependent weighting (E^{-3}) of photons.
Nevertheless, the limited active area of both the Medipix-3 chip and that of high-Z semiconductor sensors keeps it from being a viable substitute for today's large-area X-ray imaging systems. The pixel matrix of Medipix-3 only covers approximately 2 cm^2, whereas

current digital radiography detectors have sensitive areas of 40×40 cm^2 or larger. A possible way to realise a large-area detector using Medipix-3 is to construct a seamless tessellation of multiple detector modules. To avoid seams in the image, this requires use of edgeless detectors. Current Medipix detectors have three main bottlenecks that cause their limited tile-ability: (i) the bottom periphery of the Medipix chip, (ii) the Medipix chip's guard ring that functions as safety margin for dicing and (iii) the inactive periphery surrounding the active area of the sensor.
This thesis concentrates on minimising the latter by studying the electrical and detection properties of both active-edge and slim-edge sensors.

4

Active-edge sensors: electrical characterisation

In Chapter 2, two types of planar edgeless sensors were introduced: slim-edge and active-edge sensors. This chapter will focus on characterisation of the latter.

Although active-edge sensors were already proposed in 1997 [107], interest in these sensors only grew in recent years. The greatest challenge in manufacturing edgeless sensors is to minimise the inactive peripheral area without affecting the detection characteristics of the active region. To accomplish that, edge effects giving rise to leakage currents in the active region have to be minimised. It is therefore required to use dicing methods that cause minimal damage to the edge and to passivate possibly active surface states.
To evaluate the electrical integrity of a sensor, which indirectly provides feed-back on the quality of the manufacturing process, its electrical properties are commonly characterised. Two conventional characterisation methods are capacitance-voltage (C-V) and current-voltage (I-V) profiling.

In this chapter, both techniques are used to characterise active-edge sensors. The leakage current of these devices is compared to that of conventional sensors in order to evaluate their viability. In particular, the dependence of the leakage current on the electrode topology at the edge is studied to determine the minimum edge distance for which the leakage current in the active region is still acceptable.

4.1 Sample specifications

In the framework of the Relaxd project, a batch of active-edge sensors was fabricated by Canberra[1] in order to test their potential for large-area detector applications. Sensors with different edge topologies were manufactured for the purpose of comparing their performance with that of existing conventional devices, rather than performing a systematical study on the minimum acceptable edge distance. As a result, a variety of sensors with

[1] Canberra Semiconductor, Lammerdries-Oost 25, 2250 Olen, Belgium. `http://www.canberra.com`

Table 4.1: Sample overview
Four different types of sensors were fabricated, each with various electrode topologies at the edge (see Figure 4.1). The design of the TOTEM strip sensors and Medipix sensors can be found in [108] and [94], respectively.

Samples	**Electrode configuration**	**Active area** (cm^2)	**Stop ring width** (µm)	**Edge distance** (µm)
6 TOTEM sensors	128 strips	0.64	15	25
			30	50
13 Medipix sensors	256 × 256 pixels	1.98	5	10
			10	20
			15	30
11 Circular diodes	single diode	0.1943	5	13
		0.1924	10	25
		0.1885	15	50
		0.1810	25	100
10 Rectangular diodes	single diode	0.2375	5	13
		0.2350	10	25
		0.2301 – 0.1836	25	50, 150, 300

different edge designs were produced. Table 4.1 lists the samples that were available. All are p-in-n silicon sensors fabricated on 300 µm thick ν-type substrate material. Each type was manufactured with various edge topologies characterised by:

1. the distance between the active-area electrode and the physical edge of the structure, referred to as the *edge distance*.
2. the width and doping type of the ring electrode at the edge, which is referred to as the *stop ring*.

For each topology, two samples were fabricated. One with a p-type stop ring and one with an n-type stop ring. The doping type determines whether the stop ring functions as an extension of the active edge or as a drain for currents generated at the edge. This will be discussed in more detail in Section 4.4.

Figure 4.1 shows the main processing steps together with a close-up view of the edge. First, trenches of approximately 250 µm deep were made from the back side using deep reactive ion etching (see Section 2.3.3). This gave access to the side-walls, which were subsequently doped with phosphorus atoms using a spin-on diffusion process. After doping, the sensor structures were separated by a second etch from the active-area side of the sensor. The process required very careful handling of the sensor wafer, since no support wafer was used. Once the first deep trench is made, the sensor dies were held together by 50 µm of silicon only. Despite the fact that the wafer did not break during handling, there were difficulties with the sensor die separation. The sensors were processed on 150 mm wafers, while the patterning equipment was suited for 200 mm diameters only. Therefore,

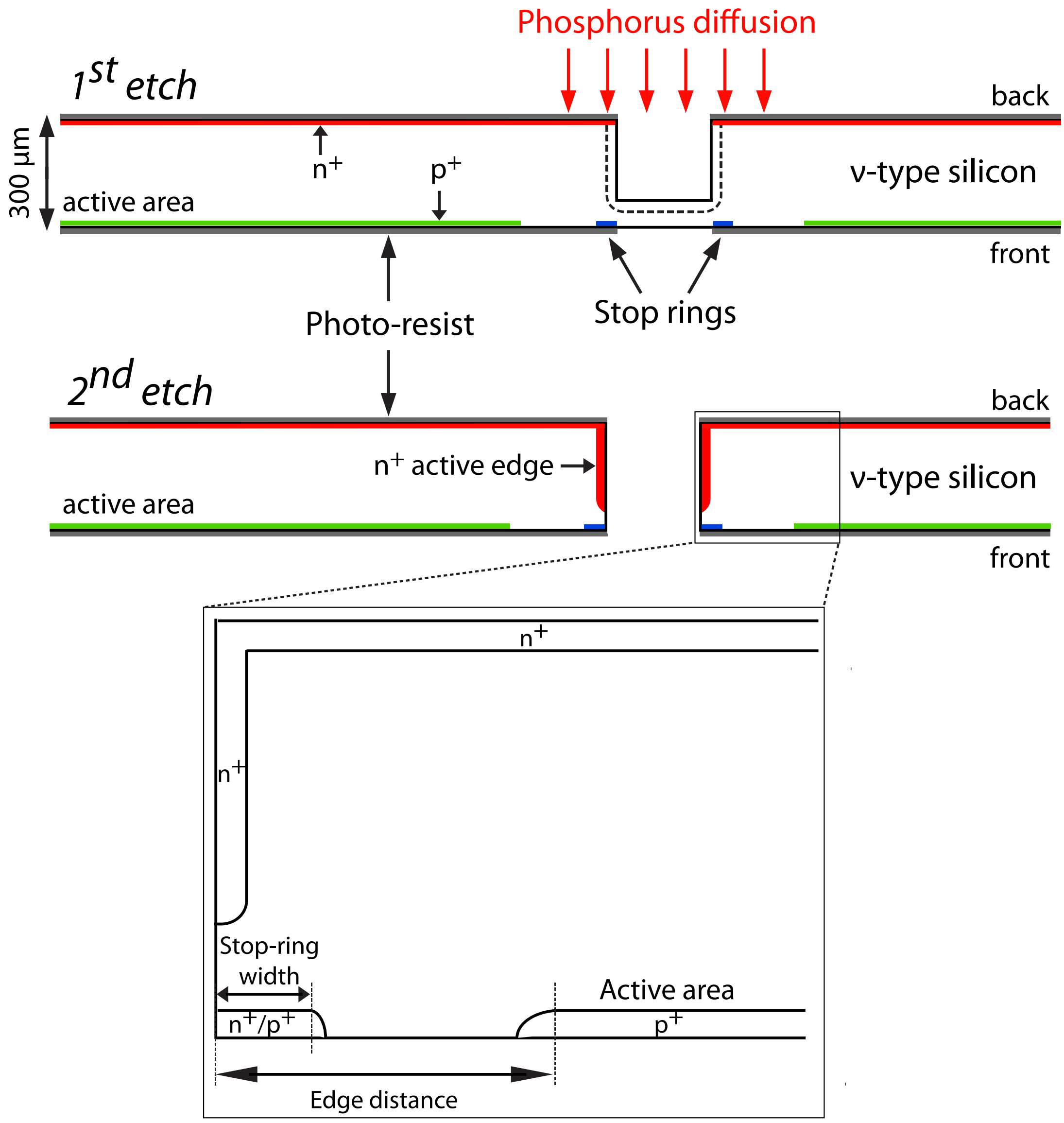

Figure 4.1: Edge processing
The edges were processed in three steps. First, a deep trench was etched from the back side. This provided access to the side-wall, which was subsequently implanted with phosphorus atoms. Finally, the structures were separated by etching from the front. The bottom part shows a schematic close-up view of the edge. Its topology is determined by the edge distance as well as the width of the n^+ or p^+ stop ring.

the sensor wafer had to be mounted on a 200 mm adaptor wafer. Non-uniformity of the bonding process, however, caused an irregularity in the separation process. As a result, not all dies were etched through completely and some of them had to be separated mechanically. This caused damage to the edge.
Moreover, no passivation layer was deposited between the stop ring and active area. Hence, the active area was not protected against possible surface currents induced by the edge. How this affects the leakage-current behaviour of these devices will be discussed in more detail in Section 4.3.2.

In Figure 4.2, the edge of a conventionally processed TOTEM sensor is compared to that of one with active edges. Whereas for conventional sensors the active area typically starts several hundreds of micrometers from the edge, this active-edge sensor has an edge distance of only 50 µm. In addition, the plasma etched sensor shows much less damage at the edge and seems to be spared from chip-outs.

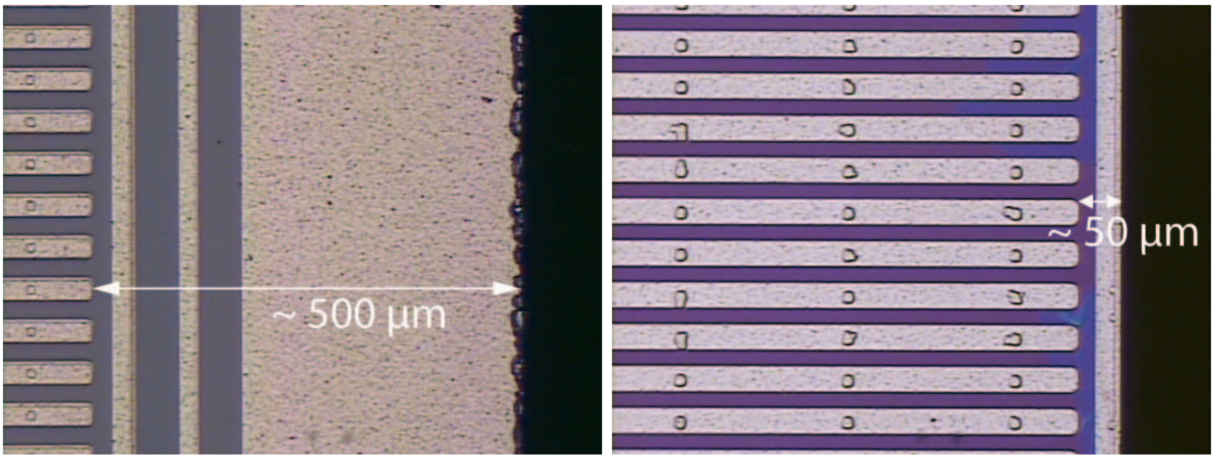

(a) (b)

Figure 4.2: Conventional edge versus active edge
Top-view photographs of a conventional TOTEM strip sensor (a) and one with an active edge (b). The edge distance of the active-edge sensor is ten times smaller than that of the conventional one. Moreover, the plasma-etched edge shows much less damage. The strip pitch is 50 µm.

4.2 Experimental set-ups

The prototypes of Table 4.1 are characterised by measuring the capacitance and leakage current at various bias voltages, which results in a characteristic C-V or I-V curve. Detailed descriptions of the set-ups for both C-V and I-V profiling are given in Appendix A. Contact with the samples is made using probe needles. An example of this can be seen in Figure 4.3. It shows a needle that makes contact with the stop ring of one of the circular diodes via a dedicated pad at the edge.
Probing is done in a probe station. It uses a chuck that supports the sensor, allows for biasing and at the same time provides precise positioning of the sensor with respect to the needles with a resolution of 0.5 µm. In addition, its housing provides electrical shielding and light tightness. Both are important requirements for this type of measurement, as will be discussed in Section 4.2.1.

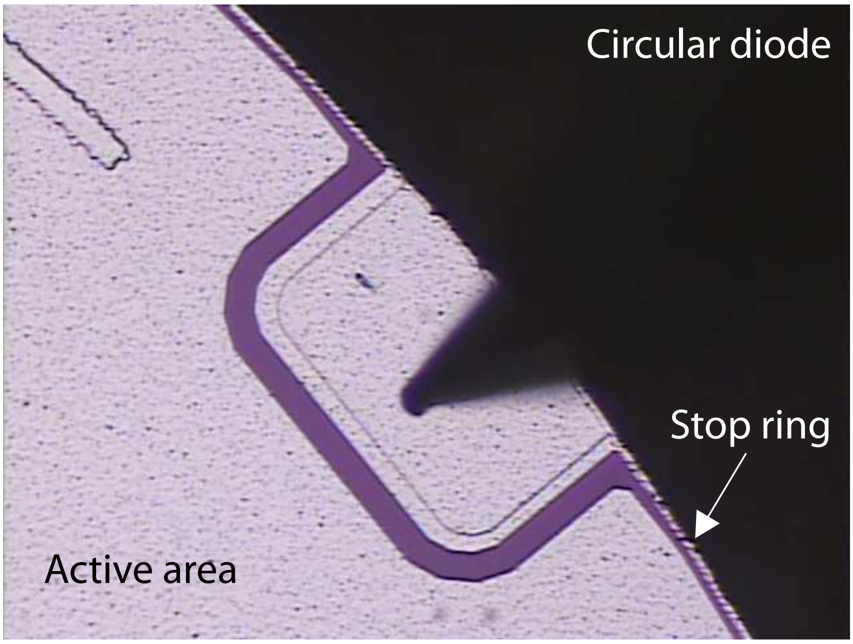

Figure 4.3: Probing
A top-view snapshot of one of the probe needles touching a dedicated probe pad at the edge of one of the circular diodes, which allows for contacting the stop ring.

4.2.1 Sources of error

Due to the small dimensions of the samples (see Table 4.1) as well as the high purity of the silicon substrate material, both capacitance and leakage current take on low values, typically of the order of pF and pA, respectively. Therefore, the instruments must be highly sensitive. This makes the measurements very susceptible to possible sources of error that affect or even obscure the actual measurement. Before a reliable measurement can be made, proper precautions must be made to avoid the most erroneous influences. In addition, remaining extraneous currents need to be subtracted from the measurement, which requires a precise calibration of the set-up. Potential sources of error are discussed below. They can be related to either the measurement set-up, referred to as circuit offsets, or to environmental influences.

Circuit offsets

Circuit offsets can be categorised into internal and external offsets.
Internal offsets are related to the measurement device itself, i.e. to the source-measure units and the LCR meter[2] (see Appendix A). These can be caused by bias currents of active devices and leakage currents through insulators within the instrument.
External circuit offsets are related to any circuit component but the measurement device itself. Possible sources and ways to minimise their influence are discussed below.

Cables of incompatible type as well as faulty connections can affect the measurement. Capacitance measurements require coaxial cables of a very precisely known length. As the cable itself has a non-negligible capacitance, the length of the cable must be very precisely known in order to correctly calibrate the LCR meter before measurement.
Low-level current measurements require triaxial cables. These cables are similar to coaxial cables, except that they have a second tubular conductor. This conductor is in between the wire and the shielding conductor and is referred to as the guard. It is driven at the same potential as the wire, which results in a zero potential difference between them and therefore eliminates possible leakage paths through the insulator. The outermost conductor is grounded, which makes that the guard is shielded from unwanted electromagnetic interference.

Tribo-electric currents are caused by friction between a conductor and an insulator. This friction can liberate electrons, which generate a charge inequality that causes current flow. This can happen when cables are bent, vibrate or when being subject to a temperature change. It is therefore required to stabilise the cable environment.

Mechanical stress on the sensor's surface can cause deformation. This can also result in a charge unbalance and hence current flow, known as the piezo-electric effect. A possible cause is the probe needle pressing on the sensor's surface. Low contact pressure is therefore desirable.

As both the probe station and the measurement device are connected to different power outlets, their ground potentials may differ. If a circuit has more than one physical ground connection, this could cause interference and may generate an unwanted current path, known as ground loop. Ground loops can be avoided by ensuring that the system is physically grounded to one common point.

[2]An LCR meter is an electronic instrument used to measure the inductance (L), capacitance (C) and resistance (R) of a device.

Environmental influences

In addition to circuit offsets, the environment may also affect the measurement. Various sources are addressed below.

Most semiconductor sensors are sensitive to light. Ambient light can cause generation currents as high as several μA/cm^2. Measurements should therefore be made in a dark environment. Settling times after exposure can be as long as minutes.

As discussed in Chapter 2, water can form chemical bonds with contamination on the surface of the sensor or at the edge. This can cause leakage paths along the edges and through the top layers of the surface. High ambient humidity can severely affect the leakage-current behaviour of the sensor. Sensors are therefore commonly stored in nitrogen-purged (i.e. dry) environments.

The temperature determines the thermal velocity of charge carriers. Both generation in the depletion region and diffusion in the bulk regions outside the depletion region are therefore a function of temperature. The proportionality between the generation current and the temperature is given by:

$$I_{\text{gen}} \propto n_i \propto T^{3/2} e^{-\dfrac{E_g}{2k_{\text{B}}T}} . \tag{4.1}$$

At two temperatures T_1 and T_2 the ratio of generation currents is then given by:

$$\frac{I_{\text{gen}}(T_2)}{I_{\text{gen}}(T_1)} = \left(\frac{T_2}{T_1}\right)^{3/2} \exp\left[-\frac{E_g}{2k_{\text{B}}}\left(\frac{T_1 - T_2}{T_1 T_2}\right)\right] . \tag{4.2}$$

From this, it follows that the thermal generation current reduces by a factor of approximately two when the temperature drops with eight degrees. The diffusion current is also temperature dependent. Its proportionality is given by:

$$I_{\text{diff}} \propto n_i^2 \propto T^3 e^{-\dfrac{E_g}{k_{\text{B}}T}} . \tag{4.3}$$

At normal operating temperatures, the generation current dominates, whereas at higher temperatures diffusion prevails.

4.3 Characterisation

A fundamental requirement for the suitability of sensors in particle and imaging detectors is electrical integrity. Before a sensor is mounted on a read-out chip, it is therefore first characterised with respect to its electrical properties. Two common methods are capacitance-voltage and current-voltage profiling.

4.3.1 Capacitance-voltage profiling

As the name of the method implies, C-V profiling provides information on a sensor's capacitance as a function of bias voltage. Hence, it gives insight into the growth of the depletion region and therefore parameters such as the full-depletion voltage as well as the average doping concentration of the bulk can be derived from the C-V curves.

As discussed in Section 2.2.1, the free-carrier depleted space-charge region forms a capacitor together with the p and n regions as electrodes. The width of this region (W_{dep}) and thus the sensor's capacitance depend on the applied reverse bias voltage. For a one-sided abrupt p-n junction, the capacitance can be approximated as:

$$C = \frac{\epsilon_r \epsilon_0 A}{W_{\mathrm{dep}}} = A\sqrt{\frac{q\epsilon_r\epsilon_0 N}{2(V_{\mathrm{bi}} - V_{\mathrm{bias}})}} \approx A\sqrt{\frac{q\epsilon_r\epsilon_0 N}{2V_{\mathrm{bias}}}}\,, \tag{4.4}$$

where A is the average area of the electrodes. A plot of the sensor's capacitance as a function of the applied bias voltage (a C-V curve) therefore provides information on the growth of the depletion region. At the full-depletion voltage the region stops growing, which translates into a minimum of the C-V curve.
Another parameter that can be derived from C-V curves is the doping concentration of the substrate. Differentiating Equation 4.4 with respect to the bias voltage leads to the following expression:

$$\frac{d(1/C^2)}{dV} = \frac{2}{q\epsilon_r\epsilon_0 A^2 N(W)}\,, \tag{4.5}$$

Because of the linear dependence of the doping concentration on $d(1/C^2)/dV$, the capacitance of C-V profiles is often represented as $1/C^2$. Figure 4.4 shows an example C-V curve together with its $1/C^2$-representation. The full-depletion voltage can be derived from the intersection of two linear fits to the $1/C^2$-curve, one in the depletion domain (i.e. below full depletion), the other in the domain beyond full depletion. The bulk donor concentration N_d can be derived from the slope of the depletion-domain fit, using the relation of Equation 4.5. This equation shows that for a correct determination of the donor concentration, the electrode area A must be accurately known (because of its quadratic dependence on $d(1/C^2)/dV$).

4.3.2 Current-voltage profiling

Current-voltage profiling gives information on the sensor's leakage current as a function of bias voltage. It is a common first measurement to test the quality of the sensor and thus the reliability of the fabrication process. As will be discussed below, the leakage current is a superposition of different contributing components.

As described in Section 4.1, all sensor samples are p-n junction diodes. An ideal diode permits current flow under forward bias conditions, while at reverse bias current cannot pass through. However, electrons and holes can be thermally generated at temperatures

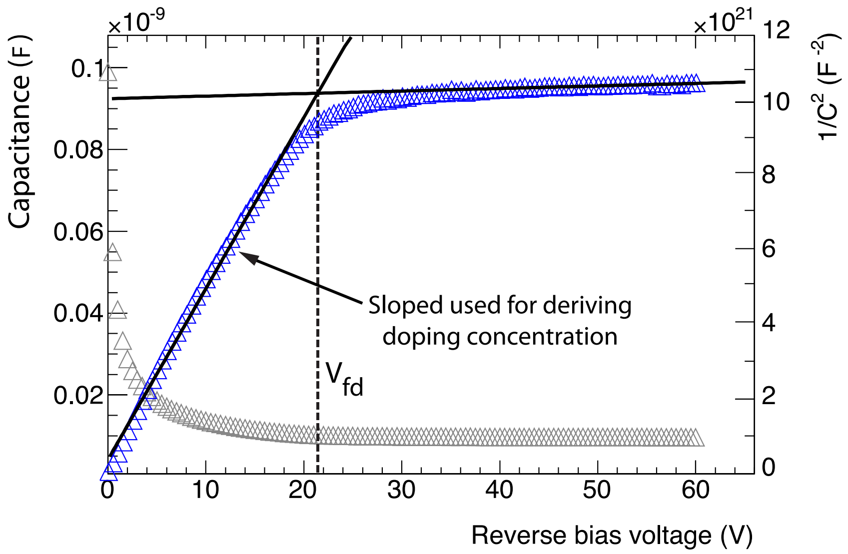

Figure 4.4: Capacitance-voltage diagrams
An example C-V curve (grey triangles) together with its $1/C^2$-representation (blue triangles). Both the full-depletion voltage and the bulk doping concentration can be derived from the $1/C^2$ representation.

above absolute zero (see Section 2.1). As a result, a small current can flow under reverse bias. This current is known as the reverse leakage current or dark current.

The I-V characteristic of an ideal diode is given by the Shockley equation:

$$I = I_{\text{sat}}\left(e^{\frac{qV_{\text{bias}}}{k_{\text{B}}T}} - 1\right). \tag{4.6}$$

Under forward bias, this equation can be approximated by:

$$I = I_{\text{sat}} e^{\frac{qV_{\text{bias}}}{k_{\text{B}}T}}. \tag{4.7}$$

For reverse bias voltages, the equation reduces to $I = -I_{\text{sat}}$, where I_{sat} is the reverse saturation current. In reality, however, the reverse current as a function of voltage is not constant. Impurities in the silicon bulk as well as damage and contamination at the edges cause an unwanted increase of current flow under reverse bias. Hence, in addition to the total leakage current at a given voltage, a current-voltage curve can provide information on the device's electrical integrity. The leakage current is a superposition of three individual currents:

1. a generation current in the depletion region
2. a diffusion current in the bulk regions outside the depletion region
3. a surface current due to the surface states at the edges and faces

Generation current Under reverse bias, free charge carriers are swept from the depletion region. As a consequence, there are no charges available for capture and thus recombination is not likely to occur. Emission processes dominate, which results in a generation current. This current depends on the carrier emission rate dN_e/dt and is determined by the intrinsic carrier concentration n_i and the generation lifetime τ_g (see Section 2.1.3). The generation current therefore reflects the concentration of emission states within the band gap and thus provides information on the purity of the crystal. Assuming a uniform distribution of emission centres throughout the depletion region, the generation current I_{gen} can be expressed as a function of the depletion-layer width:

$$I_{\text{gen}} \approx qA\frac{dN_e}{dt}W_{\text{dep}} \approx qA\frac{n_i}{\tau_g}\sqrt{\frac{2\epsilon_r\epsilon_0(V_{\text{bias}})}{qN}}\,. \tag{4.8}$$

Diffusion current In addition, charge carriers from the non-depleted regions of the sensor may diffuse into the depletion region. Once they enter this region they are subject to the externally applied electric field and drift towards one of the electrodes. This causes a an additional current flow, which is called the diffusion current. This current component is proportional to n_i^2 and is usually insignificant.

Surface current The abrupt ending of the crystal at the edge and surfaces of the sensor cause dangling bonds, which give rise to intermediate states in the forbidden gap. These states increase the conductivity of those regions, as a result of which a surface current flows along the edges and through layers on the surface. Damage and contamination, which may be caused by dicing and improper passivation, promote this current flow at the edges and hence can cause undesirably high leakage currents.

An I-V profile can reveal which of the above currents is dominant and can therefore provide feed-back on the manufacturing process. Neglecting diffusion currents, the leakage current I_{leak} in the active area can be represented by:

$$I_{\text{leak}} = I_{\text{gen}} + I_{\text{surf}} = J_{\text{gen}}A + J_{\text{surf}}P\,, \tag{4.9}$$

where J_{gen} is the generation-current density in the bulk (in A/cm^2) and J_{surf} the surface-current density (in A/cm). A and P are the area and perimeter of the active area, respectively. The generation current scales with the depletion volume and thus with the square root of the voltage, while the surface current behaves Ohmically.

Therefore, the I-V curves can be fitted by the following function [109]:

$$\begin{aligned} I(V) &= A\sqrt{V} + BV + C \quad \text{if } V \leq V_{fd} \\ I(V) &= A\sqrt{V_{fd}} + BV + C \quad \text{if } V > V_{fd}\,, \end{aligned} \tag{4.10}$$

where V$_{fd}$ is the full depletion voltage and C is a constant to absorb for measurement offsets.

An example fit together with the separate contributions of the generation current and the surface current is shown in Figure 4.5. The data are from one of the conventional TOTEM strip sensors. It shows the $\sqrt{V}$-dependence in the depletion domain and an Ohmic (i.e. linear) part beyond full depletion. In the fitting procedure, the full-depletion voltage was set as a free fit parameter. The fit-parameter values and calculated current components are listed in Table 4.2. The offset value is relatively large in this case. The current components are therefore not the true values, but they do show the ratio between the surface and volume contribution.

Table 4.2: Fit-parameter values and calculated current contributions from the fit of Figure 4.5

A	**B**	**C**	$\mathbf{V}_{\text{fd}}$	$\boldsymbol{I}_{\mathbf{gen}}$ (50 V)	$\boldsymbol{I}_{\mathbf{surf}}$ (50 V)	$\frac{\boldsymbol{I}_{\mathbf{surf}}}{\boldsymbol{I}_{\mathbf{gen}}}$ (50V)
(pA/$\sqrt{\text{V}}$)	(pA/V)	(pA)	(V)	(pA)	(pA)	
4.7	0.16	-8.8	27	24	8.1	0.33

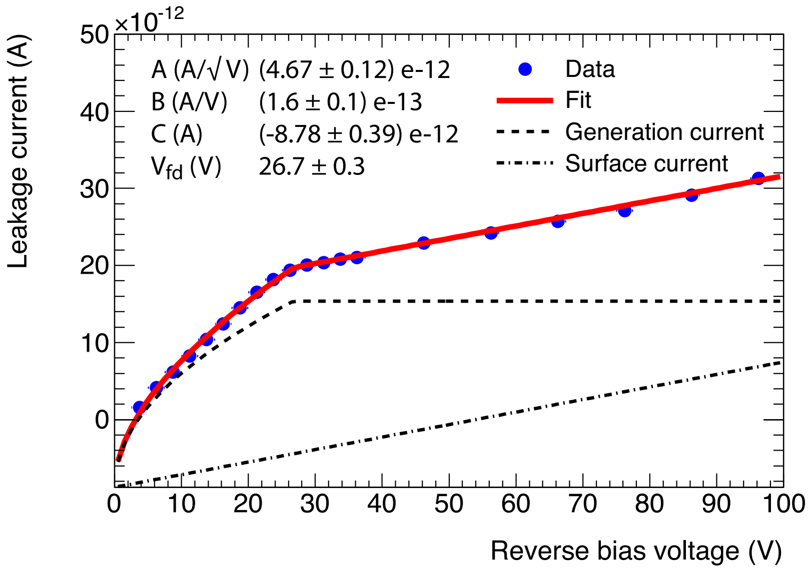

Figure 4.5: Current-voltage curve fitting
The I-V curve of one of the conventional TOTEM sensors fitted by function 4.10. The separate contributions are plotted as well, which demonstrate the $\sqrt{V}$-dependence in the depletion domain and an Ohmic part above full depletion.

4.4 Simulations

Before characterisation, the electric field distribution of both a sensor with n-type stop ring and one with a p-type stop ring was studied using TCAD[3] software for semiconductor device simulation [110]. Some details about simulating field distributions in semiconductor sensors using this software are described in Appendix B. Figure 4.6 shows simulations of the potential distribution at full depletion of an n-type stop-ring structure and one with a p-type stop ring. The n-type stop ring is left floating, whereas the p-type stop ring is biased at the same potential as the active area. This has consequences for the electrical characteristics of the edge area, which will discussed below. Both sensors are 300 µm thick.

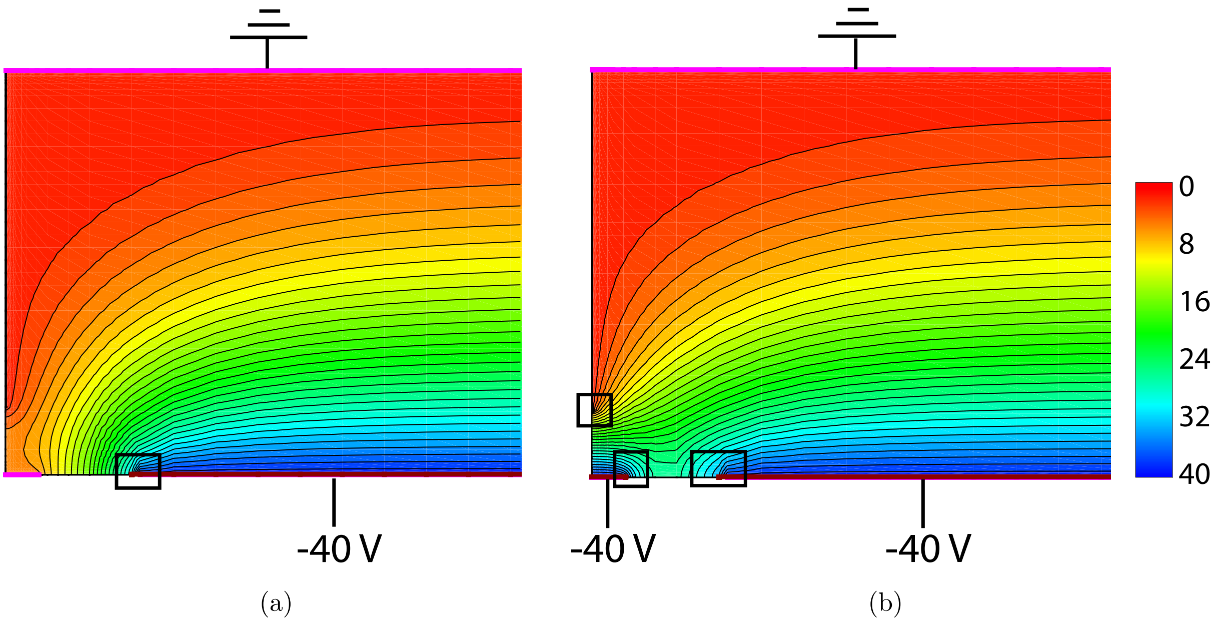

Figure 4.6: Potential distribution
Simulations of the potential distribution at the edge at 40 V reverse bias. Part (a) represents the distribution for a sensor with an n-type stop ring, whereas part (b) shows that of a p-type stop-ring sensor. At the p-type stop ring edge, three high-field regions can be distinguished (indicated by the boxes). The n-type configuration results in only one such region.

The edge distance is 100 µm and the stop ring is 25 µm wide. The simulation's input parameters for the doping were based on the specifications given by the manufacturer. A value of $5 \cdot 10^{11}$ cm^{-3} was chosen for the doping concentration of ν-type bulk. The diode junction was formed by a 0.4 µm deep boron implant with an acceptor concentration of $5 \cdot 10^{19}$ cm^{-3}. The back and edge were simulated as phosphorus implants of 0.4 µm thick with a donor concentration of $5 \cdot 10^{19}$ cm^{-3}. Using Equation 2.32, it can be calculated that at this concentration the approximate voltage at which the sensor is fully depleted

[3]TCAD stands for Technology Computer-Aided Design

is:

$$V_{\mathrm{fd}} = \frac{qNW_{\mathrm{fd}}^2}{2\epsilon_r\epsilon_0} \approx 34\mathrm{V}\,. \tag{4.11}$$

The bias voltage used for the simulation was 40 V.

There are a number of important differences between the functionality of an n-type and a p-type stop ring. The p-type stop ring is kept at the same potential as the active area. This results in zero potential difference between the stop ring and the active region and therefore ensures there is no current flow through possibly active surface states between the stop ring and the active area. Moreover, any surface current along the edge is drained through the stop ring. In addition, a p-type stop ring straightens the equipotential lines at the edge. This has two consequences. First, the depletion region may reach the edge, as a result of which edge-defect induced generation currents may flow into the active region. Secondly, the high-field region at the edge of the active region is reduced, which has a favourable effect on the break-down voltage (see Section 4.5.2). Nevertheless, multiple high-field regions arise due to the use of a p-type stop ring, which is indicated in Figure 4.6(b).
For n-type stop rings, the field configuration is different, as shown in Figure 4.6(a). Here, the stop ring is electrically in contact with the edge electrode. As a result, surface currents can flow more easily from the edge to the active area. On the one hand, because there is a potential difference between the active area and the stop ring. On the other hand, because it does not function as a drain. Nevertheless, due to the indirect contact with the edge, n-type stop rings terminate the electric field and hence confine the depletion region more effectively than p-type stop rings at the edge.

4.5 Results

The C-V measurements were done to get a better understanding of the sensors' internal characteristics. The results presented in this chapter, however, focus on the leakage-current characteristics of each device.
For all measurements the active area and stop ring were probed, while the back side was in contact with the electrically conductive chuck of the probe station.
For the C-V measurements the bias voltage was applied to the back electrode, while the active area and the stop ring (in case of p-type stop rings) were kept at ground. This configuration is required by the auto-balancing bridge, as leakage may occur when the low terminal is connected to the chuck.
For the I-V measurements, the biasing configuration was the other way around. Due to the availability of only two source-measure units, the active area and the p-type stop ring were biased individually, whereas the back electrode was connected to ground.

4.5.1 Capacitance-voltage measurements

Figure 4.7 shows the C-V curve of one of the rectangular diodes (150 µm edge distance and 25 µm wide stop ring) together with its $1/C^2$-representation. A full-depletion voltage

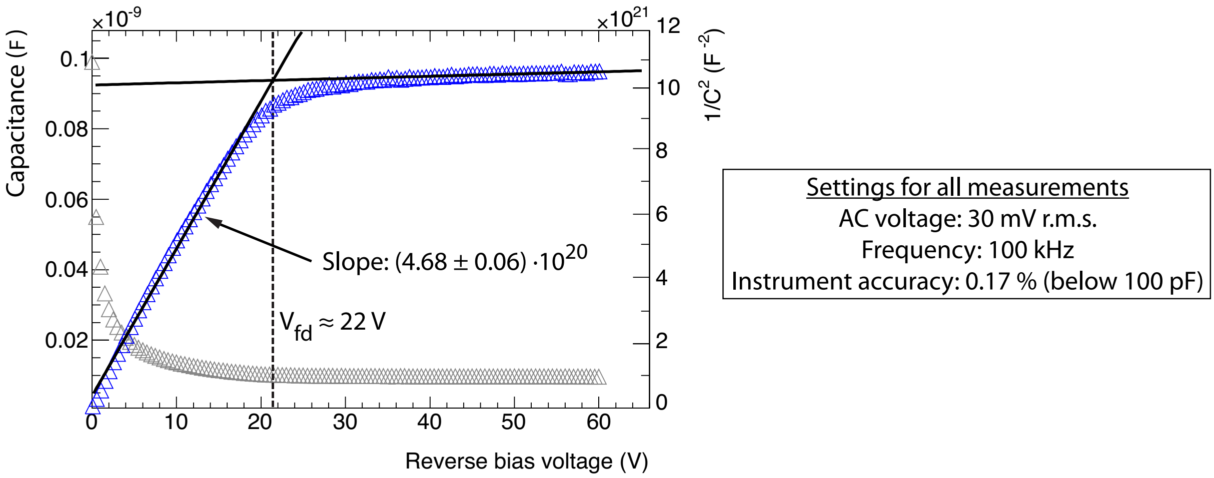

Figure 4.7: Capacitance-voltage diagram
The C-V curve (grey triangles) of one of the rectangular diodes with 150 µm edge distance and a 25 µm wide p-type stop ring. Both the full-depletion voltage and the bulk doping concentration can be derived from the $1/C^2$ representation (blue triangles). On the right-hand side, the settings for the C-V measurements are given.

of approximately 22 V is derived from the intersection of two linear fits to the $1/C^2$-curve. Subsequently, the bulk donor concentration N_d is derived from the slope of the depletion-domain fit, using the relation of Equation 4.5. To estimate the effective active area, the C-V response was simulated for sensors with various edge distances and a constant electrode area. Figure 4.8 shows the simulated capacitance as a function of edge distance for various bias voltages. It demonstrates that the capacitance is a function of the cross-sectional area of the depletion region rather than the electrode area. As a result of lateral growth of the depletion region, the C-V curve is smoother for large edge distances than for smaller ones.

In addition to a precise determination of the active area, the $1/C^2$-V curve should show good linearity in the depletion domain in order to accurately derive its slope. However, a discontinuity was observed in the depletion domain of some of the C-V curves. Figures 4.9(a) and (b) show the measured C-V curves for both active area and stop ring of two p-type stop-ring sensors with different edge distance (175 µm and 8 µm, respectively). The discontinuity effect is most pronounced for sensors with a large gap between the active area and the stop ring and especially shows up when the neighbouring electrode is floating. A possible explanation for this effect is shown in Figure 4.9(e). It depicts the presence of an accumulation layer of electrons directly below the thermal oxide between the active area and the stop ring. This layer is caused by positive oxide charges. At low

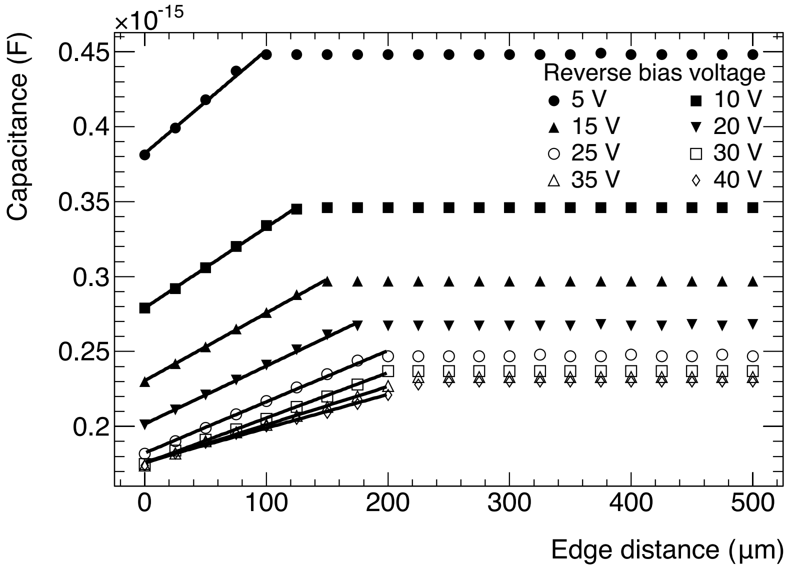

Figure 4.8: Lateral depletion
Simulated capacitance as a function of edge distance for various bias voltages. As a result of lateral growth of the depletion region, the C-V curve is smoother for large edge distances than for smaller ones. The values are of the order of fF, because the simulated capacitance is derived from a one-dimensional representation of the sensor.

bias voltages, these electrons may contribute to an increase of the capacitance. When the voltage is sufficiently high, the area below the oxide gets depleted from electrons, as a consequence of which the capacitance will drop. This translates into the observed discontinuity in the C-V curves. The effect is confirmed by simulations on structures with similar edge topologies. Figures 4.9(c) and (d) show simulated C-V curves with and without charges in the 180 nm thick thermal oxide. Figure 4.9(c) represents a sensor with a 175 μm gap, whereas Figure 4.9(d) shows the curves of a sensor with a 8 μm gap. Clearly, the discontinuity is not observed when there are no oxide charges present or when the gap is small, i.e. only little amount of oxide charges present.
Keeping these two effects in mind, the donor concentration of some of the rectangular diodes was determined. Table 4.3 lists these values. The average of the active area and the total area of the sensor was used for the calculation. For the error calculation, both the error on the slope of the fit and the estimated error on the active area were taken into account.
Also, the implantation process may cause variations in the doping concentration. The literature reports resistivity variations of up to 15 % [111].

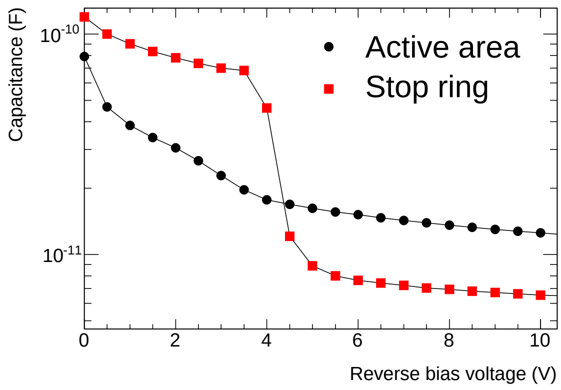

(a) Rect. diode; gap = 175 µm

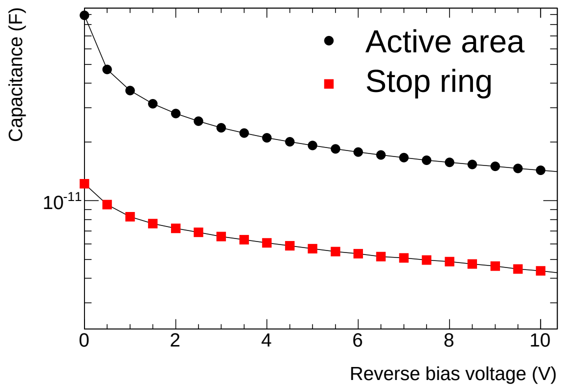

(b) Rect. diode; gap = 8 µm

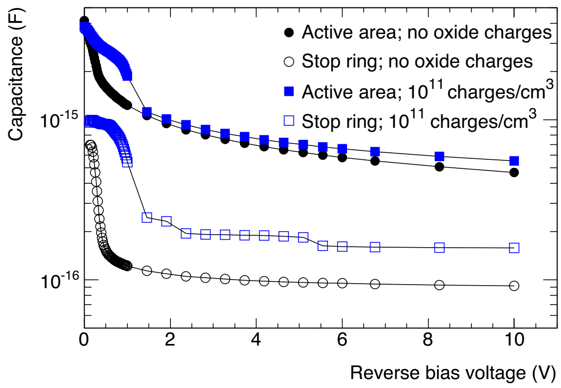

(c) Simulation; gap = 175 µm

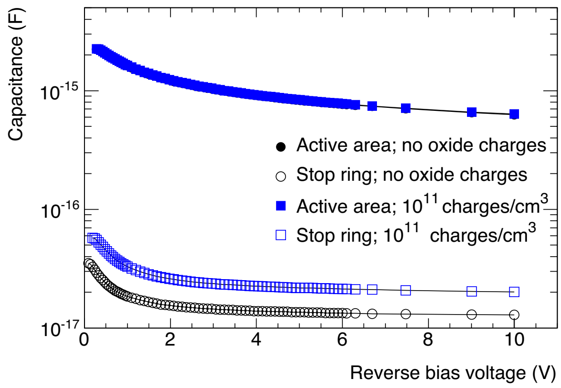

(d) Simulation; gap = 8 µm

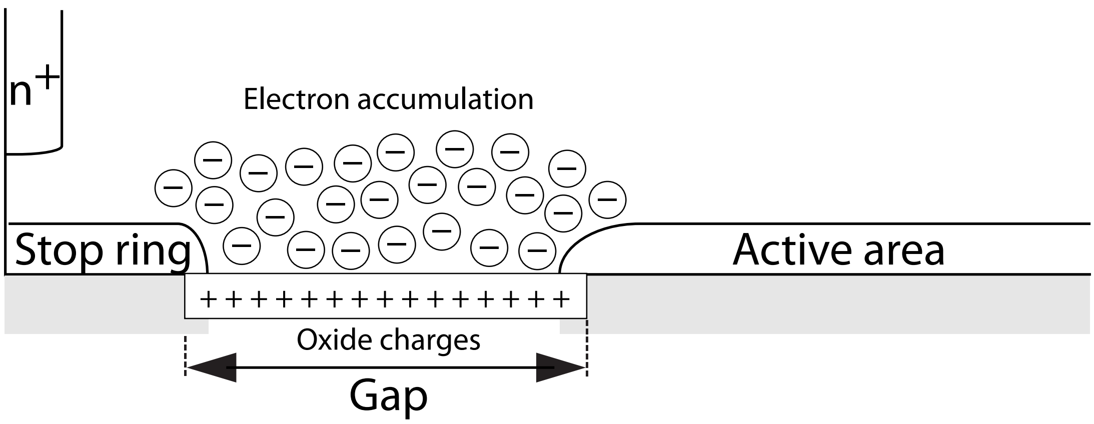

(e)

Figure 4.9:
(a), (b) A drop in capacitance is observed for sensors with a large gap between the active area and stop ring, especially when the neighbouring electrode is not grounded. The effect is most pronounced in the C-V characteristic of the stop ring. (c), (d) The same effect shows up when simulating the presence of positive charges in the thermal oxide. (e) This may be explained by an accumulation layer of electrons directly below the thermal oxide between the active area and the stop ring, which is induced by positive oxide charges.

Table 4.3: The bulk donor concentration extracted from the slope of the depletion domain of the $1/C^2$-V curve.

Rectangular diode	$\boldsymbol{\frac{d(1/C^2)}{dV}}$ ($\cdot 10^{20}$ V/C^2)	**Area** (cm^2)	$\boldsymbol{N_d}$ ($\cdot 10^{11}$ cm^{-3})
A	5.03 ± 0.12	0.21 ± 0.005	5.3 ± 0.3
B	4.68 ± 0.05	0.23 ± 0.005	5.0 ± 0.2
C	4.07 ± 0.05	0.24 ± 0.005	5.1 ± 0.2

4.5.2 Current-voltage measurements

Current-voltage measurements were made on all sensor samples with two main objectives: (i) to determine the total leakage current beyond full depletion in order to evaluate their viability and (ii) to determine a minimum edge distance for which the total leakage current is still acceptable. First, measurements were carried out to determine the overall functionality of the sensor as well as the its dependence on environmental influences.

Sensor functionality and dependencies

Before the measurements, the set-up was calibrated. The internal current offset was corrected by subtracting the open-circuit current of each source-measure unit from the measurement. By connecting the set-up components one-by-one and measuring the open circuit current for each configuration, the contributions of the individual components were determined. These are known as the external offsets of the system. A total offset of approximately 10 pA was determined, which was subtracted from the measurement results.
The measurement accuracy of both source-measure units is ±(0.050 % of reading + 30 pA) for current values below 100 nA.

Stop-ring functionality As explained in Section 4.4, n-type stop rings are left floating, while p-type stop rings are kept at the same potential as the active area. This allows to measure the current drained at the stop ring independently and to study the functionality of the stop ring. Figure 4.10(a) shows measurements of the stop-ring and active-area current as a function of voltage. The leakage current in the active region is plotted under both biased and unbiased stop ring conditions. It demonstrates that the active-area leakage current is significantly reduced, when the p-type stop ring is biased.

Break-down voltage Biasing the p-type stop ring straightens the isopotentials and therefore reduces the field at the edges of the active area. Figure 4.10(b) shows I-V curves up to the break-down voltage of both n-type and p-type stop-ring structures. The n-type

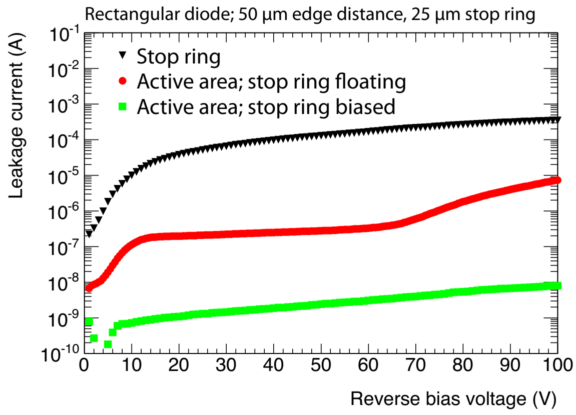

(a)

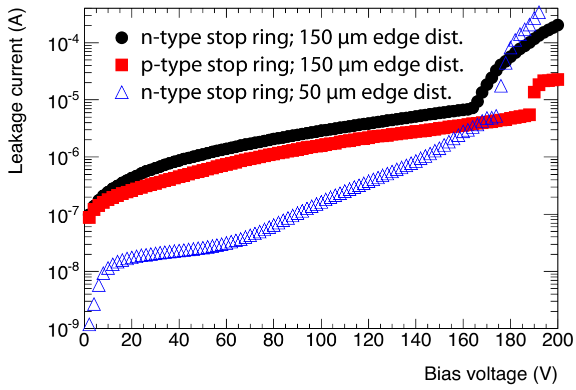

(b)

Figure 4.10: Stop-ring functionality and break-down voltage
(a) Current-voltage curves of the active area with and without biasing the p-type stop ring. A biased stop ring significantly reduces the leakage current. (b) Breakdown occurs above 160 V in the case of n-type stop-ring structures and above 190 V for p-type stop-ring structures.

stop ring sensors show breakdown between 160 V and 180 V reverse bias. Slightly higher breakdown voltages, not lower than 190V, were observed for p-type stop-ring sensors.

Temperature Generation and diffusion processes in the bulk are dependent on the temperature. Both can be modelled by the Arrhenius equation [112]:

$$I = Ae^{-\dfrac{E_a}{k_\mathrm{B}T}}, \tag{4.12}$$

where I is the reaction rate, in this case of one of the current components, A is a scale factor, an empirical relationship between temperature and rate coefficient, and E_a is the activation energy. This parameter represents the energy that must be overcome by the charge carrier to contribute to conductance. Figure 4.11(a) shows a measurement of the leakage current as a function of temperature at two different reverse bias voltages. To determine whether the diffusion or generation process is dominant, the data are fitted to the modified Arrhenius model:

$$I = AT^n e^{-\dfrac{E_a}{k_\mathrm{B}T}}, \tag{4.13}$$

where T^n accounts for the temperature dependence of the scale factor.
By taking the natural logarithm of Equation 4.13, the model is described by:

$$\ln I = \ln A + n \ln T - E_a \frac{1}{k_\mathrm{B}T}. \tag{4.14}$$

The current becomes a linear function of $1/k_\mathrm{B}T$. Figure 4.11(b) shows both the data and the fits. The scale factor A, the exponent n and the activation energy E_a were set as

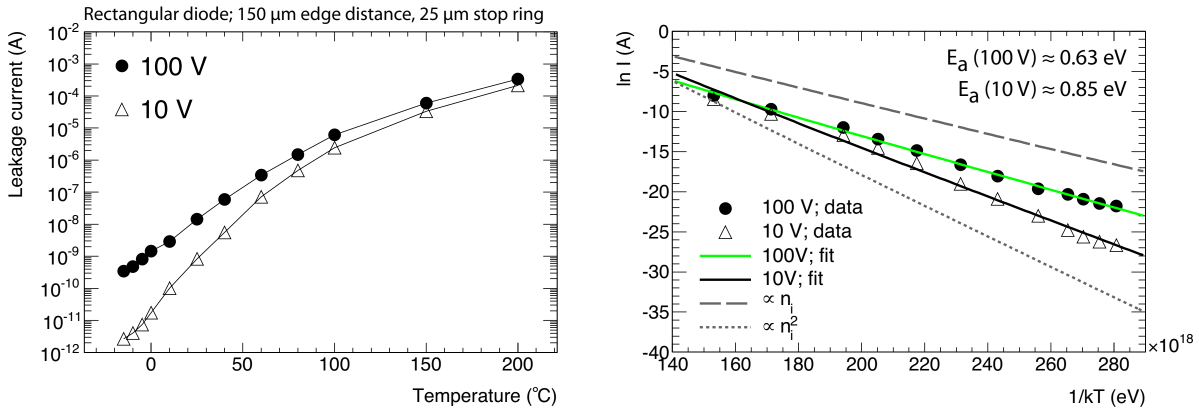

(a)

(b)

Figure 4.11: Current-temperature diagrams
(a) The leakage current as a function of temperature (I-T) at both 10 V and 100 V reverse bias. In the temperature domain from $20°C$ to $100°C$, the 100 V data show good agreement with the temperature dependence of the generation current as described by Equation 4.2. (b) The I-T diagrams are plotted in terms of $1/k_{\mathrm{B}}T$ versus $\ln I$ and fitted by the modified Arrhenius function of Equation 4.14. At 100 V, the leakage current is more dominated by generation than at 10 V.

free fit parameters. It shows that at 100 V the activation energy is lower than at 10 V. For reference, the proportionality of the generation current and diffusion current on the temperature (i.e. $I_{\mathrm{gen}} \propto n_i$ and $I_{\mathrm{diff}} \propto n_i^2$) are plotted as well. It shows that at 100 V reverse bias, generation is the dominant mechanism, whereas at 10 V diffusion seems to dominate. The reason for this may be the fact that at 10 V the device is only partially depleted. Hence, at 10 V the depletion region is smaller and the bulk region outside the depletion region is larger.
Furthermore, the dotted line that represents the proportionality to n_i^2 shows that diffusion should prevail at higher temperatures. The data do not show this trend, however. Both graphs flatten towards higher temperatures. This may be caused by surface currents, which show a weaker dependence on the temperature.

Humidity Figure 4.12(a) shows the influence of humidity on the I-V characteristics of a sample with a visually damaged edge. An increase in leakage current is observed at approximately 15 V reverse bias for relative-humidity levels above 40 %. This is likely to be caused by surface currents, especially since there is no passivation layer between the stop ring and the active area.
Figure 4.12(b) shows the leakage current at 50 V reverse bias as a function of the relative humidity for an undamaged sensor with the same edge distance. Since the humidity was not controlled in an accurate manner and measured at approximately 10 cm from the sensor, a significant error on the relative-humidity level is taken into account. Figure 4.12(c) shows the I-V characteristics of a typical undamaged sample at 5 % and

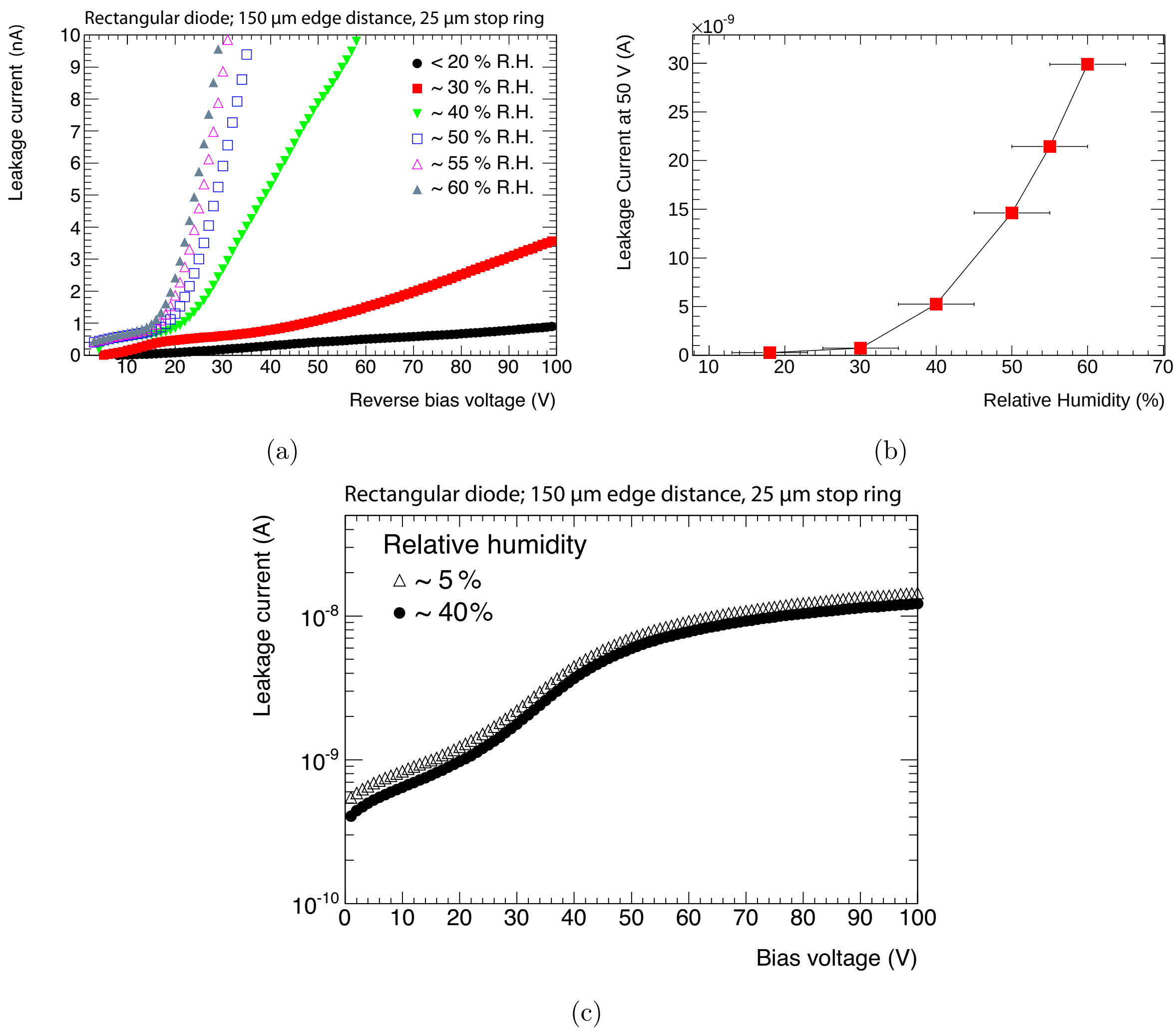

Figure 4.12: Humidity dependence
(a) I-V curves of a rectangular diode (150 µm edge distance) with damaged edge for different relative-humidity values. (b) The leakage current plotted as a function of the relative humidity at 50 V reverse bias. (c) The I-V characteristics of an undamaged rectangular diode (also 150 µm edge distance) at 5 % and 40 % relative humidity.

40 % relative humidity. Here, practically no difference was observed between the I-V curves. This indicates good edge quality, the more so because the surface between the stop ring and active area was not passivated.

Leakage current

Results presented in the previous section concern measurements made on some of the sensor samples only. In this section, all samples are compared to each other in terms of leakage current. However, a direct comparison is not always possible, due to the different types of sensors fabricated.

For all sensors, the back side was grounded, while the leakage current was measured at the reversely biased active area. Because of the different diode junction layouts of each type of sensor, a specific active-area was chosen for testing.
For both the circular and rectangular test diodes the single active area was measured. Since the active area is entirely surrounded by the edge, these sensors are suitable for direct comparison.
For the TOTEM sensors, however, a very low single strip current was measured. To isolate the strip under test from its neighbouring electrodes, adjacent strips were biased at the same potential by a separate SMU. Since only one of the short sides of the strip was adjacent to the edge, these samples were mainly used for comparing the leakage current characteristics with that of conventional sensors. In addition, the functionality of the stop ring for each of the doping types could be studied.
The Medipix sensors were characterised by probing a large pad ($\sim$1.5 mm^2) located at one side of the structure. For the same reasons as mentioned for the TOTEM sensors, the Medipix samples were not very suitable for studying the edge-distance dependence.

The measurements were made at relative-humidity levels between 35% and 38% and at temperatures between 294 K and 296 K.

Due to die-separation difficulties, as described in Section 4.1, some of the samples' edges were damaged and with it the stop ring's functionality was compromised. As a consequence, some samples were excluded from further analysis. The selection criteria for further analysis were:

1. Visual inspection should show no obvious damage at the edge.

2. In case of p-type stop ring sensors, biasing the stop ring should reduce the leakage current in the active area.

3. The total leakage-current density in the active area should be below 660 µA/cm^2. This value is based on the maximum leakage current that the amplifier circuit of a Medipix pixel can compensate in case of hole collection [94].

Table 4.4 shows the leakage-current density levels of the selected sensors at 50 V reverse bias, i.e. at approximately twice the full-depletion voltage. The current densities are all more than a factor 100 lower than the value of criterion 3. The errors are calculated by taking both the measurement accuracy of the instrument as well as the error on the active area into account.
The data have two shortcomings. The number of same-type samples with identical edge

Table 4.4: Leakage-current density in the active area (J_{AA}) at 50 V reverse bias.

Sample		**Stop ring type**	**Stop ring width** (µm)	**Edge distance** (µm)	J_{AA} (nA/cm^2)
TOTEM	Edgeless	n^+	15	25	109.0 ± 6.5
			15	25	104.7 ± 6.5
			30	50	140.9 ± 6.7
		p^+	15	25	24.2 ± 6.1
			30	50	21.0 ± 6.1
	Conv.	p^+	15	495	4.7 ± 6.0
			15	495	3.7 ± 6.0
			30	520	7.5 ± 6.0
			30	520	9.1 ± 6.0
Medipix-2	Edgeless	n^+	5	10	23.5 ± 3.1
		p^+	10	20	$(1.052 \pm 0.008) \cdot 10^3$
			15	30	33.4 ± 3.2
	Conv.	n/a		680	46.3 ± 3.2
Circular diodes		n^+	15	50	131.6 ± 0.8
			25	100	878.6 ± 5.0
		p^+	25	100	282.1 ± 1.6
Rectangular diodes		n^+	10	25	$(6.556 \pm 0.035) \cdot 10^3$
			25	50	114.5 ± 0.7
			25	150	28.18 ± 0.28
			25	300	101.3 ± 0.7
		p^+	25	50	46.46 ± 0.36
			25	150	$(1.1 \pm 1.4) \cdot 10^{-1}$
			25	300	$(0.6 \pm 1.6) \cdot 10^{-1}$
			25	300	$(0.7 \pm 1.6) \cdot 10^{-1}$

topology is too small to derive an accurate average value for the leakage-current density at a given edge distance. Moreover, the statistics are further limited due to the fact that sensors of different types do not allow for a one-to-one comparison, since the size of their active areas are very different.
Nonetheless, the values of Table 4.4 demonstrate the good general quality of these sensors. They all show leakage-current density levels that are well below the maximum level that can be compensated by the Medipix-MXR chip. Whereas the leakage currents of the active-edge TOTEM strip sensors with p-type stop ring are ~ 2-5 times higher than those of their conventionally processed counterparts, the active-edge Medipix sensor with an edge distance of 30 µm shows a leakage current similar to that of the conventional one. The characteristics are compared in Figure 4.13. The conventional sensor even seems to draw slightly more current at bias voltages beyond full depletion. While the edge distance is more than a factor twenty smaller, the leakage currents are of the same order of magnitude. The p-type stop-ring active-edge technology therefore seems viable.

Supported by the fact that samples with identical edge topology show similar leakage-current densities, sensors of the same type were compared. In general, it seems that p-type stop-ring sensors show lower leakage currents than their n-type counterparts. In particular, this applies to the TOTEM strip sensors and the rectangular diodes. The n-type stop ring structures show leakage-current density levels of approximately 100 nA/cm^2. At 50 µm edge distance, approximate levels between 20 and 45 nA/cm^2 were measured for the p-type stop ring sensors. These values are comparable to those from the literature [84] on edgeless sensors with a similar edge distance. Even lower values (down to 65 pA/cm^2 at 50 V) were obtained for structures with a 300 µm edge distance.
Possibly, the edge distance can be reduced even further, but this study does not prove

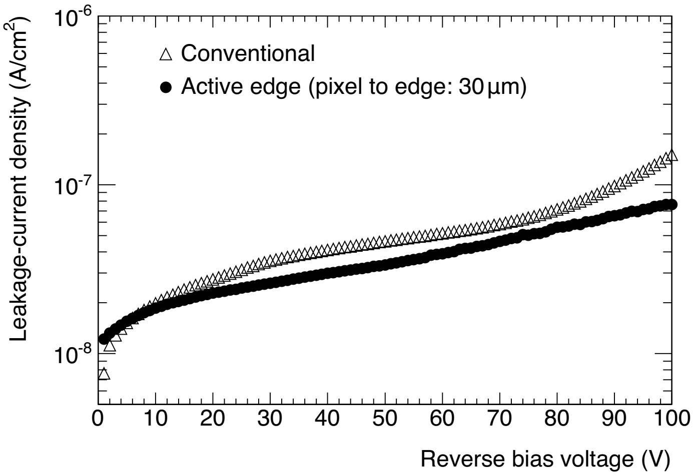

Figure 4.13: Proof-of-principle
The leakage-current characteristic of an active-edge Medipix sensor compared to that of a conventional one. They show a similar leakage current, which indicates that edge distances can be reduced to tens of micrometers using this technology.

this. The data demonstrate that an edge distance of 50 µm can be achieved without introducing leakage currents of unacceptable levels.

Leakage-current components Although a low leakage current is an important requirement for a sensor, values for the total leakage current at a certain bias voltage do not provide insight into the leakage-current behaviour and its individual current components. Since the edge of the test samples is close to the active area, it is interesting to compare the contribution of possible surface currents to the total leakage current. This is studied by decomposing the I-V curves into its main current components, as described in Section 4.3.2. In an identical way to the example fit of Section 4.3.2, the leakage-current components were studied. A substantial part of the curves, however, do not follow the relation of Equation 4.10, but show a steeper rise in the sub-depletion domain, possibly due to a dominant contribution of the surface current. Table 4.5 lists the fit-parameter values and the leakage current components at 50 V reverse bias of samples that showed successful fits to the I-V curves. In general, the surface current seems to dominate the leakage current of active-edge sensors, whereas the volume current prevails for the conventional structures. This is in accordance with our expectation, since there is only little space between the edge and the active area and there are no guard rings to absorb the surface current. Moreover, as mentioned in Section 4.1, the manufacturing process lacked deposition of a passivation layer between the active area and the stop ring.
Furthermore, it seems that the active-area of p-type stop-ring sensors draws less surface current than that of those with an n-type stop ring. Since the p-type stop ring is biased, edge-effect induced currents are drained and hence do not reach the active area.

Table 4.5: Fit-parameter values and the leakage-current components at 50 V for samples that showed successful fits to the I-V curves. To indicate the dominant contribution to the leakage current, the ratio between the surface current and generation current is given.

Sample		**Stop ring type**	**Stop ring width** (µm)	**Edge distance** (µm)	I_{gen} (A)	I_{surf} (A)	$\frac{I_{surf}}{I_{gen}}$
TOTEM	Edgeless	n^+	15	25	$3.4{\cdot}10^{-11}$	$3.5{\cdot}10^{-10}$	**10**
		p^+	15	25	$6.9{\cdot}10^{-11}$	$8.1{\cdot}10^{-11}$	**1.2**
	Conv.	p^+	15	495	$2.4{\cdot}10^{-11}$	$8.1{\cdot}10^{-12}$	**0.34**
Medipix	Edgeless	p^+	15	30	$7.2{\cdot}10^{-10}$	$2.7{\cdot}10^{-9}$	**3.7**
	Conv.	n/a		680	$1.5{\cdot}10^{-9}$	$7.2{\cdot}10^{-10}$	**0.48**
Rectangular diodes		n^+	25	50	$1.3{\cdot}10^{-8}$	$1.6{\cdot}10^{-8}$	**1.2**
		p^+	25	50	$8.3{\cdot}10^{-9}$	$4.4{\cdot}10^{-9}$	**0.53**

4.6 Conclusion

Electrical integrity is a prerequisite for image and particle sensors. It determines their suitability as conversion material for highly sensitive detectors. In particular, a sensor's leakage current is a determining factor in a detector's noise performance.

In this chapter, active-edge sensors with different edge topologies were compared in terms of their electrical characteristics. The data show that their leakage current is comparable to that of conventional sensors. This demonstrates that the edge distance can be reduced drastically, while the leakage current is still at an acceptable level. Sensors with an edge distance of 50 µm and smaller show currents of less than 100 nA/cm^2. A one-to-one comparison of the sensors is not possible, due to the fact that the sensors are of a different type and hence the active-area configuration with respect to the edge is different for each type. In addition, there were difficulties in the manufacturing process, which results in a reduction of sample statistics. Therefore, a value for the minimum acceptable edge distance cannot be derived. Distances of the order of 50 µm seem feasible.

A distinction is observed between sensors with a p-type stop ring and sensors with an n-type ring. Sensors with a p-type stop ring show lower leakage currents in the active area. In accordance with expectations, these sensors also show lower surface currents in the active area. This is very interesting, since today's "conventional" active-edge sensors are made without stop rings. It shows that a combination of active edge and a stop ring may be the solution to reduce the edge distance and at the same time protect the active area against unwanted edge effects.

5

Active-edge sensors: performance of edge pixels

In the previous chapter, the electrical characteristics of active-edge sensors were studied. The results show that the distance between the active area and the sensor's physical edge can be reduced to tens of micrometers without significantly affecting the leakage current in the active area.

This chapter studies the performance of the outer pixels of active-edge pixel sensors. Due to the edge implant, the electric field is locally distorted, which affects the detection properties of the pixels close to the edge.
In the first part of this chapter, the response functions of these pixels are measured using strongly focussed laser light of two different wavelengths.
In the second part, their effective volume is reconstructed by studying the amount of collected charge as a function of the interaction depth.

5.1 Sample specifications

Silicon pixel sensors (fabricated by VTT Micro and Nano-electronics[1]) of 150 µm thick with an edge distance of 50 µm are the subject of this study. In contrast to the structures examined in Chapter 4, these sensors have a doped edge across the entire thickness of the sensor. The pixel configuration is n-in-n, which makes the back side and edge of p-type. The pixel matrix layout follows that of Medipix-2.
Figure 5.1(a) schematically shows the process steps in which the active edges were realised. While on a support wafer, the sensors were separated by means of inductively coupled plasma etching. This allowed for edge implantation with boron atoms on the wafer level. At the back side, no aluminium electrode was deposited. Instead, it was heavily doped (10^{20} cm^{-3}) with boron atoms. This benefited the quality of the sensor-separating trench and it kept the thickness of the entrance window at the back at a minimum, which allowed for detection of infra-red light (which will be used for the measurements presented

[1] VTT Micro and Nano-electronics, Tietotie 3, Espoo, FI-02044 VTT, Finland. `http://www.vtt.fi`

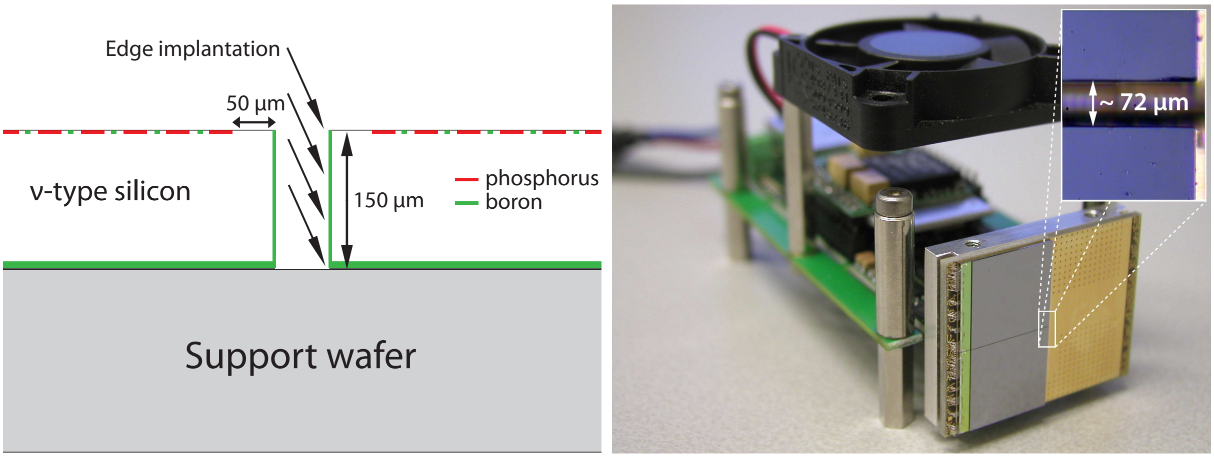

(a) (b)

Figure 5.1: The detector module
(a) Schematic representation of the edge processing step. The sensors were separated by means of inductively coupled plasma etching and subsequently doped with boron atoms using an angled ion implantation process. (b) Two edgeless-Timepix assemblies mounted side-by-side on the quad carrier board. Due to its larger size, the Timepix chip extends from underneath the sensor. Consequently, there is a small gap of approximately 72 µm wide between the adjacent edges of the sensors.

in Section 5.3.1). Two of such sensors were mounted on Timepix read-out chips and the assemblies were subsequently juxtaposed on a quad-carrier board. The side-by-side configuration was chosen to conduct the measurements on the interaction-depth dependence of the collected charge, which will discussed in more detail in Section 5.3.2. Figure 5.1(b) shows a picture of the detector module together with a close-up view of the adjacent-edge region. Because of the larger area of the Timepix chips, due to the relaxed dicing margin that was used, there is small gap of approximately 72 µm wide between the two sensors. To check the electrical integrity of the sensors, their current-voltage characteristics were measured. The main parameters are listed in Table 5.1, together with the sensor specifications. For comparison with the results of Chapter 4, the currents are given for a bias voltage of 50 V. The measurements presented hereafter, however, are made at 40 V sensor bias.

Table 5.1: Sensor specifications and leakage-current characteristics.

Pitch	55 µm
Type	n-in-n
Thickness	150 µm
Edge distance	50 µm
Full-depletion voltage	$\sim$ 14 V
Break-down voltage	$\sim$ 140 V
Leakage current-density (50 V)	$\sim$ 60 nA/cm^2
Generation current (50 V)	$\sim$ 84 nA
Surface current (50 V)	$\sim$ 11 nA
Surface current / Generation current (50 V)	$\sim$ 0.13

5.2 Simulations

After equalisation of the discriminator thresholds of the Timepix pixels, the detector was homogeneously irradiated (so called flood-field irradiated) with a polychromatic X-ray beam of 30 keV mean energy to examine the response[2] homogeneity across the active area. The output image is shown in Figure 5.2. Noticeably, the pixels of the three outer columns show an anomalous response with respect to more central pixels. This can be explained by the distribution of the electric field at the edge. Figure 5.3 shows TCAD simulations (see Appendix B) of the potential distribution at the edge of such sensors at different bias voltages. They show that the field at the edge alters the effective volume of the outer pixels. The ratio between their effective volume and that of the bulk pixels is indicated in the figure. At 10 V, the effective volume of the outermost pixels is reduced to approximately 55 % of the volume of bulk pixels, while their physical volume is $\sim$ 66 % larger. This reduction translates into an increase of the effective volume of the second outer pixels. At higher bias voltages, the difference between the effective volumes of pixels of the first and second column decreases. Moreover, the simulations show that the effective area of the outer pixels is depth dependent.

How the distortion affects the performance of edge pixels, is studied by means of sub-pixel position-defined measurements on the charge collection. In Section 5.3.1, strongly focussed laser light of two different wavelengths is used to determine the edge-pixel response functions for charge generated in two different interaction volumes. In addition, an estimate is made of the edge of the sensitive volume relative to the physical edge of the sensor.

[2] Here, and for all results presented hereafter, the response refers to the time-over-threshold information of the Timepix chip, i.e. the amount of collected charge.

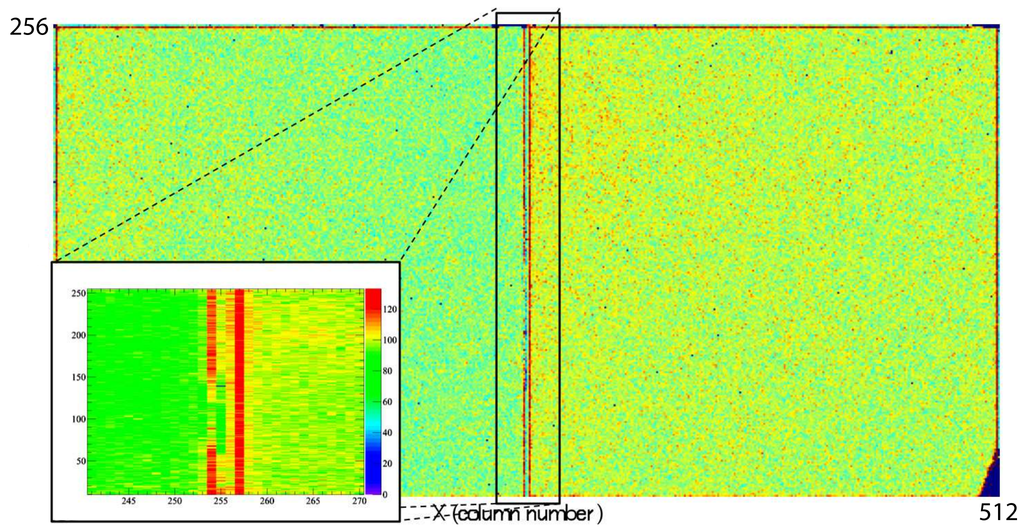

Figure 5.2: Flood-field image
A flood-field image of both sensors. The anomalous response of the two outermost pixel columns and rows becomes immediately apparent. This can be ascribed to the distorted electric-field distribution at the edge.

In Section 5.3.2, the profile of the effective volume is reconstructed by means of interaction-depth defined measurements on the amount of collected charge that is induced by high-energy muons and pions.

5.3 Results

5.3.1 Laser measurements

Strongly focussed laser light of two different wavelengths was used to measure the response functions of the outermost pixels. Figure 5.4 schematically shows how the measurement was conducted. A narrow beam of laser light was used to generate charge very locally. Subsequently, the amount of charge collected by the illuminated pixel(s) was studied as a function of the laser spot's position, which results in a map of the pixel response at the sub-pixel level.

Set-up

Sub-pixel precision was achieved with a moveable X-Y stage for detector positioning with one micrometer resolution. The output intensity of the laser was controlled by a pulse generator and guided via an optical fibre to a focussing lens to achieve a minimum spot size of 9 µm. The lens itself was attached to a moveable Z stage, also with micrometer precision.

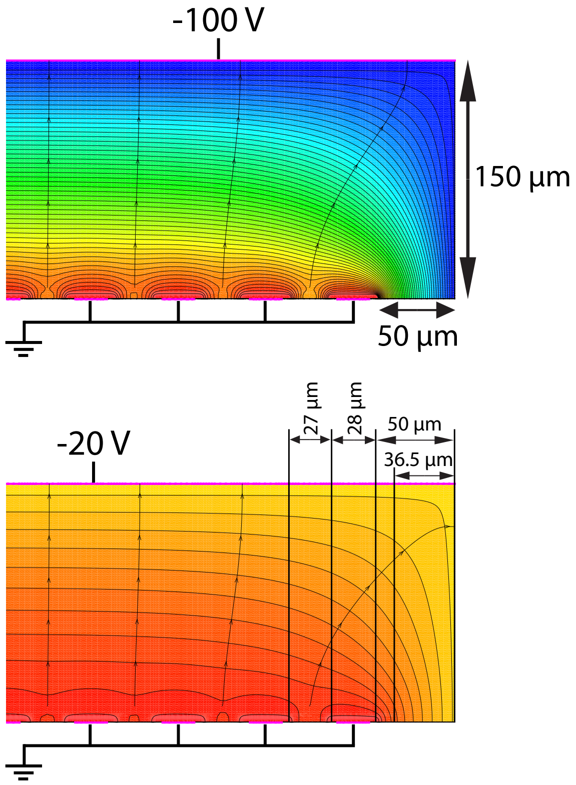

Figure 5.3: Potential distributions
TCAD simulations of the potential distribution at the edge at different bias voltages. The electric field is distorted by the edge electrode, as a consequence of which the effective volume of the outer pixels deviates from that of more central ones. The effect is more pronounced at lower bias voltages. Based on these simulations, the ratio between the effective volume of edge pixels and that of bulk pixels is estimated and indicated for both 10 V and 40 V sensor bias. In the bottom left figure, the dimensions of the pixel (implant) and edge distance are indicated.

For the determination of the laser's position relative to the pixel matrix, the detector was first placed in focus by minimising the size of the induced cluster, which varied from a maximum of approximately 100 pixels at 12 mm from the focal point to a minimum of one pixel in focus. Next, the laser position was derived by monitoring the response of the surrounding pixels as the detector was translated in x and y. To minimise the translational error on the measurement, the alignment procedure was always carried out in the region close to pixels under test.
On the right-hand side of Figure 5.4, the settings and corresponding photon input per acquisition are denoted for the results presented below.

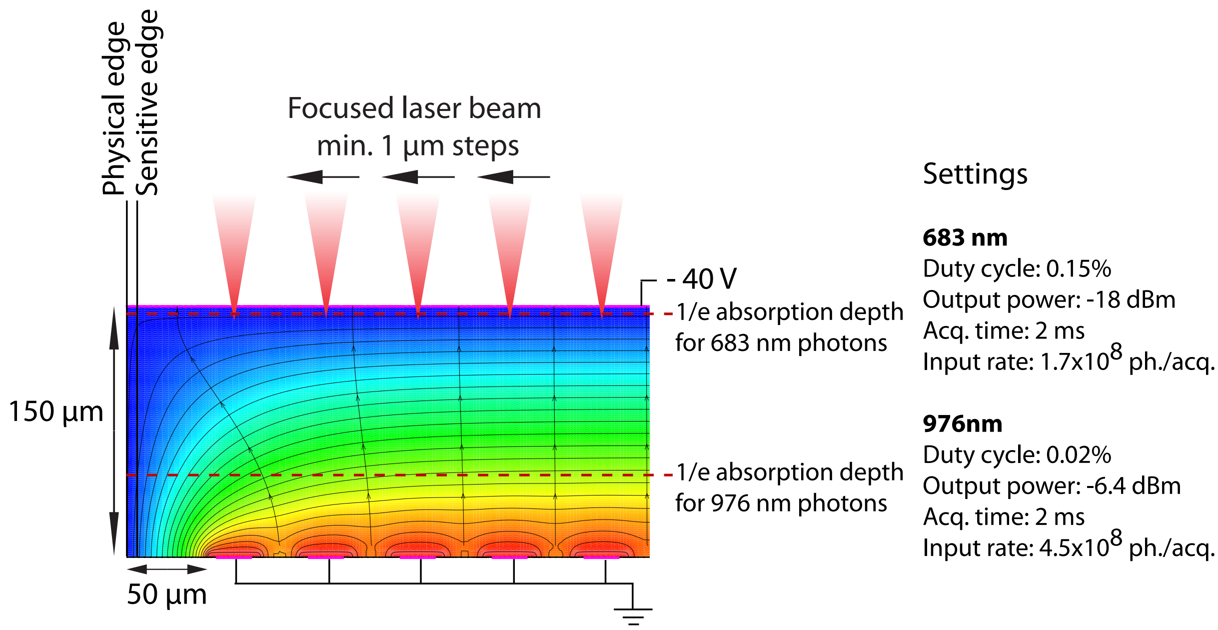

Figure 5.4: Pixel scanning
Laser light of two different wavelengths is used to scan the individual pixel response with sub-pixel resolution at two different interaction depths. The laser settings and the corresponding photon input rates are listed on the right-hand side of the figure.

Centre pixels

Before the edge was studied, the response functions of central pixels were measured. From this, the diameter of the observed part of the laser-induced charge cloud was derived. Figure 5.5 shows the fraction of collected charge as a function of the position of the laser (976 nm wavelength) relative to the pixel borders at 40 V reverse bias. It demonstrates that at about 6 µm from the pixel centre the adjacent pixel starts to respond, which implies a diameter of the observed charge cloud of approximately 43 µm. This is, to some extent, in agreement with the expected width, since the 3σ diffusion width (see Equation C.5) for 145 µm drift length at 40 V bias is approximately:

$$3\sigma = 3\sqrt{2\,\frac{kTd^2}{qU}} = 15.6\ \mu\text{m}\,,$$

and the minimum focal spot size is approximately 9 µm. This equals to a charge cloud diameter of $(2 \times 15.6 + 9)\ \mu$m $\approx 40\ \mu$m. The difference with the observation could be explained by: (i) an under-estimation of the spot size and/or (ii) an under-estimation of the diffusion, which may be larger than 3σ for high intensities.

Edge pixels

Similar measurements were performed on edge pixels. To study the depth dependence of the effective area, both photons of 683 nm and 976 nm wavelength were used to deposit

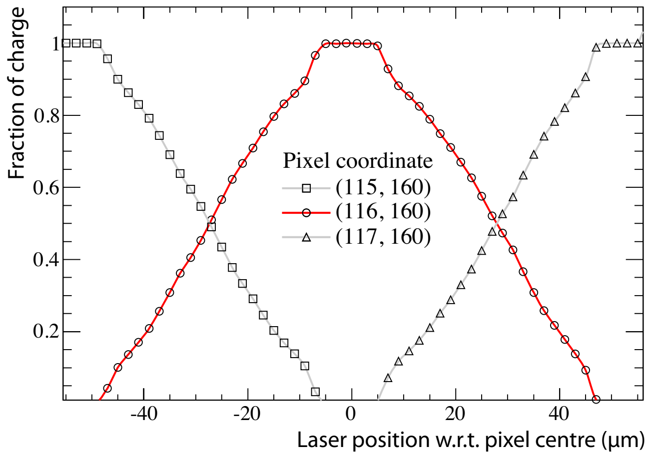

Figure 5.5: Fractional response functions of centre pixels
The fraction of laser-induced charge as a function of the laser's position relative to the pixel centre. It shows an observed charge-cloud diameter of approximately 43 µm.

charge across two different penetration depths.
Table 5.2 gives the absorption coefficients (α) and the corresponding 1/e absorption depths in silicon, which are determined by the energy of the photon as well as the band gap of silicon (1.12 eV). For 683-nm laser light, photons are predominantly absorbed close to the back side of the sensor ($\sim$ 5 µm), while photons of 976 nm wavelength penetrate silicon considerably deeper ($\sim$ 100 µm).

Figures 5.6(a) and 5.6(b) show the response functions of the five outer pixels for both wavelengths. The physical edge is positioned at 0 µm. The laser was scanned from the centre of the fifth pixel towards the edge with decreasing step size and the collected charge was assigned to the laser's spot centre position with respect to the physical

Table 5.2: Photon absorption depth
The absorption depth is determined by the photon energy and the band gap of the material, i.e. 1.12 eV for silicon. Listed are the absorption coefficients α for the centre wavelengths of the lasers.

λ (nm)	E (eV)	α (cm^{-1})	1/e abs. depth (µm)
683	1.82	$\sim 2.2 \cdot 10^3$	$\sim$4.5
976	1.27	$\sim 9.6 \cdot 10^1$	$1.0 \cdot 10^2$

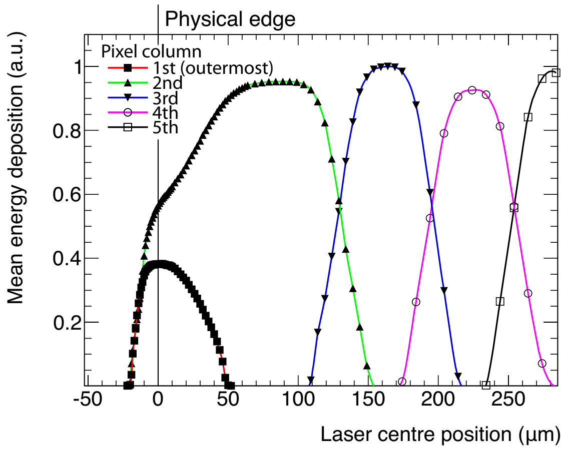

(a) 683 nm

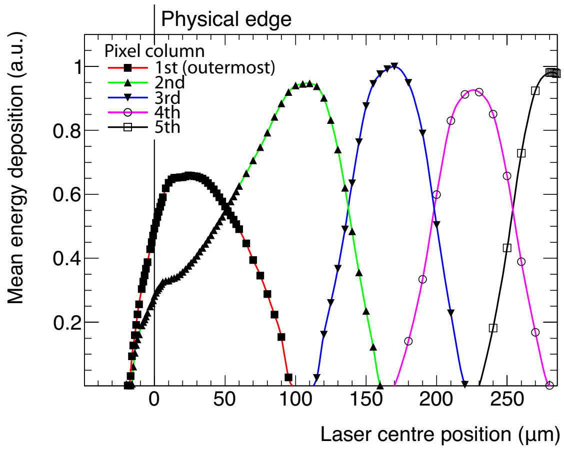

(b) 976 nm

Figure 5.6: Edge-pixel response function
The amount of collected charge as a function of the laser's spot-centre position relative to the physical edge, for both (a) 683 nm photons and (b) 976 nm photons.

edge. It clearly shows the difference between the mean effective area of edge pixels and that of non-edge pixels for two different interaction depths. From the response functions, the effective volume of each pixel is derived by integrating the mean amount of collected charge integrated over the effective width. Table 5.3 lists the volumes normalised to that of the fourth pixel from the edge. In agreement with the simulations on the profile of the effective volume as depicted in Figure 5.3, the difference between the effective volumes of the two outer pixels becomes smaller as the wavelength increases. Also, the sum of the normalised effective volumes of the three outer pixels is given in Table 5.3. From

Table 5.3: The effective volume of pixels of the three outermost columns normalised to that of pixels of the fourth column from edge. The values are derived from the mean amount of collected charge for both wavelengths.

Pixel column	$\frac{V_{\mathrm{eff}}}{V_{\mathrm{eff}}(\text{pixel } 4)}$	
	683 nm	*976 nm*
1	0.36	0.98
2	1.93	1.47
3	1.23	1.17
4	1.00	1.00
1+2+3	3.52	3.62

this value, the edge of the sensitive volume (see Figure 5.4) relative to the physical edge can be estimated. The physical width of the three outer pixels is $3 \cdot 55 + 36.5$ µm[3] = 201.5 µm (see Figure 5.3). Consequently, for each wavelength an inactive volume with the following width is derived:

$$(201.5 - 3.52 \cdot 55)\ \mu\text{m} \approx 8\ \mu\text{m} \quad \textbf{(683 nm)}$$
$$(201.5 - 3.62 \cdot 55)\ \mu\text{m} \approx 2\ \mu\text{m} \quad \textbf{(976 nm)}$$

The larger width obtained from the data taken with the 683 nm laser can only be explained by a loss of charge in the edge region.

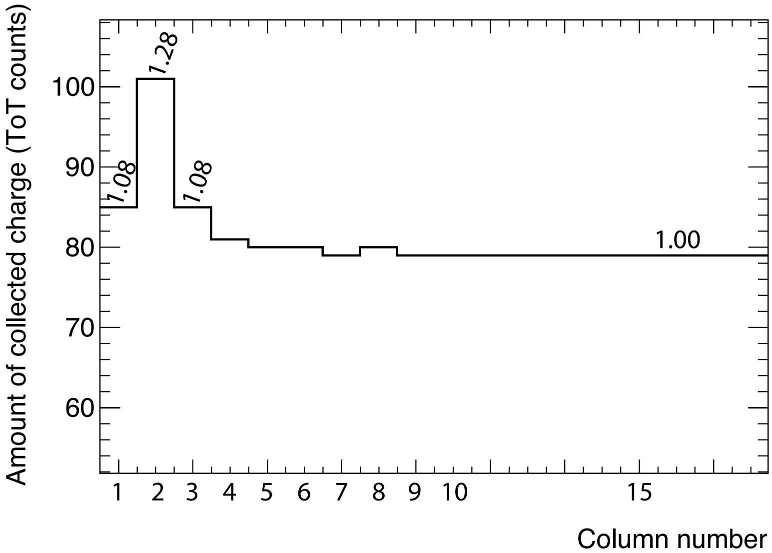

Figure 5.7: Mean edge response
The mean response of pixels of the 20 outer columns to tens of thousands of tracks of high-energy particles. From this, the total effective volume of pixels of the six outer columns was determined, which allowed for deriving the edge of the sensitive volume with respect the physical edge.

Figure 5.7 shows the mean response of pixels of the 20 outermost columns to tens of thousands of tracks of high-energy particles, which were used for the study presented in the next section. From this, it is derived that the edge of the sensitive volume is approximately 12 µm from the physical edge:

$$(201.5 - 3.44 \cdot 55)\ \mu\text{m} \approx 12\ \mu\text{m}$$

The discrepancy between this result and that of the laser measurements can be explained by the fact that part of the charge deposited by the muons is not detected by the pixels, simply because it is below the threshold value of the pixel. The mean energy loss of a minimum ionising particle is 3.9 MeV/cm, which means that the particle's path length through the pixel should be at least 10 µm in order to be detected.

[3] 36.5 µm is the width of the extra sensor volume at the edge.

5.3.2 Test-beam measurements

The depth dependence of the charge collection was studied further at the SPS H6 test beam facility at CERN. By using finite-length tracks of 120 GeV/c muons and pions that cross the two adjacent sensor edges in the centre of the module, the interaction depth could be reconstructed and related to the amount of collected charge in edge pixels.

Set-up

To determine the interaction depth at a given pixel, it is necessary to reconstruct the track in three dimensions.
The left part of Figure 5.8 shows a schematic representation of the detector's positioning relative to the beam. It was placed almost parallel to the beam, as a result of which particles traversed both sensors (only 150 µm thick) nearly parallel to the pixel planes. A small elevation angle benefited two-dimensional track reconstruction, whereas a shallow inclination angle (see side view) provided long but finite-length tracks, the entrance and exit point of which was used for reconstructing the third dimension.
An exemplary frame for the study presented below is shown in the right part of Figure 5.8. Most tracks consist of approximately 140 pixel hits. Both coordinate axes and the beam direction are indicated in the figure as well. For convenience in the discussion below, the sensors are labelled Left and Right. Hence, particles entered at the right sensor's back side and exited the pixel plane of the left sensor.
Tracks that are contained in one sensor are being referred to as single-sensor tracks, while tracks that traverse both sensors and thus cross the adjacent-edge region in the centre of the module are called double-sensor tracks. No trigger was used. Acquisition of 5 ms frames was controlled by the software.

Track finding

Every event frame was stored as an integer array of hits. Each element contains the position and the amount of collected charge of each individual hit.
As many frames contain more than one track, a track finding algorithm was used to isolate individual tracks for further study. The hits of each frame were sorted such that possible tracks formed sub-sequences of elements in the hit array. The arrows in Figure 5.9 indicate the hit order after sorting. Every sub-sequence was then selected by looping over the array elements and applying a selection criterion on the maximum difference between the coordinate values of consecutive hits. A hit was considered to be part of a sub-sequence, if its position with respect to the previous hit differed no more than 2 pixels in the y-direction and less than 10 pixels in the x-direction. The latter criterion was determined by checking the number of double hits between single-hit segments for a given elevation angle. As soon as the criterion on the consecutive hit position was not met, the sub-sequence was selected as a track candidate if its length was larger than 100. If not, the sub-sequence was excluded from further analysis.

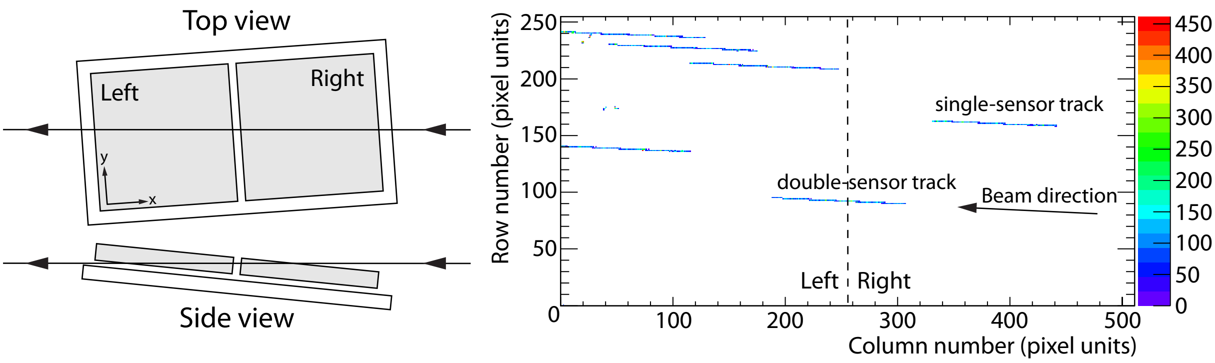

Figure 5.8: Detector orientation
A schematic representation of the detector's orientation with respect the beam direction is shown on the left side. The right-hand side shows a typical event frame containing six tracks, one of which crosses the adjacent-edge region in the middle. Due to a small elevation and inclination angle, tracks could be reconstructed in three dimensions. The xy-dimensions of the left figure scale 1:1 with the real dimensions. The sensor thickness and event frame are enlarged for better viewing.

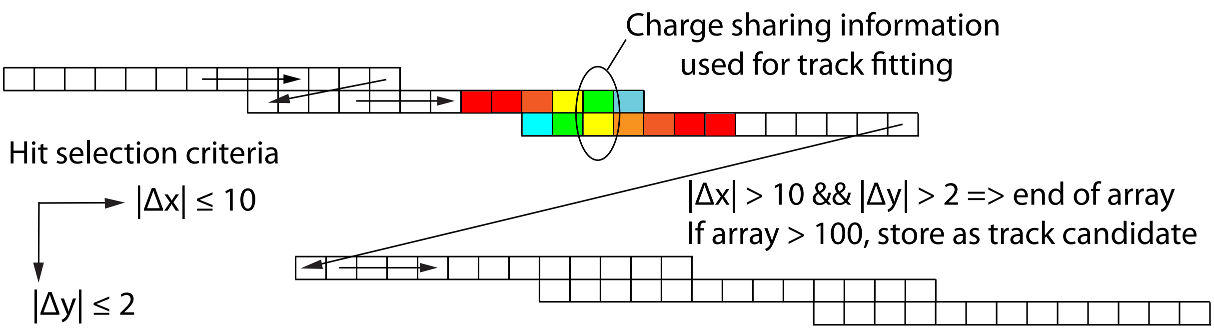

Figure 5.9: Track finding
Tracks were found by sorting the hits of each frame such that sub-sequences in the hit array could be selected. The arrows indicate how the hits were sorted, which allowed for hit selection by applying restrictions to the distance between consecutive hits. Sub-sequences of more than 100 hits were selected as track candidates.

Track fitting

As discussed above, tracks of particles that cross the adjacent-edge region in the centre of the module allow for reconstruction of the interaction depth at edge pixels. The depth was derived from the length of the track projected onto the pixel plane. Figure 5.10 shows, however, that the true track is longer than only the difference between the pixel coordinates at which the particle enters and exits the sensors. In addition, each particle had to bridge a small gap between the sensors, the width of which varies in the y direction due to a slight angular displacement. As a result of the gap and displacement, tracks crossing the edge region show a discontinuity. To reconstruct the gap width, each track was split into a left and a right segment, which were separately fitted using a linear least-squares fitting algorithm[4].

The fitting algorithm was tested using single-sensor tracks. Every track was halved

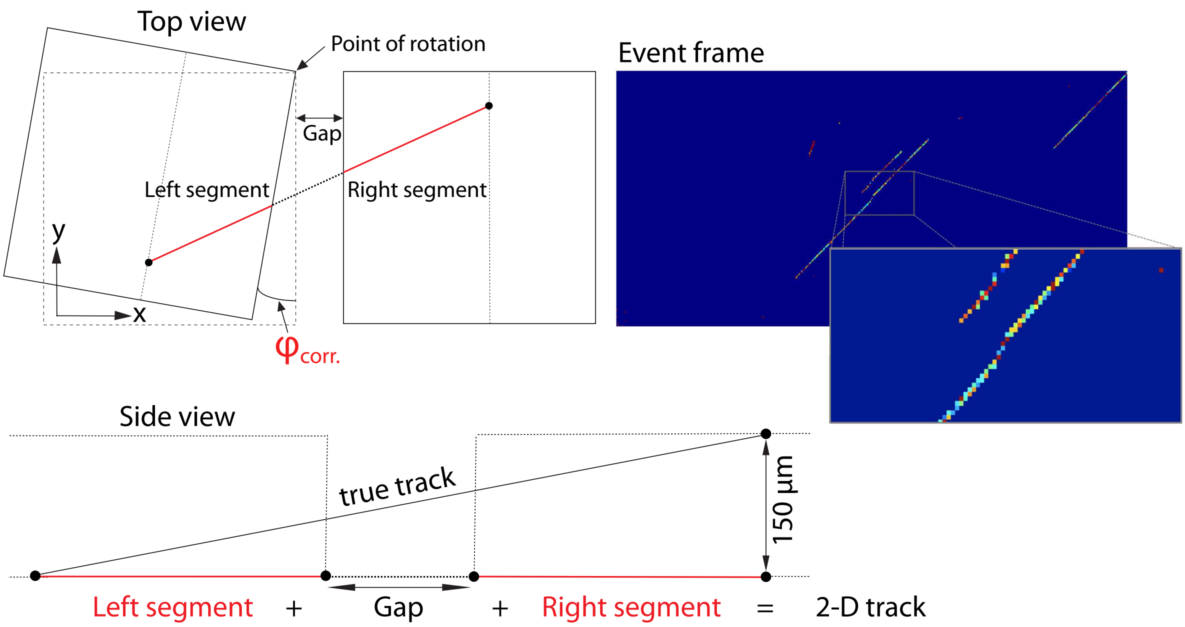

Figure 5.10: Track discontinuity
The true track length is derived from the length of the 2-D track, which is formed by the two projected track segments and the gap between the sensors. Together with a small angular displacement, the gap translates into a track discontinuity in the adjacent-edge region. All tracks were therefore split into two segments, which were separately fitted to reconstruct the true 2-D track length.

into two segments, which were each fitted up to the third pixel from the track-centre's x-coordinate (to match the fitting conditions of the double-sensor tracks discussed below). Figure 5.11(a) shows a close-up view of a track in the right sensor together with fits to each of the segments. As denoted in Figure 5.9, for double hits the particle's y-position was interpolated using the amount of charge collected in both pixels. The angular distributions for both left and right segments of more than 80 thousand tracks are plotted in Figure 5.11(b). It shows there is an almost negligible difference between the mean values of both distributions of approximately 18 µrad, which indicates good-quality fits. To evaluate the quality of fits, the residuals of more than 40 million hits are plotted in

[4]This method finds a linear function that best fits the hit pattern by minimising the sum of squares of the hit residuals in the y-direction.

Figure 5.11(c). They are nicely distributed around zero and only a small fraction of hits shows values of more than half a pixel, which may attributed to delta-electrons. The black line shows the residuals of the hits of charge shared events.
Moreover, the coefficient of determination[5] of the segment fits were determined, the distributions of which are plotted in Figure 5.11(d). This quantity expresses the proportion of the variance in the hits' y-positions that can be explained by the fit function and is therefore a measure of the goodness of fit. Approximately 81 % of the tracks show fits to both segments with a coefficient of determination higher than 0.8.

After evaluating the fit quality, double-sensor tracks were studied to determine the gap width. Each track was split into a left-sensor and right-sensor segment as shown in Figure 5.12. The angle of the individual segments was then used to correct for the angular displacement and to subsequently reconstruct the particle's path length between the sensors. To avoid the anomalously responding and larger edge pixels to negatively affect the fit, only hits up to the fourth column from the edge were used.
The angular distributions of both left and right segments of approximately 10 000 tracks are shown in the centre-left plot. From the means of the Gaussian fits to the distributions, an angular displacement of 0.27 mrad is derived. This translates into a gap-width increase along the y-axis of approximately 4 µm, which is in good agreement with microscope measurements that show a gap-width difference of around 2 µm between the top and bottom of the sensors. The corrected angular distributions are shown in the centre-right plot.
After correction, the segment fits were extrapolated to the edge, in order to determine the difference in y at the edge of both sensors. Using the angle of its right segment, the path length between the sensors was reconstructed. The extra 128 µm that is added to the gap width in the top figure, accounts for twice the edge distance of 50 µm plus two times radius of the pixel implant of 14 µm (see Figure 5.3).
Distributions of the difference in y before and after angle correction are plotted at the bottom of Figure 5.12. A mean value of 0.156 pixels difference in y-position is derived. This translates into a gap of approximately

$$\frac{0.156}{\tan(0.0428)}\ 55\ \mu\text{m} = 72\ \mu\text{m wide,}$$

which shows excellent agreement with the measurements made with the microscope (see Figure 5.1(b) on page 94).
For both the fit-quality study and the detector alignment, only tracks with segments containing more than 40 hits were used. Moreover, for the detector alignment a cut of 0.8 was applied on the coefficient of determination.

[5]The coefficient of determination takes values between 0 and 1, which describes how well a regression fits the data. A coefficient of determination close to 1 indicates that the line fits the data well.

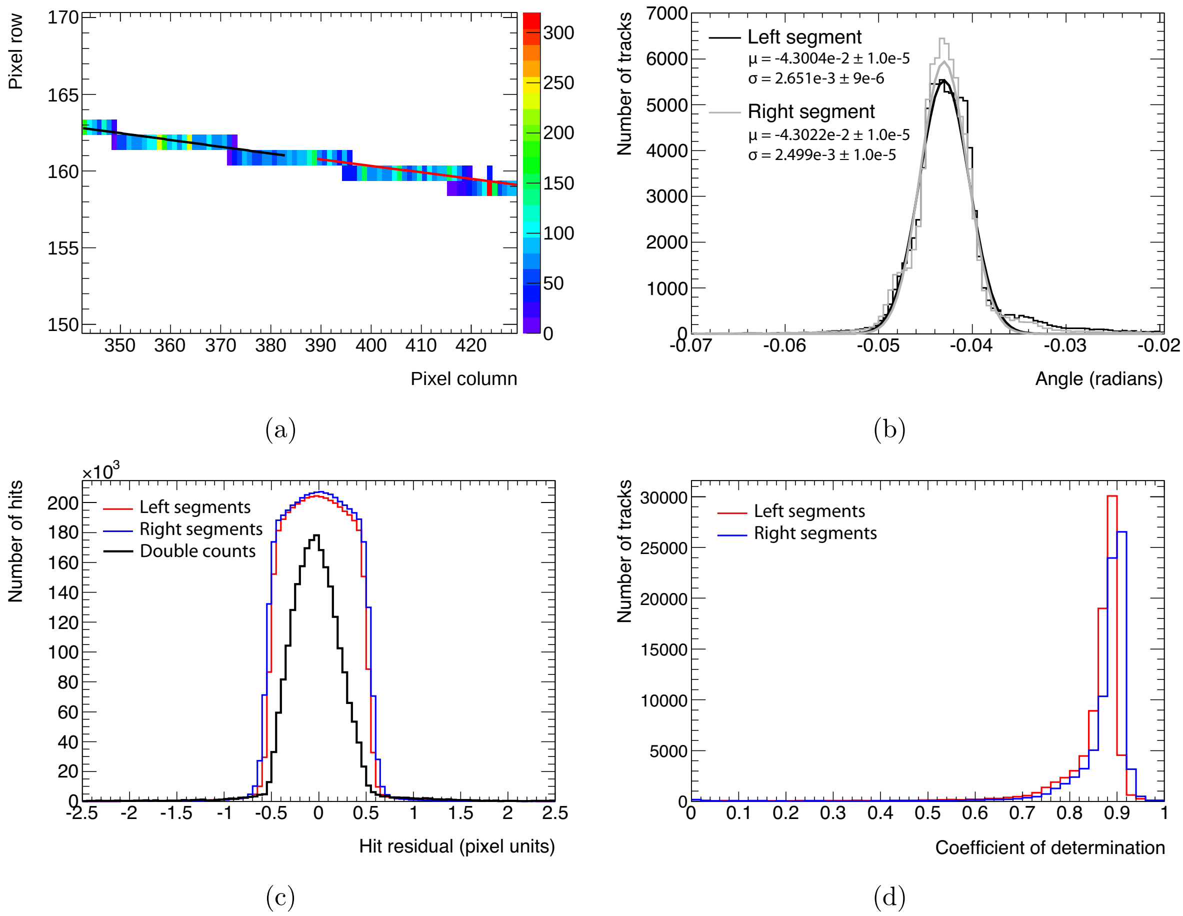

Figure 5.11: Single-sensor tracks
(a) A close-up view of the centre of a single-sensor track, together with fits to each of the segments. (b) The angular distributions of each segment, which show an angular difference of approximately 18 µrad. (c) The distributions of the perpendicular residuals to the fits. The residuals of the weighted hits of charge shared events are indicated by the black line. (d) The distributions of the fits' coefficient-of-determination.

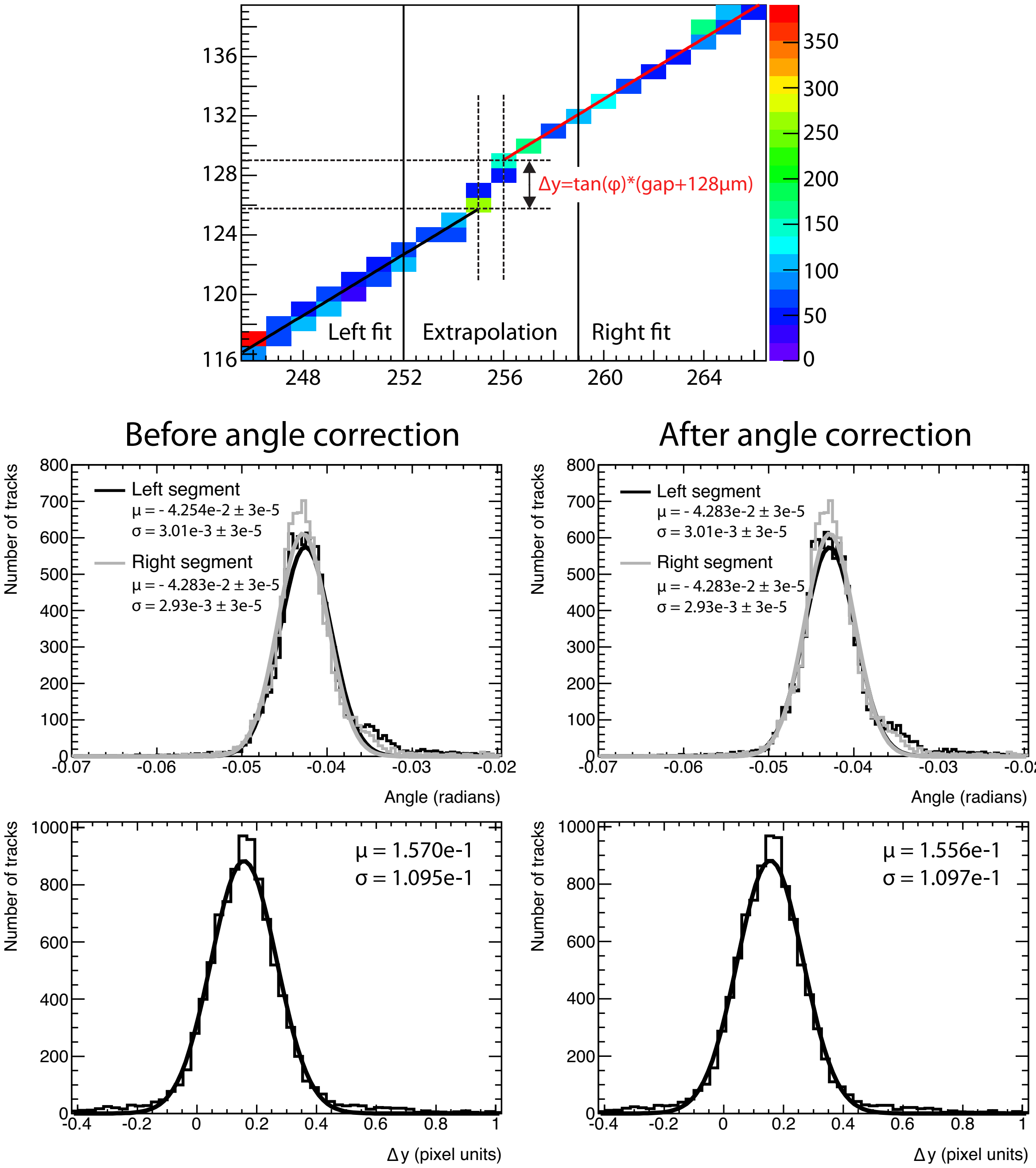

Figure 5.12: Detector alignment

Top: Each track was split into a left-sensor and a right-sensor segment, which were separately fitted. This allowed for correction of the angular displacement between the sensors and subsequent determination of the gap width.

Centre: The angular distributions of the left and right segments before and after angle correction.

Bottom: The distributions of the difference in y-position between the extrapolated fits to each of the segments before and after angle correction.

Interaction-depth dependence

After sensor alignment, the interaction depth at edge pixels was determined. To analyse the entire depth of the sensor, tracks with a minimum segment length of 5 pixels in either one of the two sensors were used. Subsequently, the path length between the sensors was determined by using the angle of the longest segment (corrected in case of left segments) and a constant value of 72 µm for the gap width. This path length was added to the differential distance between the entrance and exit pixel. Figure 5.13(a) depicts the situation at the edge: by relating the interaction depth to the amount of collected charge, which is dependent on the effective pixel size at a certain depth, the electric-field distribution can be reconstructed. These tracks entered the right sensor and exited the left.

Figure 5.13(b) shows the amount of collected charge as a function of the interaction depth for both sensors. Clearly, the outermost pixels measure a smaller amount of charge at the sensor's back side than more central pixels, while the opposite is true for the second outer pixels. As expected, the amount of collected charge in pixels of the third and fourth column is virtually constant across the entire sensor depth. The error on the collected charge is largest at the back side of the left sensor and at pixel side of the right sensor. This is due to the fact that these points are derived from tracks with a small segment in the corresponding sensor. Moreover, there are a number of oddly responding pixels at the edge of the left sensor, as can be seen in the flood-field image of Figure 5.2. Nevertheless, the reconstruction does show that the potential distribution closely matches that of the simulations, which is even more clearly depicted in Figure 5.13(c). It shows the accumulated amount of charge collected by pixels of the four outer columns. This summed amount is proportional to the path length through the effective part of the corresponding pixels. The resemblance with the field lines that separate the pixels from each other is clear, which emphasises the excellent accordance to the simulation. The anomalous response of edge pixels is therefore understood and simulations may be used for correction.

Correction

An example of such a correction is shown in Figure 5.14. The top figure shows a raw image of an anchovy, whereas the bottom part shows the image taken after a flat-field correction was applied. Clearly, the anomalous response at the edge is eliminated.

The correction procedure calibrates the response of each individual pixel with respect to the mean response over the entire detector area. First, a large number of images is taken under open-field conditions, i.e. homogeneous irradiation. Subsequently, the response of each individual pixel is normalised to the mean count-rate density of the average of the open-field images. This results in a so called flat-field map, which can be applied to the raw image in order to equalise the response. As will be discussed in Chapter 6, the effectiveness of the procedure depends largely on the response variance of the raw image as well as the number of open-field images used to create the correction map.

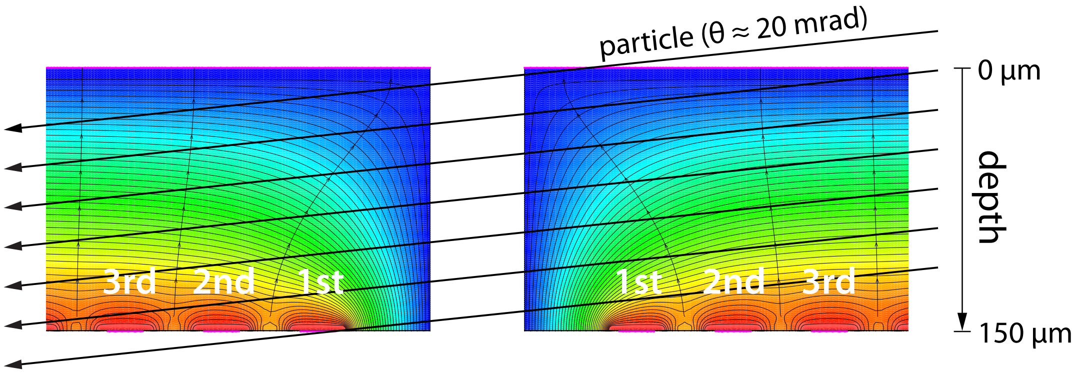

(a)

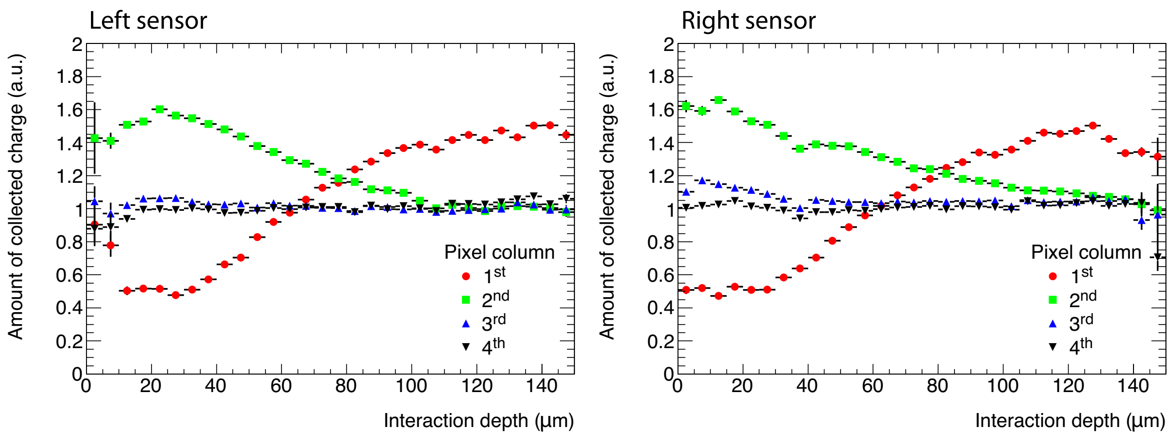

(b)

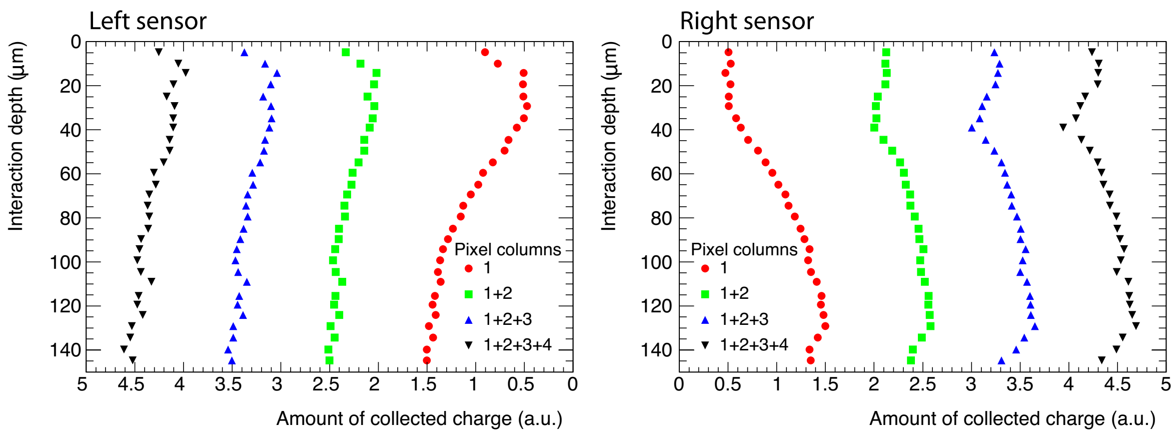

(c)

Figure 5.13: Interaction-depth dependence
(a) Particles traversed the edge pixels at different depths. This allowed for a determination of the effective pixel area at various depths across the sensor. (b) The amount of collected charge as function of interaction depth for pixels of the four outer columns. The mean values are scaled to those of pixels of the fourth column. (c) By plotting the cumulative amount of collected charge, which corresponds to path length through the effective part of the pixels, the pixel-separating field lines are revealed.

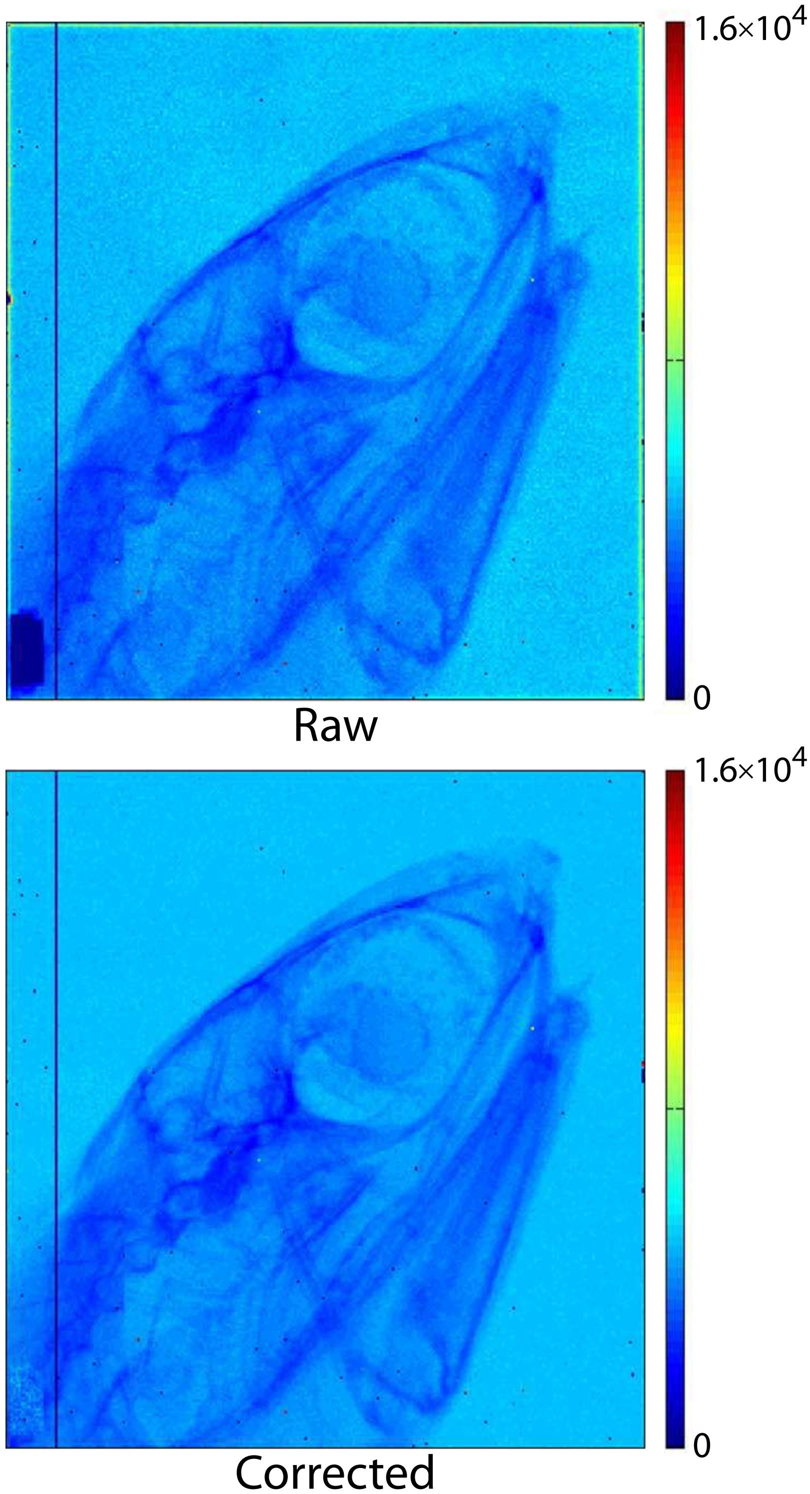

Figure 5.14: Correction
A raw image of an anchovy taken with a single detector assembly, which contains a sensor that is equal to those used for the study presented in this chapter. The bottom part shows the same image after flat-field correction. Figure from [84].

5.4 Conclusion

In this chapter, the performance of edge pixels of active-edge silicon sensors has been studied. Two complementary measurements were made to determine the sensitive volume at the edge as well as to study the interaction-depth dependence of the amount of collected charge.
The edge-pixel response functions obtained by the 683-nm laser and those measured with the 976-nm laser show a clear difference in the distribution of the collected charge among the pixels. They show a reduction of the effective area of pixels closest to the edge and an increase of that of the second outer ones in the direction towards the back plane. From the summed amount of charge collected by the three outer pixels, the width of the inactive region at the edge was derived. The data taken with the 976-nm laser indicate that the edge of the sensitive volume and the physical edge are only 2 µm apart.
A similar analysis was carried out with data from high-energy muons that traversed the sensor almost parallel to the pixel planes and indicate an inactive width of approximately 10 µm. The discrepancy between this result and that of the laser measurements can be explained by the fact that part of the charge deposited by the muons is not detected by the pixels, simply because it is below the threshold value of the pixel.
The long tracks of the high-energy particles were also used to determine the depth dependence of the effective pixel area. Tracks that crossed the adjacent-edge region were reconstructed in three dimensions to determine their length through the sensor, from which the local interaction depth was determined. By relating the interaction depth to the amount of collected charge, the effective area of edge pixels was reconstructed for various depths across the sensor.
The results are in good agreement with simulations on the electrostatic potential distribution at the edge, which show that the effective volume of the outer pixels is different from their physical volume due to a distortion of the electric field that is caused by the biased edge implant. As expected, this alteration and therewith the depth profile of the effective volume of edge pixels is bias-voltage dependent. The resemblance with the results shows that the simulations are realistic and hence can be used for correction of the non-uniform response at the edge. The effectiveness of the correction, however, is largely dependent on variance of the response over the entire detection area. For shallow interactions and low bias voltages, the ratio between the effective volume of the pixels closest to the edge and that of the second outer ones is significantly larger than for deep interactions at high bias voltages. Nonetheless, the good understanding of the anomalous response of edge pixels allows for a first-order correction and is a step forward to a seamlessly responding tessellation of detector modules.

6

Slim-edge high-Z sensors

Chapters 4 and 5 presented results regarding active-edge silicon sensors. In spite of their good characteristics and more than acceptable performance at the edge, they are not very appropriate for diagnostic X-ray imaging due to the low absorption efficiency of silicon. Sensor materials of higher atomic number, like gallium arsenide and cadmium telluride, are better suited for this purpose. The fabrication of detector-grade gallium arsenide and cadmium telluride, however, is more complicated than that of silicon. During growth, inclusions and grain boundaries may form. This could lead to local alterations of the detection properties and hence cause unwanted sensitivity variations between pixels, which compromise image quality. In a similar manner, edge effects may negatively affect the response of the outermost pixels.
In this chapter, three slim-edge high-Z detectors are studied. In the first part, the edge pixels of slim-edge cadmium telluride sensors are characterised. In the second part, the imaging performance of the detectors is examined. In particular, the noise performance of edge pixels is compared to that of non-edge pixels. For reference, the results are compared with those of measurements on a conventional silicon detector.

6.1 Sample specifications

Three different detectors with slim-edge high-Z sensors are studied:

- Two Timepix detectors with gallium arsenide sensors of different thickness (280 µm and 450 µm) and 145 µm pixel-to-edge distance.

- One Medipix-2 detector with nine identically processed pieces of cadmium telluride of 1 mm thick and 65 µm pixel-to-edge distance.

6.1.1 Gallium arsenide

The gallium-arsenide sensors, produced by JINR[1], have a Medipix layout and are bump-bonded to Timepix chips. The sensors are separated from the wafer by conventional blade dicing and do not have a guard ring between the pixel matrix and the edge. Figure 6.1(a) depicts the corner of one of the samples on the pixel side. The distance from the outermost pixels to the physical edge is approximately 145 µm. Both the pixels and back electrode are realised by Ohmic type metal contacts on chromium compensated n-type gallium arsenide. A cross section of the different contact metal layers is shown in Figure 6.1(b).

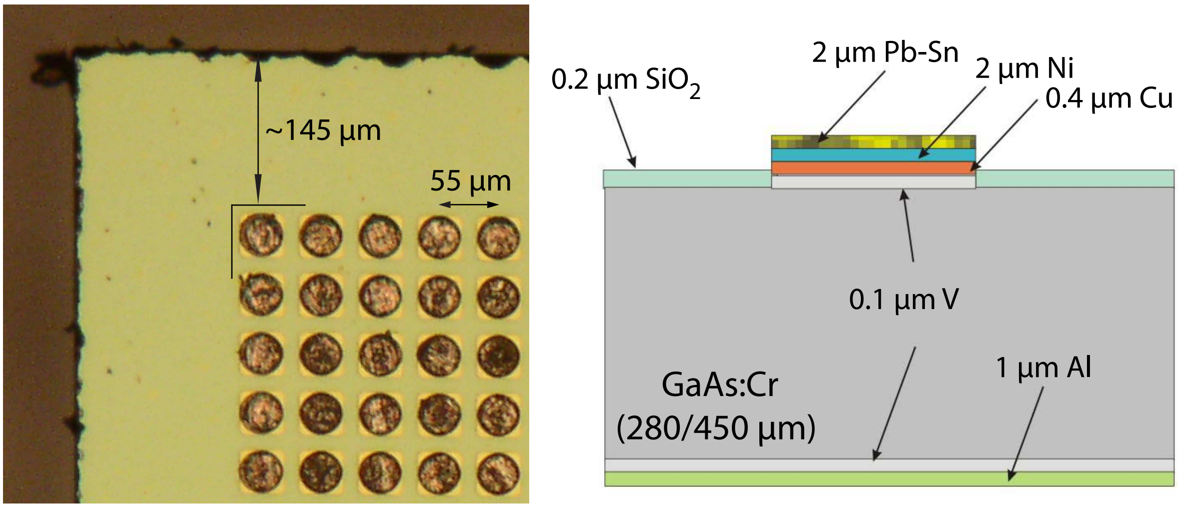

(a) (b)

Figure 6.1: Gallium arsenide
(a) Close-up view of the corner of a slim-edge gallium arsenide sensor. (b) A cross-sectional schematic view of one pixel. The pixel contact is formed by a stack of four different metals.

6.1.2 Cadmium telluride

The cadmium telluride sensors were produced by Acrorad[2]. A three-by-three tessellation of sensors is realised by bump bonding nine slim-edge pieces of detector-grade cadmium telluride to a Medipix-2 readout chip (see Figure 6.2(b)). Each sensor tile measures 4.05 mm × 4.05 mm × 1 mm, each of which is segmented into a matrix of 36 by 36 Ohmic-type platinum pixel electrodes at 110 µm pitch. At the back side, a platinum electrode forms an Ohmic contact. Figure 6.2(a) depicts the corner of one of the pieces at the pixel side. The dies are separated using conventional diamond-blade dicing. Whereas the edges of the gallium arsenide are clearly damaged, the edges of the cadmium telluride

[1] Joint Institute for Nuclear Research, Dubna, 141980 Moscow region, Russia. `http://www.jinr.ru`
[2] Acrorad Co., Ltd.. `http://www.acrorad.co.jp/us/`

show no visible signs of chip-outs or cracks. The pixel-to-edge distance is 65 µm. As a consequence, one readout column is left unbonded between the dies (see Figure 6.2(c)). The reason for using several small pieces instead of one big piece is to increase the number of edge pixels for characterisation, while only one read-out chip is needed.
The idea behind the tiled configuration was to see whether it is possible to reduce field effects at the edge by joining the sensors [113], for example by using a filler material with a dielectric constant that is similar to that of cadmium telluride. This is, however, a subject of future research and will not be reported here.

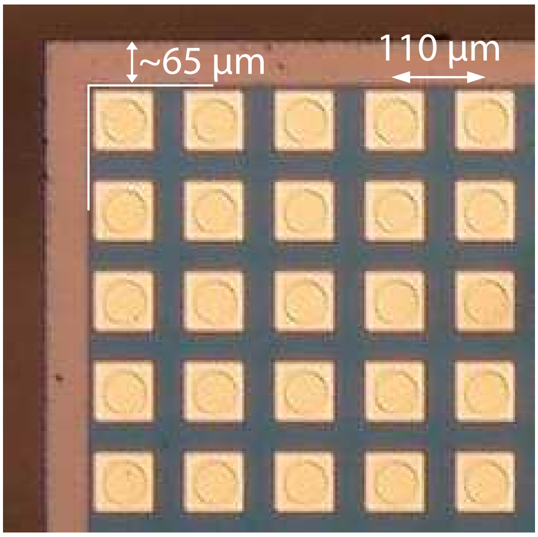

(a)

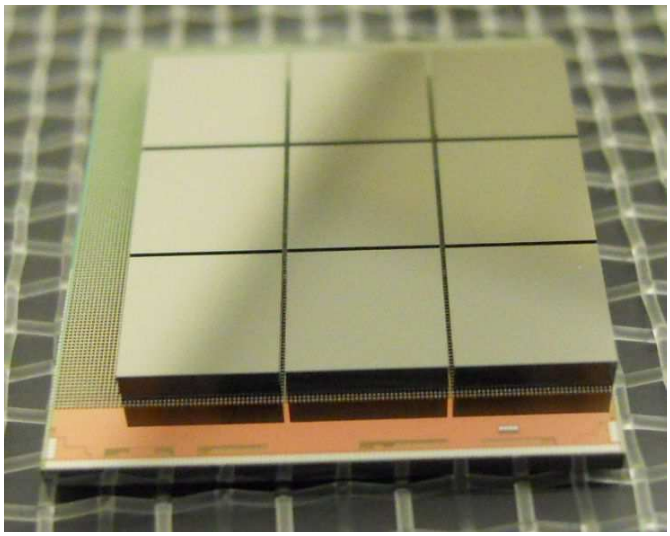

(b)

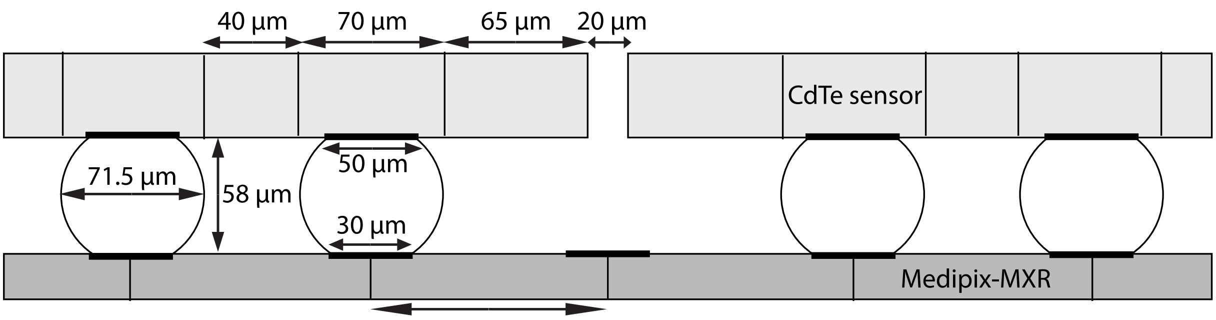

(c)

Figure 6.2: Cadmium telluride
(a) Close-up view of the corner of a piece of slim-edge cadmium telluride. (b) A three-by-three tessellation of sensors bump-bonded to a Medipix-2 readout chip. (c) A schematic side view of the assembly. Due to the pixel-to-edge distance of 65 µm, one readout column is left unbonded between the sensors.

6.2 Characterisation

This section compares the edge pixels of the cadmium telluride sensors to more central pixels in terms of leakage current and charge collection efficiency. Before these results are presented, the global leakage-current characteristics of both the gallium-arsenide and cadmium-telluride sensors is examined.

6.2.1 Current-voltage characteristics

As discussed in Chapters 2 and 4, the leakage current is a measure of the purity and homogeneity of the bulk material. It also indicates the severity of the deleterious effects at the sensor's edge in case of slim-edge structures. Micro-cracks and defects as well as improper passivation can cause high leakage currents, which can seriously degrade the edge-pixel response.

Figure 6.3 shows the leakage current as a function of time while increasing and decreasing the voltage in steps of 40 V. Whereas the gallium arsenide sensors show a near-Ohmic I-V characteristic and normal response to a change in voltage (Figure 6.3(a)), the total leakage current of the cadmium telluride sensor tiles shows a settling time of several minutes after voltage stepping (Figure 6.3(b)). This can be an indication for the presence of deep-level defects, which act as trapping centres with a long de-trapping time [114]. Figure 6.3(c) shows the count-rate map of two pieces 30 s after a voltage step and is compared to the flood-field image. It demonstrates that the dark currents settle most slowly in defect areas and at the sensors' edges, which could indicate increased deep-trap concentration in those specific areas.

To quantify the influence of the edge on the leakage current, the current-voltage characteristics of single edge-, corner- and centre pixels of unbonded sensors have been measured. High leakage currents could lead to a saturation of the leakage-current compensation circuit in the read-out chip. This results in a threshold shift and hence an incorrect count-rate response at the edge. The I-V curves of Figure 6.4(b), however, show only a slightly higher current for corner and edge pixels in both the positive and negative voltage domain. On average, across the full voltage domain, the edge and corner pixels show an increase in leakage current of 34% and 84%, respectively. This can be explained by the larger effective area of these peripheral pixels. Based on the dimensions given in Figure 6.2, edge and corner pixels are 1.4 and 2.0 larger than non-edge pixels, respectively.

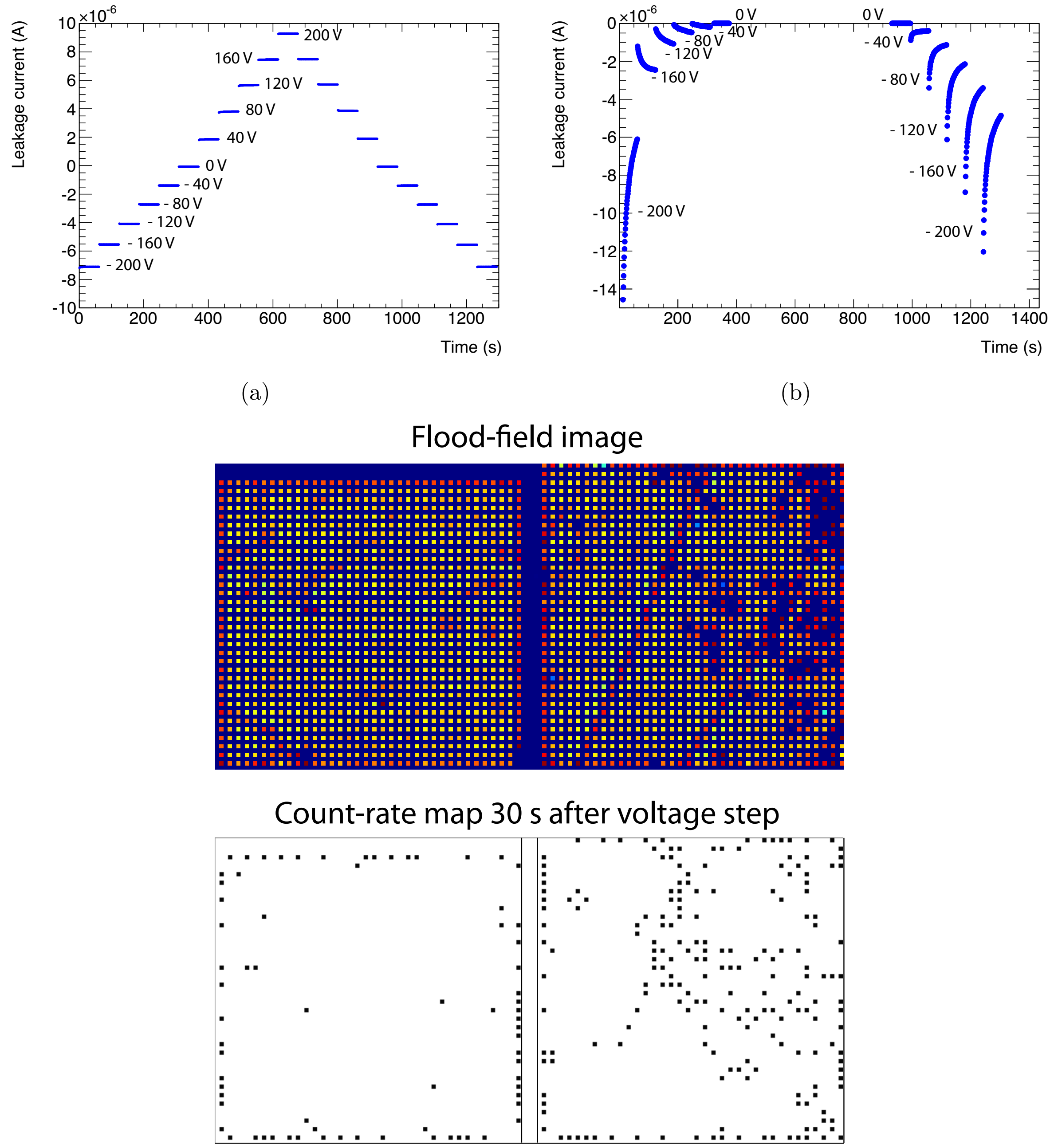

(a) (b)

(c)

Figure 6.3: Leakage current
(a) and (b) The leakage current as a function of time after voltage stepping. The current is monitored for one minute after each voltage step of 40 V. (a) The gallium arsenide sensors show the expected staircase-like behaviour. (b) The cadmium telluride sensors show current transients of up to several minutes. (c) The count-rate map of two cadmium telluride pieces 30 s after a voltage step is compared to the flood-field image at the top. The dark currents settle most slowly in defect regions and at the sensors' edges, which seem to indicate increased concentrations of deep traps in those specific areas.

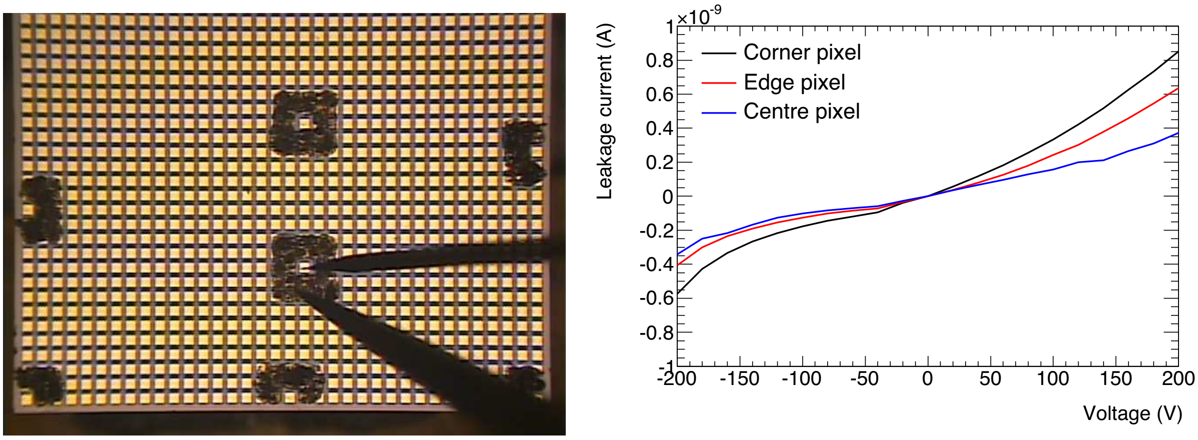

(a) (b)

Figure 6.4: I-V single pixels
(a) Top view photograph of pixel probing for I-V characterisation of single cadmium-telluride pixels of 110 µm on the side. A homogeneous electric field is realised by biasing the surrounding pixels at the same voltage as the pixel under test. To minimise the number of probing needles needed, the surrounding pixels are connected together using a electrically conductive glue. (b) The average leakage-current characteristics of single edge-, corner- and centre pixels as a function of the applied bias voltage.

6.2.2 Charge collection efficiency

The electron collection efficiency is determined by illuminating single pixels from the sensor's back side at normal incidence using a pulsed laser of 683 nm wavelength. The optical properties of cadmium telluride at this wavelength make that the absorption depth is only of the order of one micrometer [115], ensuring charge drift over the full thickness of the sensor. The amount of collected charge was measured at various sensor bias voltages by performing a top-down scan of the level of the global threshold of the Timepix chip. The mean of the Gaussian fit to each differential curve was used as a measure of the amount of collected charge. These values were plotted as a function of the applied bias voltage and fitted by a function described by the electron part of the Hecht relation [39] (see Equation 2.31 on page 32):

$$Q(U) = Q_0 \frac{(\mu\tau)_\mathrm{e}}{d^2} (U_\mathrm{bias} - U_0) \left(1 - e^{-\dfrac{x_0 d}{(\mu\tau)_\mathrm{e} U_\mathrm{bias}}} \right) , \tag{6.1}$$

where $Q(U)$ is the bias-voltage dependent fraction of the total amount of generated charge Q_0 that is collected by the pixel. Q_0 is a free fit parameter, the value of which was used to normalise the charge collection efficiency. The other fit parameters are U_0 and $(\mu\tau)_\mathrm{e}$. U_0 is a bias voltage offset, that represents the minimum voltage needed for charge collection and $(\mu\tau)_\mathrm{e}$ is the mobility-lifetime product of electrons. Figure 6.5 shows the Hecht

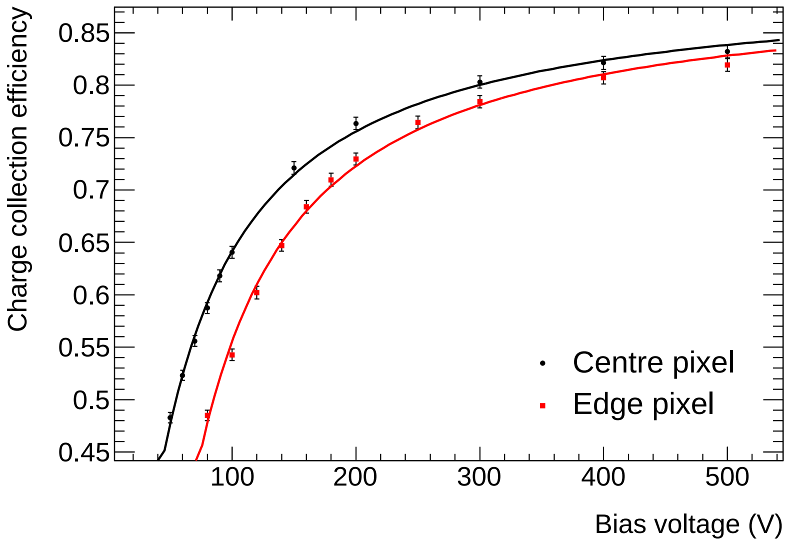

Figure 6.5: Charge collection efficiency
The charge collection efficiency as a function of the bias voltage. From this, an average electron mobility-lifetime product of $1.25 \cdot 10^{-4}$ cm^{2}V^{-1} was derived for centre pixels and $1.15 \cdot 10^{-4}$ cm^{2}V^{-1} for edge pixels. The efficiency is normalised to the value of the free fit parameter Q_0.

curves for the average of two separate centre and edge pixels. From this, an electron mobility-lifetime product of $(1.25 \pm 0.02) \cdot 10^{-4}$ cm^{2}V^{-1} was derived for centre pixels and $(1.15 \pm 0.07) \cdot 10^{-4}$ cm^{2}V^{-1} for edge pixels. The manufacturer (Acrorad) states a value of $\sim 3 \cdot 10^{-3}$ cm^{2}V^{-1} for $(\mu\tau)_e$ [116], which is one decade larger than the measured values. This significant difference could be due to the fact that Acrorad states its best ever measured value for $(\mu\tau)_e$. Importantly, no significant difference is observed between the charge collection efficiency of centre pixels and that of edge pixels.

6.3 Imaging performance

As discussed in Chapter 1, the imaging performance of a detector is determined by both its signal and noise transfer properties, which is commonly described by the detective quantum efficiency. Whereas the signal-to-noise ratio only expresses the total noise variance relative to signal power, the detective quantum efficiency is a more complete descriptor and allows to compare different imaging systems to each other. It comprises the frequency dependence of the ratio between the signal-to-noise ratio at the detector's output (which includes detector noise) and the input signal-to-noise ratio, which is defined by Poisson statistics. It is this spatial-frequency information that defines how well details in a quantum image are transferred to the final output image. As described in Equation 1.23, the detective quantum efficiency can be obtained by measuring the modulation transfer function, the noise power spectrum and the mean number of output quanta.

In this section, the modulation transfer functions and noise power spectra of the slim-edge high-Z detectors are compared to those of a conventional silicon detector, i.e. with a 300 µm thick p-in-n silicon sensor with conventional edge topology.

6.3.1 Image degradation

As discussed in Section 1.2, a detector's imaging performance is determined by its ability to transfer contrast and by the amount of noise it introduces. Noise is introduced through several mechanisms, which will be discussed in more detail in Section 6.3.3. The perceptibility of details is determined by both the size of object structures and the spatial resolution of a detector. If the granularity of the detector is not fine enough or if the resolution is compromised in the conversion process, the image gets blurred. Blur can be caused by an effect that is inherent to all pixel detectors that possess a low pixel-pitch to thickness ratio: charge sharing.
Charge sharing is due to the lateral spread of charge across multiple pixels and may be caused by:

- The path length and angle of the photoelectron, along which it creates electron-hole pairs.
- The range of Compton-scattered photons before absorption.
- The range of both fluorescent X-rays and Auger electrons before absorption.

In addition, there are effects that can be attributed to charge-carrier transport in the sensor:

- The diffusion of the created charge carriers.
- The electrostatic repulsion of electrons or holes inside charge clouds.

The range of the latter two mechanisms is derived in Appendix C.

All phenomena lead to a loss of resolution, which is commonly known as blur. Table 6.1 lists the contributions of the individual mechanisms to charge spread for the three high-Z sensor samples, the conventional silicon sensor and for 1 mm thick amorphous selenium (for comparison with today's radiography detectors). The values are obtained analytically and are based on the following assumptions and initial parameters:

- The initial photon direction is perpendicular to the detector's surface and has an energy of 50 keV. This energy corresponds to the mean energy of the input spectrum used for the measurements discussed hereafter (i.e. 70 kV tube voltage and 21 mm aluminium filtering).
- The absorption of the primary photoelectron involves only K_1-shell interactions.

- The Compton photons scatter at a most probable angle of 45 degrees.
- The energy of the fluorescence photons equals the K_α-energy of the respective materials.
- The energy of the Auger electron equals $E_{K_\alpha} - E_{L_3}$.
- The electron ranges are calculated using the Continuous Slowing Down Approximation (CSDA). The photon range equals the 1/e absorption depth derived from the photon absorption coefficients. Both the CSDA and photon absorption coefficients are provided by [6].
- The temperature is 300 K and the electric field strength is 3 kV/cm for the crystalline sensors and 100 kV/cm for amorphous selenium.
- The sensor thickness corresponds to that of the samples, i.e. 280 µm and 450 µm thick gallium arsenide, 1 mm thick cadmium telluride and 300 µm thick silicon. For comparison, the values of 1 mm thick amorphous selenium are added.

Table 6.1: Contributions of the different mechanisms that cause the primary-interaction origin to be compromised and hence give rise to a loss in resolution. All ranges are expressed in micrometers.

Charge spreading mechanism	**Si**	**GaAs** (280 µm)	**GaAs** (450 µm)	**CdTe**	**Se**
Photoelectron range (µm)	2.2	9.3		3.2	10
Compton-photon range (µm)	$6.5 \cdot 10^3$	$3.7 \cdot 10^2$		99	$3.8 \cdot 10^2$
Fluorescence-photon range (µm)	12	40/15		$1.1 \cdot 10^2$/59	69
Auger-electron range (µm)	3.4	0.6/0.8		3.0/3.8	1.1
Diffusion (3σ) (µm)	21.6	20.8	26.4	39.4	6.8
Electrostatic repulsion (µm)	17	15	18	25	5.5

Table 6.1 shows that Compton scattering causes the largest lateral range, but that does not mean it is the dominant mechanism. Only in silicon Compton scattering is likely to occur for photons of these energies. For both gallium arsenide and cadmium telluride, fluorescence photons are contributing most to the charge spread. For silicon, this is also the case, yet this charge-sharing component is not observed, since the fluorescence photon energy is below the Medipix noise floor of approximately 4 keV.
The lateral range of electrostatic repulsion is of the same order as that of diffusion for photons of these energies. However, for higher photon energies repulsion will start to dominate over diffusion. For a 300 µm thick silicon sensor. the turning point is at around 28 000 electrons, which corresponds to an X-ray photon of 100 keV.

6.3.2 Set-up

For determination of both the noise power spectrum and the modulation transfer function, the methodology as defined by the international standard IEC[3] 62220-1 is followed as closely as possible. This standard applies to all 2-D detectors used for general radiography and defines the input spectrum, set-up geometry and instructions for measuring a detector's characteristic function, modulation transfer function and noise power spectrum. Different spectra for different applications are defined. If only one spectrum is used, the standard advises to use the RQA-5[4] spectrum. RQA-5 specifies the thickness of the aluminium filter and its half-value layer, which is defined as the thickness of any material that attenuates the incident intensity to 50% of its initial value. The RQA-5 specturm is realised using a 21 mm thick aluminium filter with a half-value layer of 7.1 mm, which corresponds to operating a tungsten-target tube at a peak voltage of 70 kVp[5]. This should simulate the detector's input spectrum of a chest radiograph of an average patient. Figure 6.6 shows a simulation of this spectrum at one meter distance from the X-ray tube's focal spot, using the X-ray spectrum simulation programme SpekCalc [117]. The set-up used for the measurements is shown in Figure 6.7. A micro-focus tungsten-target X-ray source irradiates the detector, which is mounted on three translational stages that allow for movement in three directions with one micrometer stepping resolution. The detector is positioned such that its centre matches the centre of the X-ray beam at approximately 65 cm from the tube's focal spot. The beam is filtered by a 20 mm thick aluminium plate

[3]International Electrotechnical Commission
[4]Reliability and Quality Assurance 5
[5]Kilo-volts peak, the highest kilo-voltage used in producing a radiograph.

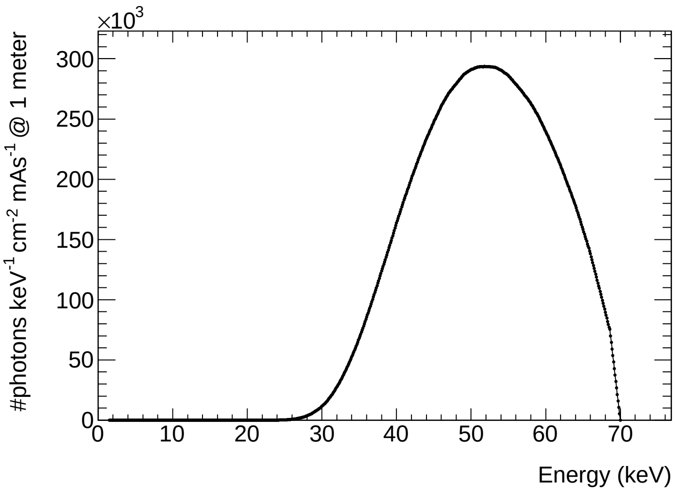

Figure 6.6: Simulated X-ray spectrum
A simulation of the RQA-5 spectrum at one meter distance from a tungsten-target tube operating at 70 kVp. The beam angle corresponds to that of the X-ray source used for the measurement.

and collimated by two 2 mm thick lead shielding stages. One stage is right under the aluminium filter to absorb Compton scattered photons from the aluminium. The other, a square tube of 18 cm in height and on the top side surrounded by lead covering the set-up's cross-sectional area, is placed right above the detector. This shielding minimises the detection of photons that are scattered off the set-up's mechanics. Just enough space is left to place an edge test device in the beam right above the detector for the measurement of the modulation transfer function (see Section 6.3.4).
The entire set-up is housed in a lead-lined cabinet. Its size makes that set-up geometry is somewhat different from that defined by the IEC 62220-1 standard. Especially the detector's distance from the tube's focal spot (should be 150 cm) as well as the position of the two shielding stages do not agree with the standard. However, the most important requirements are met: (i) the detector is placed as far as possible from the X-ray tube's focal spot and (ii) its centre matches the beam centre. In this way, the source-blurring effect of the aluminium filter is minimised and the requirement of detecting only photons that are perpendicularly incident on the detector is met as good as possible.

Detector operational settings

Given an input spectrum, there are two ways to influence the observed amount of charge sharing: by changing the bias voltage or adjusting the threshold level of the discriminator. As discussed in Appendix C, the bias voltage determines the amount of lateral diffusion. The threshold level of the discriminator determines which part of the charge cloud is detected. Effectively, it cuts off the sparse outer parts of the diffused charge carrier distribution. In other words, the apparent size of the charge cloud can be tuned by adjusting the threshold level.

To study the influence of possible charge sharing on the imaging performance, the detectors are operated at three different bias voltages and at three different threshold levels of the discriminator: at the noise floor, at 20 keV and at 35 keV. The latter threshold setting is exactly half the maximum energy of the RQA-5 input spectrum, which ensures no double counting due to charge sharing.

Threshold level For the purpose of adjusting the effective pixel size and therewith the amount of observed charge sharing, the global threshold DAC of each detector is calibrated with respect to the energy of incoming photons.
For ten different settings of the tube's peak voltage, Figure 6.8(a) shows the X-ray spectra measured by the cadmium telluride detector by performing a top-down scan of the threshold DAC (THL). The tail-end of each THL spectrum, which corresponds to maximum energy of the input spectrum, is used as a reference value for the calibration. Subsequently, these values are plotted as a function of the peak energy and fitted by a straight line to obtain the relation between the threshold DAC value and photon energy. The fit is shown in Figure 6.8(b) and demonstrates excellent linearity of the threshold discriminator (coefficient of determination near 1). In a similar manner, the following relations between the energy and threshold DAC value have been determined for each

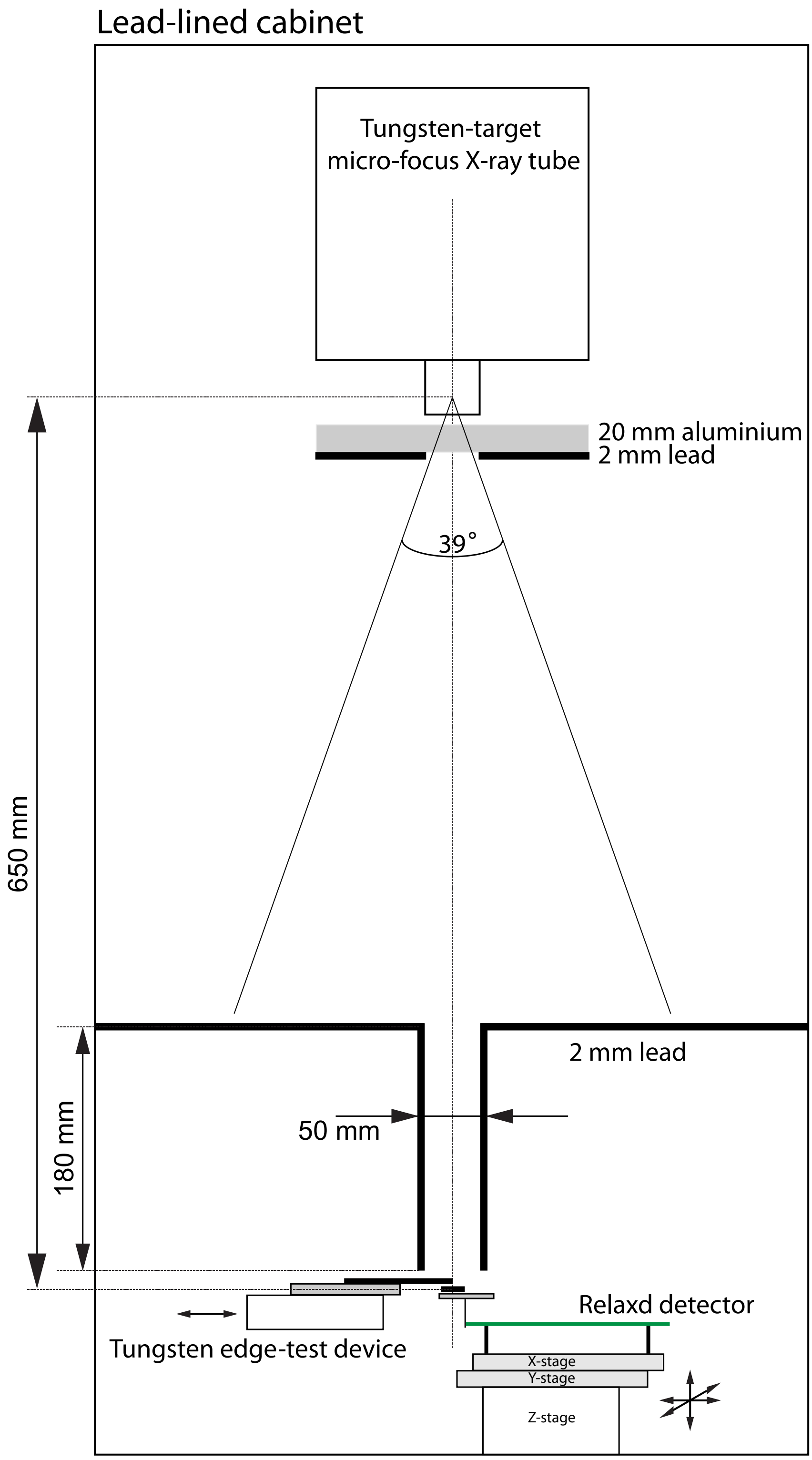

Figure 6.7: X-ray set-up
A schematic representation of the set-up for the measurement of the modulation transfer function. The tungsten edge-test device is removed for measuring the noise power spectrum. The X-ray cabinet limits the maximum distance between detector and tube.

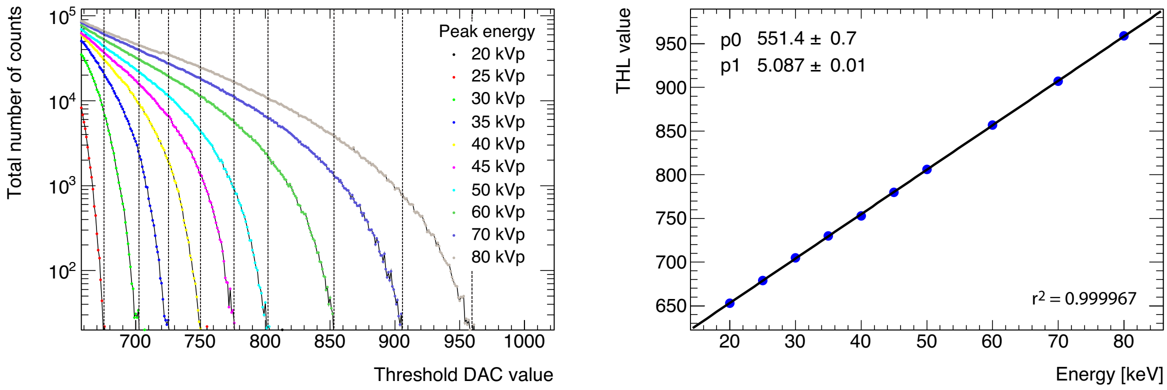

(a) (b)

Figure 6.8: Energy calibration
(a) The integrated energy spectra recorded with the cadmium telluride detector at ten different kVp settings of the X-ray tube. The tail-end of each spectrum is used as a reference value for the threshold calibration. (b) The corresponding calibration curve, which shows threshold DAC values as a function of the maximum energy of each spectrum. Good linearity is observed.

detector:

$$
\begin{aligned}
E &= (-0.0828 \pm 0.0010) \cdot \mathrm{THL} + (36.2 \pm 0.1)\ (\mathrm{keV}) && \text{(Si; hole collecting)}\\
E &= (0.140 \pm 0.003) \cdot \mathrm{THL} - (58.9 \pm 1.0)\ (\mathrm{keV}) && \text{(GaAs; 280 µm thick)}\\
E &= (0.134 \pm 0.001) \cdot \mathrm{THL} - (52.5 \pm 0.3)\ (\mathrm{keV}) && \text{(GaAs; 450 µm thick)}\\
E &= (0.197 \pm 0.001) \cdot \mathrm{THL} - (108.4 \pm 0.1)\ (\mathrm{keV}) && \text{(CdTe)}
\end{aligned}
$$

The errors on the pedestal are due to the discrete nature of the threshold DAC, the threshold dispersion and possible fluctuations caused by beam inhomogeneities.

Bias voltage The bias voltages are chosen such that they result in an equal standard deviation of the lateral diffusion for each sensor. They are calculated using equation C.5 and their values are listed in Table 6.2. The high-Z sensors are biased such that electrons are collected at the pixels. The silicon detector collects holes.

Table 6.2: Bias-voltage settings determined by the maximum standard deviation of the lateral diffusion.

Lateral diffusion (1σ)	**Bias Voltage** (V)			
	Si	*GaAs (280 µm)*	*GaAs (450 µm)*	*CdTe*
25 µm	7.4	6.5	16.9	82.7
15 µm	20.7	18.0	46.9	229.8
10 µm	46.5	40.5	105.6	517.0

6.3.3 Noise performance

Introduction

In this section, the noise performance of the detectors is assessed. In particular, spectra of edge pixels are compared to those of central pixels.
Image noise is caused by fluctuations of the photon flux and by noise introduced by the detector. Photon noise is random, whereas detector noise can be both stochastic and non-stochastic. Sources of stochastic detector noise are leakage current in the sensor as well as thermal noise in the amplifier circuits of the read-out. Non-stochastic noise can be both fluctuating and constant over time, the latter of which is commonly known as fixed-pattern noise.
Both sensor and read-out chip can contribute to fixed-pattern noise. The read-out chip may introduce fixed-pattern noise due to transistor mismatch caused by the CMOS production process. This mismatch translates into a variation of the effective threshold energy between pixels. The threshold spread for Timepix chips is approximately 35 electrons r.m.s. after equalisation of the individual pixel pulse height discriminators.
The sensor may introduce fixed-pattern noise due to imperfections of the sensor material. The inhomogeneities translate into non-uniformities of the electric field distribution and may therefore lead to local variations in both leakage current and charge collection efficiency. These local response variations as well as possible residual fluctuations in the electronics can be suppressed by applying a so called flat-field correction. This technique calibrates the response of the individual pixels with respect to the mean response over the entire detector area by taking a large number of images under flood-field conditions, i.e. homogeneous irradiation. Subsequently, the response of each individual pixel is normalised to the mean count rate of the average of the flood-field images. By applying such a correction, fixed-pattern noise can be removed. However, the effectiveness of this procedure depends largely on the count-rate distribution of the uncorrected image and on the number of images used to create the correction image. By dividing the raw data by the highly averaged flat-field image, fixed-pattern noise is reduced. Stochastic noise in areas of lower response is amplified, however. Time-varying non-stochastic noise will not be corrected either.

Count-rate density

Figure 6.9 shows the response of each of the detectors to flood-field irradiation. The silicon detector shows a homogeneous response over the entire pixel matrix, whereas both the gallium arsenide sensors show anomalous count rates at the edge. To a lesser extent, the same effect is observed at the edge of the cadmium telluride sensor pieces. In addition, the high-Z sensors show a structured response. Non-uniformities are most probably caused by crystal inhomogeneities introduced during growth.

In Figure 6.10, the mean count-rate density[6] is plotted as a function of row number for all four detectors at the threshold settings and bias voltages as given in Section 6.3.2 (except for the silicon detector, for which only the 48-V data are shown). The data points represent the mean of 200 centre pixels of each row, i.e. from column 29 to column 228, in the case of the silicon and gallium arsenide detectors. For the cadmium telluride detector, all pixels of a row except the edge pixels were used, i.e. 3x36 − 3x2 = 102 pixels. The values representing the response of the outermost pixel row of the slim-edge sensors are divided by a constant factor to compensate for the larger area of those pixels (see Figures 6.1(a) and 6.2(a)). This factor, 2.3 for the gallium arsenide sensors and 1.3 for cadmium telluride sensors, represents the estimated effective volume of one non-outer pixel plus half the additional volume at the edge, which is based on a simulation of the outer field lines from the back electrode to the outermost pixel.

As expected, the plots show lower count-rate densities at higher threshold levels, since low-energy photons may not be counted as they deposit too little charge to induce a signal that crosses the threshold. Moreover, the count rate increases as the bias voltage is increased, except for the lowest threshold setting. Those data show lower count rates at higher bias voltages. In agreement with the values of Table D.1, the count-rate density could increase due to double counting as a result of charge sharing due to diffusion. At higher voltages, spread due to diffusion is smaller and the number of double counts is less. At high threshold settings, the charge collection may be incomplete for low bias voltages and hence count rates are higher for higher bias voltages.

In agreement with the absorption efficiency and thickness of the various detectors, the centre-pixel response is highest for the cadmium-telluride detector and lowest for the silicon detector.

Remarkably, the outermost pixels of the gallium arsenide detectors show a lower response, whereas the mean count-rate density of the second outer ones is higher. A possible explanation for this is a field deformation in the edge region that causes, in a similar manner as for active edges, a decrease of effective volume of the physically larger outermost pixels and inherently translates into an increase of that of the second outer ones. This may be caused by crystalline imperfections of the edge region as well as possibly trapped surface charges, which can form a conductive area at the edge. Subsequently, this area could get biased through the back electrode and hence could locally distort the electric field at the edge.

[6] The count-rate density represents the number of hits per second per mm^2.

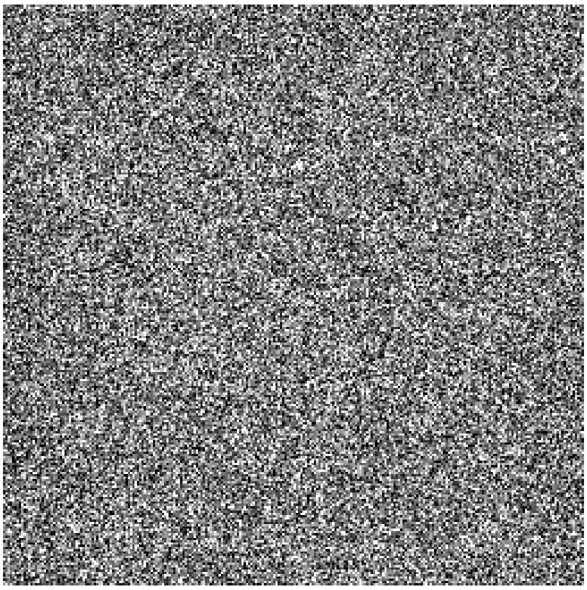

(a) Silicon

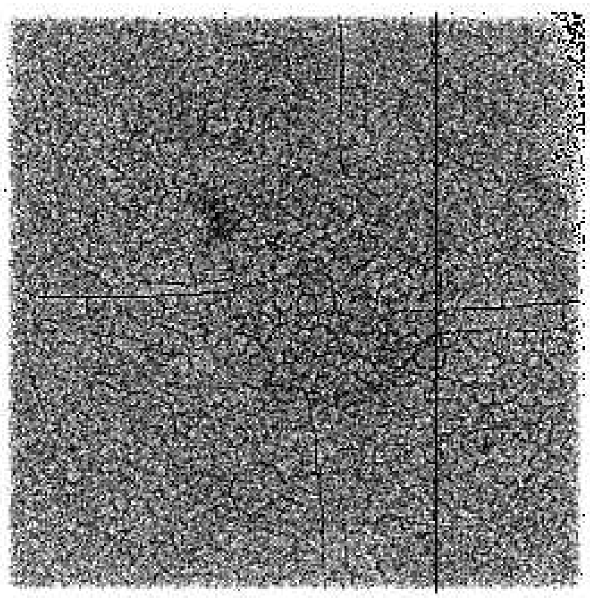

(b) GaAs, 280 µm

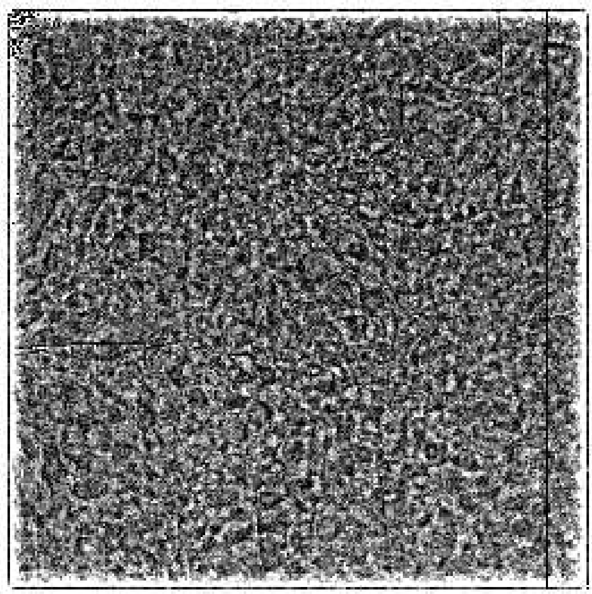

(c) GaAs, 450 µm

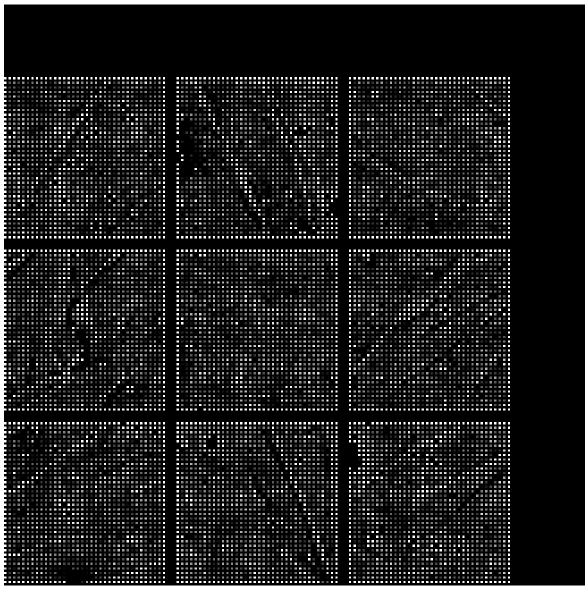

(d) CdTe

Figure 6.9: Flood-field images
Flood-field images taken with each of the detectors. The threshold level is set at 20 keV, the acquisition time is 5 seconds and the bias voltage corresponds to that of Table 6.2 for a σ_{diff} of 10 µm.

Table 6.3: The left part shows the mean count-rate density values of centre pixels at the high bias-voltage setting ($\sigma_{\text{diff}} = 10$ µm). The right part shows the theoretical absorption efficiencies of the sensors for both 40 keV and 50 keV photons. The numbers between the parentheses represent the values as a fraction of that of the cadmium telluride detector.

Sensor	**Count-rate density**			**Absorption efficiency**	
	Noise floor	*20 keV*	*35 keV*	*50 keV*	*40 keV*
Si	1790 (0.033)	589 (0.022)	230 (0.019)	0.017 (0.017)	0.033 (0.033)
GaAs (280 µm)	22640 (0.42)	9642 (0.36)	4128 (0.35)	0.34 (0.35)	0.54 (0.54)
GaAs (450 µm)	33916 (0.63)	17497 (0.65)	9660 (0.82)	0.49 (0.50)	0.71 (0.71)
CdTe	53930 (1)	26762 (1)	11842 (1)	0.98 (1)	1 (1)

Table 6.3 compares the count-rate densities of the centre pixels at the high bias-voltage setting to the detectors' theoretical absorption efficiencies [6] of both 50 keV and 40 keV X-ray photons. It shows that for high threshold levels, i.e. with minimal occurrence of charge sharing, the count-rate densities follow the values of the absorbed fraction of photons, except for the 450 µm thick gallium arsenide detector.

Temporal fluctuations

Figure 6.11 shows the coefficient of variation of the spatially averaged response as a function of pixel row. The coefficient of variation is the r.m.s. of a distribution divided by its mean. Hence, it parameterises the fluctuations as a fraction of the signal, i.e. the noise-to-signal ratio.

All plots show that the fluctuations are largest for the silicon detector. This is due to the fact that the efficiency with which silicon absorbs X-rays of these energies is rather low (less than 1% for a 50 keV photon and 300 µm thick silicon) . As a consequence, the mean count-rate density is only $\sim$ 1500 counts/s/mm^2, i.e. less than 5 counts/s/pixel, and therefore the r.m.s. on the temporal fluctuations is relatively large.

The coefficient of variation is lowest at the highest count rate, i.e. when the threshold is at the noise floor and the sensor bias is high (see bottom left plot). In the top right plot, i.e. with the threshold set at 35 keV and the sensor operated at a low bias voltage, it is observed that the 280 µm thick gallium arsenide sensor shows rather high coefficient of variation. This is due to the low count-rate density, which is probably caused by the low collection efficiency at the bias voltage of only 6.5 V. No significant difference is observed between the coefficients of variation of the centre pixels and that of edge pixels, except for the 280 µm thick gallium arsenide sensor. It shows an increase towards the centre of

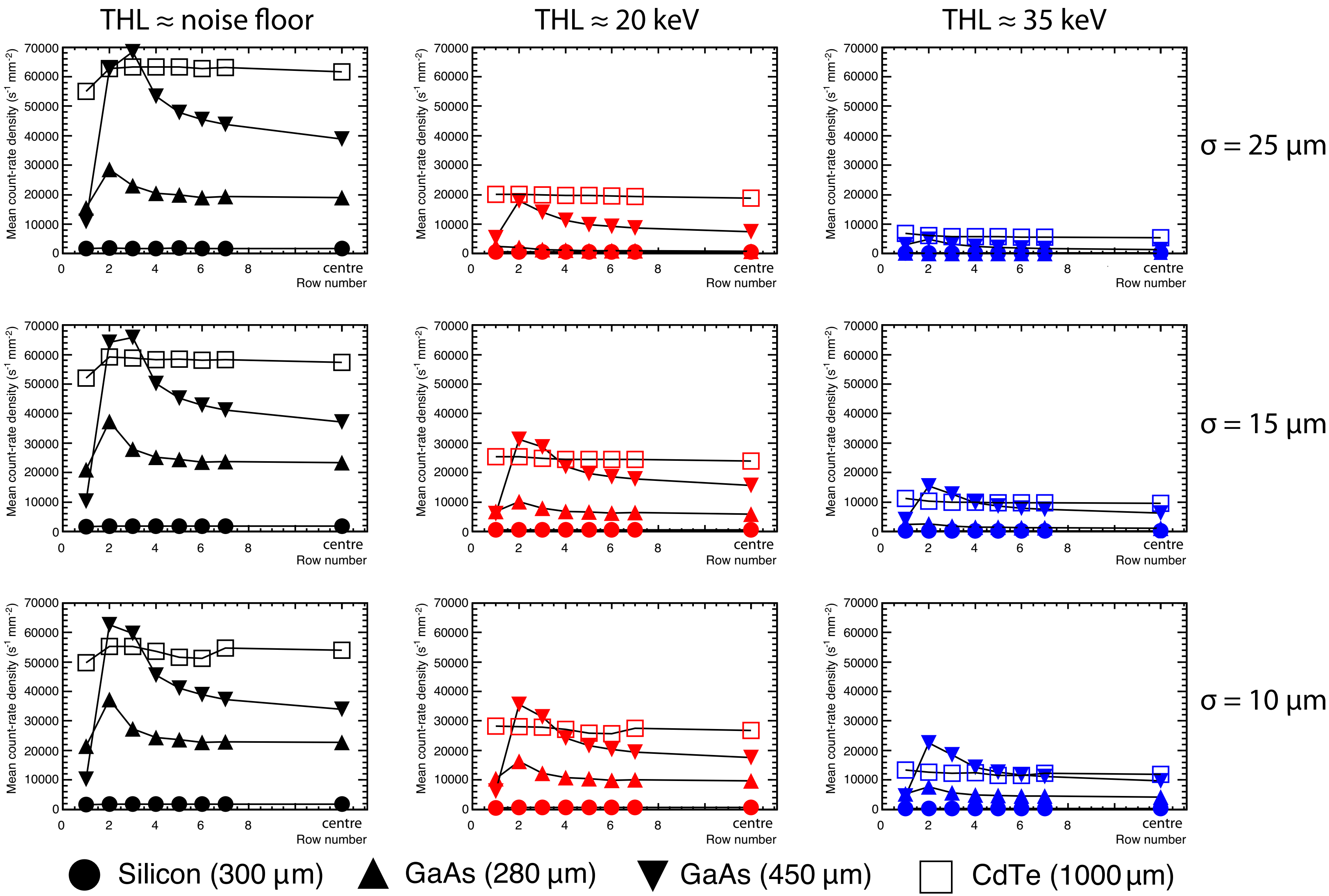

Figure 6.10: Mean count-rate densities
The mean count-rate density of 200 images of the seven outer pixel rows compared to that of the centre row at three different settings of the threshold level (noise floor, 20 keV and 35 keV) and the bias voltage (indicated by the standard deviation of the lateral diffusion (see Table 6.2). The count rates of the outermost pixel row (i.e. row 1) are divided by a constant factor to compensate for the larger area of those pixels.

the matrix at high threshold levels.

Spatial fluctuations

Figure 6.12 shows the coefficient of variation of the spatial fluctuations of the time-averaged response as a function of pixel row. Whereas the silicon detector shows the largest temporal spread, it shows the least spatial variation of the four detectors. Clearly, the homogeneity of the silicon detector is superior to that of both the gallium arsenide and cadmium telluride detectors. Again, the coefficient of variation shows an increasing trend towards high threshold levels and low bias voltages. The 280 µm thick gallium arsenide sensor shows the largest spatial fluctuations, which is due to the fact that it has the lowest count-rate density of the three high-Z detectors. Similar to the temporal fluctuations, there is no significant difference between the coefficient of variation of centre pixels and that of edge pixels. Again, a small increase towards the centre of the matrix is observed for the thinner gallium arsenide sensor at high threshold level and low bias voltages.

Noise power spectra

In this section, the power spectra of the various noise components are studied. Whereas Figures 6.11 and 6.12 only show the total variation of both the temporal and spatial fluctuations, noise power spectra comprise the spatial-frequency components of the noise. Together with the modulation transfer function, it allows for the determination of the noise power relative to signal power per unit frequency interval. A spectral decomposition, however, requires a linear correlation between the photon intensity and count-rate density measured by the detector. Each detector showed excellent response linearity. Results are presented in Appendix D.

To study the power of each noise component as a function of distance from the edge, one-dimensional spectra of rows of pixels are studied in relation to their row number (i.e. to the distance of the pixels from the edge). Again, the middle 200 pixels (102 for the cadmium telluride detector) of each row were used.

As described in Chapter 1, the noise power spectrum can be experimentally obtained by calculating the squared magnitude of the discrete Fourier transform of the signal fluctuations. First, each individual image (i.e. each row of pixels) was de-trended using a de-trending algorithm. This algorithm subtracts either the mean or a best-line fit (i.e. a trend) from the data. In this way, the fluctuations about the trend remain. Pixels with a response of more than 10 standard deviations from the mean of the de-trended image were discarded. Subsequently, the image was normalised to the mean count rate and the pixel area. After that, a FFT algorithm was used to calculate the Fourier image, the square modulus of which was taken to obtain the noise power spectrum. Finally, the ensemble average of 200 noise power spectra (from 200 flood-field images) was calculated to obtain the average normalised noise power spectrum.

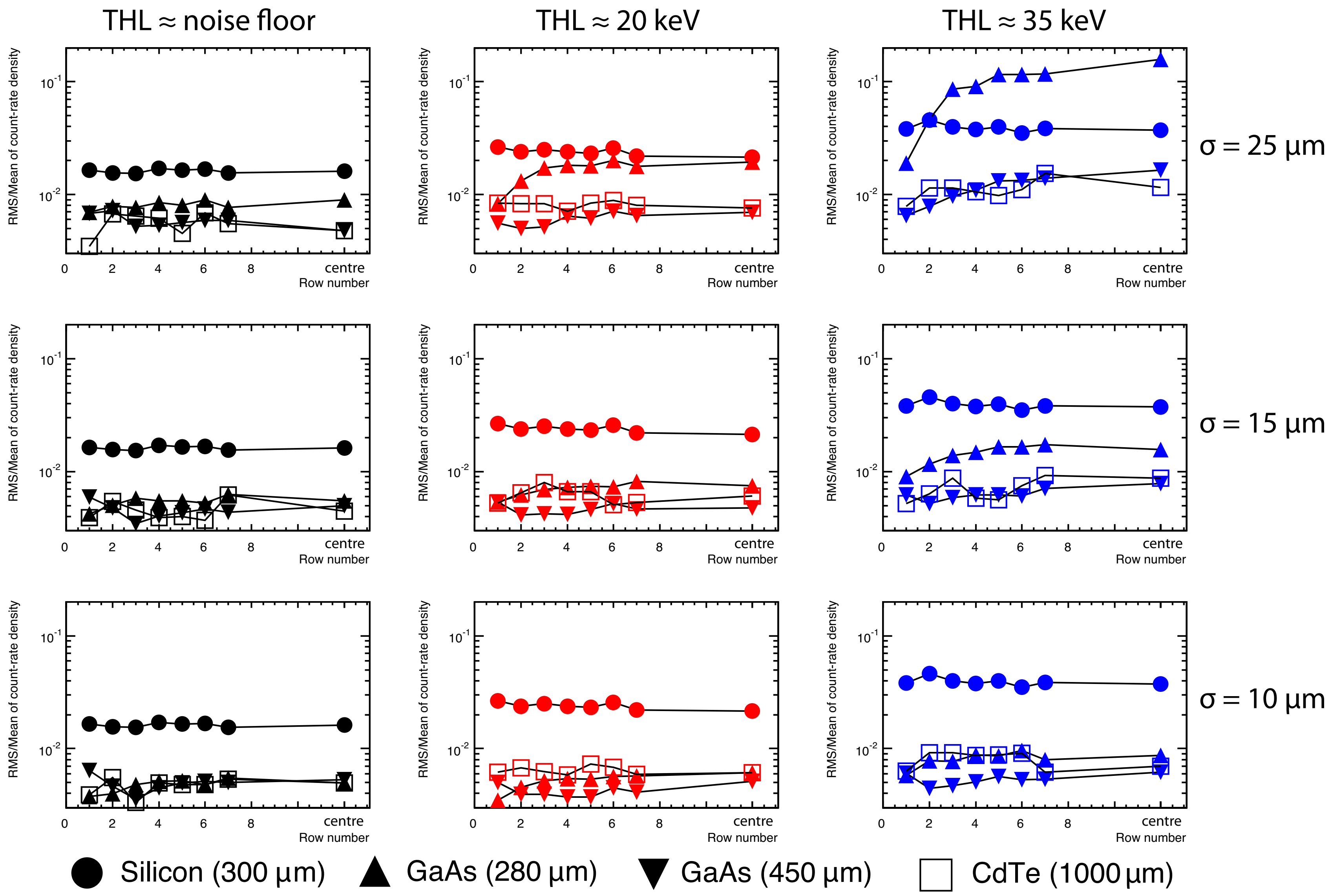

Figure 6.11: Temporal fluctuations
The coefficient of variation of the spatially averaged response (of 200 pixels) as a function of pixel row.

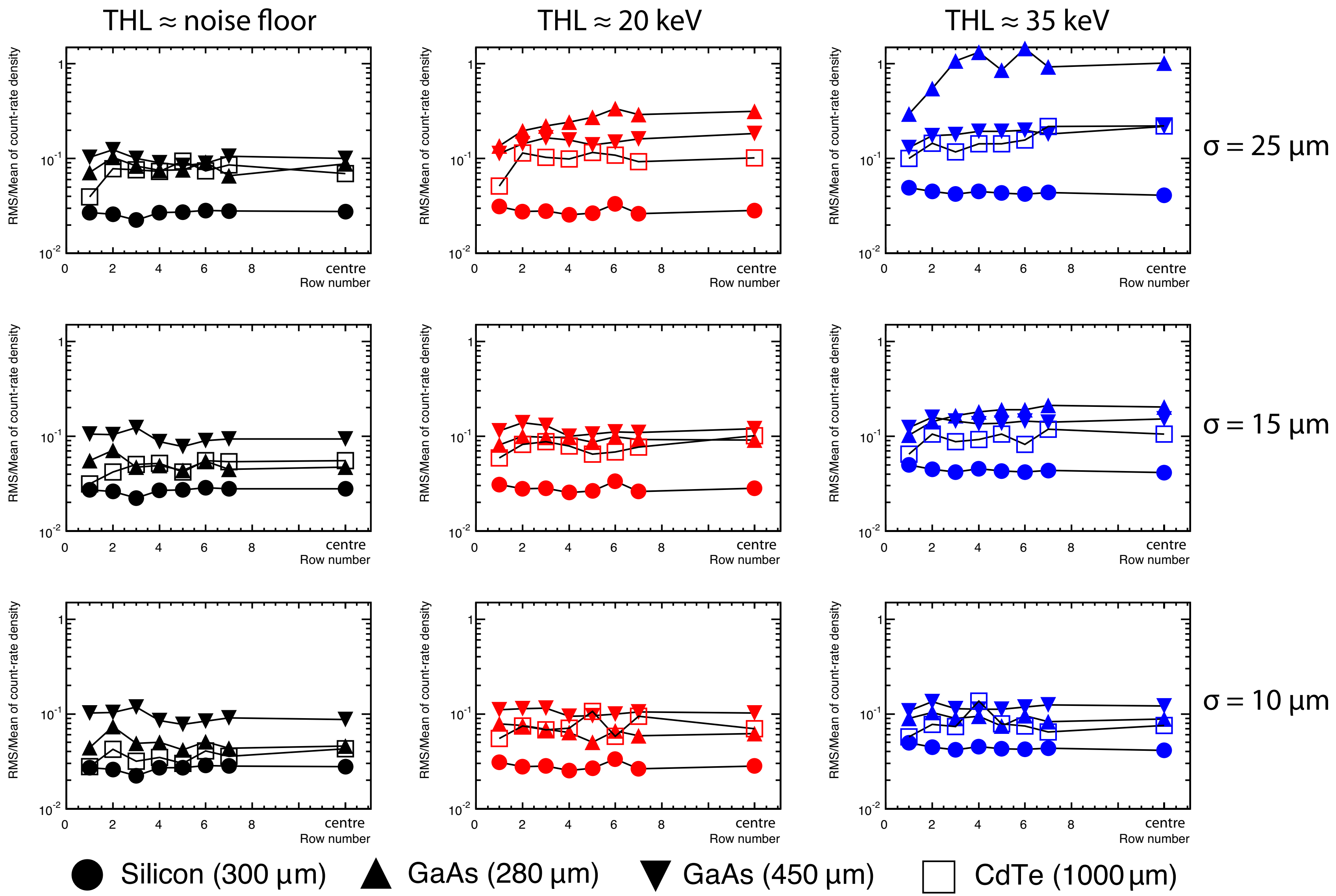

Figure 6.12: Spatial fluctuation
The coefficient of variation of the time-averaged response (of 200 frames) as a function of pixel row.

As described before, image noise contains contributions from various sources and hence the total noise power spectrum is the sum of various components. It can be expressed as:

$$\mathrm{NPS_{tot}} = \mathrm{NPS_{st.\,+\,var.\,non-st.}} + \mathrm{NPS_{f.p.}}\ , \tag{6.2}$$

where $\mathrm{NPS_{tot}}$ is the total noise power spectrum, and $\mathrm{NPS_{st.\,+\,var.\,non-st.}}$ and $\mathrm{NPS_{f.p.}}$ are the power spectra of the stochastic (+ time-varying non-stochastic) noise and fixed-pattern noise, respectively.
To separately analyse the power spectrum of each component, fixed-pattern noise was filtered out by subtracting a highly time-averaged image from the image under study. The averaged image, obtained from 200 images of 5 seconds each, contains almost no contributions of time-varying noise. Hence, the noise power spectrum of the subtracted image contains contributions from all sources except fixed-pattern noise, i.e. from stochastic photon and detector noise as well as time-varying non-stochastic noise.

Figure 6.13 shows for each detector the normalised and averaged 1-D noise power spectra of the various noise components for pixels of the centre row. The spatial frequency is expressed in line pairs per millimeter (lp/mm). The power of the total noise and the various noise components are given in Table 6.4(a). They are expressed by the mean value of the noise power spectra. The value is halved for the cadmium telluride detector, in order to account for the twice as large pixel pitch. Also, the ratio between the power of the fixed-pattern noise and the power of the stochastic and time-varying non-stochastic noise is given.
The power spectra and the values of Table 6.4(a) show that the silicon detector is dominated by stochastic noise, due to its low absorption efficiency and hence low mean response. The main reason for the stochastic-noise dominance, however, is not the low count-rate density, but the low fixed-pattern noise. This due to the excellent homogeneity of the material, which is demonstrated by the flood-field image of Figure 6.9.
The opposite is true for the slim-edge high-Z detectors. Since their absorption efficiency is orders of magnitude higher, they suffer less from stochastic noise than the silicon detector. The fixed-pattern contribution, however, is approximately ten times higher than that of the silicon detector. This can be ascribed to inhomogeneities in the sensor material, which are common for compound semiconductor crystals (see Figure 6.9 on page 128). Inhomogeneities do not explain the spikes in the spectra, though.

As discussed, fixed-pattern noise can be theoretically removed by applying a flat-field correction. Figure 6.14 shows the noise power spectra obtained in the same way, but now after flat-field correction. The power of each component, expressed by the mean value of the spectra, is given in Table 6.4(b). It clearly shows that fixed-pattern noise is drastically reduced and the noise power spectra become dominated by stochastic noise.

Threshold and voltage dependence Figure 6.15 shows the noise components for the centre row of the 450 µm thick gallium arsenide detector at different threshold levels of the discriminator before and after applying a flat-field correction. It shows that stochastic noise is increased by raising the threshold level. In addition, a low-pass filtering effect is

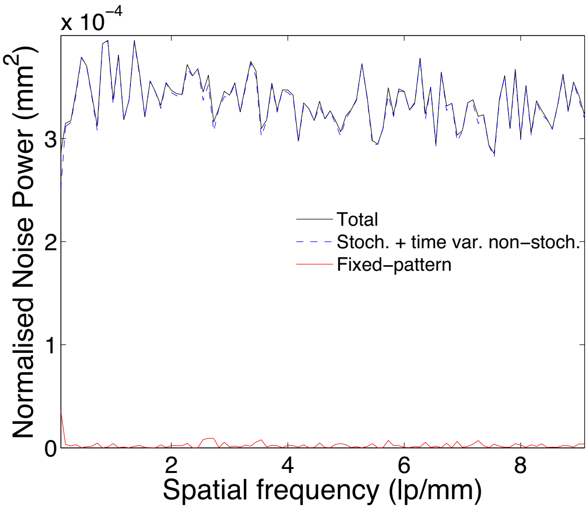

(a) Silicon

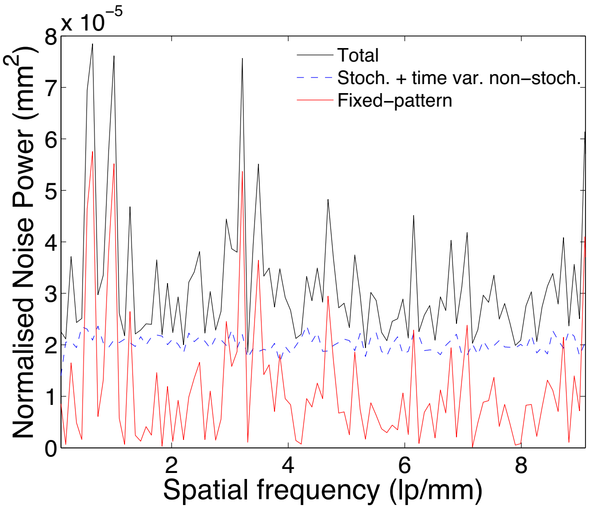

(b) GaAs, 280 µm

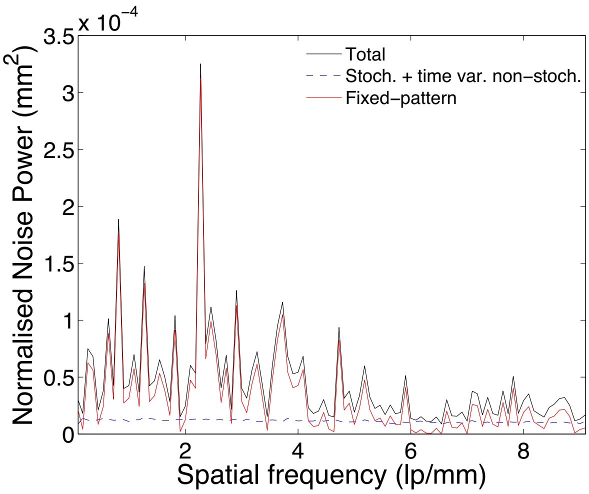

(c) GaAs, 450 µm

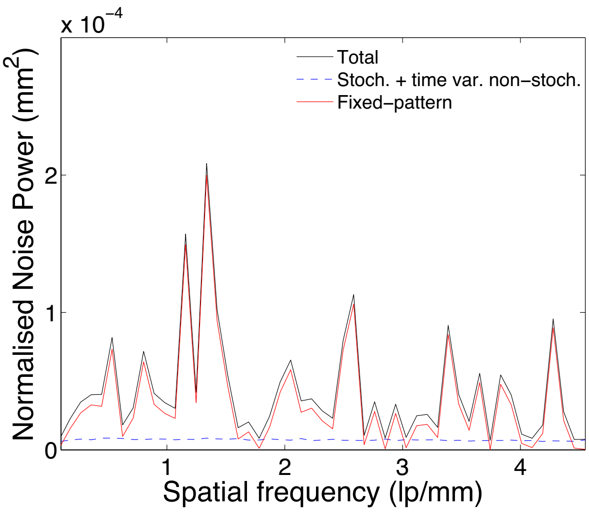

(d) CdTe

Figure 6.13: Noise components
Power spectra of the various noise components for the centre row of each of the sensors. The threshold level is at $\sim$ 20 keV and the bias voltage corresponds to a standard deviation of the lateral diffusion of 10 µm. Whereas silicon shows a stochastic-noise dominated spectrum, fixed-pattern noise prevails in the high-Z sensor spectra.

Table 6.4: The average total noise power and that of the individual components expressed by the mean value of the noise power spectra. The values for the cadmium telluride detector are halved, due to a twice as low Nyquist frequency. Also, the ratio between the power of the fixed-pattern noise and the stochastic (+ time-varying non-stochastic) noise is given. Table (a) lists the mean values of the raw power spectra of Figure 6.13. Table (b) gives the mean values of the spectra after flat-field correction, as shown in Figure 6.14.

(a) Raw

Sensor	**Total** (mm^2)	**Stochastic + var. non-st.** (mm^2)	**Fixed-pattern** (mm^2)	$\frac{\textbf{Fixed-pattern}}{\textbf{Stoch. + var. non-st.}}$
Silicon	$3.35{\cdot}10^{-4}$	$3.33{\cdot}10^{-4}$	$2.48{\cdot}10^{-6}$	$7.44{\cdot}10^{-3}$
GaAs (280 µm)	$3.12{\cdot}10^{-5}$	$2.01{\cdot}10^{-5}$	$1.12{\cdot}10^{-5}$	0.556
GaAs (450 µm)	$4.40{\cdot}10^{-5}$	$1.13{\cdot}10^{-5}$	$3.27{\cdot}10^{-5}$	2.89
CdTe	$2.12{\cdot}10^{-5}$	$3.62{\cdot}10^{-6}$	$1.76{\cdot}10^{-5}$	2.43

(b) After flat-field correction

Sensor	**Total** (mm^2)	**Stochastic + var. non-st.** (mm^2)	**Fixed-pattern** (mm^2)	$\frac{\textbf{Fixed-pattern}}{\textbf{Stoch. + var. non-st.}}$
Silicon	$3.33{\cdot}10^{-4}$	$3.33{\cdot}10^{-4}$	$<< 10^{-9}$	$<< 10^{-3}$
GaAs (280 µm)	$2.01{\cdot}10^{-5}$	$2.01{\cdot}10^{-5}$		
GaAs (450 µm)	$1.15{\cdot}10^{-5}$	$1.15{\cdot}10^{-5}$		
CdTe	$3.63{\cdot}10^{-6}$	$3.63{\cdot}10^{-6}$		

observed at low threshold levels. This is due to the fact that the effective pixel area is larger than the physical pixel area at those threshold levels. As a consequence, a fraction of the pixels records double counts and hence the fluctuations along a pixel row become correlated, which can be interpreted as if the inter-pixel variations along the row are smoothened. This correlation translates into an enhancement of the noise power spectrum at low spatial frequencies [118].

Figure 6.16 shows the power spectra of the various noise components for the centre row of the 450 µm thick gallium arsenide detector at different bias voltages. The left plot represents a threshold level that corresponds to the noise floor and in the right plot the threshold is adjusted to 35 keV. It is observed that at high threshold levels the noise reduces as the bias voltage increases. At high bias voltages, the charge collection effi-

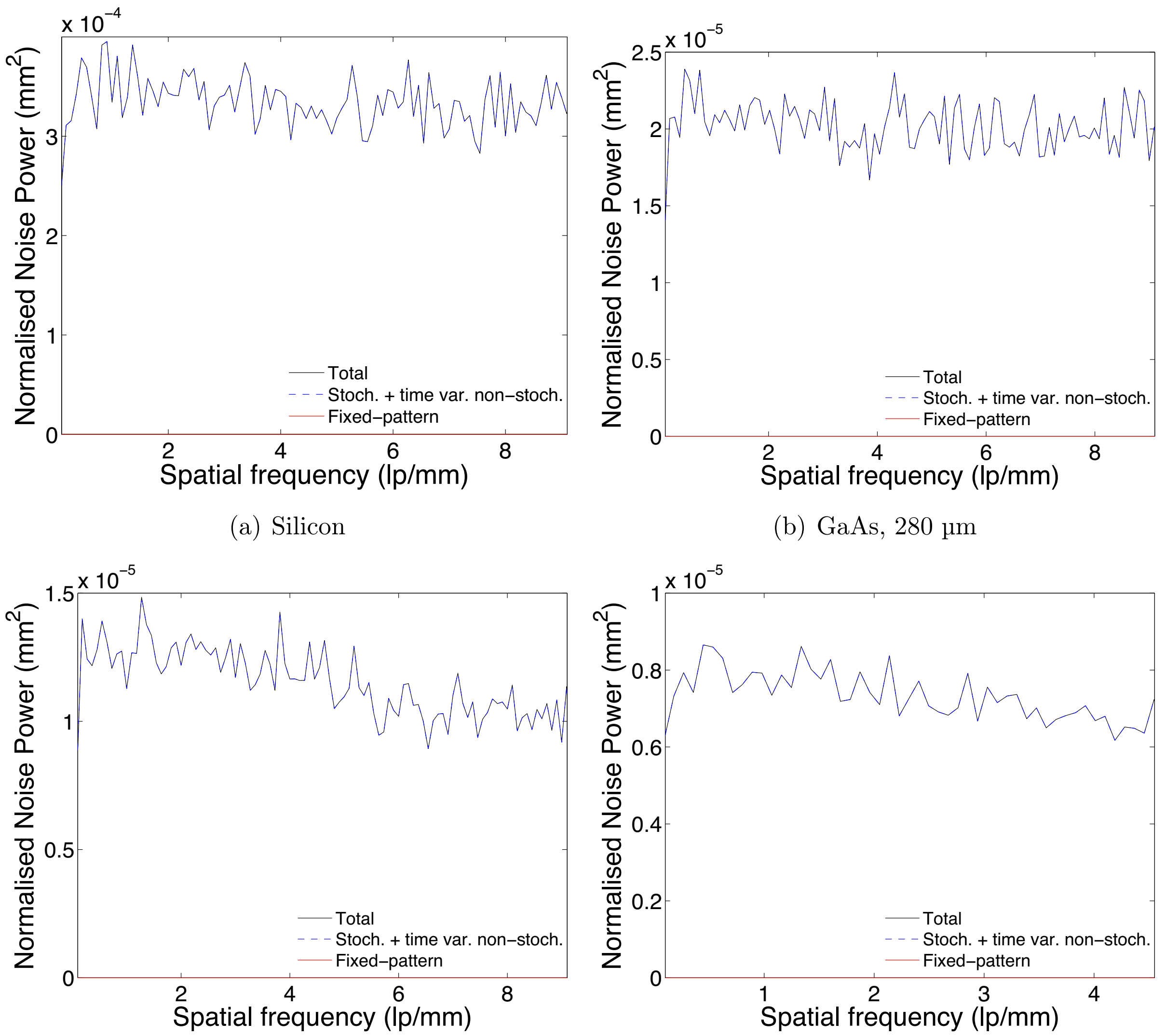

(a) Silicon

(b) GaAs, 280 µm

(c) GaAs, 450 µm

(d) CdTe

Figure 6.14: Noise components after flat-field correction
Noise power spectra of the various noise components for the centre row of each of the sensors after flat-field correction. Fixed-pattern noise is clearly reduced.

ciency is increased, which results in higher count rates and hence lower stochastic noise. Fixed-pattern noise is reduced as well, which indicates that trapping is reduced at high bias voltages.

Row dependence Up to this point, the noise power spectra of pixels of the centre row were analysed, which showed that the high-Z detectors are dominated by fixed-pattern

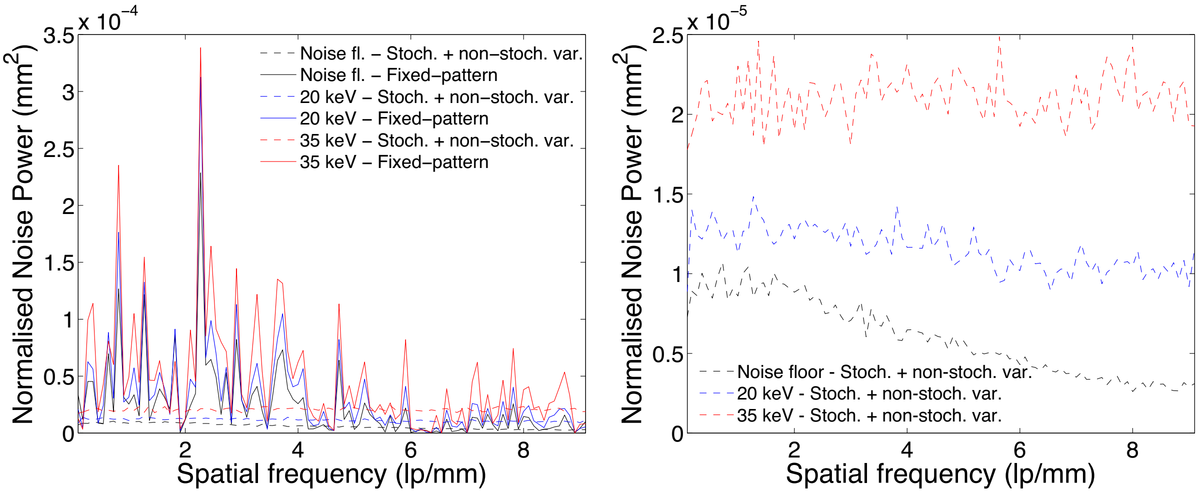

(a) Raw (b) Flat-fielded

Figure 6.15: Threshold level dependence
(a) Power spectra of the various noise components of the centre row at different threshold levels, obtained with the 450 µm thick gallium arsenide detector at 105.6 V (i.e. at σ_{diff}=10 µm). (b) The spectra after flat fielding.

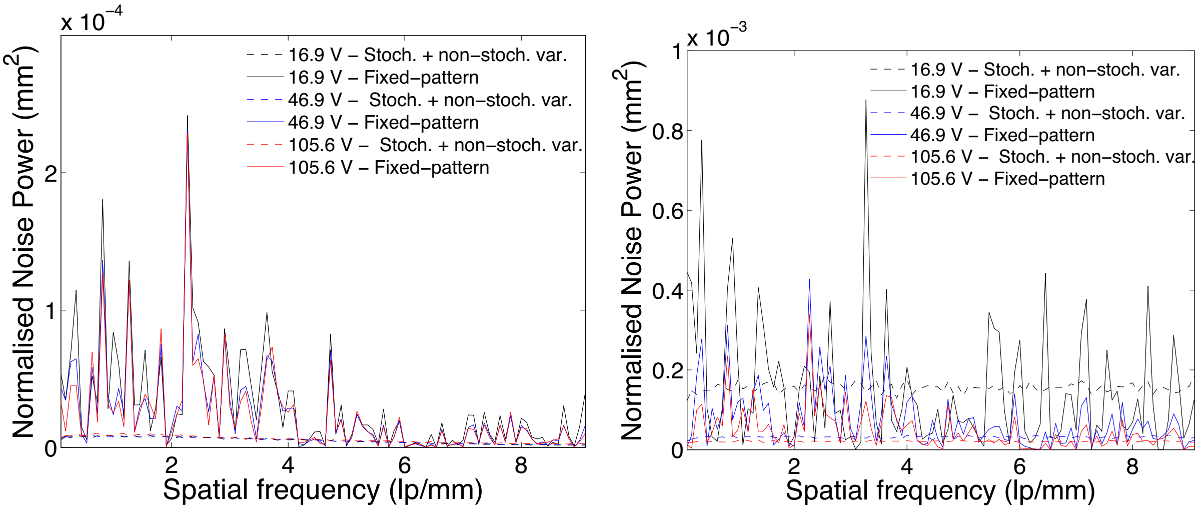

(a) THL at noise floor (b) THL at 35 keV

Figure 6.16: Voltage dependence
Power spectra of various noise components of the centre row at three different bias voltages, obtained with the 450 µm thick gallium arsenide detector. (a) The threshold level set at the noise floor. (b) The threshold set at 35 keV, which shows that at high threshold levels the noise reduces as the bias voltage increases.

noise, whereas the silicon detector is stochastic-noise dominated. In addition, the sensor's edges may affect the noise performance of edge pixels. Crystalline imperfections in those regions may translate into fixed-pattern noise and surface currents may increase stochastic noise. To study this, the contributions to the noise power spectra are analysed as a function of distance from the edge.

The spectra can be found in Appendix E. For each of the rows, Table 6.5 lists the noise power (NP) of the individual components normalised to that of the centre row. Table 6.5(a) shows that the power of the fixed-pattern noise of the silicon detector is by approximation row independent, while the values for the high-Z detectors increase as the distance to edge decreases. The outermost pixels of the gallium arsenide detectors show a three times higher fixed-pattern noise power than the centre pixels. For the cadmium telluride detector, the edge pixels show an increase of approximately 70%. In accordance with the visual inspection of the edges (see Figure 6.2(a) on page 115), this indicates that the cadmium telluride detector suffers least from the slim-edge process, while the ratio between the edge distance and sensor thickness is the largest of the three.

Table 6.5(b) gives the power of the stochastic and time-varying non-stochastic noise for each row. In addition, the values of the reciprocal of the square root of the mean count-rate density are given per row (which are also normalised to that of the centre row). The noise-power values for the silicon detector show close agreement with the measured count-rate densities. The noise powers and the count-rate densities of the high-Z detectors show a similar trend, but worse agreement with each other than the silicon detector does. In accordance with the count-rate density values of Figure 6.10, the stochastic-noise power of the outermost row of the 450 µm thick gallium arsenide detector is higher and that of the second outer one lower than the noise power of the centre row. Remarkably, the value for the second outer row of the cadmium telluride detector is much higher than what is expected from the count-rate data. It could be that its power spectrum contains contributions from hot pixels.

Table 6.5: The noise power (NP) of the individual noise components for pixels of the three outer rows normalised to those of the centre row. Table (a) lists the values for the fixed-pattern noise (see Figure E.1), whereas Table (b) represents those of the stochastic and time-varying non-stochastic noise (see Figure E.2). The values between the parentheses represent the reciprocal of the square root of the mean count-rate density of each row normalised to that of the centre row.

(a) Fixed-pattern noise

Sensor	$\frac{\mathbf{NP_{row\,1}}}{\mathbf{NP_{centre\,row}}}$	$\frac{\mathbf{NP_{row\,2}}}{\mathbf{NP_{centre\,row}}}$	$\frac{\mathbf{NP_{row\,3}}}{\mathbf{NP_{centre\,row}}}$
Silicon	1.03	0.965	0.883
GaAs (280 µm)	3.42	1.51	1.04
GaAs (450 µm)	2.57	1.41	1.26
CdTe	1.71	1.29	1.10

(b) Stochastic + time-varying non-stochastic noise.

Sensor	$\frac{\mathbf{NP_{row\,1}}}{\mathbf{NP_{centre\,row}}}$	$\frac{\mathbf{NP_{row\,2}}}{\mathbf{NP_{centre\,row}}}$	$\frac{\mathbf{NP_{row\,3}}}{\mathbf{NP_{centre\,row}}}$
Silicon	1.08 (1.04)	0.998 (1.00)	1.02 (1.00)
GaAs (280 µm)	0.925 (0.96)	0.602 (0.77)	0.791 (0.89)
GaAs (450 µm)	2.82 (1.67)	0.490 (0.70)	0.556 (0.75)
CdTe	0.947 (0.97)	1.55 (0.98)	1.01 (0.98)

6.3.4 Modulation transfer function

Introduction

In this section, the modulation transfer function (MTF) of the detectors is determined. It parameterises signal transfer as a function of spatial frequency and therefore describes how well object details can be detected. Here, it is obtained by measuring the 1-D equivalent of the point spread function: the line spread function (LSF).
Figure 6.17 shows how the line spread function is obtained using the slanted-edge method. The detector is partially covered by a so called edge-test device. This device consists of a 1 mm thick tungsten plate which is embedded in 3 mm of lead. The tungsten plate has a very sharp edge (scragginess of ± 2 µm) and is positioned just above the detector at a shallow angle of approximately two degrees with respect to the pixel matrix. An image frame in which part of the 450 µm thick gallium arsenide sensor is covered by the edge-test device is shown in part (b). The detector was moved slightly off-centre to position the edge in the centre of the X-ray beam without touching the wire bonds (which are at the top of the frame). The shallow angle causes the edge of the shadow to be situated at different distances from the pixel border. In other words, the fraction of pixel area covered by the edge slowly increases along the edge, as a result of which an oversampling of the pixel is realised. By reconstructing the position of the edge, the pixel response can be plotted as a function of the pixel's position relative to the edge. This results in the edge spread function (ESF) of the detector. Figure 6.17(d) shows the count-rate data of the gallium arsenide detector as a function of reconstructed distance from the edge, which are fitted to obtain the edge spread function. From this, the line spread function is obtained by differentiation.

MTF reconstruction

An important part of deriving the modulation transfer function from this measurement is to correctly reconstruct the position of the edge.
First, a flat-field correction was applied to compensate for inhomogeneities of the beam as well as sensitivity fluctuations between the individual pixels. The correction map was derived from the average of 200 flood-field images taken with an acquisition time of 5 s. This map was applied to the ensemble average of 200 images of 5 s each, but now with the edge test-device covering part of the detector. To avoid noisy pixels to negatively affect the edge image, a median filtering algorithm was applied.
Subsequently, the edge of the shadow was reconstructed by interpolating the data in the direction of the pixel columns (i.e. almost perpendicular to the edge) and by finding the y-position in each column (x-position) that matched best the average of the maximum and minimum count rate, i.e. the value that corresponds to the intensity value at the inflection point of the edge response profile.
Finally, a line fit was performed, the parameters of which were used to calculate the shortest distance of the hits to the edge. This information was used to plot the interpolated count-rate data as a function of this distance.

Each plot was fitted by the sum of two error functions [119, 120] to obtain the edge spread function:

$$\mathrm{ESF} = a_0 - \frac{a_1}{2}\mathrm{erf}\left(\frac{x_0 - x}{\sigma_1\sqrt{2}}\right) - \frac{a_2}{2}\mathrm{erf}\left(\frac{x_0 - x}{\sigma_2\sqrt{2}}\right), \tag{6.3}$$

where a_0, a_1 and a_2 are normalisation constants, σ_1 and σ_2 are the standard deviations of the Gaussians corresponding to the error functions and x_0 is the x-value of the error functions inflection point. It was chosen to use the sum of two error functions instead of just a single error function, to take account of the fact that the profile of the total charge distribution in the sensor is described by a sum of Gaussian functions.
The derivative of the edge spread function was taken to obtain the Gaussian-profiled line spread function (see Figure 6.17(d)). Finally, the pre-sampling modulation transfer function, i.e. the single-sided amplitude of the Fourier spectrum of the line spread function, was obtained by using a discrete Fourier transformation algorithm.

Results

Figure 6.18 shows both the edge spread functions and modulation transfer functions of the 450 µm thick gallium arsenide detector at three different bias voltages with the threshold set at the noise floor and at 35 keV. As expected, it is observed that raising the threshold level translates into a steepening of the edge spread function. As the threshold level increases, the observed charge sharing is reduced because of a reduction of observed part of the charge cloud. Consequently, the modulation transfer functions obtained with the threshold level at 35 keV show higher values for non-zero spatial frequencies than those acquired with the threshold set at the noise floor.
The values of spatial frequency at which the modulation power is halved (i.e. at $1/\sqrt{2}$ times the gain) are listed for each bias voltage in Table 6.6(a). At low threshold levels, the MTF seems to improve as the bias voltage is increased. This can be explained by the fact that lateral diffusion spread is reduced due to shorter collection times at higher strengths of the drift field. At high threshold levels, the modulation transfer function appears to worsen as the bias voltage is increased, while the opposite is observed for the silicon and cadmium telluride detector.

Figure 6.19 shows the modulation transfer functions for each of the detectors with the threshold level at the noise floor and at 35 keV. Again, it is observed that increasing the threshold level improves the modulation transfer function. Besides, the curves show similar signal transfer performance for the silicon and gallium arsenide detectors. For the high threshold setting, the spatial frequency at which the detectors show a decrease in modulation power of a factor of two is close to the resolution of a non-blurred pixel response, which is 9.1 lp/mm for a 55 µm pixel pitch and 4.5 lp/mm for 110 µm pixel pitch. This also explains why the spatial frequency at which the MTF of the cadmium telluride detector equals $1/\sqrt{2}$ is twice as low as for the other detectors.

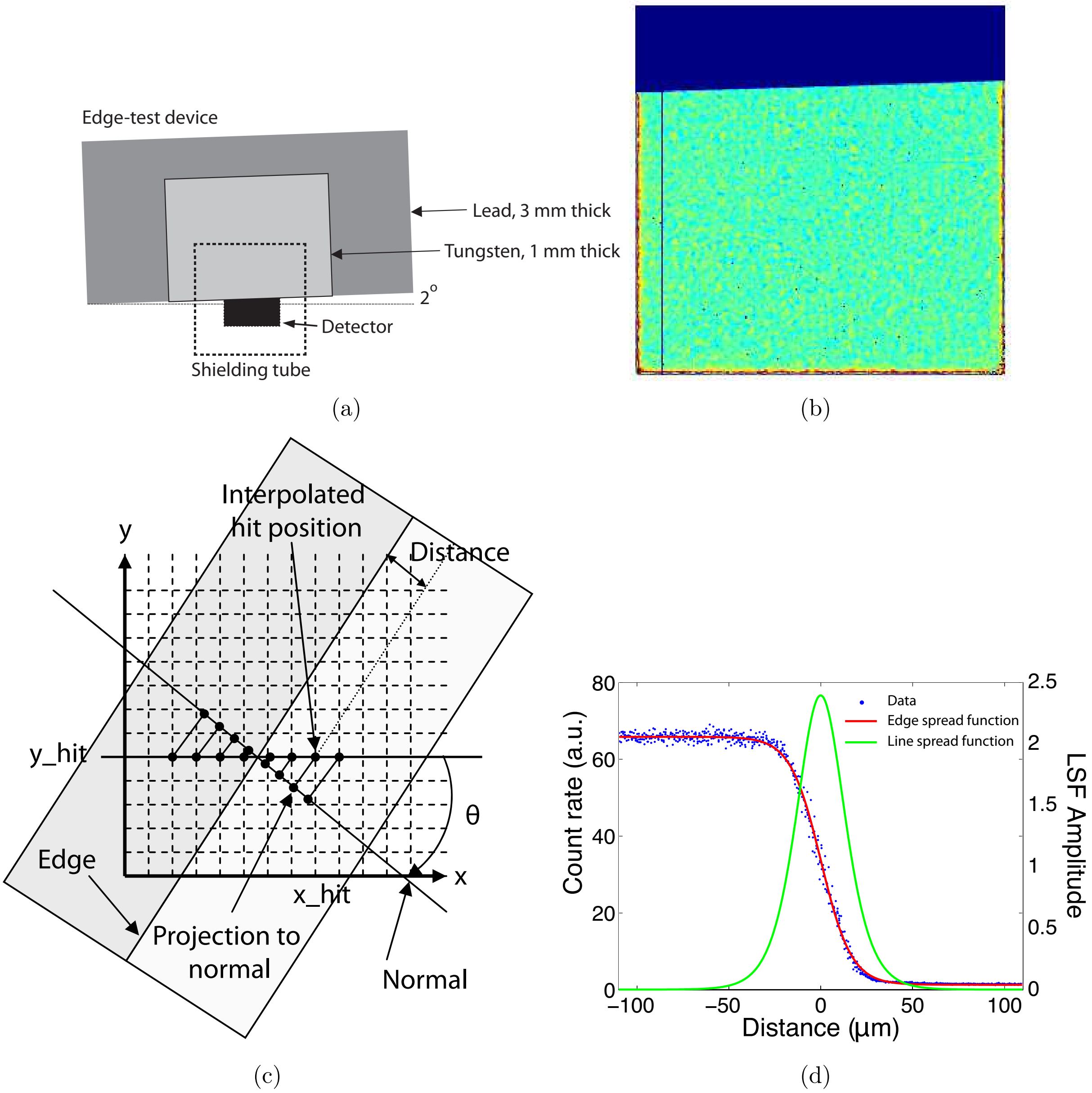

Figure 6.17: Measuring the MTF
(a) A 1 mm thick slab of tungsten is positioned just above the detector at a shallow angle of approximately two degrees with respect to the pixel matrix. (b) A typical shadow image of the edge-test device, obtained by the 450 µm thick gallium arsenide detector. (c) A schematic representation of the reconstruction of the edge spread function. The data are interpolated in the direction perpendicular to the edge in order to calculate the position of the edge. (d) Subsequently, the count-rate information of each data point is plotted as a function of its distance from the edge. This plot is fitted by the sum of two error functions to obtain the ESF, which is finally differentiated to obtain the LSF.

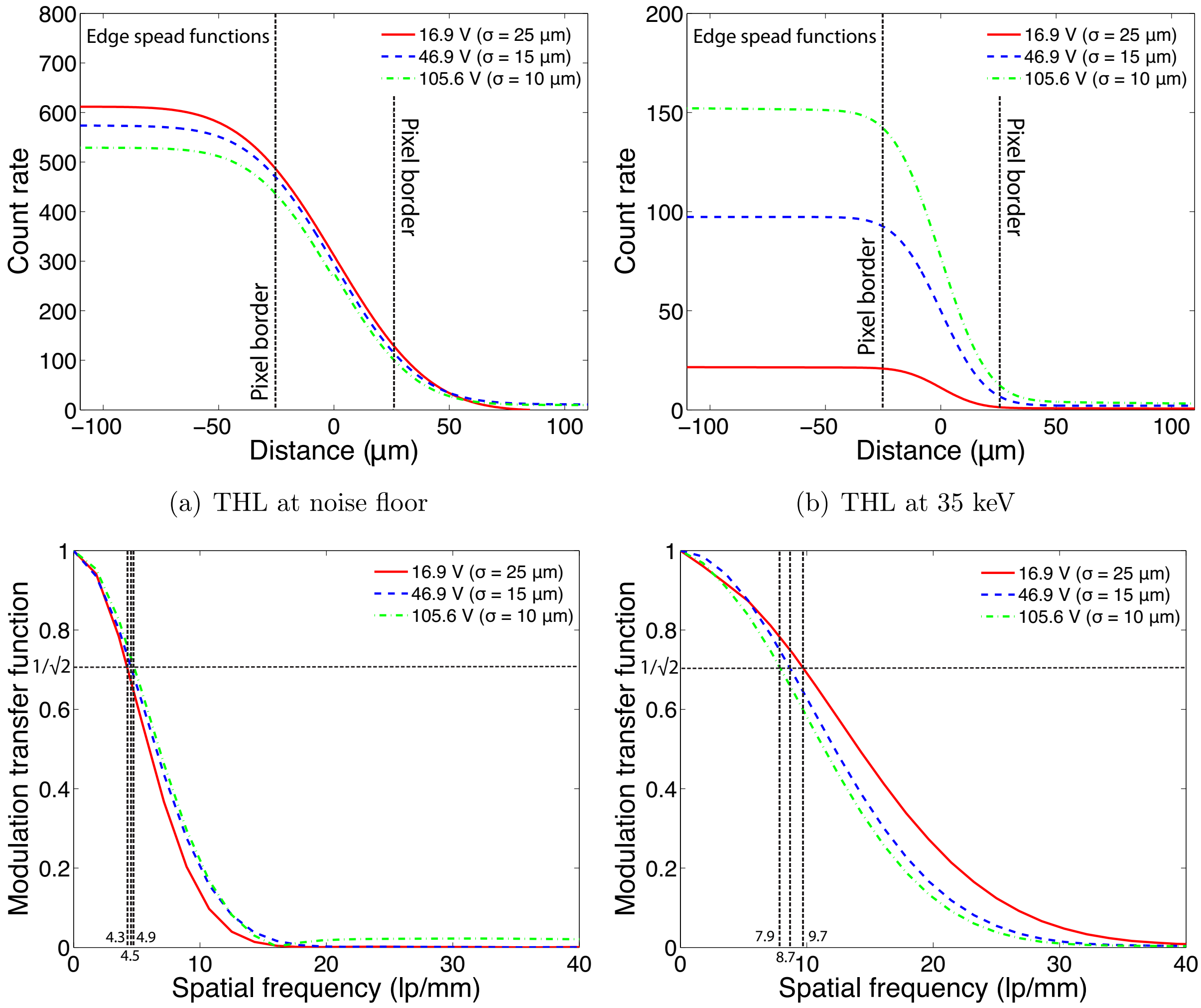

(a) THL at noise floor

(b) THL at 35 keV

(c) THL at noise floor

(d) THL at 35 keV

Figure 6.18: Bias voltage dependence of ESF and MTF
Parts (a) and (b) show the edge spread functions obtained with the 450 µm thick gallium arsenide detector for three different bias voltages with the threshold DAC set at the noise floor and 35 keV. Parts (c) and (d) show the derived modulation transfer functions.

Table 6.6: Spatial frequency at which the MTF=$1/\sqrt{2}$. Table (a) shows the frequency values for the 450 µm gallium arsenide detector as a function of bias voltage at two threshold levels of the discriminator. Table (b) lists the values for each detector at the high bias-voltage setting.

(a)

Bias voltage (V)	**Spatial frequency** (lp/mm)	
	Noise floor	*35 keV*
16.9	4.3	9.7
46.9	4.5	8.7
105.6	4.9	7.9

(b)

Sensor	**Spatial frequency** (lp/mm)	
	Noise floor	*35 keV*
Si	4.9	8.8
GaAs (280 µm)	5.3	9.7
GaAs (450 µm)	4.9	7.9
CdTe	2.3	4.5

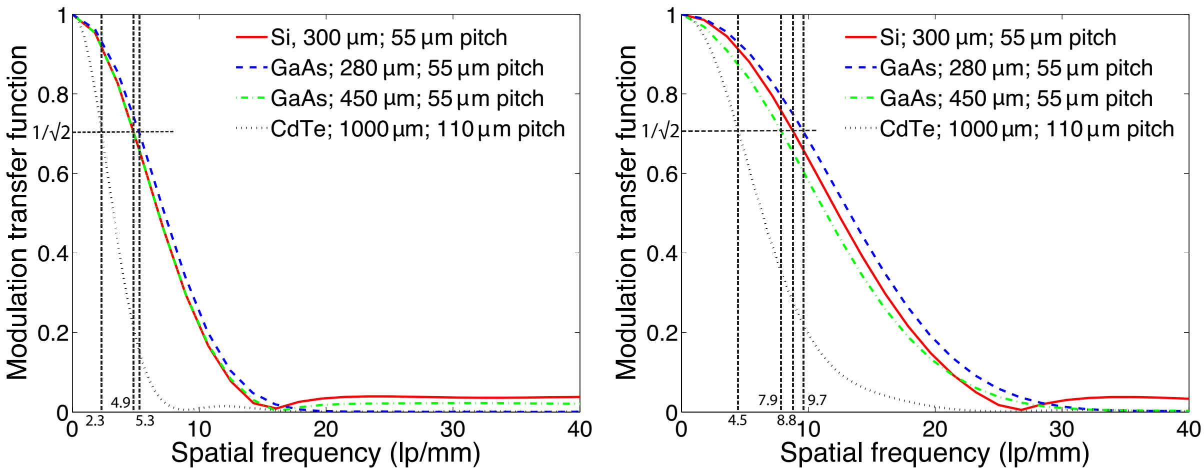

(a) THL at noise floor

(b) THL at 35 keV

Figure 6.19: Detector comparison
The modulation transfer function for each of the detectors with (a) the threshold level at the noise floor and (b) at 35 keV.

6.4 Conclusion

One of the main shortcomings of crystalline high-Z semiconductor material is the moderate homogeneity, which poses limits to the maximum obtainable uniformly responding sensor area. Whereas amorphous selenium can be produced in areas of tens of dm^2, the area of homogeneous gallium arsenide and cadmium telluride is currently limited to approximately 10 cm^2.
Nonetheless, cadmium telluride is an interesting high-Z sensor material. It has a couple of distinct advantages over amorphous selenium. With its higher absorption efficiency ($\sim$ 25% higher for 50 keV photons), lower effective electron-hole pair creation energy ($\sim$ 10 times lower), larger $\mu\tau$-products ($\sim 3{\cdot}10^3$ times larger) and hence longer mean drift lengths ($\sim 10^2$ times longer under normal operating voltages), it can operate in a large temperature range. This makes cadmium-telluride sensors more quantum efficient and more sensitive than selenium-based flat-panel detectors, which allows for use of smaller pixels and/or for shorter acquisition times and hence for imaging with lower dose.
Based on the lateral range of the various charge-spreading mechanisms, 110 µm seems an appropriate pixel pitch for high-Z sensors of 0.5 mm thick and more. This is confirmed by results on the modulation transfer function of both gallium arsenide and cadmium telluride detectors. They show that at a sufficiently high bias voltage, the spatial frequency at which the modulation power is halved approximates the Nyquist frequency, thereby demonstrating that the resolution is dominated by the pixel pitch. Compared to today's flat-panel detectors, which commonly use pixels of $(200\ \mu m)^2$, the pixel size could therefore be reduced by a factor 2 without significantly compromising the resolution.
Equally important for the imaging performance is the amount of noise a detector adds to the input image. To explore the potential of large-area X-ray detectors consisting of a seamless tessellation of multiple smaller detector modules, high-Z sensors with slim edges were fabricated to study the influence of possible edge imperfections on the performance of edge pixels. Results on the characterisation of the edge of the cadmium telluride detector indicate no significant increase of the leakage current and suggest no significant reduction of the charge collection efficiency.
Results on the noise performance show that the high-Z detectors are dominated by fixed-pattern noise, which is most probably the result of crystalline inhomogeneities. Of all three detectors, the 450 µm thick gallium arsenide detector suffers most from fixed-pattern noise, whereas the 280 µm thick gallium arsenide detector shows the least fixed-pattern noise power. Nonetheless, the latter shows the largest increase in fixed-pattern noise towards the edge. Overall, the cadmium telluride detector seems to suffer the least from the slim-edge process, while the ratio between the edge distance and sensor thickness is the smallest of the three. This can be explained by the intactness of the edges of the cadmium telluride sensor (see Figure 6.2). The gallium arsenide sensors show considerably more damage and hence more accurate dicing may lead to an improvement of the noise performance.

In conclusion, both the characterisation and noise performance results indicate that cadmium telluride sensors can be diced very close to the pixel matrix without significantly affecting the detection performance of edge pixels. Apart from crystalline inhomogeneities inherent to compound detectors, this suggests that slim-edge cadmium telluride sensors are suitable for the realisation of a tessellation of edgeless detectors.

A

Measuring I-V and C-V characteristics

Specialised instruments were used for measuring the capacitance (of order pF) and leakage current (of order pA) of the sensor samples studied in Chapter 4.

A.1 Capacitance-voltage set-up

The C-V set-up is diagrammatically depicted in the top part of Figure A.1. It contains an LCR meter[1] that uses the AC impedance technique to measure capacitance. It applies both a DC and small AC voltage to the sensor (denoted as DUT, i.e. device under test) and subsequently measures the impedance, i.e. the magnitude of and phase angle between the AC voltage and current. The imaginary part of the impedance gives the capacitance. The meter uses a so called auto-balancing bridge [121], which ensures virtual ground at the low terminal. Before a measurement is made, the meter is calibrated by determining the circuit capacitance with respect to the ideal capacitance under open-circuit conditions. Furthermore, the shields of the coaxial cables are interconnected close to the probe needles, to ensure that both terminals refer to the same ground potential.

A.2 Current-voltage set-up

The bottom part of Figure A.1 shows the block diagram of the set-up for I-V measurements. The leakage current is measured using source-measure units, which can simultaneously source relatively high voltages (of the order of kV) and measure currents as low as pA's and vice versa. For structures with a p-type stop ring, two source-measure units were used to bias both the active area and stop ring at the same potential and to measure the DC leakage current. Stop rings of n type were left floating.

[1] An LCR meter is an electronic instrument used to measure the inductance (L), capacitance (C) and resistance (R) of a device.

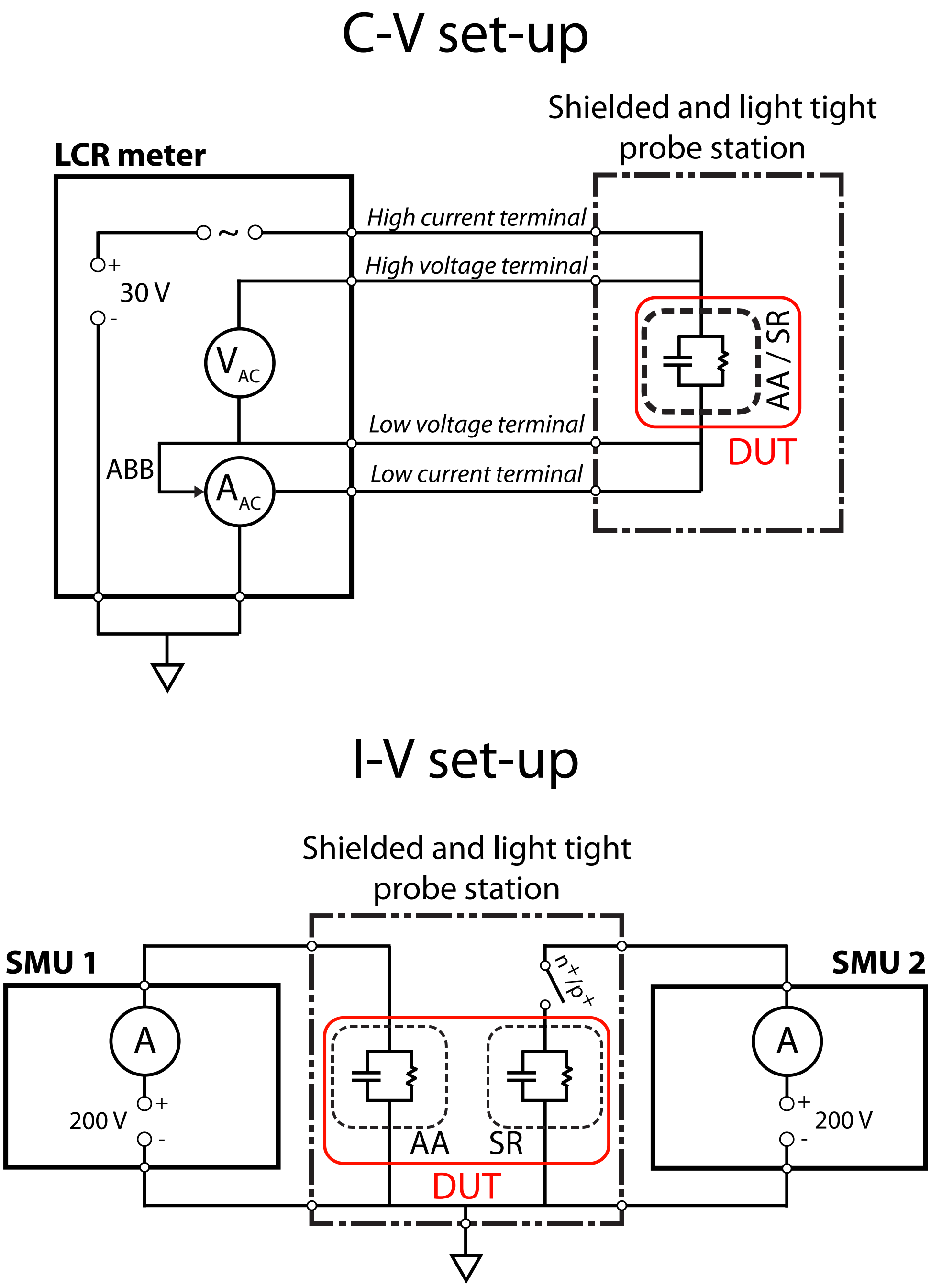

Figure A.1: Block diagrams of the C-V and I-V set-up
The C-V set-up contains an LCR meter to apply both DC and small AC voltages to the device under test (DUT). Subsequently, the AC impedance is measured, from which the capacitance is derived. An auto-balancing bridge (ABB) is used to ensure virtual ground at the low terminal.
The I-V set-up consists of two source-measure units (SMU 1 and SMU 2) that separately apply a DC voltage to the active area and the stop ring and at the same time measure the DC current. For n-type stop-ring structures the stop ring was left floating. Hence the n^+/p^+ switch, which represents the up and down position of the probe needle.

B

Semiconductor device simulation

TCAD[1] software from Synopsis [122] is used to simulate the electrical characteristics of semiconductor devices.

The simulation programme calculates the electrostatic potential distribution and charge-carrier concentrations for user-defined semiconductor structures by numerically solving Poisson's equation and the electron and hole continuity equations. The the charge density in Poisson's equation,

$$\nabla^2\psi = -\frac{\rho}{\epsilon}\,, \tag{B.1}$$

is given by the net sum of the free charge-carrier concentrations and that of the ionised n-type and p-type impurities:

$$\rho = q(p - n + N_d^+ - N_a^-)\,. \tag{B.2}$$

The electron and hole continuity equations are given by Equation 2.24.

In order to solve these equations for a given semiconductor device, the structure is typically approximated by dividing it into smaller, geometrically simple elements, a process is called meshing. Subsequently, the differential equations are applied to each element. By defining boundary conditions, e.g. potentials at each of the electrodes, the software finds the function that best approximates the solution to the equations for each element. This partial solution is determined such that the contribution to the total approximate solution outside the element equals zero. The total approximate solution is subsequently obtained by summing the partial solutions. The programme uses a numerical solver, which iterates repeatedly until the partial solution is accurate enough.

[1]TCAD stands for Technology Computer-Aided Design

Figure B.1 depicts the corner of one of the p-type stop-ring sensor structures of Chapter 4 after meshing.

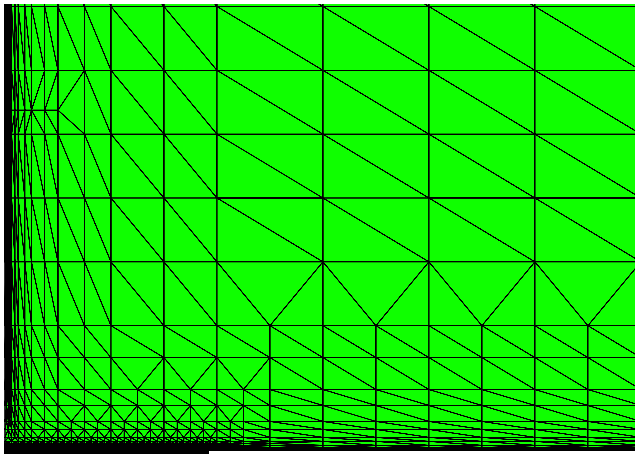

Figure B.1: Meshing
A semiconductor structure is commonly meshed, which allows for finding an approximate solution to the equations by summing the simpler approximate partial solutions of smaller elements.

C

Charge spread

In addition to blur inferred by the non-negligble range of the photoelectron as well as that of Compton scattered photons and possibly generated fluorescence photons or Auger electrons, image quality may degrade due to charge spread caused by diffusion and electrostatic repulsion.

C.1 Diffusion

As described in Section 2.1.4, the generated charge carriers diffuse due to a concentration gradient. In absence of recombination, charge can be considered a conserved quantity. As a result, charge diffusion follows the continuity equation:

$$\frac{\partial n(\vec{r},t)}{\partial t} + \vec{\nabla} \cdot \vec{J}(\vec{r},t) = 0\,. \tag{C.1}$$

It states that a temporal change in carrier concentration leads to a change in current density. Using Fick's law, the continuity equation for electrons becomes:

$$\frac{\partial n(\vec{r},t)}{\partial t} = \vec{\nabla} \cdot (D\vec{\nabla} n(\vec{r},t)) = D\Delta n(\vec{r},t)\,. \tag{C.2}$$

The solution of this differential equation is a Gaussian function, which describes the charge-carrier distribution relative to the centre of mass of the charge cloud as a function of the the drift time t.

$$n(\vec{r},t) = n_0 \left(\frac{1}{\sqrt{(4\pi D t)}}\right)^3 e^{-\dfrac{r^2}{4Dt}}\,, \tag{C.3}$$

with a standard deviation σ of

$$\sigma = \sqrt{2Dt}\,. \tag{C.4}$$

For a constant drift field, this results in the following expression for the lateral spread caused by diffusion:

$$\sigma = \sqrt{2Dt_{\mathrm{drift}}} = \sqrt{2\frac{kT\mu}{q}\frac{d}{v_{\mathrm{drift}}}} = \sqrt{2\frac{kT\mu}{q}\frac{d}{\mu\vec{E}}} = \sqrt{2\,\frac{kTd^2}{qU}}\,, \tag{C.5}$$

where the Einstein relation (see equation 2.21 on page 28) is used and it is assumed that t is the drift time over the full thickness of the sensor.
An alternative expression for the lateral extent of a distribution is the full-width-half-maximum (FWHM). The diffusion spread can therefore be defined as:

$$\mathrm{FWHM} = 2\sqrt{2\,\ln 2}\,\sigma = 4\sqrt{\ln 2\frac{kTd^2}{qU}}\,. \tag{C.6}$$

Note that the spread is only dependent on the temperature, the drift distance and the applied bias voltage. It is independent of the mobility, material used and the energy of the incoming X-ray photon.

C.2 Electrostatic repulsion

Another effect that causes charge spread is the electrostatic repulsion of same-sign charge carriers in the generated electron-hole charge cloud. In [123], the radius of the charge cloud is obtained from the part of the continuity equation that describes the charge-cloud expansion due to repulsion only.

$$\frac{\partial Q(r,t)}{\partial r}\mu E = \frac{\partial Q(r,t)}{\partial r}\mu\frac{1}{4\pi\epsilon_0 r^2} = -\frac{\partial Q(r,t)}{\partial t}\,, \tag{C.7}$$

where $Q(r,t)$ is the total amount of charge inside a spherical charge cloud and μ is the mobility. By using the method of separation of variables and satisfying the condition that the net force on the charge carriers in a sphere of radius r only depends on the number of charge carriers inside the sphere, r can be calculated by

$$r(t) = \sqrt[3]{3\frac{q}{4\pi\epsilon_r\epsilon_0}\mu N t} = \sqrt[3]{3\frac{q}{4\pi\epsilon_r\epsilon_0}N\frac{d^2}{U}}\,, \tag{C.8}$$

where ϵ_r the dielectric constant of the material and N the number of created electron-hole pairs.

D

Response linearity

As discussed in Section 1.2.3, a spectral decomposition of both signal and noise is only possible when a system can be considered linear and shift invariant. Therefore, the linearity of each detector studied in Chapter 6 is measured for a wide range of photon fluxes.

The photon flux at the detector's input stage is estimated using the X-ray spectrum simulation programme SpekCalc [117]. This software calculates the output spectrum of a tungsten-target X-ray tube at one meter distance. In accordance to the set-up as described in Section 6.3.2 on page 122, Figure 6.6 on page 122 shows the simulated spectrum for a peak tube voltage of 70 kVp, a beam angle of 19.5 °, a 21 mm thick aluminium filter and 650 mm of air. SpekCalc calculates a Bremsstrahlung output of approximately 2.8 µGy/mAs at 1 meter. From this it is estimated that the photon flux at the detector's surface is:

$$\frac{2.8}{0.65^2} \cdot 0.1 \cdot 30.17 \cdot 10^3 \approx 2 \cdot 10^4 \text{photons/mm}^2\text{s}\,,$$

where 0.65^2 accounts for the intensity at 65 cm following the inverse-square law, 0.1 is the tube's operation current of 100 µA and $30.17{\cdot}10^3$ is a conversion factor from air kerma[1] to quanta per area, which is defined by the IEC standard.
Figure D.1 shows recorded count-rate density as a function of incoming photon flux for each of the detectors at three different levels of the threshold DAC. All four detectors are operated at a bias voltage that corresponds to a lateral diffusion with a standard deviation of 10 µm (see Table 6.2 on page 126). The plots show excellent linearity (coefficients of determination near 1) and hence the detectors allow for a spectral decomposition of both signal and noise when shift-invariance is assumed.
The yields derived from the slope of the line fits are listed in Table D.1.

[1] Kerma stands for Kinetic Energy Released per MAss. Air kerma parameterises the absorbed dose in air.

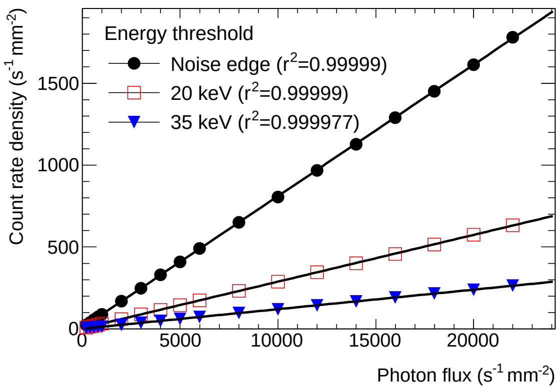

(a) Silicon

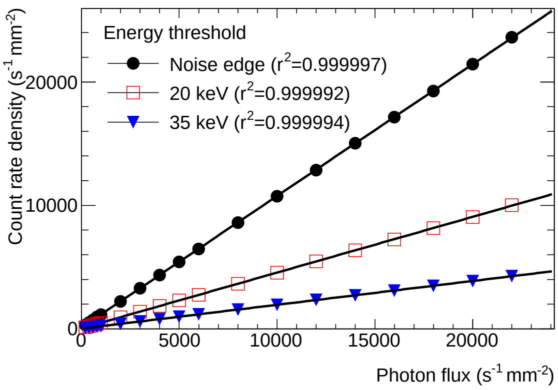

(b) GaAs, 280 µm

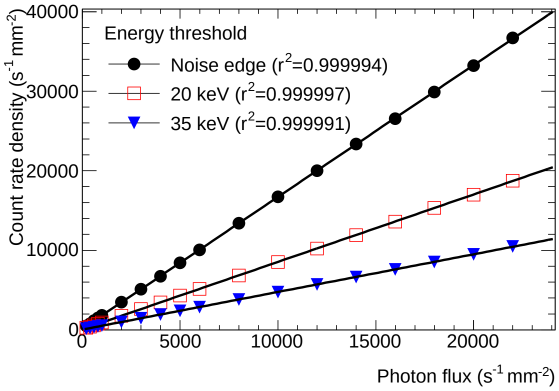

(c) GaAs, 450 µm

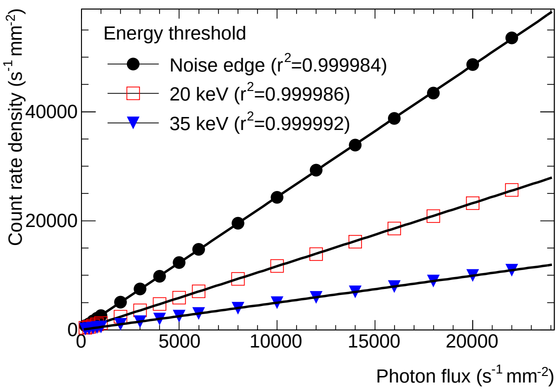

(d) CdTe

Figure D.1: Linearity
The recorded count-rate density as a function of incoming photon flux for each of the detectors at three different levels of the threshold DAC. The photon flux is estimated using the simulated Bremsstrahlung output dose at one meter distance from the tube's focal spot.

Table D.1: Detector yield

Sensor	**Yield**		
	Noise edge	*20 keV*	*35 keV*
Si, 300 µm	0.080	0.029	0.012
GaAs, 280 µm	1.1	0.45	0.19
GaAs, 450 µm	1.7	0.85	0.47
CdTe, 1000 µm	2.4	1.2	0.50

E

Noise power spectra: row dependence

This appendix shows the power spectra of the individual noise components as a function of row number for the detectors studied in Chapter 6. The detectors are operated at a bias voltage that corresponds to a lateral diffusion with a standard deviation of 10 µm and the threshold is set at $\sim$ 20 keV.

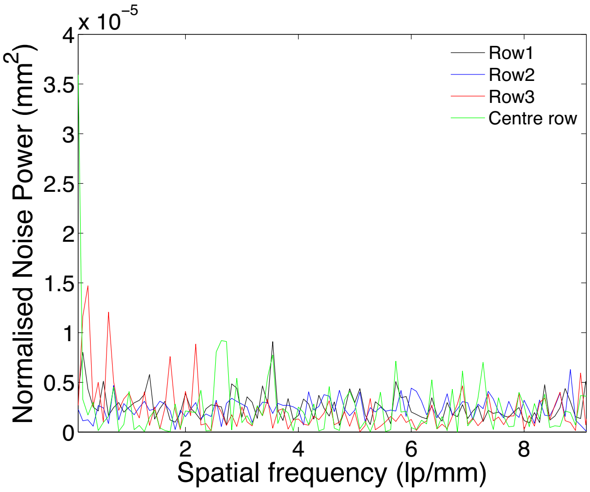

(a) Silicon

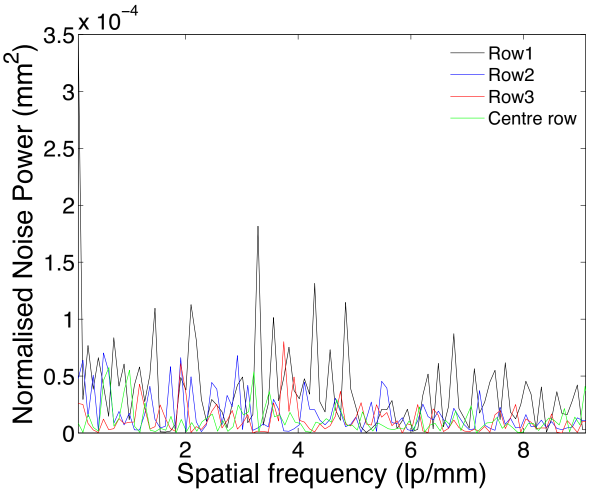

(b) GaAs, 280 µm

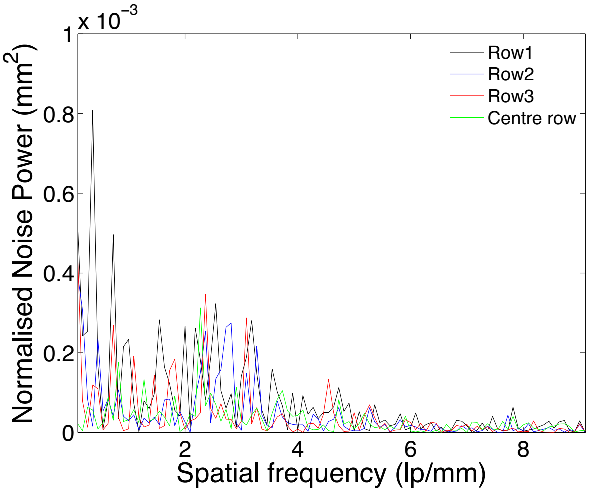

(c) GaAs, 450 µm

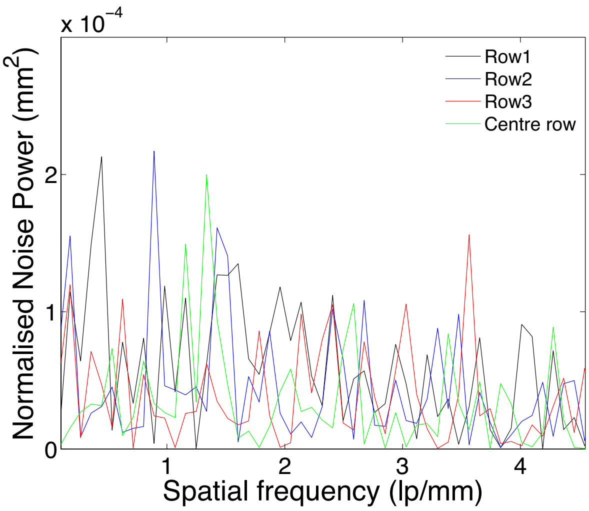

(d) CdTe

Figure E.1: Row dependence – fixed-pattern noise
Power spectra of the fixed-pattern noise of the three outermost rows compared to that of the centre row.

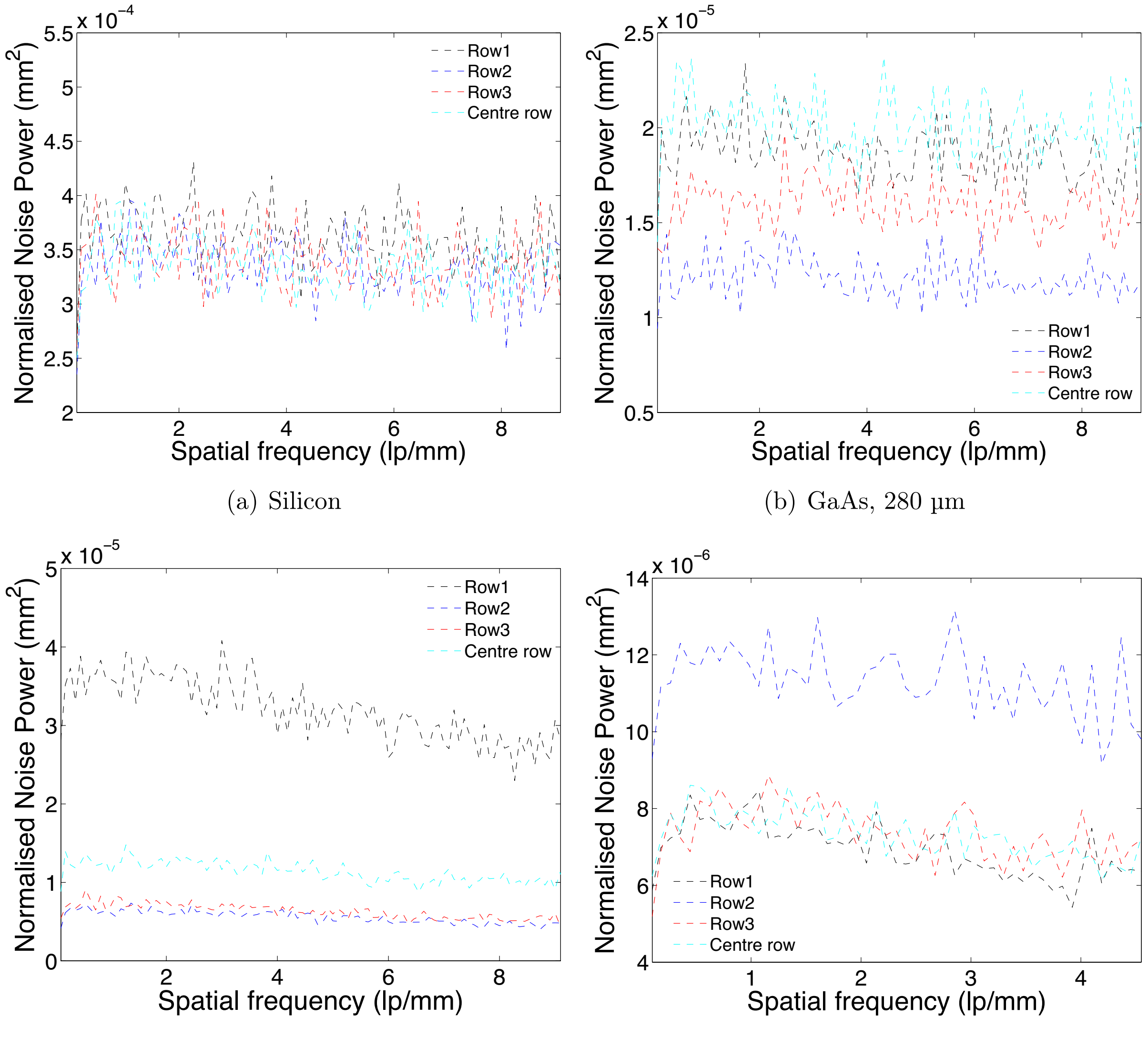

(a) Silicon

(b) GaAs, 280 µm

(c) GaAs, 450 µm

(d) CdTe

Figure E.2: Row dependence – stochastic noise
Power spectra of the stochastic noise of the three outermost rows compared to that of the centre row.

References

[1] Richard D. Deslattes et al. X-ray transition energies: new approach to a comprehensive evaluation. *Rev. Mod. Phys.*, 75:35–99, January 2003.

[2] O. Klein and T. Nishina. Über die Streuung von Strahlung durch freie Elektronen nach der neuen relativistischen Quantendynamik von Dirac. *Zeitschrift für Physik A Hadrons and Nuclei*, 52:853–868, 1929.

[3] J.H. Hubbell et al. A Review, Bibliography, and Tabulation of K, L, and Higher Atomic Shell X-Ray Fluorescence Yields. *Journal of Physical and Chemical Reference Data*, 23:339–364, March 1994.

[4] J.H. Lambert. *Photometria, sive De mensura et gradibus luminis, colorum et umbrae.* 1760.

[5] A. Beer. Bestimmung der Absorption des rothen Lichts in farbigen Flüssigkeiten. *Annalen der Physik*, 162:78–88, 1852.

[6] J. H. Hubbell and Stephen M. Seltzer. Tables of X-ray mass attenuation coefficients and mass energy-absorption coefficients from 1 keV to 20 MeV for elements Z=1 to 92 and 48 additional substances of dosimetric interest. `http://www.nist.gov/pml/data/xraycoef/index.cfm`, 1996.

[7] R. Shaw. The equivalent quantum efficiency of the photographic process. *J. Photogr. Sci.*, 11(199-204), 1963.

[8] J.C. Dainty and R. Shaw. *Image Science, Academic Press, New York*, 1974.

[9] Jacob Beutel, Harold L. Kundel, and Richard L. Van Metter. *Handbook of Medical Imaging*, volume 1. Physics and Psychophysics. SPIE Press, 2000.

[10] Albert Rose. A unified approach to the performance of photographic film, television pickup tubes and the human eye. *J. Soc. Motion Pict. Eng.*, 47:273–294, 1946.

[11] Arthur E. Burgess. The Rose model, revisited. *J. Opt. Soc. Am. A*, 16(3):633–646, March 1999.

[12] J.P. Hespanha. *Linear Systems Theory.* Princeton university press, 2009.

[13] J.T. Dobbins. Effects of undersampling on the proper interpretation of modulation transfer function, noise power spectra, and noise equivalent quanta of digital imaging systems. *Medical Physics*, 22(2):171–181, 1995.

[14] M.J. Yaffe and J.A. Rowlands. X-ray detectors for digital radiography. *Physics in Medicine and Biology*, 42(1):1, 1997.

[15] E. Kotter and M. Langer. Digital radiography with large-area flat-panel detectors. *Eur. Radiol.*, 12:2562–2570, 2002.

[16] J.A. Seibert. Flat-panel detectors: how much better are they? *Pediatr Radiol.*, 36:173–181, 2006.

[17] S.O. Kasap and J.A. Rowlands. Direct-conversion flat-panel X-ray image sensors for digital radiography. *Proceedings of the IEEE*, 90(4):591 –604, April 2002.

[18] Flat Panel X-ray Imaging. Technical report, Varian Medical Systems.

[19] `http://www.trixell.com/`.

[20] S.M. Sze and K. NG Kwok. *Physics of Semiconductor Devices; 3rd ed.* Wiley, Hoboken, NJ, 2007.

[21] Gerhard Lutz. *Semiconductor radiation detectors: device physics*. Springer, Berlin, 1999.

[22] Helmuth Spieler. *Semiconductor detector systems*. Semiconductor Science and Technology. Oxford Univ. Press, Oxford, 2005.

[23] Donald Neamen. *Semiconductor Physics And Devices*. McGraw-Hill, Inc., New York, NY, USA, 2003.

[24] Dieter K. Schroder. *Semiconductor Material and Device Characterization*. Wiley-Interscience, 2006.

[25] P.A.M. Dirac. *The Principles of Quantum Mechanics (International Series of Monographs on Physics)*. Oxford University Press, USA, 4th edition, February 1982.

[26] David Griffiths. *Introduction to Quantum Mechanics*. Pearson, 2nd edition edition, 2005.

[27] Wolfgang Pauli. Über den Zusammenhang des Abschlusses der Elektronengruppen im Atom mit der Komplexstruktur der Spektren. *Zeitschrift für Physik*, 31:765–783, 1925.

[28] E. Fermi. Zur Quantelung des idealen einatomigen Gases. *Zeitschrift für Physik A Hadrons and Nuclei*, 36:902–912, 1926.

[29] Paul F. Weller. An analogy for elementary band theory concepts in solids. *Journal of Chemical Education*, 44(7):391, 1967.

[30] Ludwig Boltzmann. *Vorlesungen uber Gastheorie*. J.A. Barth, 1896.

[31] E.J.W. Verwey, P.W. Haaijman, F.C. Romeijn, and G.W. van Oosterhout. Controlled-Valency Semiconductors. *Philips Research Repts*, 5:173–187, 1950.

[32] M. Fiederle et al. Growth of high-resistivity CdTe and (Cd,Zn)Te crystals. In *Society of Photo-Optical Instrumentation Engineers (SPIE) Conference Series*, volume 5198, pages 48–53, 2004.

[33] W. Shockley and W.T. Read. Statistics of the recombinations of holes and electrons. *Phys. Rev.*, 87:835–842, September 1952.

[34] Adolf Fick. Über Diffusion. *Annalen der Physik*, 170(1):59–86, 1855.

[35] A. Einstein. Zur Theorie der Brownschen Bewegung. *Annalen der Physik*, 324(2):371–381, 1906.

[36] S. Ramo. Currents Induced by Electron Motion. *Proceedings of the IRE*, 27(9):584 – 585, September 1939.

[37] P.J. Sellin. Modelling of the small pixel effect in gallium arsenide X-ray imaging detectors. *Nucl. Instr. and Meth. A*, 434(1):75 – 81, 1999.

[38] Johannes Fink. *Characterization of the Imaging Performance of the Simultaneously Counting and Integrating X-ray Detector CIX*. PhD thesis, University of Bonn, 2010.

[39] Karl Hecht. Zum Mechanismus des lichtelektrischen Primärstromes in isolierenden Kristallen. *Zeitschrift für Physik A Hadrons and Nuclei*, 77:235–245, 1932.

[40] H. Toyama et al. Analysis of Polarization Phenomenon and Deep Acceptor in CdTe Radiation Detector. In *Nuclear Science Symposium Conference Record, 2006. IEEE*, volume 6, pages 3694 –3699, November 2006.

[41] M Niraula et al. Stability issues of high-energy resolution diode type CdTe nuclear radiation detectors in a long-term operation. *Nucl. Instr. and Meth. A*, 491(1 - 2):168 – 175, 2002.

[42] Kyoko Okada et al. Electrode structures in diode-type cadmium telluride detectors: Field emission scanning electron microscopy and energy-dispersive x-ray microanalysis. *Applied Physics Letters*, 92(7):073501 –073501–3, February 2008.

[43] D. Vartsky et al. Radiation induced polarization in CdTe detectors. *Nucl. Instr. and Meth. A*, 263(2 - 3):457 – 462, 1988.

[44] Derek S. Bale and Csaba Szeles. Nature of polarization in wide-bandgap semiconductor detectors under high-flux irradiation: Application to semi-insulating $Cd_{1-x}Zn_xTe$. *Phys. Rev. B*, 77(3):035205, January 2008.

[45] D.S. Bale, S.A. Soldner, and C. Szeles. A mechanism for dynamic lateral polarization in CdZnTe under high flux X-ray irradiation. *Applied Physics Letters*, 92(8):082101, February 2008.

[46] R. S. Ohl. Light-sensitive electric device. U.S. Patent 2.402.662, 1941 (granted in 1946).

[47] M. Riordan and L. Hoddeson. The origins of the pn junction. *Spectrum, IEEE*, 34(6):46 –51, June 1997.

[48] W. Shockley. The theory of p-n junctions in semiconductors and p-n junction transistors. *Bell Syst. Tech. J.*, 28:435, 1949.

[49] W. Schottky. Halbleitertheorie der sperrschicht. *Naturwissenschaften*, 26:843–843, 1938.

[50] Leonardo Rossi, Peter Fischer, Tilman Rohe, and Norbert Wermes. *Pixel Detectors: From Fundamentals to Applications (Particle Acceleration and Detection)*. Springer, March 2006.

[51] Gary S. May and Costas J. Spanos. *Fundamentals of semiconductor manufacturing and process control*. Wiley, Newark, NJ, 2006.

[52] J. Czochralski. Ein neues Verfahren zur Messung der Kristallisationsgeschwindigheit der Metalle. *Zeitschrift für Physikalische Chemie*, 92:219–221, 1918.

[53] J.D. Christian. Zone refining. *J. Chem. Educ.*, 40(3):186, 1963.

[54] Hans J. Scheel and Peter Capper. *Crystal growth technology: from fundamentals and simulation to large-scale production*. Wiley, 2008.

[55] J. Roszmann, S. Dost, and B. Lent. Crystal growth by the travelling heater method using tapered crucibles and applied rotating magnetic field. *Crystal Research and Technology*, 45(8):785–790, 2010.

[56] Gideon Levinson. Principles of dicing. Technical report, Advanced Dicing Techologies Ltd.

[57] `https://jp.hamamatsu.com/sd/Index_eg.html`.

[58] Kiyoshi Arita. Panasonic's plasma dicing technology. Technical report, Suss MicroTec, 2010.

[59] Richard Beaudry. Deep reactive ion etching. Patent EP2105952, September 2009.

[60] Y. Q. Fu et al. Deep reactive ion etching as a tool for nanostructure fabrication. *Journal of Vacuum Science Technology B: Microelectronics and Nanometer Structures*, 27(3):1520 –1526, May 2009.

[61] L. Sainiemi. *Cryogenic deep reactive ion etching of Silicon Micro and Nanostructures*. PhD thesis, 2009.

[62] Franz Laermer and Andrea Schilp. Method of anisotropic etching of silicon. U.S. Patent 6.531.068, 2003.

[63] `https://rd50.web.cern.ch/rd50/`.

[64] P.A. Tove. Methods of avoiding edge effects on semiconductor diodes. *Journal of Physics D: Applied Physics*, 15(4):517, 1982.

[65] P.A. Tove, S.A. Hyder, and G. Susila. Diode characteristics and edge effects of metal-semiconductor diodes. *Solid-State Electronics*, 16(4):513 – 521, 1973.

[66] M. Da Rold et al. Study of breakdown effects in silicon multiguard structures. *Nuclear Science, IEEE Transactions on*, 46(4):1215 –1223, August 1999.

[67] Zheng Li et al. Electrical and transient current characterization of edgeless Si detectors diced with different methods. *Nuclear Science, IEEE Transactions on*, 49(3):1040 – 1046, June 2002.

[68] B. Perea Solano et al. Edgeless silicon pad detectors. *Nucl. Instr. and Meth. A*, 560(1):135 – 138, 2006.

[69] Andrew Blue et al. Edgeless sensor development for the LPD hybrid pixel detector at XFEL. *Nucl. Instr. and Meth. A*, 607(1):55 – 56, 2009.

[70] G. Pellegrini et al. Characterization of edgeless detectors fabricated by dry etching process. *Nucl. Instr. and Meth. A*, 576(1):95 – 97, 2007.

[71] Tanja Palviainen, Tuure Tuuva, and Kari Leinonen. Minimizing guard ring dead space in silicon detectors with an n-type guard ring at the edge of the detector. *Nucl. Instr. and Meth. A*, 573(1-2):277 – 279, 2007.

[72] Mario Deile et al. Tests of a Roman Pot Prototype for the TOTEM Experiment. *Proceedings of PAC05*, 2005.

[73] Vladimir Eremin, Christian Joram, and Gennaro Ruggiero. HV Test of the CTS Edgeless Silicon Detector in Vacuum and Close to a Grounded Plate. `http://totem.web.cern.ch/Totem/docs/HVTestNote.pdf`, May 2007.

[74] E. Noschis et al. Final size planar edgeless silicon detectors for the TOTEM experiment. *Nucl. Instr. and Meth. A*, 563(1):41 – 44, 2006.

[75] G. Ruggiero, V. Eremin, and E. Noschis. Planar edgeless silicon detectors for the TOTEM experiment. *Nucl. Instr. and Meth. A*, 582(3):854 – 857, 2007.

[76] E. Verbitskaya et al. Electrical properties of the sensitive side in Si edgeless detectors. *Nucl. Instr. and Meth. A*, 604(1-2):246 – 249, 2009.

[77] J.P. Balbuena et al. Simulation of irradiated edgeless detectors. In *Nuclear Science Symposium Conference Record, 2008. NSS '08. IEEE*, pages 2553 –2556, 19-25 2008.

[78] E. Verbitskaya et al. Advanced model of silicon edgeless detector operation. In *Nuclear Science Symposium Conference Record, 2008. NSS '08. IEEE*, pages 2711 –2716, 19-25 2008.

[79] G. Ruggiero et al. Characteristics of edgeless silicon detectors for the Roman Pots of the TOTEM experiment at the LHC. *Nucl. Instr. and Meth. A*, 604(1-2):242 – 245, 2009.

[80] E. Noschis, V. Eremin, and G. Ruggiero. Simulations of planar edgeless silicon detectors with a current terminating structure. *Nucl. Instr. and Meth. A*, 574(3):420 – 424, 2007.

[81] M. Christophersen et al. Laser-scribing and Al_2O_3 sidewall passivation of p-type sensors. Presentation at 6th Trento Workshop on Advanced Silicon Radiation Detectors, 2011.

[82] C.J. Kenney et al. Active-edge planar radiation sensors. *Nucl. Instr. and Meth. A*, 565:272–277, September 2006.

[83] M. Povoli et al. Development of planar detectors with active edge. *Nucl. Instr. and Meth. A*, 658(1):103 – 107, 2011.

[84] Juha Kalliopuska et al. Characterization of edgeless pixel detectors coupled to Medipix2 readout chip. *Nucl. Instr. and Meth. A*, 648(0):S32 – S36, 2011.

[85] Simo Eränen et al. 3D processing on 6 in. high resistive SOI wafers: Fabrication of edgeless strip and pixel detectors. *Nucl. Instr. and Meth. A*, 607(1):85 – 88, 2009.

[86] D. Niederlohner et al. Practical aspects of energy weighting in X-ray imaging. In *NSS Conference Record, 2004 IEEE*, volume 5, pages 3191 – 3194 Vol. 5, October 2004.

[87] P.M. Shikhaliev. Energy-resolved computed tomography: first experimental results. *Phys. Med. Biol.*, 2008.

[88] Rafael Ballabriga. *The Design and Implementation in 0.13 μm CMOS of an Algorithm Permitting Spectroscopic Imaging with High Spatial Resolution for Hybrid Pixel Detectors.* PhD thesis, Ramon Llull U., Barcelona, Barcelona, 2009.

[89] `http://medipix.web.cern.ch/medipix/`.

[90] Bjørn Tore Knudsen. Presentation of the WA97 experiment at CERN. *Czechoslovak Journal of Physics*, 47:925–929, 1997.

[91] M. Campbell et al. A readout chip for a 64×64 pixel matrix with 15-bit single photon counting. *IEEE Transactions on Nuclear Science*, 45(3):751 –753, June 1998.

[92] X. Llopart. *Design and Characterization of 64K Pixels Chips Working in Single Photon Processing Mode.* PhD thesis, Mid Sweden University, Sundsvall, 2007.

[93] F. Krummenacher. Pixel detectors with local intelligence: an IC designer point of view. *Nucl. Instr. and Meth. A*, 305(3):527 – 532, 1991.

[94] X. Llopart. *MPIX2MXR20 Manual v2.3.* CERN, 2006.

[95] Harry van der Graaf. Gridpix: An integrated readout system for gaseous detectors with a pixel chip as anode. *Nucl. Instr. and Meth. A*, 580(2):1023 – 1026, 2007.

[96] X. Llopart et al. Timepix, a 65k programmable pixel readout chip for arrival time, energy and/or photon counting measurements. *Nucl. Instr. and Meth. A*, 581(1-2):485 – 494, 2007.

[97] Vladimir Gromov et al. Development and applications of the timepix3 readout chip. *PoS*, VERTEX 2011:46, 2011.

[98] R. Ballabriga et al. Medipix3: a 64k pixel detector readout chip working in single photon counting mode with improved spectrometric performance. *Nucl. Instr. and Meth. A*, 633, Supplement 1(0):S15 – S18, 2011.

[99] R. Ballabriga, W. Wong, and X. Llopart. *Medipix3 manual.* CERN, 2009.

[100] Enrico Jr Schioppa, Josef Uher, and Jan Visser. Construction and test of an X-ray CT setup for material resolved 3D imaging with Medipix based detectors. *Journal of Instrumentation*, 7(10):C10007, 2012.

[101] Zdenek Vykydal et al. The ReLAXD project: Development of four-side tilable photon-counting imagers. *Nucl. Instr. and Meth. A*, 591(1):241 – 244, 2008.

[102] Jan Visser et al. A gigabit per second read-out system for medipix quads. *Nucl. Instr. and Meth. A*, 633, Supplement 1(0):S22 – S25, 2011.

[103] D.S. Tezcan et al. Scalable through silicon via with polymer deep trench isolation for 3d wafer level packaging. In *59th Electronic Components and Technology Conference*, pages 1159 –1164, 26-29 2009.

[104] Y. Mita et al. Aspect Ratio Dependent Scalloping Attenuation in DRIE and an Application to Low-Loss Fiber-Optical Switches. In *19th IEEE International Conference on Micro Electro Mechanical Systems*, pages 114 –117, 2006.

[105] Hamamatsu. Stealth dicing technology and applications. Technical report, Hamamatsu, March 2005.

[106] D.B. Boltje. Dimension optimization of the Medipix2 chip. Master's thesis, Nikhef, 2008.

[107] S.I. Parker, C.J. Kenney, and J. Segal. 3D – A proposed new architecture for solid-state radiation detectors. *Nucl. Instr. and Meth. A*, 395(3):328 – 343, 1997.

[108] `http://totem.web.cern.ch/Totem/docs/DetectSpec.pdf`.

[109] E.N. Koffeman. *A luminosity measurement at LEP using the L3 detector*. PhD thesis, 1996.

[110] `http://www.synopsys.com/Tools/TCAD/Pages/default.aspx`.

[111] Wilfried von Ammon and Heinz Herzer. The production and availability of high resistivity silicon for detector application. *Nucl. Instr. and Meth. A*, 226(1):94 – 102, 1984.

[112] A.D. McNaught and A. Wilkinson, editors. *IUPAC. Compendium of Chemical Terminology*. Blackwell Scientific Publications, Oxford, 2nd edition, 1997.

[113] A. Shor, Y. Eisen, and I. Mardor. Edge effects in pixelated CdZnTe gamma detectors. *Nuclear Science, IEEE Transactions on*, 51(5):2412 – 2418, October 2004.

[114] T.J. McMahon. Dark current transients in thin-film CdTe solar cells. *Proceedings of the 29th IEEE Photovoltaic Specialists Conference*, 2002.

[115] Brian E. McCandless and James R. Sites. *Cadmium Telluride Solar Cells*, chapter 14. John Wiley & Sons, 2003.

[116] `http://www.acrorad.co.jp/us/`.

[117] G Poludniowski et al. SpekCalc : a program to calculate photon spectra from tungsten anode x-ray tubes. *Physics in Medicine and Biology*, 54(19):N433, 2009.

[118] J. Marchal. Discriminator threshold dependence of the Noise Power Spectrum in single-X-ray-photon counting silicon strip detectors. *Journal of Instrumentation*, 5(11):P11002, 2010.

[119] F.-F. Yin, M. L. Giger, and K. Doi. Measurement of the presampling modulation transfer function of film digitizers using a curve fitting technique. *Medical Physics*, 17:962–966, November 1990.

[120] Liang Jin et al. Applications of direct detection device in transmission electron microscopy. *Journal of Structural Biology*, 161(3):352 – 358, 2008.

[121] *Impedance Measurement Handbook*. Agilent Technologies Inc., 4th edition, June 2009.

[122] `http://www.synopsys.com/Tools/TCAD/DeviceSimulation/Pages/default.aspx`.

[123] Emilio Gatti et al. Dynamics of electrons in drift detectors. *Nucl. Instr. and Meth. A*, 253(3):393 – 399, 1987.

Summary

Detector developments for medical radiography systems focus on improving image quality while using a lower dose of X-rays. This requires low-noise detectors with a high spatial resolution capable of accurately measuring both small and large intensity variations. To realise such a detector, the sensor as well as the read-out electronics must be optimised.
Current CCD-based and TFT-based detectors measure intensity by integrating the amount of charge generated by X-ray conversion in the sensor. As a result, high-energy photons count more than low-energy ones, at the expense of the signal-to-noise ratio. This thesis presents an alternative detector, based on a counting chip (Medipix). It measures photon intensity by counting the number of induced signal pulses and thus the number of converted X-rays. In this way, each photon is treated similarly, irrespective of its energy. Output images of such photon counters are therefore in better agreement with intensity distributions at the detector's input than those of charge integrating detectors. The latest descendant of the Medipix chip family (Medipix-3) even allows to combine signals induced on clusters of pixels, which benefits energy resolution. Alternatively – and perhaps even more important for radiographic applications – the electronics that enable communication between neighbouring pixels can be used to distinguish between photons of different energies. As a consequence, the energy dependence of the intensity attenuation through the object under study can be accounted for.
Detectors based on Medipix chips are so called hybrid pixel detectors. In this context, hybrid means that both the sensor and the read-out chip are fabricated separately before they are assembled together. Inherently, this allows for independent optimisation and offers the freedom to use a wide range of sensor materials, such as gallium arsenide and cadmium telluride.
Crystalline semiconductor sensors of such high atomic numbers are very attractive for tomorrow's radio-diagnostic systems. In comparison to amorphous selenium, a widely used conversion material in today's medical X-ray detectors, they have a higher quantum efficiency due to their higher absorption efficiency, lower effective electron-hole pair creation energy and relatively good charge transport properties. On top of that, they show low leakage currents in a large temperature domain.
Nevertheless, the area of the Medipix chip (~ 2 cm^2) as well as the limited area of currently available crystals (~ 10 cm^2) form a real challenge to make competitive large-area diagnostic systems. A solution is to realise a tessellation of Medipix-based detectors.

However, current Medipix-based detectors are insensitive at their edges and would therefore introduce seams in a tessellated image. For a relevant part, the inactive edge is caused by so called guard electrodes at the edge of the sensor. Although these electrodes protect the sensor's active area from detrimental effects induced by the often imperfect edge, they are responsible for a significant loss of sensitive sensor volume near the edge. The width of this inactive volume is referred to as edge distance and is for conventional sensors typically comparable to the sensor's thickness.
For the purpose of minimising the inactive edge, this thesis presents a study on the performance of both active-edge and slim-edge sensors. Both sensor types are characterised by edge distances that are only 5 % to 35 % of the sensor's thickness. Active-edge sensors differ from slim-edge sensors in the way their edges are processed. Active edges are doped, as a result of which the electric-field distribution in the sensor is such that the sensitive volume is isolated from the edge. Slim-edge sensors do not have such an electrode.
To minimise the influence of unwanted edge effects on the detection performance of the active area, minimally damaging dicing methods need to be used. Two examples of such techniques are anisotropic etching using a chemically active ion plasma and cutting by means of strongly focussed laser light.
Inter alia, edge effects translate into a locally increased conductivity, which may cause an unwanted increase of leakage current in the sensor's active area. In this thesis, a batch of active-edge p-in-n silicon sensors is electrically characterised. They all have a partially doped edge and a narrow guard electrode of different width and polarity at the edge, so called stop rings. Results show that the leakage current of these prototypes is comparable to that of conventional sensors, while the edge distance is reduced by a factor 5 to 10. Next to that, the results suggest that stop rings of positive polarity protect the active area better against edge-induced leakage currents than stop rings of negative polarity.
Although active edges allow for a reduction of the inactive edge, they cause an alteration of the effective volume of edge pixels. Simulations of the potential distribution in 150 µm thick overdepleted sensors with an edge distance of 50 µm (without stop ring), indicate that only $\sim$ 60% of the physical volume of outermost pixels can be considered effective, while the effective volume of second outer pixels exceeds the physical volume by $\sim$ 60%. Measurements on the charge collected by the outermost pixels show good agreement with these simulations. Three-dimensional reconstruction of the effective volumes even shows resemblance with the simulated pixel-separating field lines. The same data also allowed to estimate the edge of the sensitive volume with respect to the physical edge. The most optimistic results show that this volume is only 2 µm apart from the edge, which indicates a very small insensitive area. That suggests that such sensors are very suitable as building blocks for a tessellation of detectors.
The influence of edge effects on the detection performance of edge pixels of slim-edge sensors of both crystalline gallium-arsenide and cadmium-telluride were studied as well. Whereas the leakage current of the cadmium telluride sensors show long settling times ($\sim$ 60 s), the edge pixels do not show higher leakage-current densities than non-edge pixels do. Moreover, no significant decrease of the charge collection efficiency is observed at the edge. Results concerning the noise power demonstrate that the response of high-Z sensors is dominated by fixed-pattern noise, which is most probably caused by crystalline

inhomogeneities. Nevertheless, this noise component can be suppressed by applying a so called flat-field correction. Of all studied high-Z sensors, the edge pixels of the cadmium-telluride sensors show the least increase in noise power with respect to non-edge pixels, while the ratio between the edge distance and thickness is smallest for these sensors (only 6.5%). This shows that cadmium-telluride sensors can be diced very close to the active area without significantly affecting the response of edge pixels. Apart from its moderate homogeneity, it indicates that this high-Z material is suitable for realising a tessellation of detectors with slim-edge sensors.

It can be concluded that both active-edge silicon sensors and slim-edge cadmium-telluride sensors have potential to be used in future intelligent and dose-efficient large-area detectors. It is likely that the width of the insensitive edge can be reduced to below the size of one pixel.

Samenvatting

Detectorontwikkeling voor medische-radiografiesytemen spitst zich momenteel toe op het verhogen van beeldkwaliteit met gebruik van een lagere stralingsdosis. Een hoge beeldkwaliteit wordt gekenmerkt door een goede beeldscherpte en een minimale hoeveelheid ruis. Dit vereist detectoren met een hoge ruimtelijke resolutie, welke het vermogen hebben om zowel grote als kleine intensiteitsverschillen nauwkeurig te meten. Om een dergelijke detector te realiseren, moeten zowel de sensor als de uitlezing worden geoptimaliseerd.
De huidige op CCD- en TFT-gebaseerde detectoren integreren de hoeveelheid gegenereerde lading in de sensor en gebruiken dat als maat voor de Röntgenstralingsintensiteit per pixel. Dit maakt dat hoog-energetische fotonen zwaarder worden gewogen dan laag-energetische, hetgeen de signaal-ruis verhouding niet ten goede komt. In dit proefschrift gebruiken we een fotontellende uitleeschip (Medipix) als basis om dit probleem op te lossen. Deze chip meet de Röntgenstralingsintensiteit door het aantal geïnduceerde signaalpulsen te tellen. Op deze manier wordt ieder foton gelijk behandeld, ongeacht zijn energie. Het beeld van fotontellende detectoren komt daardoor beter overeen met de intensiteitsverdeling aan de ingang van de detector dan dat van ladingsintegrerende detectoren. De laatste afstammeling van de Medipix-chip familie (Medipix-3) kan bovendien signalen die op clusters van pixels worden geïnduceerd met elkaar combineren, hetgeen de energieresolutie ten goede komt. Maar misschien nog wel belangrijker voor radiografische toepassingen: de elektronica die communicatie tussen naburige pixels bewerkstelligt, kan worden aangewend om fotonen van verschillende energieën te onderscheiden. Dit stelt ons in staat om de energie-afhankelijkheid van de intensiteitsverzwakking door het te bestuderen object te corrigeren.
Medipix detectoren worden ook wel aangeduid als hybride pixel detectoren. In deze context betekent hybride dat zowel de sensor als de uitleeschip apart wordt gefabriceerd voordat ze samen worden geassembleerd om één detector te vormen. Dit maakt het mogelijk om beide onderdelen afzonderlijk van elkaar te optimaliseren en bovendien biedt het de mogelijkheid om verscheidene sensormaterialen, zoals kristallijn gallium arsenide en cadmium telluride, te gebruiken.
Zulke halfgeleidersensoren met een hoog atoomgetal zijn uitermate interessant voor toekomstige radio-diagnostische systemen. In vergelijking tot amorf selenium, een veelgebruikt conversiemateriaal in huidige systemen, hebben ze namelijk een hogere kwantumëfficientie vanwege hun hoge absorptievermogen, lagere effectieve elektron-gat-paar

creatie-energie en relatief goede ladingstransport-eigenschappen. Bovendien vertonen ze weinig lekstroom in groot temperatuurdomein.
Echter, zowel het oppervlak van de Medipix chip (~ 2 cm^2) als het gelimiteerde oppervlak van de huidig beschikbare kristallen (~ 10 cm^2) vormt een grote uitdaging om diagnostische systemen met een groot oppervlak te realiseren. Een getegeld oppervlak van Medipix detectoren zou de oplossing daarvoor kunnen bieden. Het huidige ontwerp is echter zo dat Medipix detectoren ongevoelig aan de rand zijn, hetgeen zich zou vertalen in naden in het samengestelde beeld. De afschermelektroden aan de rand van sensoren, die weliswaar het actieve gebied van de sensoren beschermen tegen schadelijke invloeden van hun veelal imperfecte rand, zijn één van de veroorzakers van een dode rand. De breedte van deze rand wordt aangeduid als randafstand en is in het geval van conventionele sensoren van vergelijkbare grootte als de dikte van de sensor.
Ten behoeve van minimalisatie van deze ongevoelige rand, beschrijft dit proefschrift een studie naar het detectiegedrag van zowel actieve-rand als smalle-rand sensoren. Beide typen worden gekenmerkt door een randafstand die typisch 5 % tot 35 % van de sensordikte bedraagt. Actieve-rand sensoren onderscheiden zich van smalle-rand sensoren door hun gedoteerde rand. Deze randelektrode zorgt voor een elektrisch-veldverdeling in de sensor die het gevoelige sensorvolume van de rand isoleert. Smalle-rand sensoren hebben deze elektrode niet.
Om ongewenste randeffecten zo veel mogelijk te voorkomen, is men bij de fabricage van dit type sensoren genoopt tot het gebruik van zaagmethoden die een minimale hoeveelheid schade aan de rand toebrengen. Daarbij moet gedacht worden aan technieken als anisotroop etsen met behulp van een chemisch actief ionenplasma of snijden door middel van sterk gefocusseerd laserlicht.
Randeffecten vertalen zich onder andere in een lokaal vergroot geleidingsvermogen, hetgeen leidt tot verhoogde lekstroom. Om de hoge gevoeligheid van sensoren te waarborgen, dient de lekstroom zo laag mogelijk gehouden te worden. In dit proefschrift is een groep actieve-rand p-in-n silicium sensoren elektrisch gekarakteriseerd. Alle zijn vervaardigd met partieel gedoteerde randen en smalle afschermelektroden van verschillende breedte en polariteit op de rand, zogeheten stop-ringelektroden. De resultaten laten zien dat de lekstroom van deze prototypes vergelijkbaar is met dat van conventionele sensoren, terwijl de randafstand met een factor 5 tot 10 is verkleind. Bovendien suggereren de resultaten dat stop-ringelektroden van positieve polariteit het actieve gebied beter beschermen tegen rand-geïnduceerde lekstromen dan die van negatieve polariteit. Een verklaring hiervoor is dat de p-type stop-ringelektroden oppervlaktestromen beter afvoeren.
Hoewel actieve-randtechnologie een verkleining van de inactieve rand toelaat zonder dat het gevoelige gebied door lekstroom wordt overspoeld, verbuigt de randelektrode de veldlijnen in het gebied dichtbij de rand. Dit leidt ertoe dat het effectieve volume van randpixels verschilt van hun fysieke volume. Vanzelfsprekend is de grootte van dat verschil afhankelijk van het potentiaalverschil tussen het actieve gebied en de achterkant van de sensor. Simulaties van de potentiaalverdeling in 150 µm dikke overgedepleteerde sensoren met een randafstand van 50 µm (zonder stop-ringelektrode), geven aan dat slechts circa 60% van het fysieke volume van de buitenste pixels als effectief kan worden beschouwd, terwijl het effectieve volume van de op één na buitenste pixels circa 60% groter is dan

hun fysieke volume. Metingen aan de ladingsverdeling in de buitenste pixels stemmen nauwkeuring overeen met de verhoudingen tussen de gesimuleerde effectieve pixelvolumes. Dezelfde metingen geven aan dat het actieve volume zich kan uitbreiden tot aan 2 µm van de rand. Dit betekent een goede geschiktheid van dit type sensoren voor gebruik als bouwsteen voor een getegeld oppervlak van detectoren.
Zoals gezegd hebben smalle-rand sensoren helemaal geen randelektrode. Het gevoelige volume kan zodoende de rand bereiken, maar eventuele randimperfecties kunnen de detectie-eigenschappen van het actieve gebied nabij de rand wel negatief beïnvloeden. De prestaties van randpixels van smalle-rand sensoren van zowel kristallijn gallium-arsenide als cadmium-telluride zijn daarom onder de loep de genomen. Hoewel de lekstroom van de cadmium-telluride lange insteltijden (~ 60 s) laat zien, vertonen de randpixels geen hogere lekstroomdichtheden dan niet-randpixels. Ook is er geen significante verlaging van de ladingscollectie-efficiëntie waargenomen aan de rand. Resultaten inzake het ruisvermogen laten zien dat de respons van hoge-Z sensoren gedomineerd wordt door vast-patroonruis, hetgeen wordt veroorzaakt door kristallijne inhomogeniteiten. Deze vorm van ruis kan echter worden onderdrukt door middel van het toepassen van een zogeheten flat-field correctie. Van de bestudeerde hoge-Z sensoren vertonen de randpixels van de cadmium-telluride sensoren de minste toename in ruisvermogen ten opzichte van de niet-randpixels, terwijl de verhouding tussen randafstand en sensordikte voor deze sensoren het kleinst is (slechts 6.5%). Dit toont aan dat cadmium-telluride sensoren tot op zeer kleine afstand van het actieve gebied gezaagd kunnen worden zonder dat het de respons van de randpixels significant beïnvloedt. Afgezien van de bescheiden homogeniteit, zou dit hoge-Z materiaal geschikt kunnen zijn voor een getegeld oppervlak van intelligente en dosis-efficiënte detectoren.
Concluderend kan gesteld worden dat zowel actieve-rand silicium sensoren als smalle-rand cadmium-telluride sensoren potentieel hebben om gebruikt te worden in toekomstige grote detectoren. Het is waarschijnlijk dat de breedte van de ongevoelige rand gereduceerd kan worden tot het formaat van minder dan één pixel.

Dankwoord

Allen die aan de totstandkoming van dit proefschrift hebben bijgedragen, betuig ik mijn dank. Bijzonder is mijn erkentelijkheid voor de ontvangen begeleiding en adviezen van mijn promotor Els Koffeman en co-promotores Martin van Beuzekom en Jan Visser, alsmede voor de inspirerende samenwerking met Erik Heijne.
Het in dit proefschrift beschreven werk zou niet mogelijk zijn geweest zonder toegang te hebben gehad tot proefmateriaal, faciliteiten en kennis beschikbaar gesteld door leden van verschillende samenwerkingsverbanden. Bij dezen bedank ik mijn collegae van CERN, PANalytical, IMEC, Canberra Semiconductor, VTT, Philips Healthcare en Philips Applied Technologies voor de samenwerking.
Tevens ben ik zeer dankbaar voor de technische ondersteuning van Joop Rövekamp, Bas van der Heijden en Oscar van Petten.
Tenslotte bedank ik mijn paranimfen, Nick Miesen en John Ottersbach, voor hun vriendschap en morele steun gedurende de afgelopen jaren.